

Cosmic Ray Backgrounds for Dark Matter Indirect Detection

Philipp Mertsch



Balliol College
University of Oxford

A thesis submitted for the degree of
Doctor of Philosophy
Trinity 2010

Cosmic Ray Backgrounds for Dark Matter Indirect Detection.

Philipp Mertsch, Balliol College.

A thesis submitted for the degree of *Doctor of Philosophy*. Trinity 2010.

Abstract

The identification of the relic particles which presumably constitute cold dark matter is a key challenge for astroparticle physics. Indirect methods for their detection using high energy astrophysical probes such as cosmic rays have been much discussed. In particular, recent ‘excesses’ in cosmic ray electron and positron fluxes, as well as in microwave sky maps, have been claimed to be due to the annihilation or decay of dark matter. In this thesis, we argue however that these signals are plagued by irreducible astrophysical backgrounds and show how plausible conventional physics can mimic the alleged dark matter signals.

In chapter 1, we review evidence of, and possible particle candidates for, cold dark matter, as well as our current understanding of galactic cosmic rays and the state-of-the-art in indirect detection. All other chapters contain original work, mainly based on the author’s journal publications [1, 2, 3]. In particular, in chapter 2, we consider the possibility that the rise in the positron fraction observed by the PAMELA satellite is due to the production through (hadronic) cosmic ray spallation and subsequent acceleration of positrons, in the same sources as the primary cosmic rays. We present a new (unpublished) analytical estimate of the range of possible fluctuations in the high energy electron flux due to the discreteness of plausible cosmic ray sources such as supernova remnants. Fitting our result for the total electron-positron flux measured by the Fermi satellite allows us to fix the only free parameter of the model and make an independent prediction for the positron fraction. Our explanation relies on a large number of supernova remnants nearby which are accelerating hadronic cosmic rays. Turning the argument around, we find encouraging prospects for the observation of neutrinos from such sources in km³-scale detectors such as IceCube.

Chapter 3 presents a test of this model by considering similar effects expected for nuclear secondary-to-primary ratios such as B/C. A rise predicted above $\mathcal{O}(100)$ GeV/n would be a unique confirmation of our explanation for a rising positron fraction and *rule out* the dark matter expla-

nation.

In chapter 4, we review the assumptions made in the extraction of the ‘WMAP haze’ which has also been claimed to be due to electrons and positrons from dark matter annihilation in the Galactic centre region. We argue that the energy-dependence of their diffusion means that the extraction of the haze through fitting to templates of low frequency diffuse galactic radio emission is unreliable. The systematic effects introduced by this can, under specific circumstances, reproduce the residual, suggesting that the ‘haze’ may be just an artefact of the template subtraction.

We present a summary and thoughts about further work in the epilogue.

Acknowledgements

First and foremost, I want to express my deeply felt gratitude towards my DPhil advisor, Prof Subir Sarkar. Over the last three years, Subir has granted me the freedom I wanted and given me the guidance I needed, providing the best possible environment for the completion of this thesis. I consider myself lucky having had such a committed, diligent and supportive supervisor. His vast knowledge and the enlightening discussions with him have left a lasting imprint on me.

As an Early Stage Researcher in the EU Research and Training Network “UniverseNet” I have benefited from generous financial support (supplemented by an STFC Postgraduate Studentship). Being part of this community and meeting young researchers from all over the world has been an enriching experience which I am grateful for.

Furthermore, I thank Markus Ahlers for his fruitful collaboration and the inspiring discussions we had during his time at Oxford and afterwards. There are many more people at Oxford who have contributed in one way or the other, from the helpful admin staff, my office mates and the other “first years” to all of my friends who had to put up with my going into hiding from time to time.

Finally, I want to thank my family, who I owe my education and my critical mind to, for their continuous support. It is Anneliese who has carried most of the burden over the last three years and whose witty advice and loving support has been the most precious gift.

Contents

Abstract	2
Acknowledgements	4
Contents	5
1. Introduction	7
1.1. Dark Matter	7
1.1.1. Evidence for dark matter	7
1.1.2. Particle candidates	10
1.2. Cosmic Rays	17
1.2.1. Galactic and extra-galactic cosmic rays	17
1.2.2. The standard model of galactic cosmic rays	19
1.2.3. Supernova remnants as sources	20
1.2.4. The transport equation	23
1.2.5. Diffusive shock acceleration	25
1.2.6. Galactic propagation	30
1.2.7. Observational results on the nuclear component	38
1.3. Dark Matter Indirect Detection	42
1.3.1. Antimatter	43
1.3.2. The total electron-positron flux	48
1.3.3. Gamma-rays	50
1.3.4. Radio and microwaves	57
1.3.5. Neutrinos	60
1.4. Conclusion	61
2. Additional Electrons/Positrons from Astrophysical Sources	63
2.1. Introduction	63
2.2. Acceleration of Secondaries in the Sources	66
2.3. The Discreteness of Sources	69
2.3.1. Fluctuations in the electron flux	70
2.3.2. A realistic source distribution	79
2.4. Fitting the Total Electron-Positron spectrum	83
2.4.1. Primary electrons	83
2.4.2. Secondary electrons and positrons from propagation	86
2.4.3. Secondary electrons and positrons from the sources	89
2.5. Results	92
2.6. Gamma-Rays and Neutrinos	92
2.7. Comments on the Time-Dependent Picture	96
2.7.1. An analytical argument	97
2.7.2. The numerical model	97

2.8.	Alternative Astrophysical Explanations	99
2.8.1.	Pulsars	99
2.8.2.	GRBs	101
2.8.3.	Very old supernova remnants	101
2.8.4.	Inhomogeneous source distribution	102
2.9.	Conclusion	102
3.	Acceleration of Secondary Nuclei	105
3.1.	Introduction	105
3.2.	Antiproton-to-Proton Ratio	106
3.3.	Nuclear Secondary-to-Primary Ratios	108
3.3.1.	Timescales of the problem	108
3.3.2.	Nuclear spectra at source	110
3.3.3.	Propagation of nuclei	111
3.4.	Parameters	112
3.5.	Results	113
3.6.	Conclusion	113
4.	Systematic effects in the extraction of the ‘WMAP haze’	116
4.1.	Introduction	116
4.2.	Template Subtraction	118
4.3.	Calculation	119
4.4.	Results	120
4.4.1.	Lorimer source distribution	120
4.4.2.	Exponential source distribution	122
4.5.	Discussion	125
4.6.	A Related Study	127
4.7.	Conclusion	128
	Epilogue	131
	A. Moments of Functions of Random Variables	136
	B. Determination of Spectral Indices From Synchrotron Sky Maps	137
	Bibliography	139

1. Introduction

1.1. Dark Matter

One of the most astounding results of modern astrophysics and cosmology is the finding that about 20% of the energy density of the Universe and about 80% of the matter in the Universe is in the form of non-baryonic dark matter (DM). It turns out that DM plays an important role in structures on a wide range of scales ranging from faint satellite galaxies to the largest known structures of the Universe. DM, however, also presents a veritable problem for particle physics. Since the discovery of the discrepancy between the amount of luminous matter and total matter, many different pieces of evidence have been gathered, the most important of which we review in Sec. 1.1.1. In Sec. 1.1.2 we discuss some relic particle candidates for DM, emphasising their connection to new particle physics beyond the Standard Model.

1.1.1. Evidence for dark matter

The probably most commonly known piece of evidence for DM (evidence at least for matter with a much larger mass-to-light ratio M/L than usual) comes from galaxy rotation curves, that is the variation of rotational velocity of stars with distance r from the galactic centre. Most of the luminous mass of spiral galaxies is in fact contained in the central bulge, and assuming Newtonian gravity and dynamics, the rotational velocity of stars should increase up to a certain radius r_{lum} that contains most of the luminous matter, and decrease beyond that like $1/\sqrt{r}$. What Vera Rubin however discovered [4] in 1970 for the nearby spiral galaxy M31, Andromeda, was a *flattening* in the rotation curve beyond the radius r_{lum} , implying that the Galaxy contains mass with a distribution different from the distribution of luminous matter. Flat or even increasing rotation curves have been also found for many other spiral galaxies [5], including the Milky Way (for a recent analysis,

see [6]).

Already almost 40 years earlier, the amount of luminous matter in the Coma cluster had been determined [7, 8] by Fritz Zwicky, applying the virial theorem to measurements of the velocity of individual galaxies. He discovered that the amount of matter to explain the large velocity dispersion of up to 1000 km s^{-1} would require M/L up to hundred times the solar value.

Another possibility of inferring the mass of a distant system, e.g. a galaxy cluster, is by gravitational lensing (for a review, see [9]). This makes use of the bending of light from a distant bright source, like a quasar, by the gravitational potential in between the source and the observer, as predicted by General Relativity. If the distant source, the observer and the mass in between are aligned, the picture of the source becomes strongly distorted to multiple images or arcs which allows the determination of the mass of the object in between. Such constellations that lead to this so-called *strong* lensing are however rare and the effect on the shape of individual sources is mostly too small to determine the gravitational potential. It is however possible to analyse the systematic alignment of a set of background galaxies around the interjacent mass. This technique, called *weak* gravitational lensing, is able to resolve the (DM dominated) mass distribution purely by statistical means. The strength of the lensing signal compared to the intrinsic, so-called “shape noise” depends on the nature of the interjacent mass: Lensing by galaxy clusters usually gives the strongest signals and can be used in conjunction with observations of baryonic matter to determine the mass-to-light ratio of these systems. Lensing by foreground galaxies has much smaller effects (due to the smaller mass of galaxies compared to clusters) and usually requires combining, called “stacking”, the signals from many galaxy lenses. Finally, it is also possible to determine the alignment of background galaxy shapes along the large scale structure of the Universe, called “cosmic shear” and resolve the three dimensional (again DM dominated) mass distribution using also redshift information. For instance, this allows the determination of the matter power spectrum and to constrain important cosmological parameters. The general advantage of gravitational lensing is that the mass of an object can be estimated without any assumptions about its dynamical state or even without any detectable baryonic matter in the first place. In the cases where such information is available, the inferences on the mass, from weak or strong lensing and from kinematic measurements, usually agree very well.

Of course, the above observational results do not require that the non-luminous form of missing

matter is necessarily non-baryonic. In fact, a certain fraction of the non-luminous matter may well be in the form of heavy, compact objects, like black holes, neutron stars, white dwarfs or brown dwarfs, collectively referred to as MACHOs (MASSive Compact Halo Objects), and diffuse, hot, interstellar and intergalactic gas. However, the total estimated mass (including DM) of astronomical objects (galaxies, cluster, large scale structure) is much higher than the total amount of *baryonic* matter which can be determined from cosmological measurements as follows. The abundance of light elements as predicted by big bang nucleosynthesis (BBN) [10, 11] is a function of the baryon abundance Ω_b where Ω_i denotes energy densities in terms of the critical density $\rho_c = 3H^2/(8\pi G)$ with the Hubble parameter H and Newton's gravitational constant G . Observations of the (primordial) Deuterium abundance constrain the baryon abundance to $\Omega_b h^2 \approx 0.02$, where $h = H/(100 \text{ km s}^{-1} \text{ Mpc}^{-1}) \approx 0.7$. Baryons therefore only account for about 20% of the matter in the Universe. Furthermore, the power spectrum of cosmic microwave background (CMB) anisotropies is also sensitive to the amount of baryonic and the total amount of matter through the acoustic peaks. More precisely, the recent release [12] of the WMAP 7-year data reports $\Omega_{\text{cdm}} h^2 = 0.1109 \pm 0.0056$ and $\Omega_b h^2 = 0.02258_{-0.00056}^{+0.00057}$ for $H = h 100 \text{ km s}^{-1} \text{ Mpc}^{-1} = 71.0 \pm 2.5 \text{ km s}^{-1} \text{ Mpc}^{-1}$.

According to the concordance model, the same quantum fluctuations that lead to the anisotropies in the CMB are also the seeds for the formation of structure on all scales in the Universe today which provides more evidence for DM. On the one hand, the amount of density perturbations at the time of recombination is rather small (the CMB is isotropic to one part in 10^5). On the other hand, structure formation through gravitational collapse could not start from baryonic matter before the time of recombination because of electromagnetic interactions. It turns out that the time that baryonic matter alone therefore could have had to form structure is much too short. Non-baryonic DM, however, would have started collapsing before recombination and it turns out it can explain structure formation rather accurately as shown by N -body simulations [13, 14, 15]. Furthermore, structure formation requires that DM is non-relativistic at and after the time of recombination, that is cold dark matter (CDM).

Other ideas, like MOdification of Newtonian Dynamics (MOND) [16] (for a review, see [17]) and particular theoretical representations, for example, Tensor Vector Scalar (TeVeS) theory [18] can reproduce some of the above mentioned results without the need for new, non-baryonic DM. For example, MOND reproduces galactic rotation curves better than DM, in particular needing

less free parameters. Furthermore, it gives an explanation of the “Tully-Fisher relation”, that is the observed correlation between luminosity and rotation velocity, but fails on the scales of galaxy clusters [17].

In particular, the ‘smoking gun’ signature for DM comes from the so-called ‘bullet cluster’ [19]. Weak lensing and x-ray expose the distribution of dark matter and hot gas (which makes up the majority of baryonic matter), respectively, in two galaxy clusters that have collided ~ 100 Myr ago. Not only are the distributions clearly distinct, but they also prove that while the hot gas has interacted (electromagnetically) during the collision, the DM has just passed through without interacting. Such a behaviour is basically impossible to imitate by modifying gravity.

Despite all the successes of the CDM paradigm in explaining the above mentioned astrophysical as well as cosmological data, there are a large number of questions/problems that CDM cannot answer (so far): Why are the DM haloes predicted by (pure DM) N -body simulations much “cuspier” than those actually observed? Will including baryonic matter in N -body simulations flatten the profile in the inner kiloparsecs? Why do we observe less satellites (DM substructure) than predicted by N -body simulations? Can galaxy dynamics, e.g. SN feedback or (local) reionisation [20] reconcile this discrepancy? Why are there less massive galaxies today than expected? Although the quantitative discrepancy between the predictions and observations in some of these cases might be rather large, the expectation is that the uncertainty due to astrophysics is also still quite large and more realistic modelling will resolve many, if not all contradictions.

1.1.2. Particle candidates

What all the different pieces of evidence presented in the last section have in common, is that they are based on the gravitational interaction of DM only. However, from a particle physicist’s viewpoint it is desirable to describe DM by a fundamental particle, in a similar way that the standard model (SM) of particle physics describes the fundamental matter particles and force carriers. The properties that characterise a particle in a relativistic quantum field theory are its mass, spin, quantum numbers under (gauge) transformations and also its coupling to other (SM) particles.

Even before considering any particular model, the astrophysical evidence of DM gives us some constraints on its particle physics nature. First of all, the DM particle needs to be stable on

cosmological timescales, that is its lifetime must be larger than the age of the Universe. Secondly, zero results for searches for exotic, heavy nuclei on Earth constrain DM to be at most weakly interacting since DM would form such states if it was interacting via strong or electromagnetic forces. Furthermore, DM must be cold to be able to explain structure formation. This rules out the only known neutral and purely weakly interacting particle, the neutrino, as at least one mass eigenstate is relativistic today. Hence, none of the SM particles can accommodate for CDM and this clearly hints at physics beyond the SM. Interestingly, many theories of new physics that address the short-comings of the SM predict new particles including some therefore well-motivated dark matter candidates.

WIMPs

The SM has been very successful in providing a fundamental theory of matter and its interactions that has been tested to a great accuracy in colliders and non-accelerator experiments. However, although the Higgs mechanism explains the breaking of electroweak symmetry, one of the short-comings considered more serious is the so-called hierarchy problem: How is the weak scale stabilised with respect to radiative corrections that would normally boost it to the Planck scale? One of the most elegant solutions to this problem is supersymmetry (SUSY) which entangles the usual Poincaré algebra with a new set of generators transforming fermionic into bosonic degrees of freedom and *vice versa*. In its simplest implementation, this effectively amounts to roughly doubling the particle content of the SM by mirroring each SM particle in a supersymmetric partner (sparticle) with a spin different by $1/2$. These sparticles cancel the quadratic divergencies arising in radiative corrections of the Higgs mass parameter and hence stabilise the weak scale. To keep the necessary cancellations natural, the new particles must have masses m_{DM} close to the weak scale. Among these new particles there are a number of DM candidates.

If such new particles at the weak scale were also weakly interacting, that is they are weakly interacting massive particles (WIMPs), then their relic density today as predicted from production by freeze-out, i.e. thermal decoupling [21, 22, 23, 24, 25, 26], is in excellent agreement with the constraints from astrophysics and cosmology (in particular Ω_{cdm} from the WMAP experiment, see above). More precisely, at early times, the DM particles are in thermal equilibrium. As the Universe cools, their density is being suppressed by the Boltzmann factor $\propto e^{-m_{\text{DM}}/T}$ and for late

times and hence low temperatures T , the abundance would normally vanish. However, apart from cooling, the Universe also expands, such that the rate of production/annihilation becomes smaller than the Hubble rate and the WIMPs drop out of thermal equilibrium. Quantitatively, the WIMP density n is governed by the Boltzmann (continuity) equation (first given in [21]),

$$\frac{dn}{dt} = -3Hn - \langle \sigma_{\text{ann}} v \rangle (n^2 - n_{\text{eq}}^2) \quad (1.1)$$

where H is the Hubble rate, $\langle \sigma_{\text{ann}} v \rangle$ the thermal average of the WIMP annihilation cross section and velocity and n_{eq} the WIMP equilibrium density. In general, this needs to be solved numerically but a simple analytical estimate gives

$$\Omega_{\text{WIMP}} \sim \frac{x_f T_0^3}{\rho_c M_{\text{Pl}}} \langle \sigma_{\text{ann}} v \rangle^{-1}. \quad (1.2)$$

with $x_f = m_{\text{WIMP}}/T_f \approx 20$, T_f (T_0) the temperature at freeze-out (today) and M_{Pl} the Planck mass. The WIMP mass does not enter Ω_{WIMP} directly but in most theories it is the only mass scale that determines the annihilation cross section. In particular, for weak interactions and a mass at the weak scale, one finds an s-wave annihilation cross section,

$$\sigma_{Av} \approx \frac{g^4}{16\pi^2 m_{\text{WIMP}}^2} \approx 3 \times 10^{-26} \text{ cm}^3 \text{ s}^{-1}, \quad (1.3)$$

that reproduces the relic density $\Omega_{\text{WIMP}} = \mathcal{O}(1)$. This fact has been called the ‘WIMP miracle’.

One might wonder why such a new, weak-scale particle should not decay, seeing that all SM particles above a GeV are unstable. Usually, one postulates a discrete symmetry that forbids interactions leading to decay of these particles. In the case of the minimal supersymmetric standard model (MSSM) this symmetry is called R -parity. Originally, it was introduced [27] to satisfy bounds on the proton lifetime. However, to protect the proton it is enough to forbid one of the interactions necessary for its decay which can be achieved by, e.g. baryon or lepton parity. Therefore, to make the lightest supersymmetric particle (LSP) stable, R -parity has to be introduced by hand. It was also argued [28] that R -parity violating interactions must be suppressed to prevent the washout of the cosmic baryon/lepton asymmetry but this argument does not hold when lepton-mass effects are included [29].

Examples for WIMPs arise naturally in weak scale SUSY theories as motivated above. If SUSY breaking is gravitationally mediated, the lightest supersymmetric particle (LSP) is usually the neutralino [30, 31], a mixture of the supersymmetric partners of the hypercharge gauge boson, the neutral component of the W boson and the neutral higgs partners.

Theories of universal extra dimension (UED) [32], for example, do not try to address the hierarchy problem, but also lead to new particles at the weak scale and thus WIMP DM candidates [33, 34]. The general idea is that all SM particles propagate in a higher dimensional space. In the simplest version, a single additional dimension is compactified on an S_1/Z_2 orbifold of radius $R \sim 10^{-8}$ m or smaller. In 4 dimensions this leads to an infinite spectrum for each SM particle, so-called Kaluza-Klein (KK) [35] particles, equally separated in mass by R^{-1} . KK particles possess a discrete symmetry, K -symmetry, which makes the lightest KK particle, the LKP, stable. In most models, the LKP is the first KK state of the hypercharge gauge boson, B^1 .

superWIMPs

On the one hand, the big advantage of the WIMP “miracle” is that it predicts the right DM abundance for stable, weak particles. On the other hand, constraining ourselves to stable and weakly interacting particles turns out to be too rigid a presumption. In fact, a number of the new particles suggested by beyond standard model (BSM) theories turn out to be either unstable or interact much more weakly.

However, if every WIMP produced by thermal decoupling would decay to a “superWIMP”, that is a particle which is also at the weak scale but is only “super weakly” interacting, the virtue of the right relic density can be saved [36, 37],

$$\Omega_{\text{superWIMP}} = \frac{m_{\text{superWIMP}}}{m_{\text{WIMP}}} \Omega_{\text{WIMP}}. \quad (1.4)$$

Another production mechanism is reheating [38, 39, 40, 41]. It can be shown that today’s density is proportional to the reheating temperature T_R and one finds $T_R \simeq 10^{10}$ GeV for a 100 GeV gravitino superWIMP.

Weak scale gravitinos are in fact a typical example of superWIMPs [41, 36, 37, 42, 43, 44, 45], realised in SUSY theories with gravity mediated SUSY breaking. As there is no reason to believe

that gravitinos are systematically lighter or heavier than the other superpartners in these scenarios, the gravitino is the LSP in about half the parameter space. The role of the WIMP is then played by the next-to-lightest SUSY particle (NLSP), for example the stau, which can decay to the gravitino with lifetimes naturally of the order of hours to months.

Another possible example are axinos, the superpartner of axions (see below), and both could be possibly contributing in a multi-component DM scenario [46].

Hidden dark matter

The fact that DM is not interacting through electromagnetic or strong forces has led us to the conclusion that it could at most be weakly interacting. The alternative, i.e. that it is only gravitationally interacting is usually disfavoured because of lack of predictivity, missing connections to new physics and the loss of an automatic prediction for the relic density. Generally speaking, constraints on hidden sectors can only be obtained from their gravitational interactions, e.g. from constraints on the expansion rate at BBN [47]. There are however counter-examples resolving some or all of these problems and in the following we mention one particular class of examples that provide a DM candidate with the correct relic density from thermal freeze-out, too.

In fact, going back to Eq. 1.3, one realises that every extension of the SM that predicts similar ratios of g^4/m^2 will reproduce the observed relic density, no matter whether g is a SM coupling. Let's consider for example a setup of gauge mediated SUSY breaking which one could imagine is also mediated to a hidden sector whose particles are not charged under any SM gauge group; string theories, for example, predict many such hidden sectors. The masses of the hidden sector superpartners, m_h , are however set in the same, generation-independent way as the SM superpartner slepton masses, m , by the factor F/M_m from the SUSY breaking sector,

$$m \sim \frac{g^2}{16\pi^2} \frac{F}{M_m} \quad \text{and similarly} \quad m_h \sim \frac{g_h^2}{16\pi^2} \frac{F}{M_m}, \quad (1.5)$$

with g_h the hidden sector gauge coupling. Therefore, the ratio m_h/g_h^2 that determines the relic density from freeze-out, see Eqs. 1.2 and 1.3, is universal and we expect that the hidden sector contains (some) DM candidates with just the right relic abundance. This relation is called the “WIMPless miracle” [48].

Asymmetric dark matter

It is questionable whether the freeze-out paradigm for DM production is necessarily the right one. Applied to baryon production, for example, it fails spectacularly – not only, because the predicted baryon abundance, $n_B/n_\gamma \approx 10^{-19}$, is about ten orders of magnitude smaller than the observed one, but also because it cannot explain the observed matter-antimatter asymmetry. Instead, the baryon abundance can be explained from an asymmetry of baryons over anti-baryons generated, for example, by non-perturbative sphaleron processes. If the annihilation cross section of baryons and antibaryons is large enough that all antibaryons will have annihilated away, we are left with the right density of baryons only.

The fact that the abundance of DM and baryons is only different by a factor 5, a relation which in a freeze-out scenario of DM would be merely coincidental, may hint at a common physical origin [49, 50]. If one wants to explain the DM abundance today from an asymmetry generated in a similar way, DM must have a quantum number B' , similar to the baryon number B . At temperatures above the electroweak phase transition, $T > T_*$, electroweak anomalous processes are in thermal equilibrium and equilibrate the lepton, baryon and DM asymmetries. Depending on whether the DM mass m_{DM} is smaller or larger than T_* , the B' asymmetry gets frozen at $Y_{\Delta B}$ or Boltzmann suppressed as $Y_{\Delta B'}/Y_{\Delta B} \sim e^{-m_{\text{DM}}/T_*}$, and the DM abundance, $\Omega_{B'}$, can be related to the baryon abundance, Ω_B ,

$$\frac{\Omega_{B'}}{\Omega_B} = c \begin{cases} \frac{m_{\text{DM}}}{m_B} & \text{for } m_{\text{DM}} \ll T_*, \\ 12 \frac{m_{\text{DM}}}{m_B} \left(\frac{m_{\text{DM}}}{2\pi T_*} \right)^{3/2} e^{-m_{\text{DM}}/T_*} & \text{for } m_{\text{DM}} \gg T_*, \end{cases} \quad (1.6)$$

with c an order one parameter and m_B the nucleon mass. The observed DM abundance $\Omega_{B'} = 5 \Omega_B$ can therefore be recovered by $m_{\text{DM}} \sim 5 \text{ GeV}$ for $m_{\text{DM}} \ll T_*$ [50] or $m_{\text{DM}} \sim 2 \text{ TeV}$ for $m_{\text{DM}} \gg T_*$ [49]. Technicolour, a strongly interacting theory suggested for electro-weak symmetry breaking, for example, rather naturally predicts *techni*-baryons with TeV masses.

Axions

The axion was originally postulated to solve the so-called ‘strong CP problem’ [51, 52, 53]. The QCD Lagrangian contains a four-divergence proportional to the angle $\bar{\theta}$ that would lead to P and

CP violation through non-perturbative effects. The non-observation of, e.g. a neutron dipole moment, however, constrains $|\bar{\theta}|$ to $< 10^{-10}$. The most elegant way to guarantee a small value is the Peccei-Quinn mechanism that promotes $\bar{\theta}$ to a dynamical field with a classical potential that is minimised at $\bar{\theta} = 0$. This is achieved by adding an additional, chiral symmetry $U(1)_{\text{PQ}}$, the Peccei-Quinn symmetry, which is spontaneously broken at the scale f_a . The pseudo Nambu-Goldstone boson is the axion a ; “pseudo”, because the global symmetry is not exact at the quantum level and therefore the axion is not massless but has a mass of order Λ_{QCD}/f_a ,

$$m_a \simeq 0.6 \text{ eV} \frac{10^7 \text{ GeV}}{f_a}. \quad (1.7)$$

Also, this anomaly leads to a potential for the axion, fixing it to around $\langle a \rangle = -\bar{\theta} f_a / \text{const.}$ which cancels the above four-divergence, thus solving the strong CP-problem. Expanding the axion field around its minimum $\langle a \rangle$ one obtains the axion Lagrangian which is still to be complemented by the axion couplings to, e.g. photons and fermions,

$$\mathcal{L}_{a\gamma\gamma} = -g_\gamma \frac{\alpha}{\pi} \frac{a}{f_a} \mathbf{E} \cdot \mathbf{B} \quad \text{and} \quad \mathcal{L}_{a\bar{f}f} = ig_f \frac{m_f}{v} a \bar{f} \gamma_5 f, \quad (1.8)$$

where α is the fine-structure constant, \mathbf{E} and \mathbf{B} the (colour) electric and magnetic field, respectively, and g_γ, g_f are model-dependent coefficients of order one.

There is a variety of constraints on the axion mass. Collider searches for rare decays $\pi^+ \rightarrow a(e^+e^-)e^+\nu_e$ rule out very short-lived (lifetime $< 10^{-11}$ s) axions with masses above 1 GeV. For long-lived axions (lifetime $> 10^{-11}$ s) production ($p + N \rightarrow a + X$ or $e + N \rightarrow a + X$) as well as interaction ($a + N \rightarrow X$) cross sections are constraint from beam dumps and rule out axions heavier than 50 keV [54]. Astrophysical constraints [55] like bounds on the lifetime of red giants limit the cooling due to axions and give $200 \text{ keV} \gtrsim m_a \gtrsim 0.5 \text{ eV}$ ($\gtrsim 10^{-2} \text{ eV}$ even, if the coupling to electrons is large). The duration of the neutrino burst observed from SN 1987a finally also limits the fraction of axion cooling and excludes $2 \text{ eV} \gtrsim m_a \gtrsim 3 \times 10^{-3} \text{ eV}$. Axions lighter than 10^{-6} eV are ruled out because they would over-close the Universe ($\Omega_a \propto f_a \propto m_a^{-1}$). The axion is thus extremely light and weakly interacting, making it a potential DM candidate [56, 57, 58].

Depending on whether the reheating temperature of inflation is smaller or larger than the tem-

perature T_{PQ} of the spontaneous breaking of the PQ symmetry, the axion field is homogenised over enormous distances or carries strings and domain walls as topological defects. Axions therefore get produced by vacuum-realignment only [59] or also by string and domain wall decay, and the critical density today is

$$\Omega_a \approx 0.15 \left(\frac{f_a}{10^{12} \text{ GeV}} \right)^{7/6} \left(\frac{0.7}{h} \right)^2 \alpha_1^2 \quad \left(\Omega_a \approx 0.7 \left(\frac{f_a}{10^{12} \text{ GeV}} \right)^{7/6} \left(\frac{0.7}{h} \right)^2 \right), \quad (1.9)$$

with α_1 the initial misalignment angle.

1.2. Cosmic Rays

1.2.1. Galactic and extra-galactic cosmic rays

The Earth’s atmosphere is constantly bombarded by a flux of elementary particles: cosmic rays (CRs). The spectrum of these particles measured on Earth covers 12 orders of magnitude in energy – corresponding to 40 octaves in frequency! On the other hand, the steeply falling power law spectrum between $E^{-2.7}$ and E^{-3} implies quickly declining flux rates of 1 particle $\text{m}^{-2} \text{s}^{-1} \text{sr}^{-1}$ above 100 GeV, 1 particle $\text{m}^{-2} \text{yr}^{-1} \text{sr}^{-1}$ above 10^{16} eV and 1 particle $\text{km}^{-2} \text{yr}^{-1} \text{sr}^{-1}$ above 10^{19} eV.

Spectrum

The cosmic rays with energies between ~ 1 GeV and (at least) $\sim 3 \times 10^{15}$ eV are considered to be of galactic origin and are hence called Galactic Cosmic Rays (CGRs). They exhibit a rather featureless power law with spectral index $\alpha \approx -2.75$. The low energy cut-off is due to solar modulation, that is cosmic rays of energy lower than a few hundred MeV lose all their energy by running up against the electric potential generated by the solar wind [60]. At $\sim 3 \times 10^{15}$ eV, a softening to $\alpha \approx -3.1$ is observed, a feature called the “knee”. At around 5×10^{17} eV the spectrum further softens to $\alpha \approx -3.3$ (“second knee”). As the Larmor radius at these energies starts exceeding the spatial dimensions of the Galaxy of kiloparsecs, cosmic rays at least beyond this energy must be of extra-galactic origin. At 3×10^{18} eV, the spectrum hardens again to -2.7 (“ankle”), before it gets cut off at $\sim 5 \times 10^{19}$ GeV [61], probably due to the so-called GZK cut-off, the suppression of the flux by photo-pion production on the CMB [62, 63]. The flux of cosmic rays measured on Earth, scaled

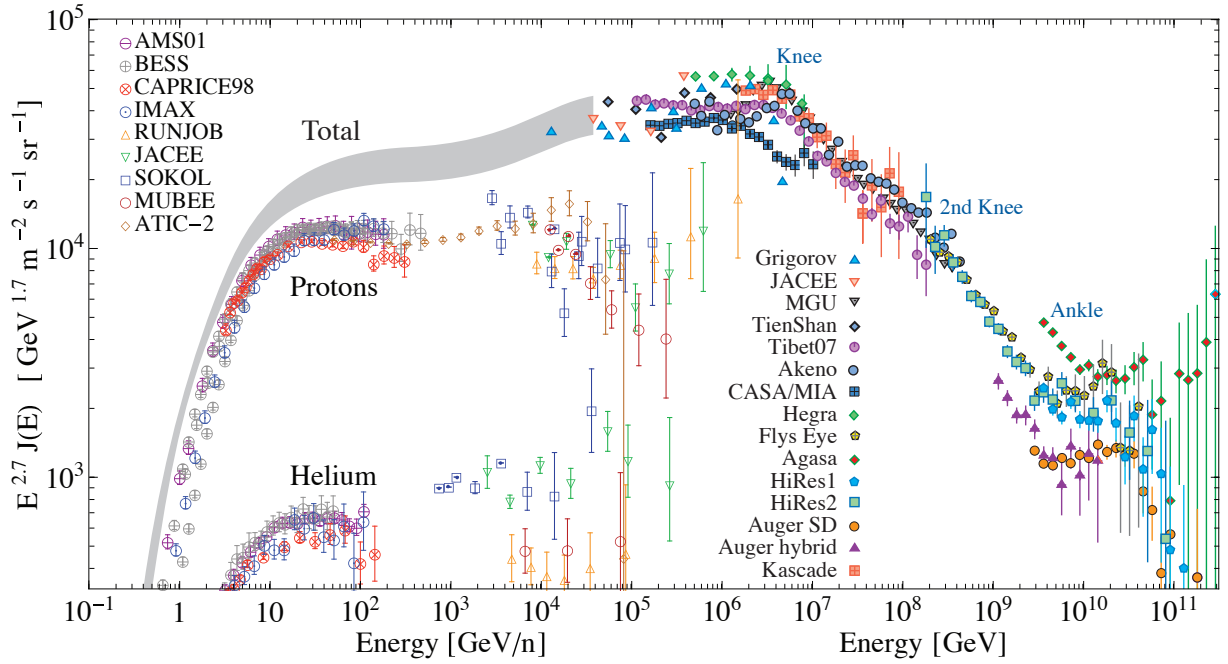


Figure 1.1.: Flux of galactic and extra-galactic cosmic rays, scaled by $E^{2.7}$ (from [11] and with additional data [64]). The energy for the helium flux is in GeV/n.

by $E^{2.7}$ to amplify the features, is shown in Fig. 1.1.

Below a GeV cosmic rays must be of local, i.e. solar system origin. In fact, the solar wind is a prime laboratory for testing models of cosmic ray acceleration (e.g. by shock waves) observed by interplanetary probes, like the Voyager spacecrafts. As these low-energy particles are however not important for dark matter indirect searches and cosmic ray backgrounds we do not consider solar cosmic rays any further.

Composition

Most chemical elements observed in GCRs occur in ratios that are consistent with their relative abundance in the solar system, hinting at a global validity of these abundances elsewhere in the Galaxy, potentially even the local Universe. Some elements however, in particular those which are rare in the solar system, are overabundant in cosmic rays. The interpretation is that although the source abundances are similar to solar system values, these so-called ‘secondaries’ get produced from the more abundant ‘primaries’ by spallation on the interstellar medium. This explanation gives in turn estimates of the average matter or ‘grammage’ of a few tens g cm^{-2} that primaries

must traverse to produce the observed number of secondaries. The energy dependence of the ratios of secondaries-to-primaries is an important test of the propagation model (see Sec. 1.2.7). It is worth noting that the electronic component has a softer spectrum (see Sec. 1.3.2) and is smaller than the nuclear one by $\sim 10^{-2}$ at 10 GeV.

The change of composition at spectral features is used to infer the nature of the sources of ultra high energy cosmic rays (UHECRs). Besides the observation of an increasingly heavy composition around the knee (see above), particular interest has been generated by recent contradictory observations by the HiRes [65] and Auger [66] experiments at the ankle. However, it seems likely that this discrepancy could be resolved once hadronic showers at the highest energies are understood better.

Anisotropies

Another important information is of course encoded in the arrival directions of cosmic rays. Up to $\sim 10^{19}$ eV these directions get randomised by scattering on magnetic turbulence in the galactic interstellar (but probably also in the intergalactic) medium. The Auger collaboration has, for example, published evidence of a correlation of their highest energy events with a catalogue of nearby AGNs [67, 68]. The correlation has however decreased ever since, as have claimed correlations of other observations and source candidates. The question of the origin of UHECRs therefore remains open.

1.2.2. The standard model of galactic cosmic rays

Since their discovery by Victor Hess in 1912, a standard picture for GCRs has emerged that can explain a large number of observations. Usually, one assumes that the problem of GCRs factorises in two parts that can be treated separately: acceleration in confined sources and transport through the interstellar medium. This assumption seems to be supported by the observed decrease of secondary-to-primary ratios (see Sec. 1.2.7). In fact, if cosmic rays were mostly accelerated in the interstellar medium by some stochastic process (first order Fermi acceleration by interstellar shock waves or second order Fermi acceleration by interstellar turbulence) then these ratios would be logarithmically rising [69, 70].

The acceleration of both the hadronic (proton and nuclei) and the electronic component of

primary GCRs is assumed to take place in the shocked shells of supernova remnants (SNRs) by first order Fermi acceleration. Cosmic rays get accelerated as long as they are confined to the shock region by up-stream turbulence and only some high-energy particles might escape if no Alfvén waves of low enough wave number are present for their scattering [71, 72]. In any case, once the SNR has entered its radiative phase all high-energy particles are released and diffuse through the interstellar medium by scattering on magnetic turbulence in the form of Alfvén waves. It is expected that convection by a possibly CR generated wind and reacceleration due to stochastic, second-type Fermi acceleration also plays a role.

In the following sections, we describe the basic building blocks in more detail. We start with a brief review of our understanding of supernova remnants, in particular their dynamics and the properties of the so-called Sedov-Taylor phase in which the bulk of particle acceleration happens. We then derive the transport equation and apply it to diffusive shock acceleration, claimed to be responsible for the acceleration of cosmic ray electrons and nuclei up to TeV energies. We also specialise the transport equation to cosmic ray propagation in the Galaxy, outlining the different physical processes at work and briefly review two simple analytical solutions which we extend on in later chapters. We conclude this section by reviewing the main predictions for fluxes and secondary-to-primary ratios and comparing them to observations.

1.2.3. Supernova remnants as sources

The assumption that the population of GCRs is powered by SNRs is based on three indications. The first one is the presence of non-thermal populations of electrons as observed in radio and x-rays, for example, for SN 1006 [73]. This is usually explained as synchrotron radiation of relativistic electrons on the ambient magnetic fields, amplified by compression and possibly by the Bell-Lucek mechanism [74, 75]. Estimates of the highest energies reach up to hundreds of TeV (for a modelling of SN 1006, see [71]).

Furthermore, there is a well-established theory that can explain the generation of such a non-thermal population of particles by first order Fermi acceleration in shocked shells, see Sec. 1.2.5. As SNRs exhibit strong shocks with very high Mach numbers, applying this theory to the parameters derived from, e.g. kinetic observations, it can be shown that efficient particle acceleration is possible.

Finally, even as early as 1953, it was pointed out [76] that SNRs with their benchmark total bulk

kinetic energy of 10^{51} erg could easily provide the right order of magnitude energy needed to power the galactic population of nuclear cosmic rays. More precisely, with a SN rate of about 0.03 yr^{-1} , a volume of the extended cosmic ray halo of $\pi(15 \text{ kpc})^2 \times 3 \text{ kpc} = 5.7 \times 10^{67} \text{ cm}^3$ and an average residence time of cosmic rays in the Galaxy (that is the time until escape from the galactic cosmic ray halo) of 20 Myr, $\mathcal{O}(10)\%$ of the kinetic energy must be transferred into GCRs to maintain the (local) energy density of 0.3 GeV cm^{-3} – a reasonable efficiency.

The spectroscopic classification of supernovae (SNe) into type I (without H lines) and type II (with H lines) does not coincide with the nature of the progenitor system. While only type Ia SNe originate in the thermonuclear burning of carbon-oxygen in a white dwarf, all other types (Ib, Ic, IIP, IIL and IIn) are core collapse (CC) supernovae. Interestingly, the kinetic energy of the ejecta of the subsequent supernova remnants (SNRs) are quite similar, typically of the order of 10^{51} erg. Once the mass of the interstellar medium swept up by the shock front exceeds the mass of the ejecta, that is from the Sedov-Taylor phase (see below) onwards, there should not be any phenomenological distinction between the remnants of thermonuclear and CC SNe.

Conservation of mass, momentum and energy across a planar, adiabatic shock front leads to the Rankine-Hugoniot relations [77]. In particular, for the compression ratio $r \equiv n_1/n_2$ of the shock front, one finds,

$$\frac{u_2}{u_1} = \frac{1}{r} = \frac{\gamma - 1}{\gamma + 1} + \frac{2}{\gamma + 1} \frac{1}{\mathcal{M}^2}, \quad (1.10)$$

and for strong shocks with a ratio of the specific heats $\gamma = 5/3$ and a Mach number $\mathcal{M} \gg 1$, $r = 4$. Furthermore, this analysis is based on the assumption that radiative processes and loss of non-thermal particles can be neglected. Also, back reaction of the energetically important fraction of accelerated cosmic rays will change the shock structure, modifying γ towards the fully-relativistic value of $4/3$.

Typical explosion velocities $\sqrt{2E_{\text{SN}}/M_{\text{ej}}}$ of the ejecta in the first phase of the SNR are 10^4 km s^{-1} for type Ia and 5000 km s^{-1} for CC SNe. This is much higher than the estimated sound speed in the surrounding medium, and therefore a blast wave with $\mathcal{M} \gtrsim 10^3$ forms, that is a shock front followed by self-similar ($v(r) \propto r$), quickly cooling ejecta. After only a few days, when the shock front has decelerated sufficiently, the SNR enters the so-called “ejecta-driven” phase and a reverse-shock forms, that reheats the ejecta of the SNR. A contact discontinuity (with constant pressure)

develops between the heated ejecta and the shock front, like a piston pushing into the ISM. This discontinuity is expected to be unstable to Raleigh-Taylor instability and therefore produces strong turbulence.

The reverse shock will reach the centre of the SNR and disappear after hundreds of years which marks the transition to the Sedov-Taylor phase [78]. The time t_{ch} at which this happens can be estimated by dimensional analysis, assuming that the only scales available to the problem are the energy E , the mass of the ejecta M_{ej} and the ambient density ρ_0 ,

$$t_{\text{ch}} = E^{-1/2} M_{\text{ej}}^{5/6} \rho_0^{-1/3}. \quad (1.11)$$

The transition usually occurs when the mass swept up by the shock front is a few times the mass of the ejecta and therefore the value of M cannot enter into the subsequent evolution. Only using E and ρ_0 , the dynamics of the Sedov-Taylor phase can be again be determined dimensionally [79],

$$R = 1.15 \left(\frac{E}{\rho_0} \right)^{1/5} t^{2/5} = 0.31 \left(\frac{E}{10^{51} \text{ erg}} \right)^{1/5} \left(\frac{\mu}{1.4} \right)^{-1/5} \left(\frac{n_0}{\text{cm}^3} \right)^{-1/5} \left(\frac{t}{\text{yr}} \right)^{2/5} \text{ pc}, \quad (1.12)$$

$$u = \frac{2R}{5t} = 1.2 \times 10^5 \left(\frac{E}{10^{51} \text{ erg}} \right)^{1/5} \left(\frac{\mu}{1.4} \right)^{-1/5} \left(\frac{n_0}{\text{cm}^3} \right)^{-1/5} \left(\frac{t}{\text{yr}} \right)^{-3/5} \text{ km s}^{-1}, \quad (1.13)$$

where μ is the mean mass per particle in units of the proton mass. Extensive analytical and numerical simulations of the ejecta-driven and Sedov-Taylor phases have been presented, for example, in [79].

The Sedov-Taylor phase eventually comes to an end when the shock front has slowed down enough, so that radiative processes can become dominant. If the ejecta are hot enough at this point, the piston can still be powered by the pressure although the expansion is not adiabatic any more. If the ejecta have cooled too much, the former shock front just continues outwards, conserving momentum. Hydrodynamical simulations [80] show that under realistic assumptions this happens at

$$t_{\text{tr}} = 2.9 \times 10^4 \left(\frac{E}{10^{51} \text{ erg}} \right)^{4/17} \left(\frac{n_0}{\text{cm}^3} \right)^{-9/17} \text{ yr}, \quad (1.14)$$

$$R_{\text{tr}} = 91 \left(\frac{E}{10^{51} \text{ erg}} \right)^{5/17} \left(\frac{n_0}{\text{cm}^3} \right)^{-7/17} \text{ pc}, \quad (1.15)$$

$$M_{\text{tr}} = 10^3 \left(\frac{E}{10^{51} \text{ erg}} \right)^{15/17} \left(\frac{n_0}{\text{cm}^3} \right)^{-4/17} M_{\odot}. \quad (1.16)$$

After a few times t_{tr} the velocity is as low as $100 - 300 \text{ km}^{-1}$ and the Mach number is of order $3 - 6$ such that particle acceleration comes to a halt.

1.2.4. The transport equation

In the following we sketch the derivation of the transport equation governing the dynamics of a test-particle under magnetohydrodynamical turbulence in a moving plasma. We closely follow the treatment given in [81] which we refer the reader to for a more detailed calculation.

The fundamental relation is the Vlasov equation [82, 83] for the Lorentz invariant phase space density $f = f(t, \mathbf{x}, \mathbf{p})$ at time t ,

$$\frac{\partial f}{\partial t} + \mathbf{v} \cdot \frac{\partial f}{\partial \mathbf{x}} + \frac{\partial}{\partial \mathbf{p}} \cdot (\mathbf{F}f) = 0. \quad (1.17)$$

We incorporate the processes of momentum, pitch angle and spatial diffusion by converting the microscopic Lorentz force term, encoding the electromagnetic interactions of the test-particle with the plasma, to macroscopic effective collision operators, thereby transforming the Vlasov into a Boltzmann equation.

Momentum diffusion

Scattering on magnetohydrodynamical turbulence leads to diffusion, both in momentum p and in pitch angle θ , $\mu \equiv \cos \theta = \cos(\mathbf{p} \cdot \mathbf{B}/(pB))$ where \mathbf{B} is the large scale magnetic field. We can treat the diffusion in momentum space in a Fokker-Planck framework (see, e.g. [82, 84]), that is considering the scattering of charged particles on magnetic inhomogeneities or Alfvén waves as a Markov process. The Fokker-Planck equation,

$$\frac{\partial f}{\partial t} + (\mathbf{v} \cdot \nabla) f = \frac{\partial}{\partial \mathbf{p}} \cdot \mathbf{D}_{pp} \cdot \frac{\partial f}{\partial \mathbf{p}} \quad \text{with} \quad \mathbf{D}_{pp} = \frac{1}{2} \left\langle \frac{\Delta \mathbf{p} \Delta \mathbf{p}}{\Delta t} \right\rangle, \quad (1.18)$$

describes diffusion in momentum space and leads to second order Fermi acceleration as originally envisaged by Fermi [85]. Anticipating isotropy of the phase space density with respect to pitch

angle (see below), the RHS of Eq. 1.18 simplifies to

$$\frac{1}{p^2} \frac{\partial}{\partial p} p^2 D_{pp} \frac{\partial f}{\partial p}. \quad (1.19)$$

The momentum diffusion coefficient, D_{pp} , is calculated by considering that the momentum gained on bouncing off scattering centres in the plasma moving with velocity V , $\Delta p = -(\mathbf{p} \cdot \mathbf{V})/v$, occurs every $\Delta t = L/v$ where L is the collision mean free path,

$$D_{pp} = \frac{1}{2} \left\langle 2 \frac{(\mathbf{p} \cdot \mathbf{V})^2}{v^2} \right\rangle \frac{v}{L} = \frac{1}{3} \frac{p^2 \langle V^2 \rangle}{vL}. \quad (1.20)$$

Pitch angle scattering

The next necessary ingredient is pitch angle diffusion. Particles of momentum \mathbf{p} with Larmor radius $r_L = p/(ZeB)$ interact resonantly with Alfvén waves of similar wave-length, $r_L \sim 1/k$, changing their pitch angle θ . Interacting with waves with random phases, the pitch angle performs a random walk and after $\sim (B/\delta B)^2$ interactions it has changed by π and the particle can be considered as scattered, that is having lost all information about its initial direction. Here, δB denotes the turbulent component of the magnetic field. The Fokker-Planck equation for pitch angle scattering reads,

$$\left(\frac{\partial f}{\partial t} \right)_c = \frac{1}{2} \frac{\partial}{\partial \mu} \left((1 - \mu^2) \nu \frac{\partial f}{\partial \mu} \right), \quad (1.21)$$

with the diffusion coefficient ν in pitch angle (i.e. the scattering frequency),

$$\nu = \left\langle \frac{\Delta \theta^2}{\Delta t} \right\rangle = \frac{\pi}{4} \left(\frac{k \mathcal{E}_k}{B^2/8\pi} \right) \Omega, \quad (1.22)$$

and where \mathcal{E}_k is the energy in the mode k while $B^2/8\pi$ is the energy of the ambient magnetic field and $\Omega = eB/(\gamma m_p)$ the Larmor frequency with m_p the proton mass. Having assumed spatial uniformity, $\partial f/\partial x = 0$, pitch angle diffusion can be implemented into the Vlasov equation 1.17 by identifying the RHS of Eq. 1.21 as an effective collision operator.

Spatial diffusion

If the mean free path length is short, spatial transport needs to be treated in the diffusion equation. To prepare for the discussion of acceleration across a shock front, we also want to consider the possible motion of the scattering centres. The idea is to transform the Vlasov equation into the plasma frame and determine the isotropic part of the phase space density, f . It turns out that after averaging over pitch angle, f satisfies the transport equation,

$$\frac{\partial f}{\partial t} + (\mathbf{u} \cdot \nabla) f - \nabla \cdot (D_{\parallel} \nabla f) = \frac{1}{3} (\nabla \cdot \mathbf{u}) p \frac{\partial f}{\partial p}, \quad (1.23)$$

where the coefficient for diffusion parallel to the magnetic field is

$$D_{\parallel} \simeq \frac{v^2}{3\nu} \propto \left(\frac{k\mathcal{E}_k}{B^2/8\pi} \right)^{-1}, \quad (1.24)$$

and the coefficient for diffusion perpendicular to the magnetic field,

$$D_{\perp} \simeq \frac{v^2\nu}{3\Omega^2} \propto \left(\frac{k\mathcal{E}_k}{B^2/8\pi} \right), \quad (1.25)$$

has been ignored.

The second and third term on the LHS of Eq. 1.23 are the usual convection and spatial diffusion term and the RHS describes the energy loss (gain) of particles in a diverging (converging) flow. Adding Eq. 1.19 to the RHS completes the transport equation.

1.2.5. Diffusive shock acceleration

Fermi's original idea [85] for the acceleration of cosmic rays was stochastic scattering on magnetic turbulence in the form of "magnetic clouds". Unfortunately, the acceleration rate is only second order in the speed u of the scattering centres (hence the name second order Fermi acceleration): Although the average energy gained in head-on collisions is $\propto u/c$, the average energy lost in an overtaking collision is equal but of opposite sign. In fact, only an asymmetry between the probability for either type of interaction, also of order u/c , leads to an overall energy gain, but only of second order, i.e. $(u/c)^2$. It turns out that with the low speed of magnetic interstellar turbulence

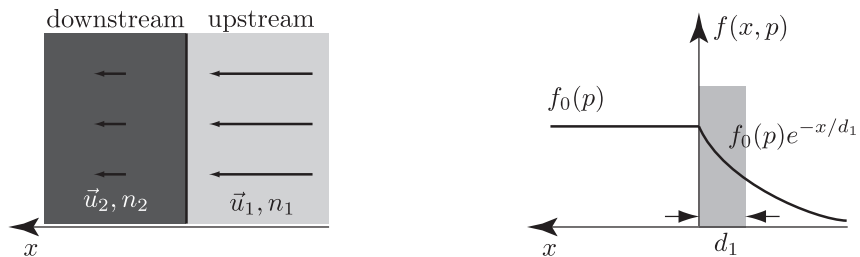


Figure 1.2.: **Left:** DSA setup in the rest frame of the shock front. u_1 (u_2) and n_1 (n_2) denote upstream (downstream) plasma velocity and density, respectively. **Right:** Profile of the phase space density at a fixed momentum p . Particles within a momentum dependent distance D/u of the shock front participate in the acceleration process.

this mechanism would take much too long. Even for the much faster turbulence in the shocked shells of SNRs, second order Fermi acceleration is still too inefficient.

The standard theory for cosmic ray acceleration is therefore a first order Fermi process in the converging flow of upstream and downstream plasma across a shock front: diffusive shock acceleration (DSA). For a contemporary review, see [86].

Macroscopic picture

We consider steady diffusive shock acceleration (DSA) at a one-dimensional, parallel shock (that is the ambient magnetic field is parallel to the shock *normal*) in the test-particle approximation, that is ignoring the back-reaction of a potentially energetically important population of hadronic cosmic rays on the shock front. This was worked out almost simultaneously by three different groups [87, 88, 89]. (For the microscopic treatment of DSA [90], also published at the same time, see 1.2.5.) Here, we follow the treatment of [91].

The setup is as follows: The shock front is in its rest-frame in the y - z -plane at $x = 0$ and upstream plasma is flowing in from $x < 0$ and downstream plasma flowing out to $x > 0$ (see left panel of Fig. 1.2). The density (velocity) of the background plasma are n_1 and n_2 (u_1 and u_2) in the upstream and downstream region, respectively.

We now consider the transport equation 1.23 in this one-dimensional setup, however, ignoring the momentum diffusion term,

$$\frac{\partial f}{\partial t} + u \frac{\partial f}{\partial x} = \frac{\partial}{\partial x} \left(D \frac{\partial f}{\partial x} \right) + \frac{1}{3} \frac{\partial u}{\partial x} p \frac{\partial f}{\partial p}. \quad (1.26)$$

where we have set $D \equiv D_{\parallel}$. The general steady state solution for $x \neq 0$ is,

$$f(x, p) = g_1(p) \exp \left(\int_0^x dx' \frac{u}{D(x', p)} \right) + g_2(p). \quad (1.27)$$

Imposing the usual boundary conditions, i.e. $f(x, p) \xrightarrow{x \rightarrow -\infty} f_1(p)$, where $f_1(p)$ is the phase space density far upstream, that is the injection spectrum, and $|f(x, p)| < \infty$ for $x \rightarrow \infty$, we find

$$f(x, p) = \begin{cases} f_1(p) + g_1(p) \exp \left(\int_0^x dx' u/D \right) & \text{for } x < 0, \\ g_2(p) = f_2(p) & \text{for } x > 0. \end{cases} \quad (1.28)$$

The exponential term reflects the fact that only upstream diffusion can counterbalance the convection by the background plasma in the upstream half-plane. The spatial dependence is illustrated for a homogeneous diffusion coefficient in the right panel of Fig. 1.2. Furthermore, the scale height of the exponential, $d_1(p) = D_1(p)/u_1$, is the distance that particles can on average diffuse away from the shock before being lost from the acceleration process. As the diffusion coefficient is growing with momentum, lower energy particles are confined more closely to the shock than high energy particles.

To relate $f_1(p)$, $g_1(p)$ and $f_2(p)$, we need to find matching conditions at the shock. These can be found most easily by multiplying Eq. 1.26 by a test function and integrating over an infinitesimal interval around $x = 0$. For the test-function $\int_0^x dx'/D(x')$, we find,

$$[f]_{-\varepsilon}^{\varepsilon} = \mathcal{O}(\varepsilon), \quad (1.29)$$

that is f is continuous across the shock. For the test-function 1 on the other hand,

$$\left[D \frac{\partial f}{\partial x} \right]_{-\varepsilon}^{\varepsilon} + \frac{1}{3} [u]_{-\varepsilon}^{\varepsilon} p \frac{\partial f}{\partial p} = \mathcal{O}(\varepsilon), \quad (1.30)$$

which for $\varepsilon \rightarrow 0$ is the matching condition for $\partial f / \partial x$.

Substituting Eq. 1.28 into Eqs. 1.29 and 1.30, and eliminating g_1 , we find

$$(r - 1)p \frac{\partial f_2}{\partial p} = 3r(f_1 - f_2), \quad (1.31)$$

which is integrated to give

$$f_2(p) = ap^{-a} \int_0^p dp' p'^{a-1} f_1(p') + bp^{-a}, \quad (1.32)$$

where $a \equiv 3r/(r-1)$ is 4 for a strong shock, $r = 4$ (see Sec. 1.2.3). Ignoring the second term, which can be interpreted as acceleration of particles from the thermal background, it turns out that, as long as $f_1(p)$ is softer than p^{-a} , the resulting spectrum $f_2(p)$ is a power law with spectral index a . The coordinate space density of accelerated particles is then $n(p)dp = 4\pi p^2 f_2(p) \propto E^{-2}$ which is the well-known result of DSA.

Microscopic picture

Although the macroscopic picture nicely proves that DSA leads to a power law spectrum $\propto E^{-2}$, there is no physical intuition involved that could explain *how* the power law form comes about. Therefore, we re-derive the result of the last section, following a more physical microscopic approach [90] (see also [92, 93]).

As mentioned above, in second order Fermi acceleration, the test-particles can gain or lose energy in approaching or following scatterings, respectively. In DSA, a first order Fermi process, however, the test-particles only encounter approaching scatterings: Seen from either plasma frame (downstream or upstream), the other side is always approaching. After crossing the shock, the test-particle quickly isotropises in the new frame experiencing only approaching scatterings which lead to energy gains. The energy gain rate is therefore proportional to the energy gained in every scattering, u/c .

To calculate the spectrum we need in fact both, the momentum gain Δp of a test-particle in a cycle across the shock-front, i.e. coming from the upstream plasma, crossing to the downstream side and crossing back to the upstream side; and the probability that a particle gets advected downstream so that it is lost from the acceleration process.

Consider a particle with momentum p , velocity v and pitch angle μ in the upstream frame. In the shock frame its momentum is $p(1 + \mu u_1/v)$. Crossing the shock front, its momentum does not get changed, but in the downstream frame it is measured as $p(1 + \mu(u_1 - u_2)/v)$. To calculate its average momentum change on crossing the shock front *once*, we average over the pitch angle,

including the weighting factor 2μ ,

$$\langle \Delta p \rangle = p \int_0^1 d\mu \mu (u_1 - u_2) / v 2\mu = \frac{2}{3} p \frac{u_1 - u_2}{v}. \quad (1.33)$$

Crossing back, u_1 and u_2 get swapped but the integration also runs from 0 to -1 , so the results is the same.

The probability that a particle gets advected downstream can be calculated from the flux of particles to downstream infinity, $n_2 u_2$, divided by the flux of particles crossing the shock front from upstream to downstream, $\int_0^1 d\mu \mu v n_2 / 2 = n_2 v / 4$. Hence, the probability that a particle gets advected to downstream infinity is $4u_2 / v$.

We now consider the cumulative spectrum $N_i(x, p) = \int_p^\infty dp' 4\pi p'^2 f_i(x, p)$ and assume that at upstream infinity all particles have the same momentum p_0 , that is $N_1(-\infty, p) = N_0 \theta(p - p_0)$. Since all the particles injected will eventually end up in the downstream region and can only have gained energy, $N_2(\infty, p) = r N_0$ for $p < p_0$.

The momentum p_n and velocity v_n of a particle that has performed n cycles and has therefore crossed the shock $2n$ times, are of course random variables but for large n , they are expected to peak sharply around a mean (deterministic) value. Then,

$$p_n \sim \prod_{i=1}^n \left(1 + \frac{4}{3} (u_1 - u_2) / v_i \right) p_0 \quad \Rightarrow \quad \log \left(\frac{p_n}{p_0} \right) \sim \frac{4}{3} (u_1 - u_2) \sum_{i=1}^n \frac{1}{v_i}. \quad (1.34)$$

The probability P_n , that the particle has not been lost from the acceleration after n cycles is,

$$P_n \sim \prod_{i=1}^n \left(1 - \frac{4u_2}{v_i} \right) \quad \Rightarrow \quad \log(P_n) \sim -4u_2 \sum_{i=1}^n \frac{1}{v_i}. \quad (1.35)$$

Combining Eqs. 1.34 and 1.35 gives

$$\log(P_n) \sim -3 \frac{u_2}{u_1 - u_2} \log \left(\frac{p_n}{p_0} \right) \Rightarrow P_n = \left(\frac{p_n}{p_0} \right)^{-3u_2 / (u_1 - u_2)} \quad (1.36)$$

The cumulative spectrum of particles downstream is then just the total density of particles

$N_2 = rN_0$ times the probability P_n ,

$$N_2(p_n) = P_n N_2 = r \left(\frac{p_n}{p_0} \right)^{-3u_2/(u_1-u_2)} N_0 \quad \text{for } p_n > p_0 \quad (1.37)$$

and

$$f_2(p) = -\frac{1}{4\pi p^2} \frac{\partial N_2}{\partial p} = \frac{N_0}{4\pi} \frac{3u_1}{u_1 - u_2} \left(\frac{p}{p_0} \right)^{-3u_1/(u_1-u_2)} \quad (1.38)$$

Although this result only reproduces the result of the macroscopic approach, Eq. 1.32, it becomes clear that as in every Fermi process, the power law spectrum is the result of the form of the energy gained on every crossing which is proportional to the energy of the incoming particle, and the probability to be lost from the acceleration process. In the case of acceleration at a shock front, both these number are fixed by the kinematics of the shock, as expressed by the compression ratio (and the Mach number).

1.2.6. Galactic propagation

The transport equation can, of course, not only be applied to the acceleration of cosmic rays but also to cosmic ray transport in the Galaxy. Expressing the original Eq. 1.23 in differential particle density $n(t, \mathbf{x}, E)$ instead of phase space density $f(t, \mathbf{x}, p)$, $n(t, \mathbf{x}, E)dE = 4\pi p^2 f(t, \mathbf{x}, p)dp$, and adding the injection of cosmic rays by SNRs as well as their production and losses due to fragmentation and decay, we find,

$$\begin{aligned} & \frac{\partial n_i}{\partial t} - \nabla \cdot (D_{xx} \cdot \nabla n_i - \mathbf{u} n_i) - \frac{\partial}{\partial p} p^2 D_{pp} \frac{\partial}{\partial p} \frac{1}{p^2} n_i - \frac{\partial}{\partial p} \left(\frac{dp}{dt} n_i - \frac{p}{3} (\nabla \cdot \mathbf{u}) n_i \right) \\ & = q + \sum_{i < j} \left(c \beta n_{\text{gas}} \sigma_{j \rightarrow i} + \gamma \tau_{j \rightarrow i}^{-1} \right) n_j - \left(c \beta n_{\text{gas}} \sigma_i + \gamma \tau_i^{-1} \right) n_i, \end{aligned} \quad (1.39)$$

where β is the speed in units of the speed of light c and $\gamma = (1 + \beta^2)^{-1/2}$. In the following, we discuss the different terms and their physical meaning in some more detail.

- **diffusion:** $-\nabla \cdot D_{xx} \cdot \nabla n_i$

The main transport mode of cosmic rays is resonant pitch angle scattering on magnetic irregularities. Diffusion is strongly anisotropic ($\delta B \ll B$) locally, but the particle density gets isotropised by the fluctuations of the magnetic field at larger scales of $\mathcal{O}(100)$ pc. The parallel

diffusion coefficient $D_{xx} \approx (\delta B_{\text{res}}/B)^{-2} v r_g/3$, with r_g the Larmor radius and δB_{res} the field strength at the resonant wave number $k = 1/r_g$, is inversely proportional to the energy density in the turbulent component (see also Eq. 1.24), $w(k)dk \sim k^{-2+\delta}dk$, which can be of Kolmogorov ($\delta = 1/3$) or Kraichnan ($\delta = 1/2$) type. Expressing the diffusion coefficient in energy E , one finds $D_{xx} \propto \beta E^\delta$. Furthermore, with $\delta B_{\text{res}} \approx B \simeq \text{few } \mu\text{G}$ at the principal scale of $\sim (100 \text{ pc})^{-1}$, $D_{xx0} \equiv D_{xx}(1 \text{ GeV}) \simeq 10^{28} \text{ cm}^2 \text{ s}^{-1}$. The effective values for δ and D_{xx0} are usually determined from local observations of secondary-to-primary ratios (see Sec. 1.2.7).

- **convection:** $\nabla \cdot \mathbf{u} n_i$

There is evidence of a (CR driven [94]) wind in other galaxies and one might wonder whether SNRs also power a similar wind in the Milky Way [95, 96, 97, 98, 99, 100]. Direct observational evidence, however, only comes from x-rays close to the Galactic centre. A common way to achieve symmetry with respect to the galactic plane, $\mathbf{u}(-z) = \mathbf{u}(z)$, is to consider a velocity linearly increasing with distance from the plane, $\mathbf{u} \propto \mathbf{e}_z (du/dz) z$. As the convection rate is decreasing with energy, convection can only play a role at lower, $\mathcal{O}(1)$ GeV, energies and convection flattens out the steepening of source spectra (due to energy-dependent diffusion), observable for example in secondary-to-primary ratios. These also allow to constrain the convection velocity to $u = \mathcal{O}(10) \text{ km s}^{-1}$ (for one-zone models [101, 102]).

- **adiabatic energy losses/gains:** $\frac{\partial}{\partial p} \frac{p}{3} (\nabla \cdot \mathbf{u}) n_i$

Diverging flows lead to adiabatic energy losses. This effect is for example important in propagation models with non-uniform galactic winds.

- **reacceleration:** $-\frac{1}{p^2} \frac{\partial}{\partial p} p^2 D_{pp} \frac{\partial}{\partial p} \frac{1}{p^2} n_i$

Substituting for the spatial diffusion coefficient, Eq. 1.24, in Eq. 1.20 gives the relation $D_{xx} D_{pp} = p^2 v_A^2/9$ where the Alfvén velocity v_A is somewhere around 30 km s^{-1} . (In fact, the energy dependence of the diffusion coefficients can be modified if one accounts for the energy lost from the ISM turbulence into CRs which leads to damping and consequently a steep rise in the spatial diffusion coefficient at lower energies [103].) As already mentioned, distributed acceleration in the ISM cannot be the main source of acceleration because of the observed energy dependence of secondary-to-primary ratios. However, as the diffusion-loss time, z_{max}^2/D_{xx} , is decreasing with energy and the time-scale of distributed acceleration,

$p^2/D_{pp} \propto D_{xx}/v_A^2$, is increasing, second order Fermi acceleration by diffusion in momentum space, so-called reacceleration, can play a role at lower energies. For example, reacceleration can show up in secondary-to-primary ratios and can potentially explain a bump in the boron-to-carbon ratio around 1 GeV [104, 105].

- **continuous energy losses:** $-\frac{\partial}{\partial p} \frac{dp}{dt} n_i$

All CRs lose energy due to ionisation and Coulomb interactions which are however only important at energies below a few GeV. In addition, electrons and positrons interact with the ISM emitting bremsstrahlung (again, only important at \sim GeV energies), but also synchrotron radiation on the galactic magnetic fields and inverse Compton scattering (ICS) on interstellar radiation fields (ISRFs). In the Thomson approximation, the energy loss rate is proportional to the energy squared [106],

$$\frac{dp}{dt} = -\frac{4\sigma_T c}{3} (\rho_{\text{ISRF}} + \rho_{\text{B}}) \left(\frac{E}{mc^2} \right)^2. \quad (1.40)$$

where σ_T is the Thomson cross section. The energy densities for a $3 \mu\text{G}$ magnetic field is 0.22 eV cm^{-3} ; for the CMB, IR and stellar radiation they are 0.26 eV cm^{-3} , 0.2 eV cm^{-3} and 0.45 eV cm^{-3} , respectively [107]. (See [108] for a sophisticated 3D modelling of ISRFs.) At higher centre-of-mass energies, the Thomson approximation is not valid any more and at even higher energies the cross section is in the Klein-Nishina regime and the loss rate becomes suppressed [107, 109] (see also [110]). For ICS, the critical energy depends on the average energy of the radiation background considered and is about $1.1 \times 10^6 \text{ GeV}$ for the CMB, $7.6 \times 10^4 \text{ GeV}$ for IR and $8.7 \times 10^2 \text{ GeV}$ for starlight [111].

- **primary injection:** q

As discussed in Sec. 1.2.2, acceleration of primary CRs is supposed to take place in SNRs and the spectrum is a power law in energy (or rigidity) with spectral index close to -2 (in the test-particle approximation).

- **nuclear spallation:** $\sum_{i < j} \left(c \beta n_{\text{gas}} \sigma_{j \rightarrow i} + \gamma \tau_{j \rightarrow i}^{-1} \right) n_j - \left(c \beta n_{\text{gas}} \sigma_i + \gamma \tau_i^{-1} \right) n_i$

Spallation or decay of primary (secondary) cosmic rays during their propagation lead to their depletion and to the injection of secondary (tertiary) CRs. Furthermore, catastrophic energy

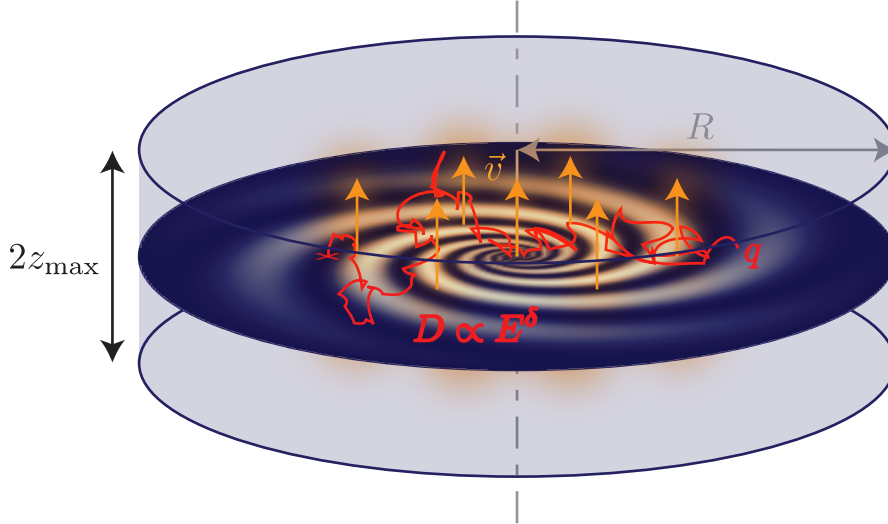


Figure 1.3.: Propagation setup. The thin disk of sources and interstellar gas is contained within a cylindrical cosmic ray halo of half-height z_{\max} and radius R . Within the halo cosmic rays diffuse in coordinate and momentum space, get convected, spallate and lose energy, depending on the details of the propagation model.

losses can in principle be accounted for by these terms. Note that spallation is dominantly on interstellar hydrogen and helium, i.e. $n_{\text{gas}} \sigma_{j \rightarrow i} = n_H \sigma_{j \rightarrow i}^H + n_{He} \sigma_{j \rightarrow i}^{He}$ and similar for $n_{\text{gas}} \sigma_i$. Parametrisations for meson production are discussed in Refs. [112, 113] and an overview of nuclear spallation cross section models is given in Ref. [114] and references therein.

Usually, GCR propagation is considered to be limited to a cylindrical volume of radius R and half-height z_{\max} that the galactic plane is contained in, see Fig. 1.3. The transport equation is thus required to satisfy the boundary conditions,

$$n(\mathbf{r}_{\parallel}, z, t) \equiv 0 \quad \text{for } |\mathbf{r}_{\parallel}| = R \text{ and for } z = z_{\max}, \quad (1.41)$$

where $\mathbf{r}_{\parallel} = \mathbf{e}_x x + \mathbf{e}_y y$. Alternatively, solutions without boundary conditions, but with a quickly increasing diffusion coefficient at the halo boundaries have been considered in [115] (see also [116]).

Solar modulation is usually modelled by a simple effective (electric) potential $\Phi \sim \mathcal{O}(100)$ MV [60] which is assumed to be the effect of dynamical effects in the solar wind which are still not fully understood. The effect on charged CRs is that the flux at the top of the atmosphere (TOA),

$J_{\text{TOA}}(E)$, is suppressed with respect to the interstellar flux $J_{\text{IS}}(E)$,

$$J_{\text{TOA}}(E) = \frac{E^2 - m^2}{(E + |Z|e\Phi)^2 - m^2} J_{\text{IS}}(E + |Z|e\Phi), \quad (1.42)$$

where (Ze) is the charge and m the mass of the CR particle.

Leaky box model

One of the earlier attempts to solve the problem of cosmic ray transport is the so-called Leaky Box model [117]. In this approach, all spacial dependencies are ignored and the Galaxy is described as a system that particles can escape from with a certain – in its simplest formulation, energy-independent – probability. In the steady state, this results in an exponential distribution of the column depth or grammage that cosmic rays particles have traversed. The average value of the order of a few g cm^{-2} must be a function of energy to explain the falling secondary-to-primary spectra. The simple Boltzmann-type equation describing this model,

$$\frac{dn_i}{dt} = -\frac{n_i}{\tau_{\text{esc}}} - \frac{n_i}{\tau_{\text{cool}}} + \sum_{i < j} \left(c\beta n_{\text{gas}} \sigma_{j \rightarrow i} + \gamma \tau_{j \rightarrow i}^{-1} \right) n_j - \left(c\beta n_{\text{gas}} \sigma_i + \gamma \tau_i^{-1} \right) n_i, \quad (1.43)$$

can be derived from the full transport equation by integrating over the cosmic ray halo and the contributions to the escape time τ_{esc} from diffusion and convection are $\sim D_{xx}/z_{\text{max}}^2$ and $\sim u/z_{\text{max}}$, respectively, and the cooling time $\tau_{\text{cool}} \sim p/(dp/dt)$.

Applying the simple leaky box model to a network of stable nuclei, one can compute the relative abundances of different isotopes assuming ratios at source that are similar to solar system abundances. For stable nuclei, it can be shown that the leaky box model reproduces the results of a diffusion model in certain limiting cases [118]. This can be understood considering that nuclei have a rather long residence time in the halo and therefore basically achieve the spatial averaging thereby justifying the leaky box approach. A generalisation of the leaky box model is the so-called weighted-slab technique [119, 120] that allows for more flexible path-length distributions.

Green's function approach

A more sophisticated, but still analytic approach is to determine the solution to the transport Eq. 1.39 for a δ -like injection $\delta(t)\delta(\mathbf{r})\delta(E - E_0)$, that is, to find the Green's function $G(t, \mathbf{r}, E)$. The differential spectral density for a continuous source distribution is then given by its convolution with the Green's function. A particularly nice and useful example has been worked out for the propagation of electrons and positrons¹ [121] (see also [122, 123, 124]), which we will also employ in Chapter 2.

As we are mainly interested in energies above ~ 10 GeV, we can ignore convection ($\mathbf{u} \equiv 0$) and reacceleration ($D_{pp} \equiv 0$), i.e. the transport equation 1.39 for the differential spectral density n of electrons and positrons reads,

$$\frac{\partial n}{\partial t} - \nabla \cdot (D \cdot \nabla) n - \frac{\partial}{\partial E} (b(E)n) = q(\mathbf{r}, t), \quad (1.44)$$

where the source term q now includes primary and secondary sources and the diffusion coefficient $D \equiv D_{\parallel}$ is assumed to be homogeneous in the following. If one could ignore the energy loss term $b(E)$ the energy of individual electrons and positrons would not change during their propagation, and the energy would simply be a parameter of a diffusion problem of the heat equation type and the corresponding Green's function is

$$\frac{1}{(4\pi Dt)^{3/2}} e^{-\mathbf{r}^2/4Dt}. \quad (1.45)$$

However, electrons and positron do lose energy and as the energy losses are continuous, the energy of a particle is monotonously decreasing from the energy at injection, $E_0 = E(t = 0)$, obeying,

$$\frac{dE}{dt} = b(E) = -b_0 E^2 \quad \Rightarrow \quad \frac{1}{E_0} - \frac{1}{E} = -b_0 t. \quad (1.46)$$

where we limit ourselves to the Thomson approximation. Given the time t since injection and the energy E at observation, the energy at injection E_0 is therefore unambiguously defined. As the diffusion coefficient is energy-dependent, we need to average it over time or equivalently over

¹In the following, "electrons" is meant to denote both, electrons and positrons.

intermediate energies, E' . The diffusion length squared $\ell^2 = 4Dt$ is a function of both, E and E_0 ,

$$\ell^2(E, E_0) = \int_0^t dt' 4D(E(t')) = 4 \int_{E_0}^E dE' \frac{D(E')}{b(E')}. \quad (1.47)$$

With Eq. 1.46 and $D(E) = D_0 E^\delta$, we find,

$$\ell^2(E, E_0) = 4 \int_{E_0}^E dE' \frac{D_0 E'^\delta}{b_0 E'^2} = \frac{4D_0}{b_0(1-\delta)} \left(E^{\delta-1} - E_0^{\delta-1} \right), \quad (1.48)$$

or with $E_0 = E/(1 - b_0 E t)$,

$$\ell^2(E, t) = \frac{4D_0}{b(1-\delta)} \left[E^{\delta-1} - \left(\frac{E}{1 - b_0 E t} \right)^{\delta-1} \right]. \quad (1.49)$$

The contribution from an injection of electrons of energy E_0 at $t = 0$, $\mathbf{r} = 0$ to the electrons of energy E at t , \mathbf{r} is therefore,

$$g(t, \mathbf{r}, E) = \frac{e^{-\mathbf{r}^2/\ell^2(E,t)}}{[\pi\ell^2(E,t)]^{3/2}} \delta \left(E - \frac{E_0}{1 + b_0 E_0 t} \right), \quad (1.50)$$

and a burst-like injection of a source spectrum $Q(E_0)$ hence contributes,

$$G(t, \mathbf{r}, E) = \int_0^\infty dE_0 Q(E_0) g(t, \mathbf{r}, E) = \frac{e^{-\mathbf{r}^2/\ell^2(E,t)}}{[\pi\ell^2(E,t)]^{3/2}} Q \left(\frac{E}{1 - b_0 E t} \right) (1 - b_0 E t)^{-2}. \quad (1.51)$$

To get the density for a steady source, this Green's function is integrated over time,

$$G^{\text{stdy}}(\mathbf{r}, E) = \int_0^\infty dt G(t, \mathbf{r}, E) = \frac{1}{b_0 E^2} \int_E^\infty dE_0 \frac{e^{-\mathbf{r}^2/\ell^2(E,E_0)}}{[\pi\ell^2(E, E_0)]^{3/2}} Q(E_0). \quad (1.52)$$

This result can also be obtained from the time-independent transport equation, i.e. Eq. 1.44 with $\partial n/\partial t \equiv 0$, see [125].

As electrons and positrons of tens and hundreds of GeV will lose most of their energy before travelling more than a few kiloparsecs and reaching the radial boundary of the cosmic ray halo, we ignore the radial boundary condition $n(t, r = R, z) = 0$. The boundary condition at $z = z_{\text{max}}$ can be implemented by the method of ‘‘mirror charges’’ [125],

$$G_{\text{disk}}(t, \mathbf{r}, E) = \sum_{n=-\infty}^{\infty} G(t, \mathbf{r}_n, E) \quad \text{where } \mathbf{r}_n = \begin{pmatrix} x \\ y \\ (-1)^n z + 2z_{\text{max}} n \end{pmatrix}. \quad (1.53)$$

It is useful to factorise the spatial dependence into a dependence on (x, y) and z , $\mathbf{r} = \mathbf{r}_{\parallel} + \mathbf{e}_z z$,

$$G_{\text{disk}}(t, \mathbf{r}, E) = \sum_{n=-\infty}^{\infty} \frac{1}{(\pi \ell^2)^{3/2}} e^{-\mathbf{r}_n^2 / \ell^2} Q(E_0) (1 - b_0 E t)^{-2} \quad (1.54)$$

$$= \frac{1}{\pi \ell^2} e^{-\mathbf{r}_{\parallel}^2 / \ell^2} Q(E_0) (1 - b_0 E t)^{-2} \frac{1}{z_{\text{cr}}} \chi \left(\frac{z}{z_{\text{cr}}}, \frac{\ell}{z_{\text{cr}}} \right) \quad (1.55)$$

where the sum has been expressed in terms of the elliptic theta function, ϑ_3 ,

$$\chi(\hat{z}, \hat{\ell}) = \frac{1}{\pi} \left[\vartheta_3 \left(\hat{z}, e^{-\hat{\ell}^2} \right) - \vartheta_3 \left(\hat{z} + \frac{\pi}{2}, e^{-\hat{\ell}^2} \right) \right], \quad (1.56)$$

and $z_{\text{cr}} = 4z_{\text{max}}/\pi$. As most primary and secondary sources as well as our position are basically in the thin galactic disk, $z \approx 0$ and $\chi(\hat{z}, \hat{\ell}) \rightarrow \chi(\hat{\ell}) \equiv \chi(0, \hat{\ell})$.

The Green's function with boundary condition for a steady source is

$$G_{\text{disk}}^{\text{stdy}}(\mathbf{r}, E) = \frac{1}{bE^2} \int_E^{\infty} dE_0 \frac{1}{\pi \ell^2} e^{-\mathbf{r}_{\parallel}^2 / \ell^2} Q(E_0) \frac{1}{z_{\text{cr}}} \chi \left(\frac{\ell}{z_{\text{cr}}} \right). \quad (1.57)$$

(Semi-)numerical codes

Both these propagation models oversimplify the problem but their assumptions are justified in certain limits: the leaky box model, for example, is accurate when considering stable nuclei, and the Green's function approach can be used for the propagation of electrons and positrons.

A more realistic approach must take into account the morphology of the galactic magnetic field (GMF) and the interstellar radiation fields (ISRFs) as well as the resulting spatial dependence of the energy loss rate and the production of secondary radiation like diffuse radio and gamma-ray. It should further use the information on the gas density in the ISM, which does not only enter through the energy loss rate but also in the production of gamma-rays through π^0 decay. The resulting transport equation cannot be solved analytically any more and therefore numerical solutions are the only resort.

There are a number of numerical codes for GCR propagation in the literature, some of them are publicly available. GALPROP [126, 127] numerically integrates the transport equation 1.39 on a spatial lattice by a Crank-Nicholson scheme. It can be run in a time-dependent mode or iteratively until a steady state, $\partial n_i / \partial t \approx 0$ is reached. GALPROP uses input from 21-cm and CO (tracer of H_2) maps for the ISM gas density and a sophisticated modelling of the interstellar radiation fields. It therefore allows not only calculations of nuclear and electron-positron fluxes but also more realistic predictions for gamma-rays and synchrotron radiation. The broad range of the predictions possible allows for important cross-checks, however, at the moment the full code is still not fast enough to allow for automated scans of the full multi-dimensional parameter space of the diffusion model.

A similar, though slightly more general code is DRAGON [116] which allows, for example, for position dependent, anisotropic diffusion and separate injection spectra for different species. As an example for a semi-analytical approach we mention USINE [128, 129, 130] which employs analytical solutions found for a simplified setup with, *e.g.*, simplified gas maps. This allows for sophisticated studies of the parameter space using MCMC techniques [131].

1.2.7. Observational results on the nuclear component

In the following, we summarise the observational results in nuclear GCRs which are, to a large extent, in agreement with the predictions from the standard model of GCRs, as described above. We postpone the discussion of the leptonic component as well as synchrotron and gamma-rays, all of which have recently been claimed to show anomalies possibly connected to DM, to Sec. 1.3 where DM indirect detection is discussed.

Primary nuclei

As mentioned before, it has been shown [118] that for stable primary and secondary nuclei the diffusive-convective transport equation 1.39 is in some limits equivalent to a leaky-box model. In particular, further neglecting secondary production, energy losses and reacceleration, the ambient spectrum I_i of a primary species i is [118],

$$I_i \propto Q_i \frac{1}{1/X_{\text{esc},i} + \sigma_i/m} \quad \text{with} \quad \frac{\sigma_i}{m} = \frac{n_H \sigma_H + n_{He} \sigma_{He}}{n_H m_H + n_{He} \sigma_{He}}, \quad (1.58)$$

where the column depth or grammage $X_{\text{esc},i} \propto 1/D$ is a power law in energy, $\propto E^{-\delta}$, above a few GeV/nucleon and $1/X_{\text{esc},i}$ dominates over the loss term σ_i/m . With a source spectrum $Q \propto E^{-\gamma}$, $\gamma \approx 2$, the theoretical prediction for absolute primary fluxes is therefore $I_i \propto E^\alpha$ with $\alpha = -\gamma - \delta$. From the local observation of primary nuclei (protons, Carbon etc.), we have $\alpha \approx -2.75$ which would imply $\delta \approx 0.75$. However, from secondary-to-primary ratios (see below), one can determine δ independent of the source spectrum and finds $\delta \approx 0.6$ for plain diffusion, $\delta \approx 0.4$ when including reacceleration (see Sec. 1.2.7). This implies a source spectrum of $\gamma \approx 2.15$ and $\gamma \approx 2.35$, for plain diffusion and diffusive reacceleration, respectively, which is only marginally in agreement with the expectation from diffusive shock acceleration, cf. Sec. 1.2.5. At energies below a few GeV, ionisation energy losses need to be taken into account.

In Fig. 1.4 we show a number of observations of the total proton and carbon flux, together with GALPROP results [103], for illustration.

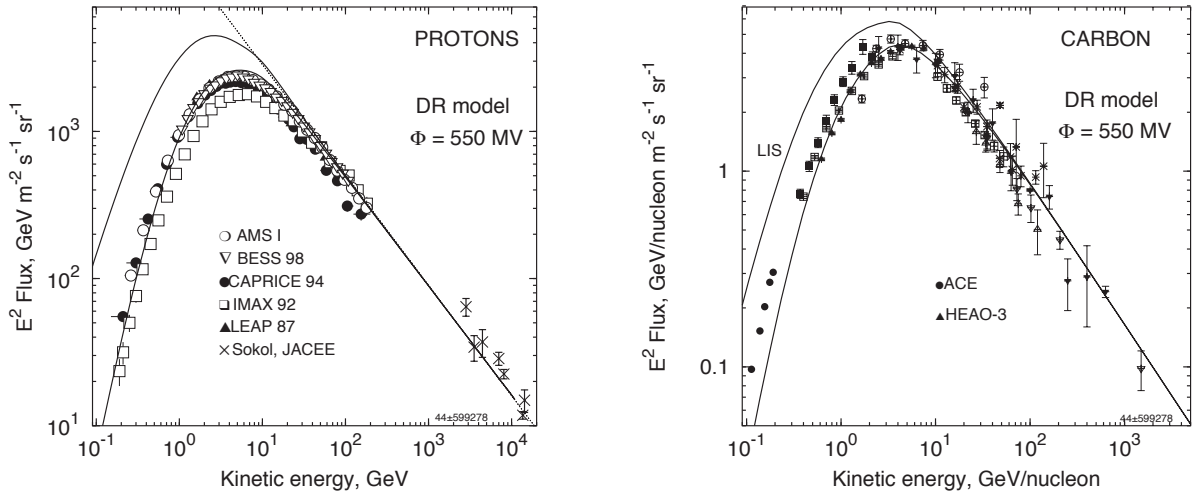


Figure 1.4.: **Left:** Absolute proton flux in a diffusive reacceleration (DR) model (from [103]). The upper line shows the local interstellar (LIS) flux, the lower line the solar modulated one with $\Phi = 550$ MV and the thin dotted line the LIS spectrum best fitted to the data above 20 GeV [132]. Data: AMS [133], BESS 98 [134], CAPRICE 94 [135], IMAX 92 [136], LEAP 87 [137], Sokol [138], JACEE [139]. **Right:** Absolute carbon flux in a diffusive reacceleration model (from [103]). Data from ACE [140, 141], HEAO-3 [142], for other references see [143] (symbols are changed).

Stable secondary nuclei

Secondary-to-primary ratios are used as test of the propagation model or to constrain its parameters, like the spectral index δ and normalisation D_{xx0} of the diffusion coefficient as well as the height of the diffusion zone z_{\max} . However, as D_{xx} and z_{\max} only enter into the fluxes of stable nuclei as the ratio D_{xx}/z_{\max} , there is a degeneracy between these quantities.

The steady-state ambient spectrum of species i of secondary cosmic rays can also be understood in the framework of the leaky box model,

$$I_j \propto \frac{\sum_{j < k} \left(\sigma_{k \rightarrow j} / m + \gamma (c \beta n_{\text{gas}} \tau_{k \rightarrow j})^{-1} \right) I_k}{1/X_{\text{esc},j} + \sigma_j / m}. \quad (1.59)$$

The numerator is dominated by primary species I_k and above a few GeV/nucleon, $I_k(E) \propto E^{\gamma-\delta}$. The denominator behaves similarly as for primaries, $X_{\text{esc},j} \propto E^{-\delta}$. Therefore, the secondary flux is softer than the primary one by $E^{-\delta}$ and the secondary-to-primary ratio is falling, $I_2/I_1 \propto E^{-\delta}$.

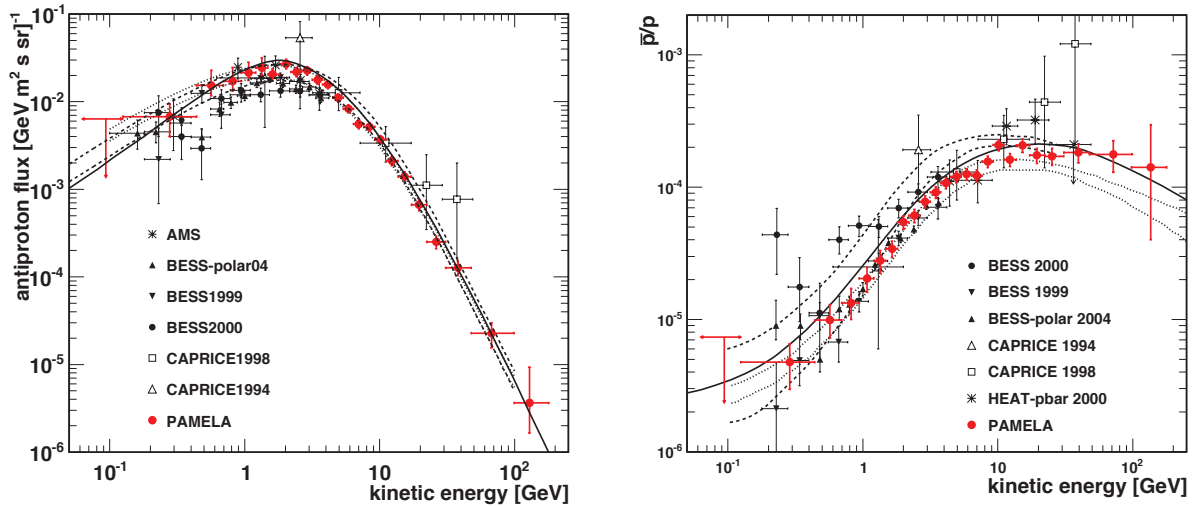


Figure 1.5.: **Left:** Absolute antiproton flux from PAMELA and some other contemporary measurements [144, 145, 146, 147, 148] (from [149]). The dotted and dashed lines show the upper and lower limits for a range of diffusion models, taking into account the uncertainties on diffusion model parameters and cross sections [129] and the solid line shows the prediction from a different, plain diffusion model [103]. **Right:** Antiproton-to-proton ratio as measured by PAMELA and some other contemporary experiments [144, 145, 146, 147, 150] (from [149]). The dashed lines show the upper and lower limits for a leaky box model [151], the dotted lines for a diffusive reacceleration convection model [152] and the solid line the prediction for a plain diffusion model [103].

Measurements of the antiproton-to-proton ratio and the absolute antiproton flux are shown in Fig. 1.5 together with some typical theoretical predictions. Figure 1.6 shows the B/C ratio, with predictions from the same GALPROP model as in Fig. 1.4 and for a diffusive reacceleration model [103]. The range of spectral indices allowed by the data ranges from 0.3 for diffusive reacceleration to ~ 0.6 for plain diffusion models.

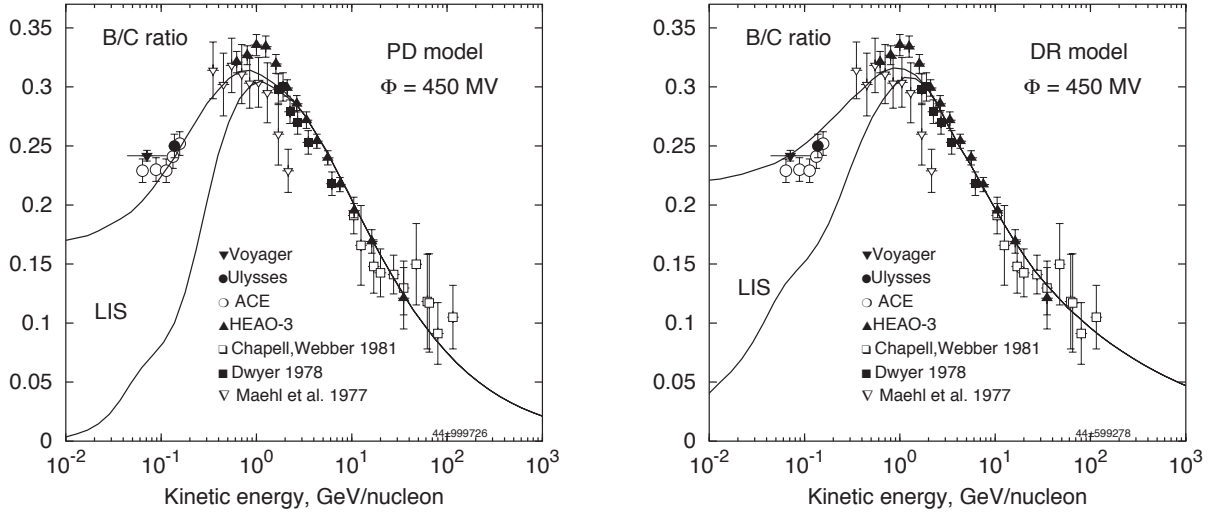


Figure 1.6.: Boron-to-carbon ratio as a function of kinetic energy per nucleon in a plain diffusion (PD) model (left panel) and a diffusive reacceleration (DR) model (right panel) (from [103]). The lower lines show the local interstellar (LIS) flux, the upper lines the solar modulated one with $\Phi = 450$ MV. The experimental data below 200 MeV/nucleon are from ACE [140], Ulysses [153] and Voyager [154] and some high energy data are from HEAO-3 [142]. For other references see [143].

Unstable secondary nuclei

Stable nuclei propagate over kiloparsecs before escaping from the cosmic ray halo, and hence the leaky box approximation is a good approximation for, if not even equivalent to, a diffusion model. For unstable nuclei the situation is however different. If their lifetime is smaller than or of the order of the average residence time in the Galaxy, their decays must be taken into account and escape is now competing with nuclear decay. As the survival probability, however, only depends on the time spent since production and not on the distance (the amount of matter traversed), secondary-to-primary ratios, like $^{10}\text{Be}/^9\text{Be}$, can in principle break the degeneracy between diffusion coefficient

D_0 and halo height z_{\max} . At the moment however, the quality of the data, in particular the statistics, is not good enough to really allow determining both parameters independently. Future cosmic ray experiments will provide better data, that will hopefully allow for the determination of either parameters, as both are in fact important for other observables, for example diffuse radio or gamma-ray backgrounds.

1.3. Dark Matter Indirect Detection

If the DM particle is in fact a weakly interacting particle produced by thermal freeze-out, see Sec. 1.1.2, then DM particles and antiparticles exist in equal amounts. By virtue of the weak annihilation cross section, the rate of annihilation is appreciable. A simple estimate of the annihilation rate per volume of a solar system DM density ρ_{\odot} gives,

$$\frac{1}{2} \frac{\rho_{\odot}^2 \langle v\sigma \rangle}{m_{\text{DM}}^2} \simeq 1.4 \times 10^{-31} \text{ cm}^{-3} \text{ s}^{-1} \left(\frac{\rho_{\odot}}{0.3 \text{ GeV cm}^{-3}} \right)^2 \left(\frac{m_{\text{DM}}}{100 \text{ GeV}} \right)^{-2} \left(\frac{\langle v\sigma \rangle}{3 \times 10^{-26} \text{ cm}^3 \text{ s}^{-1}} \right). \quad (1.60)$$

This amounts to a total rate of $1.6 \times 10^{34} \text{ s}^{-1}$ in a 1 kpc sphere around the Sun or $4.1 \times 10^{37} \text{ s}^{-1}$ for an NFW DM density profile, $\rho(r) = 2\rho_{\odot}(r/r_{\odot})^{-1}(1 + (r/r_{\odot}))^{-2}$ [155].

Another possibility is DM decay. Although many DM models invoke a discrete symmetry to make the DM particle stable what is needed for an effectively stable DM candidate is actually only that its lifetime is much longer than the age of the Universe. In order to produce observable fluxes, the lifetime should however not be too large. A similar estimate as above gives,

$$\frac{\rho_{\odot}}{m_{\text{DM}}} \frac{1}{\tau_{\text{DM}}} \simeq 3 \times 10^{-30} \text{ cm}^{-3} \text{ s}^{-1} \left(\frac{\rho_{\odot}}{0.3 \text{ GeV cm}^{-3}} \right) \left(\frac{m_{\text{DM}}}{100 \text{ GeV}} \right)^{-1} \left(\frac{\tau_{\text{DM}}}{10^{27} \text{ s}} \right)^{-1}. \quad (1.61)$$

Lifetimes of 10^{26} s are naturally expected from, e.g. dimension-6 operators in grand unifying theories (GUTs) which are suppressed by two powers of the GUT scale $M_{\text{GUT}} = 2 \times 10^{16} \text{ GeV}$,

$$\tau \sim \frac{M_{\text{GUT}}^4}{m_{\text{DM}}^5} \sim 10^{26} \text{ s}, \quad (1.62)$$

for $m_{\text{DM}} = 1 \text{ TeV}$.

The particles produced this way, i.e. cosmic ray protons, antiprotons, electrons, positrons,

gamma-rays and neutrino, could in principle be observed on or around the Earth. Furthermore, annihilation products can produce secondary radiation like radio/microwaves from synchrotron or gamma-rays from ICS in addition to those from astrophysical CRs. The idea of indirect DM detection is then to extract the (possible) signal of DM annihilation or decay from the astrophysical backgrounds and use their spectral or spatial information to constrain the particle physics model of DM.

Of course, a crucial question and the main purpose of this work is the determination of the contribution from backgrounds, i.e. the fluxes from purely astrophysical sources, to the new signals from the annihilation or decay of DM. On first sight, the constraint on these fluxes seem to be rather robust: According to the standard paradigm (cf. Sec. 1.2.2), the primary sources of GCRs are supernova remnants (SNRs) which are expected to produce power law spectra (see Sec. 1.2.5) and even after propagation, these fluxes should have rather featureless spectra. DM annihilation or decay is however expected to have very different injection spectra: if DM annihilated in a $2 \rightarrow 2$ process or decayed to two particles, $1 \rightarrow 2$, the energy of the annihilation/decay products would be M_{DM} or $M_{\text{DM}}/2$, respectively. Hadronisation, for example of $q\bar{q}$ pairs directly produced or from gauge bosons, $W^+ \rightarrow q\bar{q}'$, $Z \rightarrow q\bar{q}$ etc., would considerably broaden the energy spectrum. In any case, the injection would be much more concentrated in energy and even after propagation, the spectra should be different from the generic power law type of astrophysical origin.

In the following sections, we will briefly review the ideas, prospects and current status of DM indirect detection in different channels assuming the *standard* astrophysical backgrounds as defined by the standard picture of GCRs. We present the claims of DM signature made in the charged lepton channels as well as the microwave and gamma-ray sky maps.

1.3.1. Antimatter

Using antimatter produced by annihilation or decay of DM for indirect detection harnesses the standard predictions for antimatter from astrophysical sources: a generally much lower abundance than matter and a particular energy dependence of the ratio of antimatter to matter. Due to their secondary nature, the spectrum of antimatter cosmic rays, like antiprotons or positrons, is softer than (primary) matter spectra and the secondary-to-primary ratios are falling above a few GeV, $\propto E^{-\delta}$, see Sec. 1.2.7.

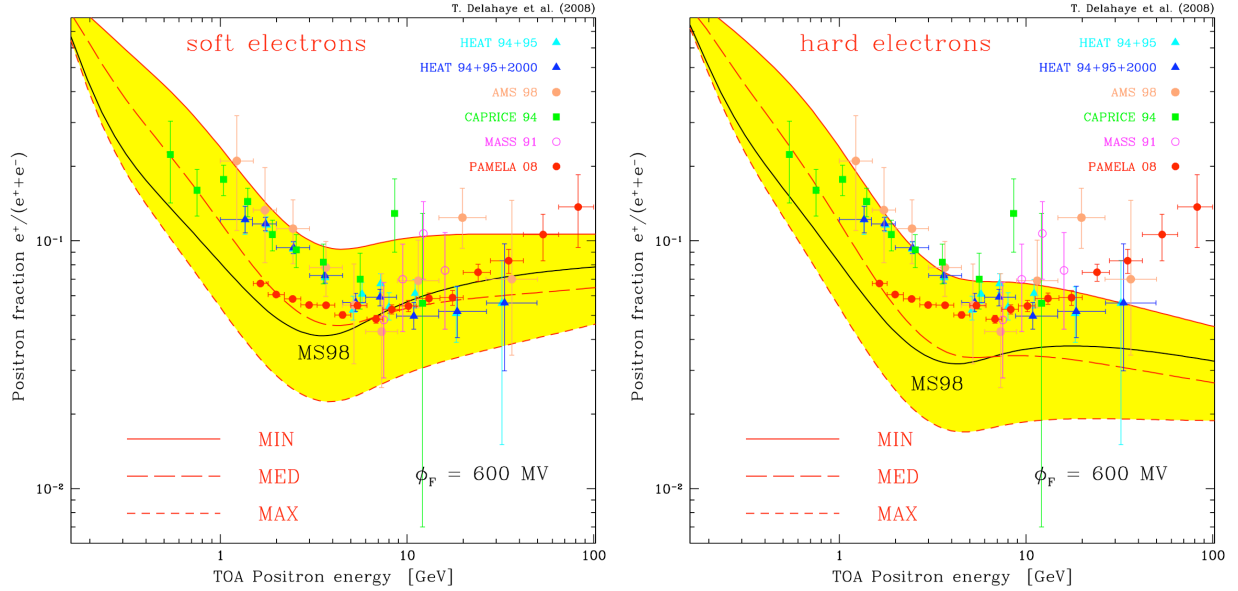


Figure 1.7.: The positron fraction as predicted in different cosmic ray propagation models for a rather soft (left panel) and harder (right panel) electron spectrum (from [157]). The yellow band is spanned by the fluxes from a range of sets of propagation model parameters. Three particular models, MIN, MED and MAX (named according to the effect on secondary antiprotons) are shown by the red solid, long dashed and short dashed lines. The data are from CAPRICE [158], HEAT [159], AMS [160, 161], MASS [162] and PAMELA [163].

In the following, we will briefly review the prospects for detection in two possible secondary-to-primary ratios, the positron fraction and the antiproton-to-proton ratio and quickly mention antideuterons.

Positron fraction

The positron fraction is defined as the ratio of the flux of positrons J_{e^+} to the total flux of electrons and positrons ($J_{e^+} + J_{e^-}$),

$$\text{positron fraction} \equiv \frac{J_{e^+}}{J_{e^+} + J_{e^-}}. \quad (1.63)$$

As mentioned above, in the standard picture of GCRs, positrons are only produced as secondaries by spallation of primary protons and nuclei which leads to lower abundances and softer spectra for the positrons and hence a falling positron fraction above a few GeV [156]. The benchmark prediction in [126] was one of the first applications of the GALPROP code.

The various sources of uncertainties and their impact on both the absolute positron flux and

the positron fraction have been assessed in [157]. The authors calculate the possible range in the absolute positron flux and the positron fraction from a broad range of models which differ in the primary proton fluxes adopted, the cross sections used and the primary electron spectrum assumed. The range induced by the uncertainty in the propagation model covers a factor of six between the lowest and the highest possible flux at 1 GeV but decreases to a factor 2.9 at 100 GeV. In particular, two different spectral indices for the locally measured electron flux are used, $\alpha = -3.35$ (hard) and $\alpha = -3.53$ (soft), and the positron fraction is always found to be falling for the hard electron spectrum and only very slightly rising for the soft electron spectrum, cf. Fig. 1.7. In fact, the (still preliminary) absolute electron flux measured by PAMELA [164], can be fitted with a power law with spectral index $\alpha = -3.226 \pm 0.020$ between 10 and 60 GeV and is even harder below. Therefore, the soft electron spectrum is ruled out and even within the rather large uncertainties, the positron fraction from secondary production is always falling.

This is however in disagreement with the recent findings [163] from the PAMELA experiment which shows a *rising* positron fraction above ~ 5 GeV, see Fig. 1.7. This trend was already apparent in the combined (1994, 1998, 2000) HEAT data [165], although with much larger uncertainties. Even more than 20 years ago, the rise in the positron fraction was realised [166] and tried to explain with some exotic contribution, possibly from pulsars.

Of course, in particular in connection with claims of excesses in the absolute electron plus positron flux by PPB-BETS [167], ATIC [168] and Fermi-LAT [169] (see also Sec. 1.3.2 below), this result has generated much attention, mainly prematurely interpreted as evidence for WIMP annihilation. In fact, within a year of the presentation and publication of the PAMELA data, a multitude of models was put forward (see, for example, [170] for a comprehensive, though non-exhaustive list of references) that could explain the upturn in terms of the onset of a new, harder primary positron component from DM annihilation or decay.

The contribution from DM annihilation can be taken into account both in (semi) analytic and in fully numerical computations by an additional source term on the RHS of the transport equation 1.39,

$$q_{e^\pm}^{\text{DM}}(r, z, E_{e^\pm}) = \frac{1}{2} \langle \sigma_{\text{ann}} v \rangle g(E_{e^\pm}) \left(\frac{\rho_\chi(r, z)}{m_{\text{DM}}} \right)^2. \quad (1.64)$$

Here, $\langle \sigma_{\text{ann}} v \rangle$ denotes the averaged annihilation cross section times velocity, $\rho_\chi(r, z)$ the DM halo

profile and $g(E_{e^\pm})$ is the differential production spectrum. The latter encodes the particle physics (obviously dependent on the DM model considered). Adding this flux to the one from astrophysically produced secondary positrons, predictions for the positron fraction can be made.

However, with a thermal annihilation cross section, $\langle\sigma_{\text{ann}}v\rangle \approx 3 \times 10^{-26} \text{ cm}^3 \text{ s}^{-1}$, and standard astrophysical assumptions about the DM halo, e.g. NFW [155] or isothermal [171] profile, local DM density of $\sim 0.3 \text{ GeV cm}^{-3}$, it turns out that the additional fluxes fall short by between a factor of 10 to 1000, depending on the DM mass (see, e.g. [172]). It would be very difficult to detect such small deviations from the astrophysical backgrounds, in particular considering the uncertainties involved.

In fact under certain assumptions one can expect an additional “boost factor” to appear in Eq. 1.64, either from astrophysics or particle physics. Astrophysical boost factors are induced by overdensities in the distribution of DM as for example predicted by N -body simulations. This does not only lead to a global amplification compared to a smooth DM density, $\int dV \rho^2 > (\int dV \rho)^2$, but in particular to potentially “bright” nearby clumps of DM. However, the probability of such a DM overdensity close enough to the Earth to explain the excess in the positron fraction is very small [173]. Particle physics boost factors can come from a low-velocity enhancement of the annihilation cross section, for example by a resonance just below $2M_{\text{DM}}$ [174] or so-called Sommerfeld enhancement [175, 176, 177]. It is also possible to overcome the helicity suppression of the s -wave annihilation into two fermions by emitting a photon. Alternatives include giving up the WIMP paradigm by, e.g. assuming non-thermal DM production (see [178] for the example of Wino-like neutralino DM).

In terms of annihilation channels, the PAMELA positron fraction *alone* allow annihilation to charged leptons for a wide range of DM masses, $m_{\text{DM}} \gtrsim 100 \text{ GeV}$ [172]. For light DM, $m_{\text{DM}} \sim 100 \text{ GeV}$, annihilation into W bosons is also possible.

Absolute antiproton flux and antiproton-to-proton ratio

For a generic WIMP model, there is *a priori* no reason why DM should only annihilate or decay into electrons and positrons or other charged leptons. In fact, heavy quarks possibly produced by DM annihilation or decay will hadronise to all sorts of baryons, ultimately also yielding protons

and antiprotons. The antiproton-to-proton ratio,

$$\text{antiproton-to-proton ratio} \equiv \frac{J_{\bar{p}}}{J_p}, \quad (1.65)$$

and the absolute antiproton flux can therefore be used as a cross check for DM explanations for the positron excess.

First of all, one should note that predictions for the background of antiprotons from the spallation of (mostly) GCR protons on the interstellar H and He are able to reproduce the measurements by BESS [147], CAPRICE [145] and AMS-01 [148] on the absolute antiproton flux as well as the most recent PAMELA data (see Sec. 1.2.7 and Fig. 1.5). A detailed study of the background investigating the uncertainties from the cross sections used and the diffusion parameters adopted, has been presented in [129].

The potential contribution from the annihilation of DM into antiprotons can be calculated within the theoretical frameworks presented in 1.2.6 or using fully numerical codes like GALPROP, starting from a spatially varying injection term,

$$q_{\bar{p}}^{\text{DM}}(r, z, E_{\bar{p}}) = \frac{1}{2} \langle \sigma_{\text{ann}} v \rangle g(E_{\bar{p}}) \left(\frac{\rho_{\chi}(r, z)}{m_{\text{DM}}} \right)^2. \quad (1.66)$$

Here, $g(E_{\bar{p}})$ is the differential production spectrum, assembled from the branching ratios B_h into quarks or gluons h in different channels F, as well as the fragmentation and hadronisation functions $dN_{\bar{p}}^h/dE_{\bar{p}}$,

$$g(E_{\bar{p}}) = \sum_{F,h} B_h^{(F)} \frac{dN_{\bar{p}}^h}{dE_{\bar{p}}}, \quad (1.67)$$

where $E_{\bar{p}}$ is the antiproton's kinetic energy.

Considering again the uncertainties introduced by the GCR propagation parameters but also by the DM halo model adopted, the semi-analytic analysis of [179] finds a large proportion of a scan over a particular MSSM parameter space to be consistent with the antiproton fluxes. We note that in this study no boost factors were introduced.

However, antiproton measurements can give stringent constraints [172, 152] on a number of models invoking boost factors to explain the anomalies in the lepton channels, e.g. the positron excess. Lepton channels are still available at all masses, but the antiproton data basically exclude

hadronic annihilation channels with $m_{\text{DM}} \lesssim$ a few TeV. Above 10 TeV, both leptonic and hadronic channels (excluding, perhaps, direct annihilation into quarks) give both good fits to positron and antiproton data. For light and intermediate masses, however, annihilation into gauge and Higgs bosons must somehow be suppressed. For an example of a model building way out of this, see [180].

Anti deuterons

Following the idea of DM indirect detection in rare nuclei it was suggested [181] to look for anti deuterons \bar{D} from the annihilation of DM. Secondary antideuterons get produced by GCR p , He and \bar{p} impinging on interstellar H and He, with $p\text{H}$ and $p\text{He}$ interactions dominating but contributions from \bar{p} becoming comparable below 1 GeV/ n . Uncertainties from the cross section and again from the cosmic ray model amount to an order of magnitude at ~ 0.1 GeV/ n , decreasing to about a factor four at ~ 100 GeV/ n [182], similar to the behaviour for the antiproton flux [129].

Although currently only upper limits on the \bar{D} flux exist [183], it turns out that with reasonable assumptions for the propagation model the ratio of DM signal to astrophysical secondary background is usually larger than 0.5 below 1 GeV/ n for DM masses up to hundreds of GeV. Anti deuterons are therefore one of the most promising detection channels for light and intermediate WIMP masses, and it has been shown [182] that with the sensitivity of the forthcoming GAPS long-duration balloon flight experiment [184] a large fraction of a low-energy MSSM parameter space is accessible.

1.3.2. The total electron-positron flux

In contrast to stable nuclei, electrons and positrons lose their energy quickly through synchrotron radiation and inverse Compton scattering, see Sec. 1.2.6. They can therefore only travel finite, energy-dependent distances before losing all their energy. The flux on Earth at the highest, $\mathcal{O}(1)$ TeV energies, is therefore dominated by the closest and youngest sources. In particular, considering that due to the discreteness of the sources in space and time there is/are necessarily a (few) source(s) of minimum distance and age, one predicts a propagation cut-off in energy. The older and further sources however add up to a smooth spectrum below ~ 100 GeV. For a more detailed and quantitative discussion see Sec. 2.3.1.

The combined differential flux of GCR electrons and positrons, $(J_{e^-} + J_{e^+})$, has been measured

by a number of experiments over the last decades, however, with considerable scatter, see Fig. 1.8. Here, we focus on two more recent, but somewhat contradictory results which both hint at some sort of excess with respect to pre-Fermi, standard GCR propagation models [126, 185].

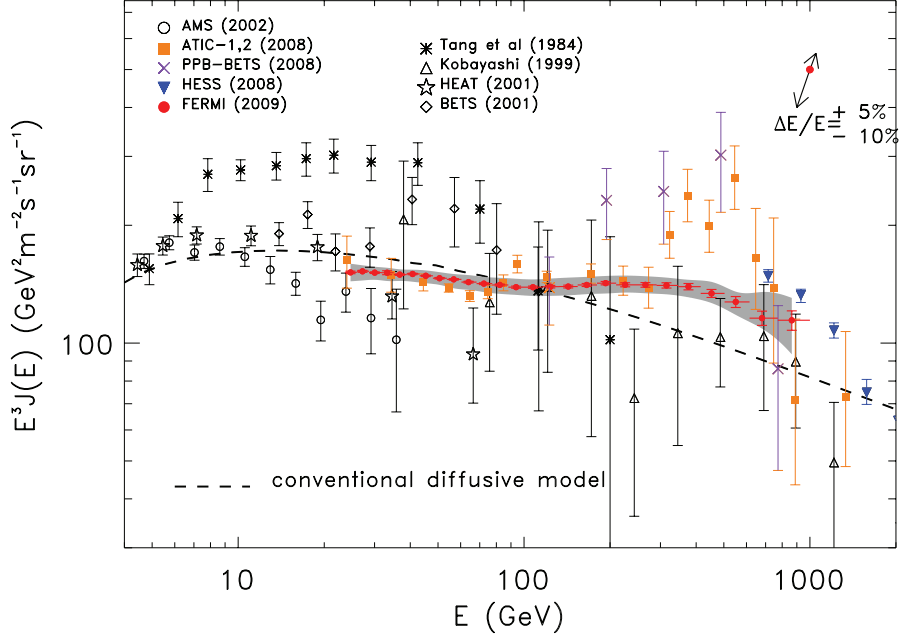


Figure 1.8.: Absolute electron plus positron flux $J(E)$, scaled by E^3 (from [169]). The red data points with statistical error bars are from the Fermi-LAT measurement [169], the grey band denotes the systematic uncertainty and the double headed arrow the energy scale uncertainty. Other measurements [148, 168, 167, 186, 187, 188, 189, 190] are referenced in the legend. The dashed line is from a GALPROP conventional diffusive model [191].

On the one hand, a sharp feature, i.e. a hardening from an E^{-3} spectrum at ~ 100 GeV and a rather strong shoulder at ~ 800 GeV, has been observed independently by PPB-BETS [167] and ATIC [168]. On the other hand, the Fermi collaboration has performed an analysis [169] with data from their Large Area Telescope (LAT) which shows a smooth continuation of the E^{-3} spectrum up to hundreds of GeV where the spectrum starts to soften. This is in agreement with a determination of the flux by HESS [186, 192] which also shows a softening to E^{-4} around a TeV and is basically also inconsistent with the PPB-BETS/ATIC findings. Both signals, i.e. either a sharp feature or a broader excess, can in principle be interpreted as a contribution from DM annihilation or decay into leptonic channels in the galactic DM halo, cf. Sec. 1.3.1.

We note that an E^{-3} total electron-positron flux *per se* does not constitute an excess with respect to the standard picture of GCRs. For example a steady, homogeneous $E^{-2.2}$ injection of electrons together with a diffusion coefficient $\propto E^{-0.6}$ could reproduce such a spectrum. The pre-Fermi models were adjusted to earlier measurements which indicated a softer spectrum. On the other hand, the slight dip and bump in the Fermi-LAT data at ~ 100 GeV and ~ 300 GeV, respectively, as well as a rather soft primary injection spectrum derived from, e.g. gamma-rays from SNRs (see 2.4.1) can however be interpreted as indications for the presence of an additional component in the total electron-positron flux.

Again presuming that the excesses seen in the total electron-positron flux are DM induced, we can further constrain possible annihilation channels and DM masses. Whereas the PPB-BETS/ATIC data favour annihilation into $\mu^+\mu^-$ with $m_{\text{DM}} \sim 1$ TeV, the smoother Fermi-LAT spectrum is better fit by annihilation to $\tau^+\tau^-$ with $m_{\text{DM}} \sim 2$ TeV [193]. For a harder background the Fermi-LAT data also allow the $\mu^+\mu^-$ channel [194]. Heavier DM can however not reproduce either excess and therefore, DM models leading to hadronic excesses (even beyond the current reach of antiproton measurements) are ruled out.

1.3.3. Gamma-rays

The major appeal of DM indirect detection through gamma-rays is that in contrast to charged particles, gamma-rays free-stream through the Galaxy and allow to be traced back to their sources. This allows, for example, to investigate directions in the Galaxy that are particularly apt for DM detection, e.g. due to low astrophysical backgrounds. Furthermore, gamma-rays reach the Earth without attenuation or energy losses, apart from redshift losses. (This is true at least up to energies of hundreds of TeV; above, the mean free path for gamma-rays sharply drops due to e^+e^- pair production on the CMB down to 10 kpc at a few PeV.)

The physical processes possibly contributing to gamma-rays from DM annihilation or decay are prompt emission, i.e. internal bremsstrahlung (final state radiation and virtual internal bremsstrahlung) and neutral pion decay (from hadronic decay modes), or ICS of electrons and positrons, all of which have continuous spectra. The annihilation or decay to $\gamma\gamma$, γZ or γH is, although loop-suppressed (DM is electrically neutral) and with a branching fraction of 10^{-3} or smaller, important because the resulting mono-energetic line emission is a very clean signature.

Again, we distinguish between DM annihilation and decay because of the different dependence on the DM density. As the annihilation rate depends on the DM density square, the differential flux of gamma-rays ϕ_γ^{ann} in a particular solid angle $\Delta\Omega$ around a direction (ℓ, b) in the sky contains the line of sight (l.o.s.) integral of the density square, $\rho^2(r)$,

$$J_\gamma^{\text{ann}}(\ell, b) = \frac{1}{4\pi} \frac{1}{2} \frac{\langle\sigma_{\text{ann}}v\rangle}{m_{\text{DM}}^2} \sum_f \frac{dN_\gamma^f}{dE_\gamma} B_f \int_{\Delta\Omega} d\Omega \int_{\text{l.o.s.}} ds \rho^2(r(s, \ell, b)), \quad (1.68)$$

where $\langle\sigma_{\text{ann}}v\rangle$ is the thermal average annihilation rate, dN_γ^f/dE_γ is the differential spectrum for final state f and B_f is the branching ratio for gamma-rays.

The decay rate on the other hand is proportional to the DM density, so the differential gamma-ray flux ϕ_γ^{dec} from DM decay reads,

$$J_\gamma^{\text{dec}}(\ell, b) = \frac{1}{4\pi} \frac{\Gamma}{m_{\text{DM}}} \sum_f \frac{dN_\gamma^f}{dE_\gamma} B_f \int_{\Delta\Omega} d\Omega \int_{\text{l.o.s.}} ds \rho(r(s, \ell, b)), \quad (1.69)$$

with Γ the DM decay rate.

The recent data from the Large Area Telescope (LAT) on board the Fermi satellite [195] allow for various searches for possible DM signatures with a so far unprecedented accuracy. The LAT is a pair-conversion gamma-ray detector consisting of 4×4 towers of tungsten trackers on top of a electromagnetic calorimeters with a thickness of 7 radiation lengths and is surrounded by anti-coincidence detectors. It has a broad energy range of 20 MeV to 300 GeV and with its large field of view of 2.4sr it covers the whole sky in two orbits, i.e. three hours. Its energy-resolution is around 10% and its point spread function decreases from a few degree at 20 MeV to less than 0.1° at hundreds of GeV.

In the following, we briefly review the different targets for DM indirect detection in gamma-rays.

Galactic centre

The galactic centre is a prime target for DM searches since it contains the highest DM density and is therefore expected to be the brightest DM source in the sky. Of course, astrophysical backgrounds are also very bright close to the galactic centre, and so the prospects strongly depend on the form of the DM density profile in the inner kiloparsecs. On the one hand, density profiles fitted

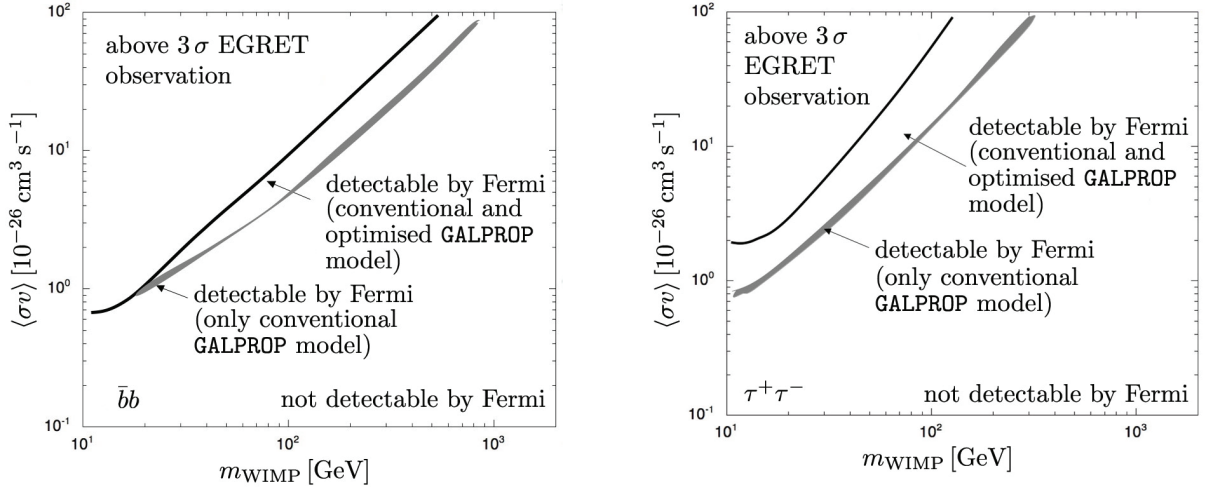


Figure 1.9.: Significance for detection in $b\bar{b}$ (left panel) and $\tau^+\tau^-$ (right panel) in the $m_{\text{DM}} - \langle\sigma_{\text{ann}}v\rangle$ plane (from [197]). The region above the black line is excluded by EGRET, the region below the grey line is not detectable by Fermi-LAT and the region in between is detectable by Fermi-LAT if the ‘conventional’ [198] or ‘optimised’ [191] background model is realised. The shaded region can only be detected under assumption of the ‘conventional’ background [198].

to “observations” in N -body simulations hint at a “cuspy” NFW profile [155, 196] with a rather steep, r^{-1} decline in the central kpc. On the other hand, kinematical observations show rather flat, iso-thermal profiles [171]. Again, the amplification due to the $\rho^2(r)$ factor leads to much larger signals from DM annihilation than from decay.

A sensitivity study [197], considering two different GALPROP diffuse backgrounds [198, 191], but no point sources, has been performed pre-flight. For generic DM annihilation into W^+W^- , $b\bar{b}$, $t\bar{t}$ and $\tau^+\tau^-$, an NFW density profile and accounting for detector response, the sensitivity after 5 years of data is good enough to dig deeper into the $m_{\text{DM}} - \langle\sigma_{\text{ann}}v\rangle$ plane than possible with EGRET [199, 200]. In Fig. 1.9, we reproduce the sensitivity plots for gamma-rays for annihilation to $b\bar{b}$ and $\tau^+\tau^-$ from [197].

Shortly after the public release of the first 11 month data, an excess above astrophysical backgrounds has been claimed. A bump-like feature around ~ 2 GeV above power-law background has been identified [201] within the inner 3° . The excess has a steeper radial profile and is more spherically symmetric than astrophysical backgrounds. It could be explained by 25 – 30 GeV dark matter particle, annihilating to $b\bar{b}$ with $\langle\sigma_{\text{ann}}v\rangle \sim 9 \times 10^{-26} \text{ cm}^3 \text{ s}^{-1}$ in a cusped density profile.

The Fermi collaboration is of course performing their own studies of the emission around the

Galactic centre but has, so far, only presented very preliminary results. A binned likelihood analysis [202] with a simultaneous spatial and spectral fit has been performed within a region of interest (ROI) of $7^\circ \times 7^\circ$ around the galactic centre, using only high-quality reconstructed events gathered during the first 11 month of operation. Various contributions have been considered, in particular, point sources have been modelled and subtracted, the diffuse galactic emission is accounted for by a GALPROP model and an isotropic, extra-galactic background is allowed for. The residuals, see Fig. 1.10, also show an unmodelled excess in the 2 – 5 GeV range. The Fermi collaboration however concludes, that better modelling of the galactic diffuse emission and possibly unresolved point sources is necessary before any excess can be confirmed.

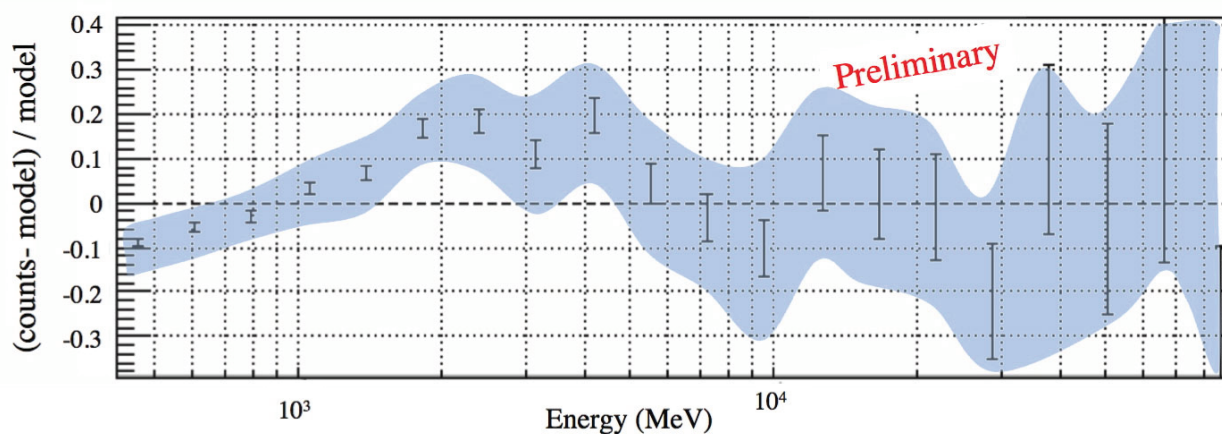


Figure 1.10.: Residual spectrum from the likelihood analysis of [202], integrated over the $7^\circ \times 7^\circ$ ROI (from [202]). The blue band shows the systematic error from the uncertainty on the effective area.

Galactic halo

Although DM contribution to gamma-ray fluxes from the galactic halo are comparatively lower than from the galactic centre, the astrophysical backgrounds, in particular from (unresolved) sources, are also less strong. Still, diffuse backgrounds remain a formidable challenge for these studies. Furthermore, the spectrum from DM annihilation or decay is the same anywhere in the halo and is expected to have a particular shape with sharp cut-off at the DM mass (half the DM mass for decay) which is difficult to explain astrophysically. Usually, one excludes a region around the galactic centre or the galactic plane, thereby also limiting the influence of the uncertainty of the

halo profile in the inner kiloparsecs.

The pre-flight study [197] has estimated the necessary $\langle\sigma_{\text{ann}}v\rangle$ for a detection with 3σ sensitivity after only one year of data as a function of the DM mass. The uncertainty in the background model turns out to be large and the necessary $\langle\sigma_{\text{ann}}v\rangle$ increases from $7 \times 10^{-26} \text{ cm}^3 \text{ s}^{-1}$ (for $m_{\text{DM}} = 50 \text{ GeV}$) to $6 \times 10^{-26} \text{ cm}^3 \text{ s}^{-1}$ (for $m_{\text{DM}} = 250 \text{ GeV}$) for the ‘conventional’ background model [198]. It was concluded that Fermi-LAT could probe a large region of MSSM or mSUGRA parameter spaces.

Constraining the analysis to intermediate galactic latitudes $10^\circ \leq |b| \leq 20^\circ$, the Fermi collaboration has investigated [203] the diffusive background, maximising the fraction of background produced within a few kiloparsecs from the solar system and thereby minimising the dependence on the uncertainty of ISM and CR densities elsewhere in the Galaxy. The shape of the spectrum is consistent with an *a priori* diffusive emission model, an update of the ‘conventional’ GALPROP model [198]. The excess measured by EGRET [204] is also not reproduced and the deviation is therefore likely to be an instrumental effect of the EGRET experiment [205].

A conservative analysis that does not attempt to subtract or fit any astrophysical backgrounds is presented in [206]. Model-independent two-body annihilation or decay to leptonic and hadronic channels are considered and the resulting gamma-ray flux from final state radiation and π^0 -decay as well as from ICS of e^\pm are required not to exceed the Fermi-LAT measurements by more than 3σ in different, selected regions of the sky. This gives already quite considerable constraints in the $m_{\text{DM}} - \langle\sigma_{\text{ann}}v\rangle$ plane. Interestingly, a large fraction of the parameter space needed to explain the electron-positron excesses from DM, see Secs. 1.3.1 and 1.3.2, are ruled out. In particular, for NFW or Einasto profiles all fits to PAMELA, Fermi-LAT and HESS e^\pm -data from DM annihilation are excluded, and even for a cored isothermal profile, only annihilations into muons remains marginally consistent.

A different analysis [207] is based on template subtraction of foregrounds that are assumed to be traced by spatial templates. An excess, called the ‘Fermi haze’, is found up to $|b| \approx 40^\circ$ above the galactic centre which is satisfactorily fit by a bivariate Gaussian. This is argued to be most likely due to inverse-Compton scattering (ICS) by relativistic electrons, and that the underlying electron distribution is compatible with the ‘WMAP haze’ [207], see Sec. 1.3.4. While such a signature in ICS is naturally expected if there is indeed an additional population of electrons with

a hard spectrum, it was pointed out [208] that the template maps applied in Ref. [207] are in fact inappropriate and underestimate both the π^0 decay and ICS contributions to the gamma-ray emission, in particular in the galactic centre region. The ‘Fermi haze’ may therefore be an artefact due to incorrect foreground removal. Furthermore, with 1.6 years of data from Fermi-LAT, a recent analysis [209] finds this excess to be distributed above the galactic centre in an hourglass-shaped morphology. Both because of this elongation and the peculiar angular profile, the authors conclude that a DM explanation of this signal seems to be disfavoured.

The Fermi collaboration has so far not confirmed this excess but is performing analyses with more sophisticated foreground models and is investigating possible correlations with (local) structures seen in radio maps, like the North polar spur, see [210].

Milky Way satellites

The CDM paradigm and in particular N -body simulations [13, 14, 15] predict a large number of bound substructures. The masses of these so-called Milky Way satellites go down to $(10^{-4} \dots 10^{-12}) M_\odot$, depending on the free-streaming length of the particular DM model considered. However, the minimum of the satellite masses that will be observable with Fermi is rather $10^6 M_\odot$.

A simple estimate of the significance expected from a satellite with truncated NFW profile and typical WIMP annihilation cross section sets the number of Milky Way satellites detectable by Fermi to 5σ within 5 years to ~ 12 [197]. Particular care must be taken not to misidentify statistical fluctuations in the gamma-ray flux as DM annihilation or decay from substructure but it was shown in [197] that a log-likelihood analysis can distinguish between both cases for a ‘ 5σ ’ satellite. Furthermore, the DM substructure needs to be distinguished from astrophysical sources.

It is worth stressing that in the case of DM annihilation, substructures are not only targets in themselves but also increase the diffuse flux by the ρ^2 dependence (see Eq. 1.68). Estimates relying on the frequency of such structures seen in N -body simulations however limits the boost factor to $\mathcal{O}(10)$ [211].

Dwarf spheroidal galaxies

Dwarf spheroidal galaxies (dSphs) are particularly faint companion galaxies of the Milky Way or Andromeda. They may well be the most abundant type of galaxies in the Universe but difficult to detect due to their faintness. Before 2005, there were only 9 known dSphs [212, 213, 214, 215, 216] but the Sloan Digital Sky Survey (SDSS) [217] has increased their number by 11, also improving our understanding of this type of galaxies. From stellar kinematics it can be inferred that some have mass-to-light ratios of up to $\mathcal{O}(1000)$, that is many times more than in conventional types of galaxies. Furthermore, dSphs contain only little neutral or ionised gas which could otherwise contribute to its gamma-ray emission. Therefore, dSphs are the most extremely DM dominated environments known which makes them an interesting target for DM searches.

A recent study [218] of 14 local group dSphs with data from the first eleven month of Fermi-LAT operation does not find any significant gamma-ray emission above 100 MeV and sets upper limit on their gamma-ray fluxes, both for power-law injection and spectra motivated by different WIMP models. Using stellar velocity data to model the DM content of a subset of 8 of the above dSphs, the Fermi team can constrain the cross section for annihilation into gamma-rays by $b\bar{b}$, $\tau^+\tau^-$ and a mixture of both, as motivated from neutralino DM. More precisely, the limits are starting to be competitive with cross sections from a scan over mSUGRA parameter space and already exclude a fraction of the MSSM parameter space. A model of UED with $B^{(1)}$ KK DM is not constrained but SUSY models with Wino-like DM in the context of anomaly mediated SUSY breaking (AMSB), see e.g. [178], can be ruled out for $m_{\text{DM}} \lesssim 300$ GeV. Interestingly, models invoked to explain the cosmic ray lepton excesses (see Secs. 1.3.1 and 1.3.2), can be constrained in so far as masses above ~ 1 TeV can be ruled out by considering the ICS emission produced.

Line emission

Although DM is found to be electrically neutral and annihilation or decay to photons can therefore only occur at loop order, the preferred smoking-gun signature of DM in indirect detection is the gamma-ray line. The internal width of the line is for most annihilation (excluding, perhaps annihilation via a Z boson resonance) and decay (due to the necessarily long lifetime) processes rather small. The width of the line, $\sim 10^{-3}$, is therefore mostly due to Doppler broadening although this

effect is also small because of the non-relativistic WIMP velocities today. The lack of astrophysical sources with lines in the GeV - TeV regime finally makes this signature virtually background free. Theoretical frameworks include SUSY WIMP and gravitino DM models. Unfortunately, the branching fraction of the necessary processes is found to be 10^{-3} or smaller.

A recent Fermi study [219] has found no significant excess and has set limits on gamma-ray lines between 30 and 200 GeV. By considering three different halo profiles, NFW [196], Einasto [220, 221] and isothermal [171], upper limits on the annihilation and decay cross section have been derived. Although for the annihilation cross sections the bound is about an order of magnitude weaker than the cross section for thermally produced WIMPs, some non-thermal production models, e.g. [178], can again be ruled out. The upper limits on the life-times are also constraining for some models with monoenergetic lines from decay of gravitinos.

Other targets

Other targets include so-called cosmological DM [222], that is extra-galactic haloes and large-scale structure which contribute to the isotropic gamma-ray flux, and DM signals from clusters of galaxies [223].

1.3.4. Radio and microwaves

The measurement of anisotropies in the cosmic microwave background (CMB) by COBE and WMAP has ushered in an exciting new era in cosmology. The study of the cosmic signal requires careful subtraction of galactic foreground emissions and this will become even more crucial for studies of the ‘B-mode’ polarisation signal by PLANCK and the proposed CMBPol satellites [224]. A by-product of this foreground subtraction is the study of diffuse galactic microwave emission in its own right. (In fact most of the diffuse foreground emission is of galactic origin, a counter-example being unresolved extra-galactic radio sources.) Usually, one distinguishes three different physical components which have different underlying processes and frequency behaviour:

1. Free-free emission

Thermal electrons produce bremsstrahlung on the gas in the ISM. The intensity produced by free-free emission, $I_\nu \propto \nu^{-0.15}$, is proportional to the line of sight integral of the ISM gas

density squared which is why it is believed to be traced by recombination $H\alpha$ line maps [225]. Dust can absorb some of this emission and usually regions close to the galactic plane with dust optical depth too high are excised.

2. Dust-correlated emission

Dust grains vibrating in equilibrium with the surrounding radiation fields are producing emission in the microwave range. This ‘thermal dust’ emission has been mapped [226] and evaluated at 94 GHz [227]. In addition, larger dust grains can have an electric dipole moment and be excited by collisions with ions [228]. While individual dust grains radiate with a bump like spectrum, the superposition of many dust grains with different frequencies can generate a soft power law spectrum. To a first approximation, this ‘spinning dust’ is expected to be spatially correlated with thermal dust and in fact an anomalous, soft component was found in Ref. [229]. Although the presence of an anomalous component is widely accepted, its interpretation as spinning dust is still being debated, for example by the WMAP team itself who do not conclusively confirm the spinning dust hypothesis.

3. Galactic synchrotron

GCR electrons and positrons produce synchrotron radiation on the galactic magnetic field (GMF). For a power law spectrum of relativistic electrons, $n_{e\pm} \propto E^{-\alpha}$, the synchrotron emissivity is also a power law, $I_\nu \propto \nu^{(1-\alpha)/2}$. For an electron spectral index $\alpha \approx 3$, $I_\nu \propto \nu^{-1}$ which is close to the observed $\nu^{-1.2}$ [230]. Tracer maps include radio maps or difference maps at microwave frequencies, used, for example by the WMAP collaboration [231].

For dark matter indirect searches more important is, however, the claimed presence [232] of a new foreground that does not correlate spatially with any of the above processes. Using the template fitting technique (see 4.2), a residual remains after subtraction of the known foregrounds – the so-called ‘WAMP haze’. This residual has a roughly spherical morphology localised around the centre of the Galaxy, see Fig. 1.3.4, and a harder spectrum [233] than synchrotron radiation by relativistic GCR electrons from standard astrophysical sources like SNRs. An independent analysis has confirmed the existence of the haze [234], but others [235, 236] do not find the evidence to be significant, including the analysis [237] by the WMAP collaboration itself.

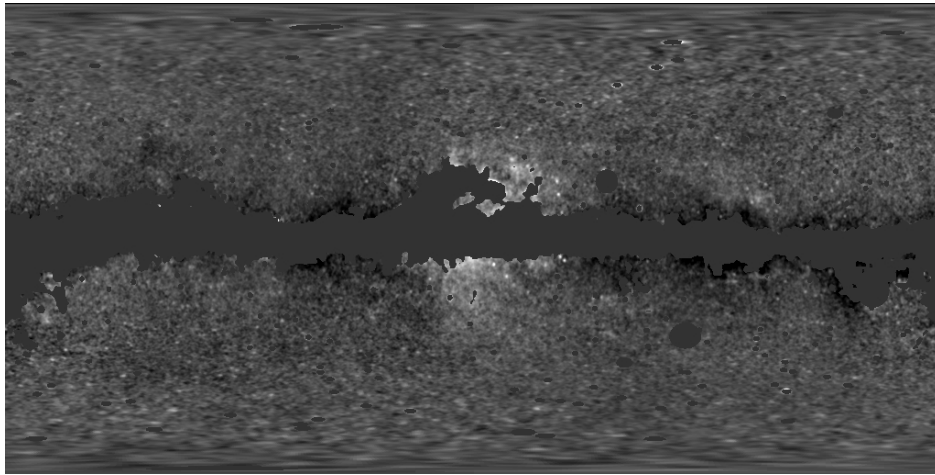


Figure 1.11.: Sky map of the ‘WMAP haze’ (from [233]).

Initially, it was believed that the haze is free-free emission from ionised gas too hot to be traced by recombination line maps but too cold to be visible in X-rays [232]. However it was suggested later that it is in fact synchrotron emission from a new population of relativistic electrons and positrons, produced by dark matter annihilation [238]. It is indeed possible to explain the haze [239] by the synchrotron radiation of an additional population of relativistic electrons and positrons, produced by WIMP annihilation with a thermal cross section. Other authors however argue that the annihilation cross-section needs to be significantly boosted over the usual value [236] or that the parameters of the diffusion model used are somewhat non-standard [240]. There have also been attempts to fit both the morphology and spectrum of the haze by ascribing it to electrons emitted by pulsars with a hard spectrum [241, 242]; however the expected haze is then less spherical since most pulsars are in the galactic disk. This is also true of SNRs which have in fact recently been invoked [243, 2] as sources of positrons with a hard spectrum to explain the rise in the cosmic ray positron fraction at high energies measured by PAMELA [163].

More conservative constraints on DM annihilation or decay can be derived by demanding that the possible contribution from DM does not exceed the observed fluxes in radio and microwaves (including astrophysical backgrounds). For examples of such studies, see [244, 245].

1.3.5. Neutrinos

Dark matter indirect detection with neutrinos benefits from the same advantages as indirect detection with gamma rays: Neutrinos propagate through the Universe truly unimpeded and also point back to their sources. Their small interactions however require detector volumes of cubic kilometre size and provide event rates of a few per year, both for conventional astrophysical application as well as for DM searches. The weak interaction cross sections are however also an advantage as they could possibly make neutrinos the only messengers that can escape very dense environments.

One such situation can lead to a particularly interesting idea for DM indirect detection. The Sun is constantly moving through the DM halo. Although the scattering cross section of WIMPs off the nucleons in the Sun is small, occasionally, a WIMP can scatter elastically and become gravitationally trapped inside the sun. Over the lifetime of the Sun, a large number of WIMPs can become trapped and an equilibrium between WIMP capture and annihilation will be reached. Neutrinos detected from the Sun with energies of tens to hundreds of GeV can be unambiguously assigned to these annihilation processes and used to constrain WIMP annihilation cross sections and DM models.

Such neutrinos could be detected by the SUPER-Kamiokande experiment which has the best sensitivity for WIMP masses of about a GeV, whereas for larger masses the neutrinos could be detected in IceCube [246] (in particular in its low-energy extension, “DeepCore”), currently under construction under the South pole. IceCube consists of a cubic kilometre of clean ice, about 2000 km under ground and instrumented with thousands of photo multiplier tubes. A muon converted from a muon neutrino in the surrounding material or the detector itself leaves a track of Čerenkov light in the detector which allows the reconstruction of the neutrino direction and energy.

The beauty of detection of neutrinos from WIMP annihilation inside the Sun is its relative robustness against astrophysical uncertainties; the flux depends only the local DM density and velocity distribution which also affect DM direct searches since in equilibrium the neutrino production only depends on the capture rate. The rate has contributions from both spin-independent (SI) and spin-dependent (SD) cross sections and it turns out that for the SI cross section, upper limits from direct detection experiments basically rule out any prospects for event rates $\mathcal{O}(1)\text{yr}^{-1}$.

SD cross sections, on the other hand, can become much larger than SI ones, e.g. for certain

regions of the MSSM parameter space that are experimentally not too well constrained and could lead to event rates of up to 1000 yr^{-1} . Large SD cross sections for neutralino WIMPs are usually associated with large Z couplings and hence a large Higgsino mixing. Therefore, the focus point region of the $m_0 - m_{1/2}$ plane is particularly promising.

IceCube has already provided limits on the elastic scattering cross section better by 2-3 orders of magnitude for the spin-dependent case [247]. For spin-independent cross sections, however, the event rates allowed by direct detection limits are much too low to be discovered by IceCube.

Of course, similar to gamma-ray searches, neutrinos can be searched for from other targets, for example the galactic centre [248, 193]. For preliminary result from IceCube, see [249].

1.4. Conclusion

Indirect detection of DM, that is the search for deviations in the fluxes of cosmic ray nuclei and charged leptons as well as radio/microwaves, gamma-rays and neutrinos, is a very promising idea. Not only capitalises it on the large amount of dark matter contained in the Milky Way halo and possibly also in extra-galactic haloes, but it also uses a huge variety of astrophysical environments or targets, ranging from substructures of the halo of a few solar masses to large galaxy clusters.

Astrophysical backgrounds, however, play a crucial role for the prospect of detecting DM in these channels. In particular, with most DM explanations of the positron and electron-positron excesses starting to be ruled out by gamma-ray constraints, for example, it is clear that these signatures must be of astrophysical origin. Therefore, a better understanding of the astrophysical backgrounds is crucial both to resolve these problems in our understanding of current excesses but also for future indirect searches.

Even when DM indirect detections provide a (first) evidence of DM annihilation or decay, provided it had some non-gravitational interactions, it is unlikely that we could identify the interesting DM parameters, mass, couplings etc., let alone the full DM model. In most cases, the uncertainties inherent to the DM modelling itself as well as uncertainties induced by the astrophysics of its detection are considerable and all we can hope for are some rough indications. DM indirect detections can therefore only unfold its true potential in combination with other approaches to DM detection. Direct detection (for a recent review, see, e.g. [250]) and accelerator searches (e.g. [251])

are two other, equally important approaches that, unfortunately, could not be discussed in this introduction due to page limitations. Other possible constraints can come from other effects that DM would have, for example, on cosmological observables: DM with large annihilation rates or short lifetimes could also affect big bang nucleosynthesis [252, 253, 254, 255, 256]. One of the most stringent constraints however comes from the effect of DM annihilation or decay on the CMB and during the epoch of reionisation [257, 258, 259, 260].

For the phenomenology of indirect searches, what is needed at the moment are a better understanding of the backgrounds that go beyond the (often) oversimplified assumptions and hence predictions of the standard picture of GCRs. In the rest of this work we present our humble contribution to this ongoing challenge.

2. Additional Electrons/Positrons from Astrophysical Sources

2.1. Introduction

The excess in the positron fraction recently measured by the PAMELA collaboration clearly hints at some additional positron component. The astrophysical background is expected to be falling at energies above ~ 1 GeV if positrons are indeed mainly produced as secondaries by decay of charged pions from the spallation of cosmic ray protons and nuclei on the interstellar medium (ISM). In addition, recent measurements of the total electron-positron flux by the Fermi collaboration have shown it to be harder than previously expected.

The evaluation of the astrophysical predictions has gained in importance due to the possibility of these excesses being due to exotic physics, in particular due to additional electrons and positrons produced in annihilation or decay of dark matter (DM) in the galactic halo. A large number of these models is starting to be ruled out by constraints from other messenger, e.g. radio waves from synchrotron radiation or gamma-rays from inverse Compton scattering (ICS). It is therefore of utmost importance to investigate how these excesses can be understood in terms of astrophysical sources.

One of the most minimal approaches is to consider whether the additional electrons/positrons could possibly be produced in the standard setup *without* making any additional assumptions about new sources, new interactions or the like. Such minimality is a basic principle of scientific heuristics as most famously expressed in ‘Occam’s razor’: ‘*Numquam ponenda est pluralitas sine necessitate*’ [261]. (Plurality ought never be posited without necessity.) or ‘*Frustra fit per plura quod potest fieri per pauciora*’ [262]. (It is futile to do with more things that which can be done

with fewer.) Instead, the assumptions of the current model of galactic cosmic rays (GCRs) are to be reconsidered, possibly premature arguments about the importance of different effects are to be revisited and the available parameter space is to be reassessed.

In particular, we are going to question the assumption that positrons get exclusively produced by spallation of CR protons and nuclei on the ISM and, instead, we consider the production of secondary electrons and positrons by protons and nuclei *inside* the paradigm sources: supernova remnants (SNRs). Not only can the total fluxes of these secondaries reach levels comparable to the primaries but the secondary spectra will also differ quite drastically from the primary ones. Hereby, we follow a recent idea to explain the rise in the positron fraction by such a harder injection of secondaries from SNRs [243], however improving on this model in several respects.

The effect of secondaries produced inside the GCR sources had so far always been neglected due to a crude column depth argument, recently reiterated [263]: The average residence time of primary nuclei in a SNR is necessarily shorter than the SNR lifetime, $\mathcal{O}(10^4)$ yr, and therefore happens to be much smaller than the residence time in the ISM, $\sim \mathcal{O}(10)$ Myr. Even if the gas density inside the SNR is higher than in the ISM, due to compression by the shock, the grammage experienced inside the SNR, $0.2 (n_{\text{gas,SNR}}/(10 \text{ cm}^{-3})) \text{ g cm}^{-2}$, is still much smaller than the average grammage of the ISM, a few g cm^{-2} . Therefore, the production of secondaries inside SNRs was believed to be negligible.

What this argument ignores is that the secondaries produced inside the source get also accelerated and their spectrum becomes considerably harder than that of the secondaries produced during propagation of the primaries in the ISM. As we will see below, the accelerated secondary positrons in sources have a power law index of $-\gamma + 1$ where $-\gamma$ is the index of the primaries at source. After propagation this gives a spectral index $-\gamma$ at energies above 10 GeV where cooling is the dominant loss process. The secondary positrons from propagation, however, have a spectral index of $-\gamma - \delta - 1$. We remind ourselves that the value predicted for γ by diffusive shock acceleration (DSA) is $\gamma \approx 2$ and δ is determined from nuclear secondary to primary ratios as $\delta \approx 0.6$. We now compare the fluxes $J_{\text{src}} = J_{\text{src}}^0 (E/E_0)^{-\gamma}$ of secondaries from the source and $J_{\text{ISM}} = J_{\text{ISM}}^0 (E/E_0)^{-\gamma - \delta - 1}$ of secondaries

from propagation. Although the ratio of the total number of particles is indeed small,

$$\frac{N_{\text{src}}}{N_{\text{ISM}}} = \frac{\int_{E_0}^{E_{\text{max}}} dE J_{\text{src}}(E)}{\int_{E_0}^{E_{\text{max}}} dE J_{\text{ISM}}(E)} \simeq \frac{J_{\text{src}}^0}{J_{\text{ISM}}^0} \frac{\gamma + \delta}{\gamma - 1} \simeq 2.6 \times 10^{-3}, \quad (2.1)$$

if we chose, for example $J_{\text{src}}^0/J_{\text{ISM}}^0 = 2 \times 10^{-3}$ and $E_{\text{max}} \gg E_0$, the differential fluxes become comparable at $(J_{\text{ISM}}^0/J_{\text{src}}^0)^{1/(1+\delta)} E_0 \simeq 50 E_0$ already.

The appeal of the acceleration of secondaries, besides its minimality, is that its effect is guaranteed, in the sense that secondaries will definitely be produced in cosmic ray source and are subject to subsequent acceleration. However, the normalisation of the flux of these secondaries, for example, with respect to the secondaries from propagation is the crucial question.

In this chapter, we will study the acceleration of secondaries in sources in some detail. In Sec. 2.2 we will calculate the spectra of the secondaries in the simple test particle approximation of DSA and explain why the secondary spectrum is harder than the primary one. We will then consider the effect of discreteness of sources and suggest a realistic distributions of sources in the spiral arms of the galactic disk and how to determine it from cosmic ray spectra alone in Sec. 2.3. Sec. 2.4 contains a summary of the different populations of electrons and positrons and some comments on how to normalise them by fitting to data. Previously, the flux of secondary e^- and e^+ in the sources has been normalised with respect to the primary electrons in an *ad hoc* fashion [243]. Instead, we exploit the hadronic origin of these secondaries and normalise using the gamma-ray fluxes (assumed to be from π^0 decay) detected from known SNRs by Imaging Air Čerenkov Telescopes (IACTs) like HESS. We can thus fix the only free model parameter by fitting the total $e^- + e^+$ flux to Fermi-LAT and HESS data. The e^+ fraction is then *predicted* up to TeV energies and provides a good match to PAMELA data (Sec. 2.5). Having constrained the distribution of the closest SNRs via the measured e^- and e^+ spectra, we present in Sec. 2.6 an example of a likely source distribution in order to illustrate that there are good prospects for IceCube to detect neutrinos from nearby SNR. In Sec. 2.7, we counter some criticism on this model, in particular the claim that the acceleration of mechanism does not hold in a time-dependent treatment. A consistent picture thus emerges for all presently available data in the framework of the standard DSA/SNR origin model of GCR. Some alternative, astrophysical explanations of the excesses in GCR leptons are being mentioned in Sec. 2.8. We conclude and comment on some open issues and grounds for concern in Sec. 2.9.

2.2. Acceleration of Secondaries in the Sources

Similar to the diffusive shock acceleration of primary cosmic rays, we describe the acceleration of secondaries produced and accelerated in the source in the simple test particle approximation, that is ignoring the back reaction of the energetically important nuclear component of the cosmic rays on the structure of the shock front.

The setup is similar to the one discussed in Sec. 1.2.5. We consider the phase space density, f_{\pm} , of secondary e^{-} and e^{+} produced by the primary GCR, both undergoing DSA, which is described by the steady state transport equation,

$$u \frac{\partial f_{\pm}}{\partial x} = \frac{\partial}{\partial x} \left(D \frac{\partial}{\partial x} f_{\pm} \right) + \frac{1}{3} \frac{du}{dx} p \frac{\partial f_{\pm}}{\partial p} + q_{\pm}, \quad (2.2)$$

where the source term q_{\pm} is determined by solving an analogous equation for the primary GCR protons (see Sec. 1.2.5). (Ideally we should solve the time-dependent equation, however we do not know the time-dependence of the parameters and can extract only their effective values from observations. This ought to be a good approximation for calculating *ratios* of secondaries to primaries from a large number of sources which are in different stages of evolution.) We consider the usual setup in the rest-frame of the shock front (at $x = 0$) where u_1 (u_2) and n_1 (n_2) denote the upstream (downstream) plasma velocity and density, respectively (cf. left panel of Fig. 1.2). The compression ratio of the shock $r = u_1/u_2 = n_2/n_1$ determines the spectral index, $a = 3r/(r - 1)$, of the GCR primaries in momentum space.

For $x \neq 0$, Eq. 2.2 reduces to an ordinary differential equation in x that is easily solved taking into account the spatial dependence of the source term, cf. Eq. 1.28,

$$q_{\pm}^0(x, p) = \begin{cases} q_{\pm,1}^0(p) e^{x u_1 / D(p_p)} & \text{for } x < 0, \\ q_{\pm,2}^0(p) & \text{for } x > 0, \end{cases} \quad (2.3)$$

where the proton momentum p_p should be distinguished from the (smaller) momentum p of the produced secondaries, the two being related through the inelasticity of e^{\pm} production: $\xi \simeq 1/20$. Assuming $D \propto p$ (Bohm diffusion) in the SNR, the solution to the transport equation 2.2 across

the shock, satisfying the boundary conditions,

$$\lim_{x \rightarrow -\infty} f_{\pm} = 0, \quad \lim_{x \rightarrow -\infty} \frac{\partial f_{\pm}}{\partial x} = 0 \quad \text{and} \quad \left| \lim_{x \rightarrow \infty} f_{\pm} \right| < \infty, \quad (2.4)$$

can then be written:

$$f_{\pm} = \begin{cases} f_{\pm}^0 e^{x/d_1} - \frac{q_{\pm,1}^0}{u_1} d_1 \left(\frac{e^{x/d_1} - e^{\xi x/d_1}}{\xi - \xi^2} \right) & \text{for } x < 0, \\ f_{\pm}^0 + \frac{q_{\pm,2}^0}{u_2} x & \text{for } x > 0, \end{cases} \quad (2.5)$$

where $d_1 \equiv D/u_1$ is the effective size of the region where e^- and e^+ participate in DSA (see right panel of Fig. 1.2).

Continuity at the shock front $x = 0$ requires:

$$D \frac{\partial f_{\pm}}{\partial x} \Big|_{x=0^-} - D \frac{\partial f_{\pm}}{\partial x} \Big|_{x=0^+} = \frac{1}{3} (u_2 - u_1) p \frac{\partial f_{\pm}^0}{\partial p}, \quad (2.6)$$

yielding the differential equation,

$$p \frac{\partial f_{\pm}^0}{\partial p} = -a f_{\pm}^0 + a \left(\frac{1}{\xi} + r^2 \right) \frac{D q_1^0}{u_1^2}. \quad (2.7)$$

This is readily integrated with boundary condition $f_{\pm}^0(0) = 0$ and gives

$$f_{\pm}^0(p) = a \left(\frac{1}{\xi} + r^2 \right) \int_0^p \frac{dp'}{p'} \left(\frac{p'}{p} \right)^a \frac{D(p') q_{\pm,1}(p')}{u_1^2}. \quad (2.8)$$

Assuming Feynman scaling for the pp interaction, i.e. $p d\sigma_{pp}/dp \propto \Sigma_{\pm}$ we can express the momentum dependence of the source term as

$$q_{\pm,1}(p) = \frac{c n_{\text{gas},1}}{4\pi p^2} \int_p^{\infty} dp' N_{\text{CR}}(p') \frac{d\sigma_{pp \rightarrow e^{\pm} + X}}{dp} \simeq \frac{c n_{\text{gas},1}}{4\pi p^2} N_{\text{CR}}(p) \frac{\Sigma_{\pm}}{\gamma - 2}. \quad (2.9)$$

We can easily interpret the solution Eq. 2.5 in terms of power laws in momentum. The second term downstream, $(q_2^0/u_2)x$, follows the spectrum of the primary GCRs ($\propto p^{-a}$) and describes the production of secondary e^- and e^+ that are then advected away from the shock front. However, secondaries that are produced within a distance $\sim D/u$ from the shock front are subject to DSA

(see Eq. 2.3 and right panel of Fig. 1.2). The fraction of secondaries that enters the acceleration process is thus given by the ratio of the relevant volumes, i.e. $(D/u_1)/(u_2 \tau_{\text{SNR}})$, and the number density injected into the acceleration process is $(1/\xi + r^2)Dq_{\pm,1}/u_1^2$. This rises with energy because of the momentum dependence of the diffusion coefficient ($D(p) \propto p$) so the first term downstream in Eq. 2.5 gets harder: $f_{\pm}^0(p) \propto p^{-a+1}$.

The total injection spectrum R_{\pm} from one SNR is obtained by integrating the steady state solution over the volume of the SNR:

$$R_{\pm} = 4\pi p^2 4\pi \int_0^{u_2 \tau_{\text{SNR}}} dx x^2 f_{\pm}(x, p). \quad (2.10)$$

The resulting source spectrum, R_{\pm} , is thus the sum of two power laws,

$$R_{\pm} \simeq R_{\pm}^0 p^{-a+2} \left[1 + \left(\frac{p}{p_{\text{cross}}} \right) \right], \quad (2.11)$$

where the ‘‘cross-over’’ momentum, p_{cross} , satisfies

$$D(p_{\text{cross}}) = \frac{3}{4} \frac{r u_1^2 \tau_{\text{SNR}}}{a(1/\xi + r^2)}. \quad (2.12)$$

As has been noted [243], this mechanism is most efficient for *old* SNRs where field amplification by the shock wave is not very effective any more. We therefore introduce a fudge factor K_B that parametrises the effect of the smaller field amplification on the otherwise Bohm-like diffusion coefficient in the SNR,

$$D(E) = 3.3 \times 10^{22} K_B \left(\frac{B}{\mu\text{G}} \right)^{-1} \left(\frac{E}{\text{GeV}} \right) \text{cm}^2 \text{s}^{-1}. \quad (2.13)$$

The number of particles entering the acceleration process can of course not exceed the total number of secondaries produced inside the SNR. This effectively caps the growth of the term $D(p')q_{\pm,1}^0(p')/u_1^2$ once $(D/u_1)/(u_2 \tau_{\text{SNR}})$ becomes larger than unity, a relation that defines a char-

characteristic momentum scale p_{break} . We therefore substitute in Eq. 2.8,

$$\frac{D(p)q_{\pm,1}^0(p)}{u_1^2} \rightarrow \begin{cases} \frac{D(p)q_{\pm,1}^0(p)}{u_1^2} & \text{for } p < p_{\text{break}}, \\ \frac{D(p_{\text{break}})q_{\pm,1}^0(p)}{u_1^2} & \text{for } p > p_{\text{break}}. \end{cases} \quad (2.14)$$

The source spectrum R_{\pm} thus returns to a $p^{-\gamma}$ dependence around $p = p_{\text{break}}$. At even higher energies the secondary spectrum cuts off at the same E_{cut} as for primary electrons (see Sec. 2.4.1).

2.3. The Discreteness of Sources

In the standard picture, see Sec. 1.2, the explanation for the observed galactic cosmic rays (GCRs) is factorised into two parts which can be treated separately: the acceleration in supernova remnants (SNRs) and the diffusive-convective transport through the Galaxy.

Although SNRs can become quite large (up to $\mathcal{O}(100)$ pc towards the end of their lifetime, see Sec. 1.2.3 and Eq. 1.15), they are under most circumstances still much smaller than the scale on which the propagation of GCRs take place, i.e. kiloparsecs, and their extent can usually be neglected for all practical purposes.

We are therefore not dealing with a continuous distribution of sources within the galactic disk but with a large number of discrete sources. The usual assumption is that diffusion will wash out this source distribution. This is however only true as long as the diffusion length is long compared to the average distance of sources (which is of the same order as the average distance of an observer to the closest source). For protons and (stable) nuclei the diffusion length is indeed quite long – of the order of tens of kpc – since energy losses are negligible above a few GeV and therefore escape from the cosmic ray halo is the dominant loss process. For charged leptons on the other hand, in particular for electrons and positrons, the diffusion length is strongly energy dependent. The dominating energy losses are through synchrotron radiation and ICS and the diffusion-loss length, $\lambda(E) \equiv \sqrt{\ell^2(E, 2E)} \propto E^{(\delta-1)/2}$, (see Eq. 1.48), is quickly declining. Therefore we expect to start seeing contributions from individual, nearby sources above the energy at which the diffusion length drops below the average source distance. Depending on the particular values of the diffusion parameters, one predicts “bumps”, that is Green’s functions of individual sources, to appear above (50 . . . 200) GeV. The superposition of a few such bumps leads to features which we will investigate

in the following section.

In addition to the discreteness in space, GCR sources like SNRs also have a finite lifetime. A common assumption is that the bulk of cosmic rays will only be released after the SNR has entered the radiative stage and DSA comes to an end.¹ This makes the distribution of sources also finite in the time-domain and will lead to even stronger features.

2.3.1. Fluctuations in the electron flux

Apart from some inferences about (only the observed) near SNRs we do not know much about the position of sources of GCRs. Even in the limit of a continuous source distribution, which is justified when considering old, far away sources and hence fluxes at lower energies, our knowledge of the global source distribution is limited, see also Chapter 4. We have however argued that at higher energies, the contribution to the electron-positron flux from particular sources depend strongly on their distances. Our ignorance of the source positions therefore introduces an uncertainty into our prediction for the electron-positron fluxes at Earth. Put differently, the electron-positron flux stochastically fluctuates between different realisations of a statistically smooth source distribution.

In the following we will use central limit theorems and the analytical form of the Green’s function for the diffusion-energy loss problem described in sec. 1.2.6 to infer the statistical properties of the flux, i.e. its average, its quantiles and the energy dependence of both. For numerical studies of this effect based on a Monte Carlo approach, see [264, 265, 266].

The flux from a source that injected a spectrum $Q(E) = Q_0 E^{-\gamma}$ of electrons or positrons a time t ago at a distance L from the observer is given by the Green’s function G_{disk} (cf. Eq. 1.51) of the diffusion equation,

$$J_i(E) = \frac{c}{4\pi} G_{\text{disk}} = \frac{c}{4\pi} (\pi \ell^2)^{-1} e^{-L^2/\ell^2} Q_0 E^{-\gamma} (1 - b_0 E t)^{\gamma-2} \frac{1}{z_{\text{cr}}} \chi\left(\frac{\ell}{z_{\text{cr}}}\right), \quad (2.15)$$

where $c/(4\pi)$ denotes the “flux factor” for relativistic particles and $\ell^2(E, t)$, $\chi(\ell/z_{\text{cr}})$ and z_{cr} are defined in Sec. 1.2.6.

¹In more sophisticated modelling, one expects that a certain fraction of the particles accelerated will be able to escape the SNR during the Sedov-Taylor phase already [71, 72]. For example, due to a lack of turbulence at low wave numbers ahead of the shock, high energy particles cannot be confined to the shock region and are instead injected into the interstellar medium.

The flux J of N identical² sources at distances $\{L_i\}$ and times $\{t_i\}$ is the sum of the individual fluxes,

$$J = \sum_{i=1}^N J_i(E) = \frac{c}{4\pi} \sum_{i=1}^N (\pi\ell^2)^{-1} e^{-L_i^2/\ell^2} Q_0 E^{-\gamma} (1 - b_0 E t_i)^{\gamma-2} \frac{1}{z_{\text{cr}}} \chi\left(\frac{\ell}{z_{\text{cr}}}\right). \quad (2.16)$$

To investigate the fluctuations introduced by the stochasticity of source distances and times, we calculate the expectation value and standard deviation of the total flux J exploiting the central limit theorem [267].

If the central limit theorem was applicable, at a fixed energy E the fluxes $J(E)$ for different realisations of the same source density would follow a normal distribution with mean μ_J and standard deviation σ_J ,

$$\mu_J = \frac{c}{4\pi} N \mu_Z = \frac{c}{4\pi} N \langle Z \rangle, \quad (2.17)$$

$$\sigma_J = \frac{c}{4\pi} \sqrt{N} \sigma_Z = \frac{c}{4\pi} \sqrt{N} \sqrt{\langle Z^2 \rangle - \langle Z \rangle^2}, \quad (2.18)$$

where $\langle Z^m \rangle$ denotes the moments of the Green's function $Z \equiv G_{\text{disk}}(E, L, t)$,

$$\langle Z^m \rangle = \int dz f_Z(z) z^m. \quad (2.19)$$

As a function of the random variables L and t , Z itself is a random variable with the probability density f_Z . In the case under consideration, L and t are assumed to be independent random variables with probability densities f_L and f_t , respectively, and thus the joint probability density $f_{L,t}$ factorises, $f_{L,t}(L, t) = f_L(L) f_t(t)$.

Let's assume that the sources are, although discrete, homogeneously distributed in a ring around the observer with an inner and outer radius r_1 and r_2 , respectively (see Fig. 2.1). The distance L

²Here and in the following we assume that all the sources considered have a common injection spectrum $Q(E)$. Of course, in reality the sources differ in total power output and spectrum which will introduce additional fluctuations into the spectrum observed at Earth. Here, we however constrain ourselves to investigate the effects of the discreteness of sources.

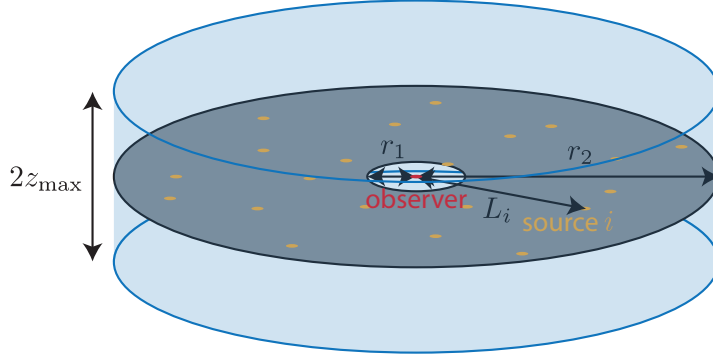


Figure 2.1.: Propagation setup. The sources are discrete, but homogeneously distributed around the observer in a ring of inner radius r_1 and outer radius r_2 . The disk is contained in a diffusion volume of half-height z_{\max} . We neglect the boundary condition in radial direction.

to some source is a random variable with the probability density,

$$f_L(L) = \begin{cases} 2L/(r_2^2 - r_1^2) & \text{for } r_1 \leq L \leq r_2, \\ 0 & \text{otherwise.} \end{cases} \quad (2.20)$$

Also, we assume that the source rate, e.g. the supernova rate, is constant over the time scales considered, $\mathcal{O}(100)$ Myr (electrons and positrons of GeV energies can diffuse over $\mathcal{O}(100)$ Myr before losing their energy but are, of course, subject to escape losses). Therefore, we take the sources to be equally distributed up to a maximum time $t_{\max} = 1/(b_0 E_{\min})$, set by the minimum energy E_{\min} which is to be considered,

$$f_t(t) = \begin{cases} 1/t_{\max} & \text{for } 0 \leq t \leq t_{\max}, \\ 0 & \text{otherwise.} \end{cases} \quad (2.21)$$

Rewriting the m -th moment of the Green's function as an integral over L and t (see Appendix A), we have,

$$\langle Z^m \rangle = \int dz f_Z(z) z^m \quad (2.22)$$

$$= \int_{r_1}^{r_2} dL \int_0^{t_{\max}} dt f_{L,t}(L, t) G^m(L, t) \quad (2.23)$$

$$= \int_{r_1}^{r_2} f_L(L) dL \int_0^{t_{\max}} dt f_t(t) G^m(L, t) \quad (2.24)$$

$$= \frac{1}{t_{\max}} \int_0^{t_{\max}} dt \int_{r_1}^{r_2} dL \frac{2L}{r_2^2 - r_1^2} \left((\pi \ell^2)^{-1} e^{-L^2/\ell^2} Q_0 E^{-\gamma} (1 - b_0 E t)^{\gamma-2} \frac{1}{z_{\text{cr}}} \chi \left(\frac{\ell}{z_{\text{cr}}} \right) \right)^m \quad (2.25)$$

$$= \frac{1}{t_{\max}} \int_0^{t_{\max}} dt \int_{r_1^2}^{r_2^2} \frac{dL^2}{r_2^2 - r_1^2} e^{-mL^2/\ell^2} \left((\pi \ell^2)^{-1} Q_0 E^{-\gamma} (1 - b_0 E t)^{\gamma-2} \frac{1}{z_{\text{cr}}} \chi \left(\frac{\ell}{z_{\text{cr}}} \right) \right)^m \quad (2.26)$$

$$= \frac{1}{t_{\max}} \frac{1}{r_2^2 - r_1^2} \int_0^{t_{\max}} dt \left[\frac{\ell^2}{m} e^{-mL^2/\ell^2} \right]_{r_2^2}^{r_1^2} \left((\pi \ell^2)^{-1} Q_0 E^{-\gamma} (1 - b_0 E t)^{\gamma-2} \frac{1}{z_{\text{cr}}} \chi \left(\frac{\ell}{z_{\text{cr}}} \right) \right)^m \quad (2.27)$$

We now substitute,

$$E_0 = \frac{E}{1 - b_0 E t} \quad \Rightarrow \quad \frac{dt}{(1 - b_0 E t)^2} = \frac{dE_0}{b_0 E^2}, \quad (2.28)$$

to obtain an integral in energy E_0 at source,

$$\langle Z^m \rangle = \frac{1}{t_{\max}} \frac{1}{r_2^2 - r_1^2} \int_E^\infty \frac{dE_0}{b_0 E_0^2} \left[\frac{\ell^2}{m} e^{-mL^2/\ell^2} \right]_{r_2^2}^{r_1^2} \left((\pi \ell^2)^{-1} Q_0 E_0^{-\gamma} \left(\frac{E_0}{E} \right)^2 \frac{1}{z_{\text{cr}}} \chi \left(\frac{\ell}{z_{\text{cr}}} \right) \right)^m, \quad (2.29)$$

with

$$\ell^2 = \frac{4D_0}{b_0(1 - \delta)} \left(E^{\delta-1} - E_0^{\delta-1} \right). \quad (2.30)$$

For $m = 1$, this is,

$$\langle Z \rangle = \frac{1}{t_{\max}} \frac{1}{r_2^2 - r_1^2} \int_E^\infty \frac{dE_0}{b_0 E^2} \left[\ell^2 e^{-L^2/\ell^2} \right]_{r_2^2}^{r_1^2} (\pi \ell^2)^{-1} Q_0 E_0^{-\gamma} \frac{1}{z_{\text{cr}}} \chi \left(\frac{\ell}{z_{\text{cr}}} \right), \quad (2.31)$$

which can, for example, be evaluated numerically. The expectation value $\mu_J = c/(4\pi)N\langle Z \rangle$ for the flux is identical to the flux from a continuous, homogeneous and steady source distribution,

$$\frac{N}{\pi(r_2^2 - r_1^2)} \frac{Q_0 E_0^{-\gamma}}{t_{\max}} \quad (2.32)$$

in a ring with inner and outer radius r_1 and r_2 , respectively. The first term is the surface density of sources and the second one the power spectrum per source (although we are, strictly speaking, comparing to a continuous source distribution).

Expanding the term $\chi(\ell/z_{\text{cr}})$ in Eq. 2.29 (associated with the diffusion in the z direction) for $\ell \ll z_{\text{cr}}$, which is only justified for energies above ~ 50 GeV for $z_{\text{max}} \simeq 4$ kpc and amounts to ignoring the boundary (condition) in the z direction,

$$\frac{1}{z_{\text{cr}}}\chi\left(\frac{\ell}{z_{\text{cr}}}\right) \simeq \frac{1}{\sqrt{\pi\ell^2}}, \quad (2.33)$$

we can get analytical estimates for the moments $\langle Z^m \rangle$. To this end we further substitute,

$$\begin{aligned} \lambda^2 &= \frac{b_0(1-\delta)}{4D_0} E^{1-\delta} \ell^2 = \left[1 - \left(\frac{E_0}{E} \right)^{\delta-1} \right] \\ \Rightarrow E_0 &= E (1 - \lambda^2)^{\frac{1}{\delta-1}} \quad \Rightarrow \quad dE_0 = \frac{E}{1-\delta} (1 - \lambda^2)^{\frac{1}{\delta-1}-1} d\lambda^2, \end{aligned} \quad (2.34)$$

similarly define,

$$\Lambda^2 = \frac{b_0(1-\delta)}{4D_0} E^{1-\delta} L^2, \quad \rho_i^2 = \frac{b_0(1-\delta)}{4D_0} E^{1-\delta} r_i^2, \quad (2.35)$$

and find,

$$\begin{aligned} \langle Z^m \rangle &= \frac{1}{t_{\text{max}}} \frac{1}{r_2^2 - r_1^2} \frac{(4D_0)^{1-\frac{3}{2}m}}{(b_0(1-\delta))^{2-\frac{3}{2}m}} \frac{Q_0^m}{m\pi^{\frac{3}{2}m}} E^{-2+\delta+\frac{3}{2}m(1-\delta)-m\gamma} \\ &\quad \times \int_0^1 d\lambda^2 (1-\lambda^2)^{\frac{m(\gamma-2)+\delta}{1-\delta}-1} (\lambda^2)^{1-\frac{3}{2}m} \left[e^{-m\Lambda^2/\lambda^2} \right]_{\rho_2^2}^{\rho_1^2}. \end{aligned} \quad (2.36)$$

Eventually, we want to send r_1 to zero since the distance to the nearest source is not physically limited. At the energies for which the above expansion holds, we also have $\ell^2 \ll r_2^2$, and therefore the exponential term in the integrand is ≈ 1 . For $m = 1$, the integral converges,

$$\int_0^1 d\lambda^2 (1-\lambda^2)^{\frac{\gamma-1}{1-\delta}-1} (\lambda^2)^{-1/2} = \frac{\sqrt{\pi} \Gamma\left(\frac{\gamma-1}{1-\delta}\right)}{\Gamma\left(\frac{2\gamma-\delta-1}{2(1-\delta)}\right)}, \quad (2.37)$$

where Γ is the gamma function and the average flux is,

$$\mu_J = \frac{c}{4\pi} N \mu_Z = \frac{c}{4\pi} \frac{1}{\sqrt{4D_0 b_0(1-\delta)}} \frac{N}{\pi r_2^2} \frac{Q_0}{t_{\text{max}}} E^{-\gamma-1+(1-\delta)/2} \frac{\Gamma\left(\frac{\gamma-1}{1-\delta}\right)}{\Gamma\left(\frac{2\gamma-\delta-1}{2(1-\delta)}\right)}. \quad (2.38)$$

With the parameters chosen as shown in Table 2.1 this gives,

$$E^3 \mu_J \simeq 150 \text{ GeV}^{-1} \text{ cm}^{-2} \text{ s}^{-1} \text{ sr}^{-1}, \quad (2.39)$$

close to the featureless E^{-3} spectrum measured with Fermi-LAT [169].

For $m = 2$, the integral in Eq. 2.36 however diverges; the second moment, $\langle Z^2 \rangle$, and hence the variance σ_Z^2 is infinite. This could be cured by reinstating $\exp(-2\rho_1^2/\lambda^2)$ with a finite ρ_1 as a cut-off in the integral for small λ^2 , however, for the price of an additional and, even worse, physically unmotivated parameter. For $r_1 = 0$, the standard deviation of the flux therefore does not exist and cannot be used as an indicator of the amplitude of the stochastic fluctuations. Furthermore, the usual central limit theorem cannot be applied any more.

The reason that the expectation value is finite but not the variance is that the probability density $f_Z(z)$ has a broad power-law tail. For such cases, a generalised central limit theorem [268] is applicable: The centred and normalised sum X_N of N independent and identically distributed (iid) random variables Z_i converges against a stable distribution $\mathcal{S}(\alpha, \beta, 1, 0, 1)$ [269] if the probability density $f_Z(z)$ behaves like $|z|^{-\alpha-1}$ for $z \rightarrow \infty$. In general, the distribution function for \mathcal{S} is not known analytically but can be calculated as the inverse Fourier transform of its characteristic function. To determine the parameters α and β , we need to find the asymptotic behaviour of the probability density $f_Z(z)$ for large z .

Table 2.1.: Summary of parameters used in the Monte Carlo simulation.

Diffusion Model		
D_0	$10^{28} \text{ cm}^2 \text{ s}^{-1}$	} from GCR nuclear secondary-to-primary ratios
δ	0.6	
z_{max}	3 kpc	
b_0	$10^{-16} \text{ GeV}^{-1} \text{ s}^{-1}$	CMB, IBL and B energy densities
Source Distribution		
t_{max}	$3 \times 10^8 \text{ yr}$	from $E_{\text{min}} \simeq 1 \text{ GeV}$
N	1×10^7	from supernova rate and t_{max}
Source Model		
Q_0	$8.4 \times 10^{49} \text{ GeV}^{-1}$	} fit to absolute $e^+ + e^-$ flux
γ	2.2	
r_2	15 kpc	

The distribution function $F_Z(z)$ satisfies,

$$F_Z(z) = \iint_{\mathcal{D}_Z} dt dL f_t(t) f_L(L) \quad (2.40)$$

with the region \mathcal{D}_Z given by the condition $Z < z$. With $Z = G(t, L, E)$ this can be transformed into a condition on L :

$$Z < z \quad \Leftrightarrow \quad L^2 > L_{\min}^2 \equiv -\ell^2 \log z + \ell^2 \log \left((\pi \ell^2)^{-3/2} Q_0 E^{-\gamma} (1 - b_0 E t)^{\gamma-2} \right), \quad (2.41)$$

and hence

$$F_Z(z) = \frac{1}{t_{\max}} \frac{1}{r_2^2} \int_0^{t_{\max}} dt \int_{\max[0; L_{\min}]}^{r_2} dL 2L \quad (2.42)$$

$$= \frac{1}{t_{\max}} \frac{1}{r_2^2} \left(\int_0^{t_*} dt \int_{L_{\min}^2}^{r_2^2} dL^2 + \int_{t_*}^{t_{\max}} dt \int_0^{r_2^2} dL^2 \right), \quad (2.43)$$

where $L_{\min} \geq 0$ for $0 \leq t \leq t_*$ and $L_{\min} < 0$ for $t > t_*$. The probability density can then be obtained by differentiating,

$$f_Z(z) = \frac{dF_Z(z)}{dz} = \frac{1}{t_{\max}} \frac{1}{r_2^2} \int_0^{t_*} dt \left(-\frac{\partial L_{\min}^2}{\partial z} \right). \quad (2.44)$$

With the substitutions, Eqs. 2.28 and 2.34, this reads,

$$f_Z(z) = \frac{1}{t_{\max}} \frac{1}{r_2^2} \frac{4D_0}{(b_0(1-\delta))^2} E^{\delta-2} \int_0^{\lambda_*^2} d\lambda^2 (1-\lambda^2)^{-\delta/(\delta-1)} \lambda^2 \frac{1}{z} \quad (2.45)$$

with λ_*^2 defined by $\Lambda_{\min}^2|_{\lambda^2=\lambda_*^2} = 0$ where

$$\Lambda_{\min}^2 = -\lambda^2 \left(\log z - \log \left[\left(\frac{4\pi D_0}{b_0(1-\delta)} \right)^{-\frac{3}{2}} E^{\frac{3}{2}(1-\delta)-\gamma} Q_0 \right] + \frac{3}{2} \log \lambda^2 + \frac{\gamma-2}{\delta-1} \log (1-\lambda^2) \right). \quad (2.46)$$

As we are looking for the asymptotic behaviour of $F_Z(z)$ for large z which we anticipate corresponds

to $\lambda_*^2 \ll 1$, we can neglect the $(1 - \lambda^2)$ term in Λ_{\min}^2 and solve Λ_{\min}^2 for λ_*^2 ,

$$\lambda_*^2 \simeq \frac{b_0(1 - \delta)}{4\pi D_0} E^{(1-\delta) - \frac{2}{3}\gamma} Q_0^{2/3} z^{-2/3}. \quad (2.47)$$

With the same approximation, the integral in Eq. 2.45 gives $(\lambda_*^2)^2/2$ and

$$f_Z(z) \simeq \frac{1}{t_{\max}} \frac{1}{r_2^2} \frac{1}{8\pi^2 D_0} E^{-\delta - \frac{4}{3}\gamma} Q_0^{4/3} z^{-7/3}. \quad (2.48)$$

The asymptotic behaviour of the distribution function $F_Z(z)$ is therefore

$$1 - F_Z(z) \sim c^+ z^{-4/3} \quad \text{with} \quad c^+ = \frac{3}{4} \frac{1}{t_{\max}} \frac{1}{r_2^2} \frac{1}{8\pi^2 D_0} E^{-\delta - \frac{4}{3}\gamma} Q_0^{4/3}, \quad (2.49)$$

and $F_Z = 0$ for $z < 0$.

The generalised central limit theorem [270] then states that the centred and normalised sum X_N ,

$$X_N = \frac{1}{b_N} \left(\sum_i^N X_i - a_N \right), \quad (2.50)$$

weakly converges to the stable distribution $\mathcal{S}(\alpha, \beta, 1, 0, 1)$ with $\alpha = 4/3$ and $\beta = 1$. The normalisation constants are

$$a_N = N\mu_Z \quad \text{and} \quad b_N = \left(\frac{\pi c^+}{2\Gamma(\frac{4}{3}) \sin(\frac{\pi}{2} \frac{4}{3})} \right)^{3/4} N^{3/4}. \quad (2.51)$$

The expectation value μ_J for the flux on Earth is therefore still $c/(4\pi)N\mu_Z$ but instead of the standard deviation, we use quantiles of the stable distribution to quantify the level of fluctuations. For $\mathcal{S}(4/3, 1, 1, 0, 1)$ the 5%, 16%, 84% and 95% quantiles are approximately -3.3 , -2.6 , 1.0 and 4.7 , respectively. The energy dependence of the quantiles of J is contained in $b_N \propto (c^+)^{3/4} \propto E^{-\gamma - 3\delta/4}$, which is always harder than $\mu_J \propto E^{-\gamma - (1+\delta)/2}$, so the fluctuations are growing with energy. For the particular values from Table 2.1, $b_N \propto E^{-2.65}$. Fig. 2.2 shows the uncertainty bands that 68% and 90% of the total fluxes should be contained in, that is $[\mu_J + c/(4\pi)b_N x_{16\%}, \mu_J + c/(4\pi)b_N x_{84\%}]$ and $[\mu_J + c/(4\pi)b_N x_{5\%}, \mu_J + c/(4\pi)b_N x_{95\%}]$, together with the expectation value for the flux μ_J .

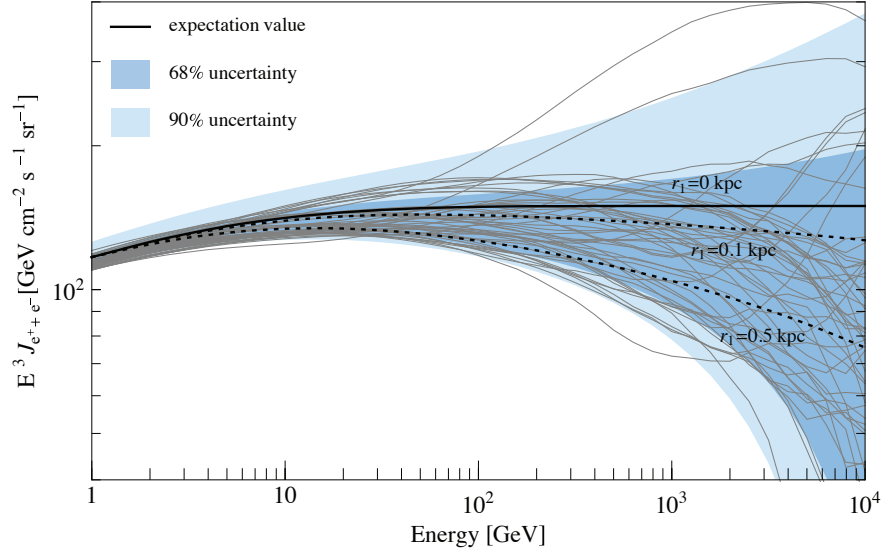


Figure 2.2.: Fluxes of Cosmic Ray electrons from ensembles of sources uniformly distributed in a disk around the observer. The solid line denotes the expectation value for the sum of fluxes from N discrete, transient sources. The dashed lines show the expectation values if the sources are limited to a ring with inner radius r_1 (normalised to the expectation value for $r_1 = 0$ at 1 GeV). The coloured bands quantify the fluctuations and contain the fluxes 68% and 90% of the time, respectively. The fluxes from 50 realisations of an ensemble of N individual sources are shown by the grey lines.

One notices that a spectral softening occurs in the spectrum around 10 GeV. Below ~ 50 GeV, the expansion for $\chi(\ell/z_{\text{cr}})$ made above is not valid any more and the spectrum is not dominated by energy losses but by losses due to the escape from the halo. We also show the the total fluxes from a Monte Carlo calculation of 50 realisations of a uniform source distribution with the same model parameters, see Table 2.1. Although the bands do indeed contain the right fraction of fluxes, the majority appears to be not only lower but also more curved downwards than the expectation value for $r_1 = 0$.

The deficit in the majority of realisations is in fact a consequence of the stable distribution which is highly asymmetric with a long tail. On the one hand, it is because of the asymmetry that a majority of the fluxes from different realisations of the source density is below the expectation value. The long tail of the probability density on the other hand makes the average from a large number of realisations finally and slowly converge to the expectation value. This convergence is slowing down with increasing energy as because of the decreasing diffusion-loss length less sources effectively contribute at higher energies.

A more physical way of explaining the deficit at higher energies is that every realisation of a finite number of sources necessarily contains one closest source at $L_{\text{cl}} = \min_i [L_i]$ which contributes the most at the highest energies. Once the diffusion-loss length $\lambda(E)$ becomes however shorter than the distance L_{cl} even this contribution gets cut-off by the exponential term in the Green's function, Eq. 2.15, $\exp(-L_{\text{cl}}^2/\ell^2)$. The curving of the fluxes, called propagation cut-off, is therefore nothing but the shoulder of (a few) Green's function(s) from the closest source(s). We note that such a cut-off cannot simply be modelled by reinstating the minimum radius r_1 in Eq. 2.36 as shown by the dashed lines in Fig.2.2 for $r_1 = 0.1$ and 0.5 kpc.

2.3.2. A realistic source distribution

Of course, the sources of cosmic rays are not evenly distributed in a disk around the solar system. Above, this was only assumed to simplify the calculation of the effect of the discreteness of sources. In fact, SNRs are expected to spatially correlate with star formation activity and to be mainly based in the thin galactic disk, tracing the spiral structure. As discussed above, we have seen that effects of their actual distribution will play a role at energies above ~ 100 GeV.

Some authors [107, 271] have assumed a continuous distribution of sources for distances beyond a few hundred parsecs, supplemented by a set of SNRs, known from x-ray or radio surveys, for smaller distances. This approach is however biased by the choice of young, nearby sources which have been detected in radio and/or X-rays. Older sources may not be visible in photons any longer but still be contributing to the GCR electron flux. This relation is illustrated in Fig. 2.3. We note that the effect of this incomplete assumed source distribution is a dip in the electron flux seen in both analyses [107, 271], although at different energies because of the different diffusion model parameters chosen.

Determining the complete distribution of sources in our vicinity (i.e. up to a few kpc) from observations seems challenging. However it turns out that we do not need to know the exact distribution in order to make a prediction for the e^+ flux and fraction but require only a limited amount of information, all of which is encoded already in the total $e^- + e^+$ flux. By including the recent measurements by Fermi-LAT [169] and HESS [186, 192] of the total $e^- + e^+$ flux in the energy region of interest, we have sufficient information at hand to make a prediction for the positron fraction under the assumption that the additional positrons originate in the same sources.

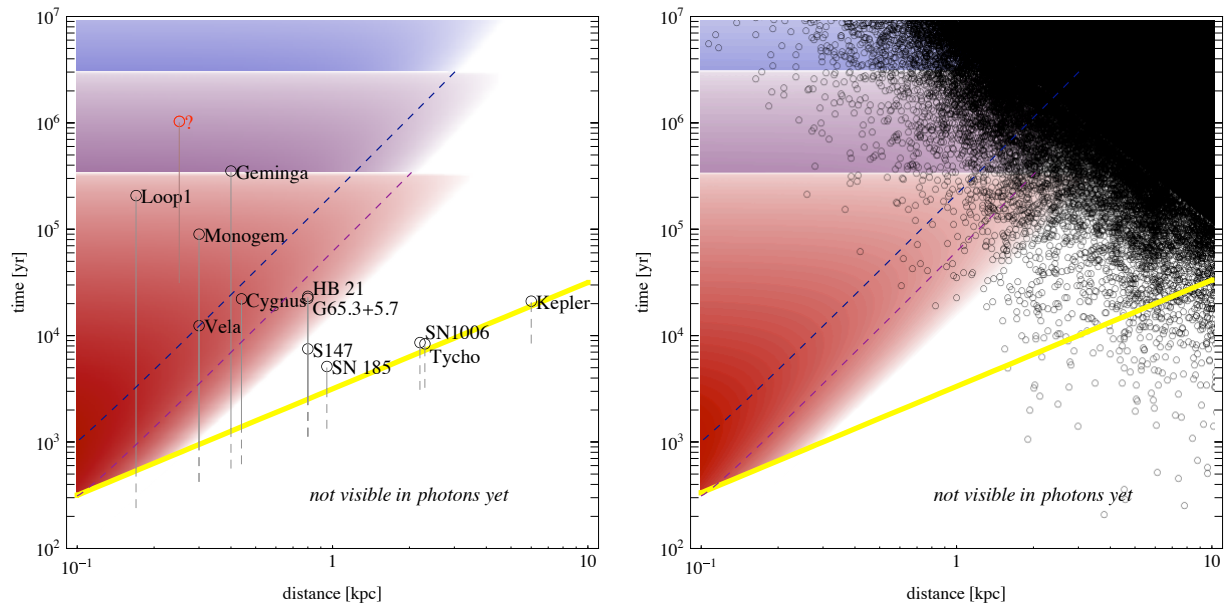


Figure 2.3.: Distance-time diagram for nearby SNRs (after Ref. [266]). **Left:** The open circles mark supernova events and the world-lines of the discovered remnants are indicated. The thick yellow line is our past light-cone; all events lying on it, e.g. the SNR world-lines touching it, can be observed presently. The blue, purple and red shadings (top to bottom) show the relative contribution of sources to the diffuse e^- and e^+ flux observed at Earth at 10, 100 and 1000 GeV, respectively. The open red circle is an example of a hypothetical supernova whose remnant is too old to be visible any longer but which might still be contributing to the diffuse e^- and e^+ flux. **Right:** A distance-time diagram for hypothetical nearby SNRs. The open black circles are an example of a possible realisation of the supernova density (the world lines have been suppressed) as simulated by our Monte Carlo calculation (see Section 2.3.2).

We perform a Monte Carlo calculation by considering a large number of random distributions of sources drawn from a probability density function that reflects our astronomical knowledge about the distribution of SNRs in the Galaxy. The better the flux of e^- and e^+ from such a realisation of the source density reproduces the measured fluxes, the closer is the underlying distribution of sources likely to be to the actual one. We do not consider any scatter in the parameters of the SNRs but assume a prototypical set of source parameters that we determine from a compilation of gamma-ray SNRs, see Sec. 2.4.1. Of course all SNRs are not the same, however variations of the source parameters would only introduce additional fluctuations into the fluxes without altering their average. We can choose the best “fit” to the data and thus determine the e^+ flux.

The smoothed radial distribution of SNRs in the Galaxy is well modelled by [272]

$$f(r) = A \sin\left(\frac{\pi r}{r_0} + \theta_0\right) e^{-\beta r}, \quad (2.52)$$

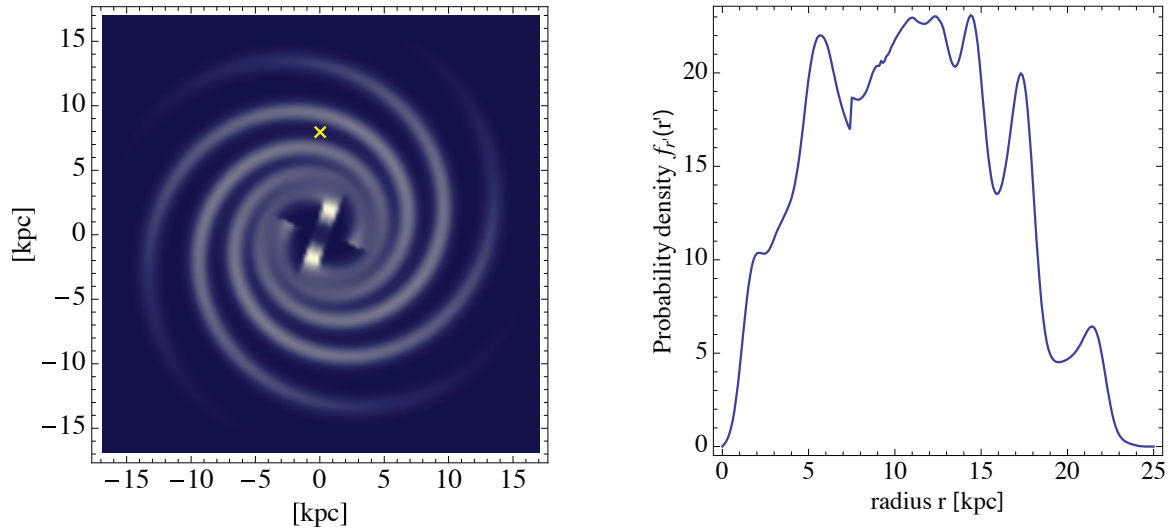


Figure 2.4.: The assumed distribution of SNRs in the Galaxy; the cross denotes the position of the Sun in between two spiral arms. Figure 2.5.: The probability density for the distance of a SNR from the Sun.

where $A = 1.96 \text{ kpc}^{-2}$, $r_0 = 17.2 \text{ kpc}$, $\theta_0 = 0.08$ and $\beta = 0.13$. To obtain a realistic probability density for the distance between the Earth and a SNR we have to also take into account the spiral structure of the Galaxy. We adopt a logarithmic spiral with four arms of pitch angle 12.6° and a central bar of 6 kpc length inclined by 30° with respect to the direction Sun - galactic centre [273]. The density of SNRs is modelled by a Gaussian with 500 pc dispersion for each arm [264]. The resulting distribution $g(r, \phi)$ (see Fig. 2.5) has been normalized with respect to azimuth in such a way that the above radial distribution Eq. 2.52 is recovered. To obtain the probability density for the distances we transform to the coordinates (r', ϕ') centred on the Sun. As the e^- and e^+ fluxes are assumed to be isotropic, we can average over the polar angle ϕ' , such that the probability density $f_{r'}$ depends only on the distance r' to the source,

$$f_{r'}(r') = \frac{1}{2\pi} \int_0^{2\pi} d\phi' r' g(r(r', \phi'), \phi(r', \phi')). \quad (2.53)$$

This function is shown in Fig. 2.5.

We assume that the sources are uniformly distributed in time, i.e. their probability density $f_t(t)$

is

$$f_t(t) = \begin{cases} 1/t_{\max} & \text{for } 0 \leq t \leq t_{\max}, \\ 0 & \text{otherwise,} \end{cases} \quad (2.54)$$

with t_{\max} denoting the earliest time considered, which is again related to the minimum energy for which our calculation is valid through

$$t_{\max} = (bE_{\min})^{-1}. \quad (2.55)$$

The total number N of sources that are needed in the Monte Carlo simulation to reproduce the (observed) number $\mathcal{N} \simeq 300$ of SNRs active in the galaxy at any given time depends on the average lifetime of a SNR, τ_{SNR} , which is suggested to be $\sim 10^4$ yr [274], hence

$$N = 3 \times 10^6 \left(\frac{\mathcal{N}}{300} \right) \left(\frac{t_{\max}}{10^8 \text{ yr}} \right) \left(\frac{\tau_{\text{SNR}}}{10^4 \text{ yr}} \right)^{-1}. \quad (2.56)$$

We take a Green's function approach to calculate the contribution from these N discrete, burst-like sources to the total electron-positron flux in the solar system today for a halo of extent $\pm z_{\max}$ in z direction, again neglecting the boundaries in the radial direction. We remind ourselves that the Green's function for the flux of electrons from a source at \mathbf{r} that went off a time t ago with a spectrum $Q(E)$, is

$$\begin{aligned} G_{\text{disk}}(E, \mathbf{r}, t) &= \sum_{n=-\infty}^{\infty} (\pi \ell^2)^{-3/2} e^{-\mathbf{r}_n^2 / \ell^2} Q\left(\frac{E}{1 - b_0 E t}\right) (1 - b_0 E t)^{-2} \\ &= (\pi \ell^2)^{-1} e^{-\mathbf{r}_{\parallel}^2 / \ell^2} Q\left(\frac{E}{1 - b_0 E t}\right) (1 - b_0 E t)^{-2} \frac{1}{z_{\text{cr}}} \chi\left(\frac{z}{z_{\text{cr}}}, \frac{\ell}{z_{\text{cr}}}\right), \end{aligned} \quad (2.57)$$

where

$$\chi(\hat{z}, \hat{\ell}) \equiv \frac{1}{\sqrt{\pi} \hat{\ell}} \sum_{n=-\infty}^{\infty} e^{-\hat{z}_n^2 / \hat{\ell}^2}, \quad (2.58)$$

and the diffusion length ℓ is defined by

$$\ell^2 = 4 \int_E^{E/(1-b(E)t)} dE' \frac{D(E')}{b(E')} = \frac{4D_0}{b_0(1-\delta)} \left[E^{\delta-1} - \left(\frac{E}{1-b_0 E t} \right)^{\delta-1} \right],$$

with $z_{\text{cr}} \equiv 4z_{\text{max}}/\pi$. If we neglect the spatial extent of the disk and set $z = 0$, the function $\chi(\hat{\ell}) \equiv \chi(0, \hat{\ell})$ is approximately:

$$\chi(\hat{l}) \simeq \begin{cases} \frac{4}{\pi} e^{-\hat{l}^2} & \text{for } \hat{l} \gg \frac{\pi}{4}, \\ \frac{1}{\sqrt{\pi}\hat{l}} & \text{for } \hat{l} \ll \frac{\pi}{4}. \end{cases} \quad (2.59)$$

In practice both limits can be connected at $\hat{l} \simeq 0.66$ such that the approximated $\chi(\hat{\ell})$ has a relative error of at most 0.5%. We motivate the choice of the parameters of our diffusion model from an analysis of nuclear secondary-to-primary ratios [275]: $D_0 = 10^{28} \text{ cm}^2\text{s}^{-1}$, $\delta = 0.6$, $L = 3 \text{ kpc}$, and from the galactic magnetic field and interstellar radiation fields [107]: $b_0 = 10^{-16} \text{ GeV}^{-1} \text{ s}^{-1}$.

2.4. Fitting the Total Electron-Positron spectrum

A schematic description of the present framework is shown in Fig. 2.6. Cosmic rays are shock accelerated in SNRs and then diffuse through the Galaxy to Earth undergoing collisions with interstellar matter *en route* and creating secondary e^+ . As discussed, the ratio of the secondary e^+ to the primary e^- from the sources should *decrease* with energy, in contrast to the behaviour seen by PAMELA. We follow Ref. [243] in explaining this by invoking a new component of e^+ which is produced through cosmic ray interactions in the SNRs, and then shock *accelerated*, thus yielding a harder spectrum than that of their primaries. We discuss these components in turn below and calculate their relative contributions by normalising to the gamma-ray flux from the SNRs, which provides an independent measure of the hadronic interactions therein.

2.4.1. Primary electrons

The radio and X-ray emission observed from SNRs is interpreted as synchrotron radiation of electrons accelerated up to energies of $\mathcal{O}(100) \text{ TeV}$ [274]. The spectrum of this radiation then determines the spectrum of the underlying relativistic electrons. Moreover, the theory of diffusive shock acceleration [276, 86] predicts similar spectra for the accelerated protons and nuclei as for the electrons. If the gamma-ray emission observed by HESS from a number of identified SNRs is assumed to be of hadronic origin, we can use the measured spectra to constrain both the relativistic proton and electron population.

Table 2.2.: Summary of spectral parameters for SNRs detected in gamma-rays from a power-law fit to the spectrum, $J_\gamma = J_\gamma^0(E/\text{TeV})^{-\gamma}$, with an exponential cut-off at E_{max} in the case of HESS J1713.7-397. The errors shown are statistical only — the systematic error is conservatively estimated to be 20% on the flux J_γ and ± 0.2 on the spectral index γ . Also shown is the estimated distance L and the injection rate Q_γ^0 derived from Eq. 2.66.

Source	Other name(s)	γ	$J_\gamma^0 \div 10^{-12}$ [[cm ² s TeV] ⁻¹]	E_{max} [TeV]	L [kpc]	$Q_\gamma^0 \div 10^{33}$ [[s TeV] ⁻¹]	Ref.
HESS J0852-463	RX J0852.0-4622 (Vela Junior)	2.1 ± 0.1	21 ± 2	> 10	0.2	0.10	[277]
HESS J1442-624	RCW 86, SN 185 (?)	2.54 ± 0.12	3.72 ± 0.50	$\gtrsim 20$	1	0.46	[278]
HESS J1713-381	CTB 37B, G348.7+0.3	2.65 ± 0.19	0.65 ± 0.11	$\gtrsim 15$	7	3.812	[279]
HESS J1713-397	RX J1713.7-3946, G347.3-0.5	2.04 ± 0.04	21.3 ± 0.5	17.9 ± 3.3	1	2.55	[280, 281]
HESS J1714-385	CTB 37A	2.30 ± 0.13	0.87 ± 0.1	$\gtrsim 12$	11.3	13.3	[282]
HESS J1731-347	G 353.6-07	2.26 ± 0.10	6.1 ± 0.8	$\gtrsim 80$	3.2	7.48	[283, 284]
HESS J1801-233 ¹	W 28, GRO J1801-2320	2.66 ± 0.27	0.75 ± 0.11	$\gtrsim 4$	2	0.359	[285]
HESS J1804-216 ²	W 30, G8.7-0.1	2.72 ± 0.06	5.74	$\gtrsim 10$	6	24.73	[286]
HESS J1834-087	W 41, G23.3-0.3	2.45 ± 0.16	2.63	$\gtrsim 3$	5	7.87	[286]
MAGIC J0616+225	IC 443	3.1 ± 0.3	0.58	$\gtrsim 1$	1.5	0.156	[287]
Cassiopeia A		2.4 ± 0.2	1.0 ± 0.1	$\gtrsim 40$	3.4	1.38	[288] ³
J0632+057	Monoceros	2.53 ± 0.26	0.91 ± 0.17	...	1.6	0.279	[289]
Mean		~ 2.5		$\gtrsim 20$		~ 5.2	
Mean, excluding sources with $\gamma > 2.8$		~ 2.4		$\gtrsim 20$		~ 5.7	
Mean, excluding sources with $\gamma > 2.6$		~ 2.3		$\gtrsim 20$		~ 4.2	

¹ We assume that W 28 powers only the emission from J1801-233 (and not the nearby J1800-240 A, B and C).

² W30 is taken to be the origin of the VHE (very high energy) emission [290].

³ Cas A was first detected by HEGRA [291].

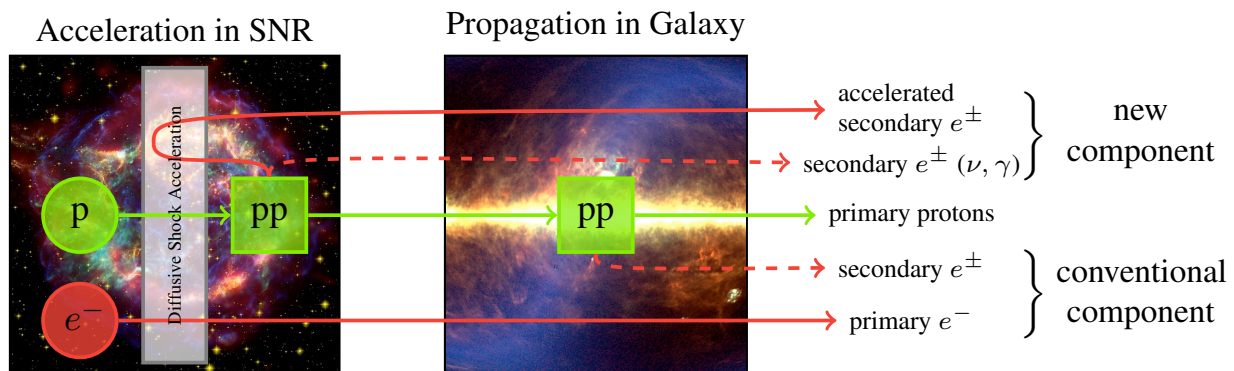


Figure 2.6.: Schematic description of contributions to the galactic cosmic rays observed at Earth in the present framework.

Table 2.2 shows a compilation of gamma-ray sources observed by HESS that have been identified as SNRs. We have included all identified shell-type SNRs and strong SNR candidates in the HESS source catalogue [292] (as of September 2009), and also added the SNRs IC 443, Cassiopeia A and Monoceros. Actually it is not clear that the acceleration of secondaries does occur in all the SNRs considered, especially when the gamma-ray emission is associated with a neighbouring molecular cloud rather than coming from the vicinity of the shock wave. In fact the gamma-rays could equally well be due to inverse-Compton scattering by the relativistic electrons responsible for the observed synchrotron radio and X-ray emission. Therefore, we have considered three possibilities — including all sources implies a mean power-law spectral index for the protons of $\langle\gamma\rangle = 2.5$, while excluding steep spectrum sources with $\gamma > 2.8$ gives $\langle\gamma\rangle = 2.3$ and excluding sources with $\gamma > 2.6$ yields $\langle\gamma\rangle = 2.4$. In the following we adopt the central value, $\gamma = 2.4$, for the electron population too, unless stated otherwise. This requires a compression factor of $r \leq 3.3$ in contrast to the value of $r = 4$ expected for a strong shock, so there is clearly some tension between the DSA theory and observations. This can possibly be resolved if we consider only a subset of the SNRs in Table 1 to be hadronic accelerators, or if the gamma-ray spectrum is steepened, e.g. by the onset of an exponential cut-off in the electron spectrum. Our model assumptions are intimately connected to the production of neutrinos, the detection of which will therefore provide an independent test, see Sec. 2.6. In this work we adopt a cut-off of $E_{\text{cut}} \simeq 20$ TeV which is consistent with DSA

theory [274]. The source spectrum of primary electrons is then:

$$R_{e^-} = R_{e^-}^0 \left(\frac{E}{\text{GeV}} \right)^{-\gamma} e^{-E/E_{\text{cut}}}. \quad (2.60)$$

The normalisation $R_{e^-}^0$ is determined by fitting the electron flux at Earth resulting from our Monte Carlo computation to the preliminary measurement by PAMELA at 10 GeV [293]; the secondary fluxes can be neglected for this normalisation. We find $R_{e^-}^0 = 1.8 \times 10^{50} \text{ GeV}^{-1}$ for $\gamma = 2.4$ which corresponds to a total injection energy of

$$\int_{1 \text{ GeV}}^{20 \text{ TeV}} dE E R_{e^-}(E) \simeq 7 \times 10^{47} \text{ erg}. \quad (2.61)$$

This compares well to the value of 9.2×10^{47} erg said to be required to power the GCR electrons [274].

Solar modulation which is important below ~ 10 GeV, has been accounted for using the force field approach [60], with a charge-independent potential of $\phi = 600$ MV. However, our simple model ignores convection and (re)acceleration in the interstellar medium which become important below ~ 5 GeV, hence the electron flux cannot be predicted at lower energies. The primary e^- fluxes as measured on Earth for 30 different source configurations are shown in the top panel of Fig. 2.7. With an injection power-law index $\gamma \simeq 2.4 \pm 0.1$ as required for consistency with the gamma-ray data, there clearly is a deficit at high energies compared to the $e^+ + e^-$ flux measured by Fermi-LAT and HESS.

2.4.2. Secondary electrons and positrons from propagation

Positrons in GCR are generally assumed to be of purely secondary origin, arising through the decay of pions and kaons produced in the interactions of GCR protons (and nuclei) with the interstellar medium (ISM) [126]. The neutral pions decay into gamma-rays which then contribute to, if not dominantly constitute, the galactic gamma-ray background. The charged pions on the other hand decay into neutrinos and muons, the latter subsequently decaying into electrons and positrons. Assuming that spatial and temporal variations in the GCR proton flux J_p and the ISM gas density n_{ISM} are small, the source density of these secondary background e^- and e^+ is also homogeneous,

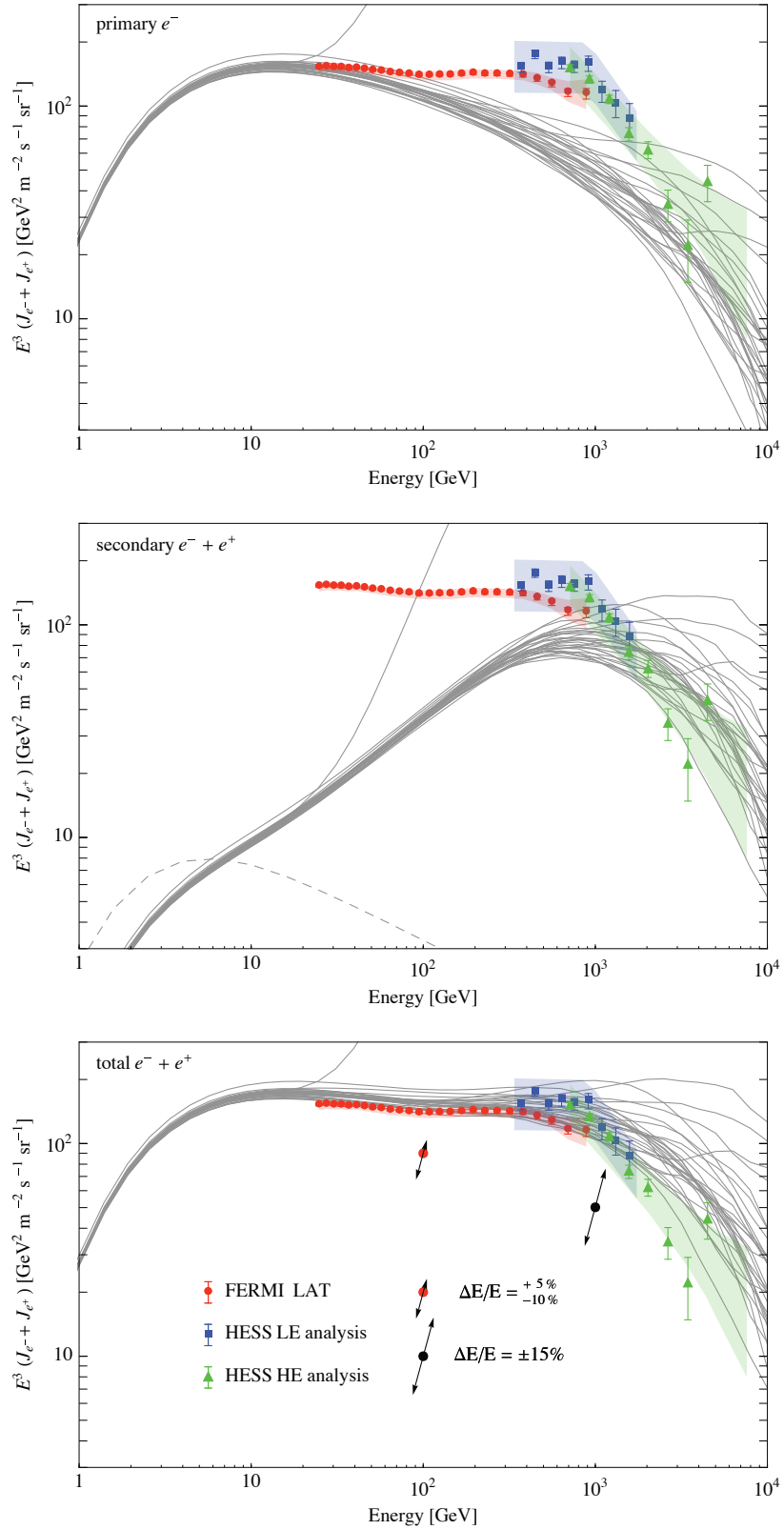


Figure 2.7.: Predicted spectra of electrons and positrons with data from Fermi-LAT [169] (red circles) and HESS [186, 192] (blue squares & green triangles). The diagonal arrows show the energy scale uncertainty. **Top:** Primary electrons after propagation to Earth. **Middle:** Secondary electrons and positrons from cosmic ray interactions, created during propagation (dashed line) and created during acceleration in SNRs (full lines). **Bottom:** The sum of primary and secondary electrons and positrons.

both in space and in time:

$$q_{\pm}^{\text{ISM}} = n_{\text{ISM}} c \int_{E_{\text{thr}}}^{\infty} dE' \frac{4\pi}{\beta c} J_{\text{p}}(E') \frac{d\sigma_{\text{pp} \rightarrow e^{\pm} + X}}{dE}, \quad (2.62)$$

where $d\sigma_{\text{pp} \rightarrow e^{\pm} + X}/dE$ is the partial differential cross-section for e^{\pm} production and $\beta \simeq 1$ is the velocity of the GCR. We can then integrate the Green's function for a single source over space and time to calculate

$$J_{\pm}(E) \simeq \frac{c}{4\pi} \frac{1}{|b(E)|} \int_E^{\infty} dE' q_{\pm}^{\text{ISM}}(E') \frac{2h}{z_{\text{cr}}} \chi\left(0, \frac{\ell}{z_{\text{cr}}}\right), \quad (2.63)$$

where $h \sim 0.1$ kpc is the height of the galactic disk.

We calculate the flux of secondary background e^{-} and e^{+} from the Solar-demodulated flux of GCR protons as derived from the BESS data [294] and model the cross-sections according to Ref. [112]. The contribution from kaon decay is subdominant and is therefore neglected. The presence of He both in GCRs and in the ISM is taken into account by multiplying the proton contribution by a factor of 1.2. Our results are in good agreement with Ref. [157], taking into account the different diffusion model parameters and keeping in mind that convection and reacceleration have been neglected here. These fluxes are shown (dashed line) in the middle panel of Fig. 2.7 and are clearly a subdominant component which cannot account for the deficit at high energies.

Moreover, the positron flux is *falling* faster than the primary e^{-} flux at all energies whereas the PAMELA data [163] clearly show a *rise* above a few GeV. One way this can be resolved is if there is a dip in the electron spectrum between ~ 10 and 100 GeV. It has been suggested that Klein-Nishina corrections to the Thomson cross section for inverse Compton scattering [110] or inhomogeneities in the distribution of sources [271] can produce such a dip. However the former would require a rather enhanced interstellar background light (IBL) field [110], while the latter calculation [271] assumes an incomplete source distribution (see Sec. 2.3.2) and moreover adopts diffusion model parameters quite different from those derived from the measured nuclear secondary-to-primary ratios [275] and the measured galactic magnetic field and IBL [107].

The other, perhaps more straightforward possibility is to consider an additional component of GCR positrons with a *harder* source spectrum that results in a harder propagated spectrum and therefore leads to an increase in the positron fraction.

2.4.3. Secondary electrons and positrons from the sources

Following Refs. [243, 295], the parameters are those typical of an old SNR: $u_1 = 0.5 \times 10^8 \text{ cm s}^{-1}$, $n_{\text{gas},1} = 2 \text{ cm}^{-3}$, $B = 1 \mu\text{G}$. Choosing $r = 3.1$ to recover $\gamma = 2.4$ the characteristic momenta p_{cross} and p_{break} (see Sec. 2.2) turn out to be,

$$p_{\text{cross}} = 427 K_{\text{B}}^{-1} \left(\frac{\tau_{\text{SNR}}}{10^4 \text{ yr}} \right) \text{ GeV}, \quad (2.64)$$

$$p_{\text{break}} = 7.7 K_{\text{B}}^{-1} \left(\frac{\tau_{\text{SNR}}}{10^4 \text{ yr}} \right) \text{ TeV}. \quad (2.65)$$

What is still missing is the normalization of the injection spectrum, R_{\pm}^0 , in the sources which is proportional to the normalisation of the GCR protons, N_{GCR} , through Eq. 2.3. Usually a factor $K_{\text{ep}} \simeq 10^{-4} - 10^{-2}$ is introduced to normalize the electron component with respect to the protons; this depends on how particles are injected from the thermal background into the acceleration process and is not reliably calculable from first principles. We can get around this by assuming that the gamma-rays detected from known SNRs by HESS are of hadronic origin, as is expected in this framework. Thus we can use the total luminosity of individual sources in gamma-rays,

$$Q_{\gamma} = 4\pi L^2 J_{\gamma}, \quad (2.66)$$

to determine the normalization of the proton component and therefore also the secondary injection rate q_{\pm}^0 if we know their distance L .

The compilation of γ ray data on SNRs from HESS, see Table 2.2, suggests an average value $Q_{\gamma}^0 \simeq 5.7 \times 10^{33} \text{ s}^{-1} \text{ TeV}^{-1}$. We find then for the total spectrum

$$R_{\pm}^0 = \tau_{\text{SNR}} Q_{\pm}^0 \simeq \tau_{\text{SNR}} \frac{\Sigma_{\pm}}{\Sigma_{\gamma}} Q_{\gamma}^0, \quad (2.67)$$

where Σ_{\pm} (and analogously Σ_{γ}) is defined by Eq. 2.9, or explicitly

$$R_{\pm}^0 = 7.4 \times 10^{48} \left(\frac{\tau_{\text{SNR}}}{10^4 \text{ yr}} \right) \left(\frac{Q_{\gamma}^0}{5.7 \times 10^{33} \text{ s}^{-1} \text{ TeV}^{-1}} \right) \text{ GeV}^{-1}. \quad (2.68)$$

In the Monte Carlo code we have explicitly input the experimentally measured pp cross-section

Table 2.3.: Summary of parameters used in the Monte Carlo simulation, for an injection spectral index $\gamma \simeq 2.4$.

Diffusion Model		
D_0	$10^{28} \text{ cm}^2 \text{ s}^{-1}$	} from GCR nuclear secondary-to-primary ratios
δ	0.6	
z_{max}	3 kpc	
b	$10^{-16} \text{ GeV}^{-1} \text{ s}^{-1}$	CMB, IBL and B energy densities
Source Distribution		
t_{max}	$1 \times 10^8 \text{ yr}$	from $E_{\text{min}} \simeq 3.3 \text{ GeV}$
τ_{SNR}	10^4 yr	from observations
N	3×10^6	from number of observed SNRs
Source Model		
$R_{e^-}^0$	$1.8 \times 10^{50} \text{ GeV}^{-1}$	fit to e^- flux at 10 GeV
γ	2.4	average gamma-ray spectral index
E_{max}	20 TeV	typical gamma-ray maximum energy
E_{cut}	20 TeV	DSA theory
R_+^0	$7.4 \times 10^{48} \text{ GeV}^{-1}$	cf. Sec. 2.4.3
K_B	15	only free parameter (for fixed γ)

which gives a similar normalisation as the estimate presented above assuming Feynman scaling. Also, we have taken into account the cut-off of the underlying primary protons. Their maximum energy is determined from the average maximum gamma-ray energy $E_{\text{max}} \simeq 20 \text{ TeV}$ (see Table 2.2) through the inelasticity of the $pp \rightarrow \gamma + X$ process as $\sim 20 \text{ TeV}/0.15 \approx 100 \text{ TeV}$ [281]. The normalisation for secondary electrons is computed similarly.

The middle panel of Fig. 2.7 shows an example of the flux of secondary source e^- and e^+ for 30 realisations of the SNR density in our Galaxy. Clearly this component can potentially match the high energy Fermi-LAT and HESS data.

We note that in our model, the contribution from secondary electrons and positrons to the total flux is about twice as large as in Ref. [243] where the primary injection spectrum was assumed to be $\propto E^{-2}$, motivated by DSA theory. However this is not consistent with gamma-ray observations of SNRs as seen from Table 2.2.

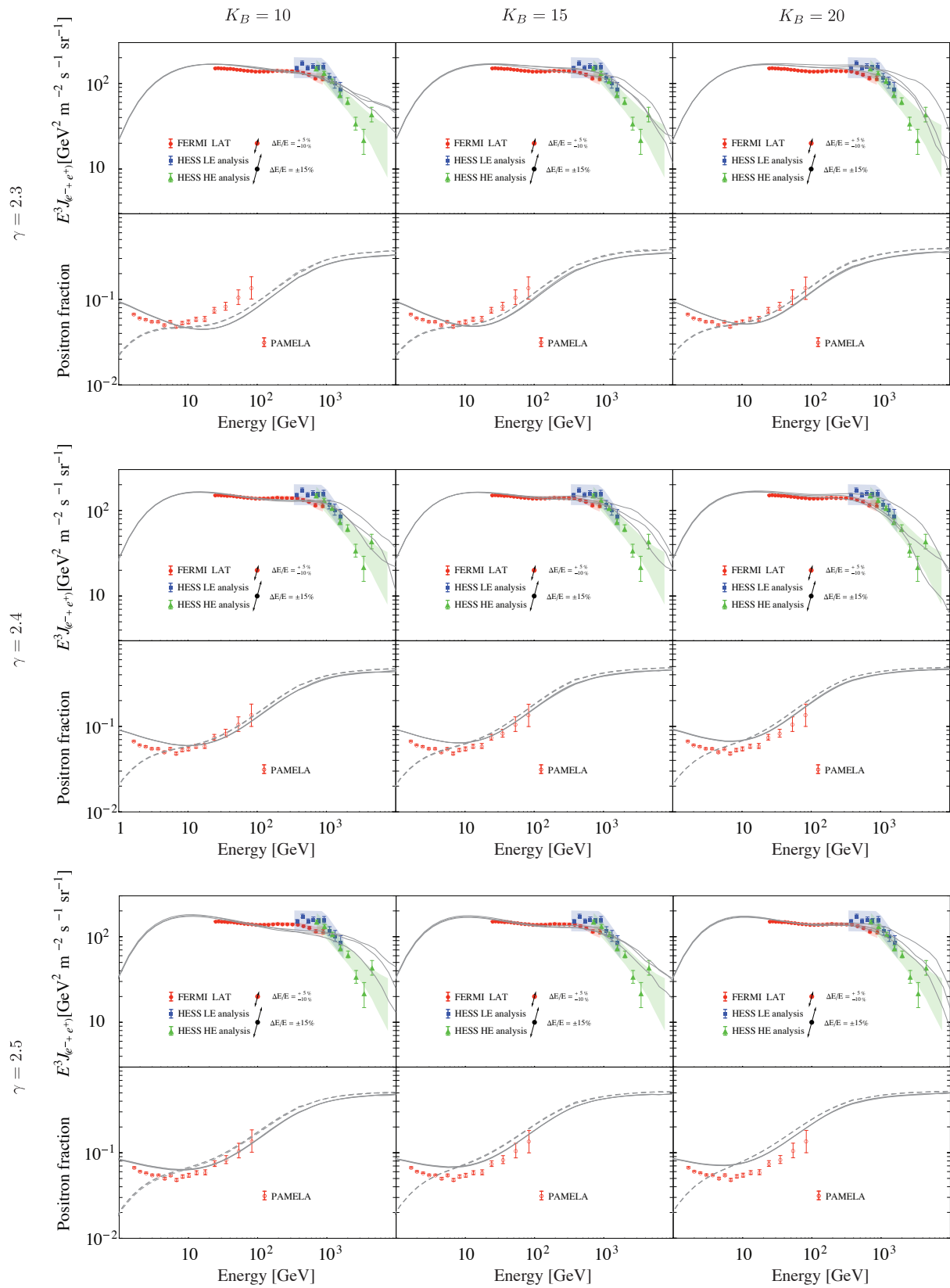


Figure 2.8.: The three best fits (out of 30 source realisations) to the total spectrum of electrons and positrons measured by Fermi-LAT [169] (red circles) and HESS [186, 192] (blue squares & green triangles), and the corresponding prediction for the positron fraction for different values of γ and K_B , for both charge-sign independent (full line) and charge-sign dependent (dashed line) Solar modulation (see text for details). The PAMELA data [163] is shown for comparison (open red circles).

2.5. Results

The parameters used in the Monte Carlo simulation are given in Table 2.3. For an assumed injection spectral index γ , the only free parameter is p_{cross} (cf. Eq. 2.12) or, equivalently, the factor K_{B} (cf. Eq. 2.13) which is determined by fitting the total flux of electrons and positrons to the Fermi-LAT and HESS data (see Fig. 2.7).

We have calculated the χ^2 with respect to the combined Fermi-LAT and HESS data for each realisation m of source distances and times, $\{L_i, t_i\}_m$, over all energy bins. The three best “fits” are shown in Fig. 2.8 for different values of K_{B} and for $\gamma = 2.3, 2.4$ and 2.5 (see Table 2.3). The corresponding predictions for the e^+ fraction are shown in the bottom panels. Adopting $\gamma = 2.4$, we find good agreement for $K_{\text{B}} \simeq 15$, which corresponds to a cross-over of the accelerated and the non-accelerated secondary components from the sources at $p_{\text{cross}} \simeq 28$ GeV and a spectral break at $p_{\text{break}} \simeq 510$ GeV (cf. Eqs. 2.64 and 2.65). The predictions for the e^+ fraction agrees reasonably well with the data down to 6 GeV; we would not expect agreement at lower energies since we have neglected convection and reacceleration during interstellar propagation. In fact the PAMELA measurements of the e^+ fraction are systematically lower than previous measurements, e.g. AMS-01 [148] or HEAT [165], and it has been noted that this discrepancy can be resolved by considering charge-sign *dependent* Solar modulation with $\phi_+ = 438$ MV for e^+ and $\phi_- = 2$ MV for e^- [296] (rather than $\phi_+ = \phi_- = 600$ MV). This however seems to be at odds with preliminary PAMELA data on the absolute electron flux [293] which *does* show substantial Solar modulation. Accordingly in Fig. 2.8 we have shown the predicted e^+ fraction for both cases; note that this does not affect our predictions for energies above 10 GeV.

2.6. Gamma-Rays and Neutrinos

Our fits to both the PAMELA (absolute e^-) and the Fermi-LAT (total $e^- + e^+$) spectra, allow to predict the PAMELA positron fraction by including secondary e^+ accelerated in SNRs and thus provides a consistent picture of current data on cosmic ray e^- and e^+ between a few GeV and tens of TeV. Turning the argument around, since a large fraction of the e^- and e^+ observed in GCR above hundreds of GeV are required to be secondaries in this model, there *must* be a large number of hadronic cosmic ray accelerators in our Galaxy, some of which should be quite nearby.

An independent test of the model is provided by the usual ‘messengers’ of such hadronic acceleration environments, namely gamma-rays and neutrinos. Taking the known distribution of SNRs in the Galaxy (see Sec. 2.3.2) we have calculated the column depth in SNRs in the galactic disk as seen from Earth,

$$X(\phi') = \int_0^\infty dr' r' g(r(r', \phi'), \phi(r', \phi')), \quad (2.69)$$

and show this in the top panel of Fig. 2.9. As expected, the column depth is largest towards the galactic centre. However, the quantity that is more important for observations is the brightness of sources. We have therefore weighted the integrand in Eq. 2.69 by $1/r'^2$ and this flux weighted column depth is also shown in the top panel of Fig. 2.9. We note that although the maximum brightness is still expected around the galactic Centre, the brightness in other directions is smaller by only $\sim 30\%$ because the sources in the closest spiral arms are then dominant (if they are actually there, of course).

This is illustrated in the bottom panel of Fig. 2.9 by an example distribution of SNRs from the Monte Carlo simulation, denoted by circles. The position of the circle denotes the galactic longitude and the radius is proportional to the brightness in units of the Crab Nebula, i.e. an integrated flux of $(1.98 \pm 0.08) \times 10^{-11} \text{ cm}^{-2} \text{ s}^{-1}$ above 1 TeV [297]. For a source of luminosity of $Q_\gamma^0 = 5.7 \times 10^{33} \text{ TeV}^{-1} \text{ s}^{-1}$ (see Table 2.2) at distance L , the integrated flux above 1 TeV is,

$$F_\gamma(> 1\text{TeV}) = \frac{1}{4\pi L^2} \int_{1\text{TeV}} dE Q_\gamma \simeq 8.5 \times 10^{-12} \left(\frac{L}{2\text{kpc}} \right)^{-2} \text{ cm}^{-2} \text{ s}^{-1}, \quad (2.70)$$

i.e. about 40 % of the Crab Nebula flux at $L = 2 \text{ kpc}$. It is seen that although most of the sources are clustered towards the galactic centre, there are several bright sources at large longitudes as well. We find typically ~ 3 sources brighter than the Crab (or ~ 7 brighter than 50 % Crab).

The adopted distribution of SNRs (Sec. 2.3.2) and the average luminosity per source determined from a compilation of known sources (Table 2.2) thus leads to the prediction of several nearby SNRs with fluxes of the order of the Crab Nebula. Note, however, that close sources could be rather extended and thus have escaped detection by HESS in one of its surveys of the Milky Way [286, 298, 299]. For example, a diameter of $\sim 50 \text{ pc}$ which is a typical value for a very old SNR, corresponds to 1.5° at 2 kpc.

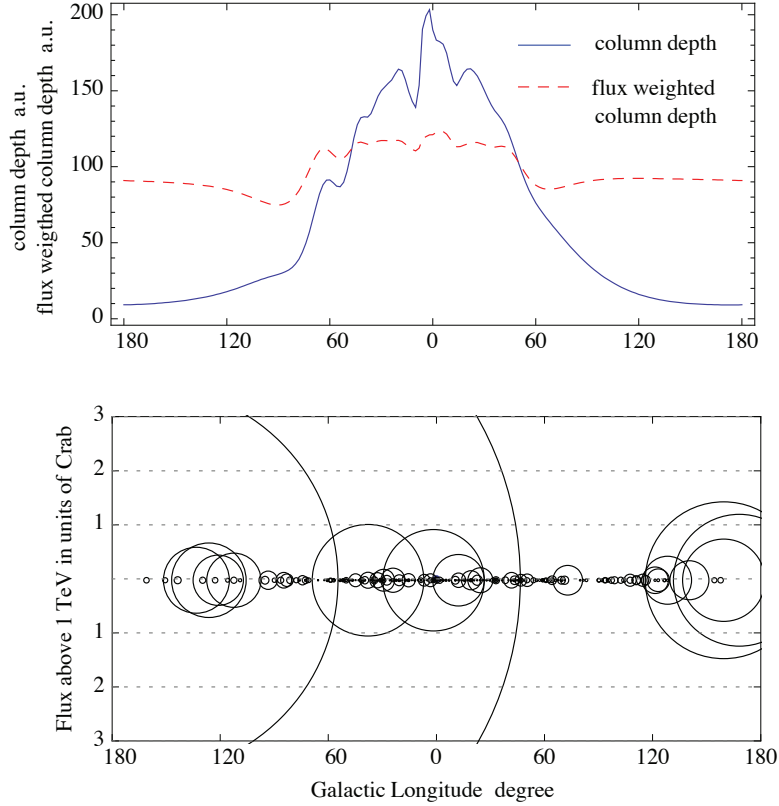


Figure 2.9.: **Top:** The column depth and flux weighted column depth of the SNR density in the galactic plane. **Bottom:** Example of a distribution of SNRs in gamma-rays/neutrinos from the Monte Carlo simulation. The position of a circle denotes the galactic longitude of the source and the radius is proportional to the brightness in units of the Crab nebula. One source whose circle exceeds the vertical scale is ~ 500 pc from Earth and has a total integrated flux above 1 TeV of ~ 6 times the Crab Nebula.

Extended gamma-ray luminous SNRs can however be detected by MILAGRO [300] with its larger field of view. A survey in galactic longitude $l \in [30^\circ, 220^\circ]$ and latitude $b \in [-10^\circ, 10^\circ]$ has revealed 6 new sources at a median energy of 20 TeV, several of which are spatially extended. The flux from a SNR of the above luminosity at $L = 2$ kpc is $Q_\gamma^0/(4\pi d^2) \simeq 1.2 \times 10^{-11} \text{ TeV}^{-1} \text{ cm}^{-2} \text{ s}^{-1}$ at 1 TeV. Scaled with a spectral index of 2.4 to 20 TeV, this gives $Q_\gamma^0/(4\pi d^2) 20^{-2.4} \simeq 9.0 \times 10^{-15} \text{ TeV}^{-1} \text{ cm}^{-2} \text{ s}^{-1}$ which is in the range of the unidentified MILAGRO sources [300]. We note that the MILAGRO source MGRO J1908+06 was recently confirmed by HESS [301], though with a smaller angular extent of $\sim 0.7^\circ$. However, correlating unidentified MILAGRO sources with the FERMI Bright Source List [302, 303] seems to favour associations with pulsars, although several new unidentified extended sources have also been found.

Hadronic sources of cosmic rays should also be visible by their neutrino emission. On general grounds, the neutrino luminosity (from π^\pm decay) can be directly related to the gamma-ray luminosity (from π^0 decay) and should be of the same order of magnitude since p-p interactions produce π^+ , π^0 and π^- in roughly equal numbers. Each of the three neutrinos produced in the decay chains $\pi^+ \rightarrow \mu^+ \nu_\mu \rightarrow e^+ \nu_e \bar{\nu}_\mu \nu_\mu$ and $\pi^- \rightarrow \mu^- \bar{\nu}_\mu \rightarrow e^- \bar{\nu}_e \nu_\mu \bar{\nu}_\mu$ carries about half of the energy of each photon produced in the decay $\pi^0 \rightarrow \gamma\gamma$. Hence, the ratio of neutrinos to photons produced on average is $\sim 3 : 1$ and the total neutrino luminosity is

$$Q_{\text{all } \nu}(E_\nu) \simeq 6 Q_\gamma(2E_\nu) \simeq 6 \times 2^{-\gamma} Q_\gamma^0 \left(\frac{E_\nu}{\text{TeV}} \right)^{-\gamma}.$$

Presently the largest cosmic neutrino detector is the IceCube observatory [246] under construction at the South Pole. IceCube observes high energy neutrinos via their interactions with nucleons in the vicinity of the detector and subsequent Čerenkov light emission of energetic charged particles in the transparent glacial ice. The most important signal for neutrino astronomy is the Čerenkov radiation by muons produced via charged current interactions of muon neutrinos. Since the muon inherits the large boost of the initial neutrino the point source resolution is $\sim 1^\circ$. The large background signal of atmospheric muons is efficiently reduced for upward-going muons, i.e. neutrino sources which are somewhat below the horizon. Hence, IceCube is mainly sensitive to neutrino point sources in the northern sky, which excludes SNRs in the direction of the galactic centre.

Neutrino emission associated with galactic TeV gamma-ray sources has been investigated by many authors [304, 305, 306, 307, 308, 309, 310, 311, 312] including also the HESS sources used in our analysis. In particular, Ref. [308] investigates the prospects of neutrino detection for the SNRs HESS J0852.0–463, J1713–381, J1804–216, J1834–087 (see Table 2.2) in the proposed KM3NeT detector in the Mediterranean which will see the galactic centre region. The muon neutrino rate is expected to be a few events per year for such sources.

Due to flavour oscillations of neutrinos with large mixing angles, the initial flavour composition $Q_{\nu_e} : Q_{\nu_\mu} : Q_{\nu_\tau} \simeq 1 : 2 : 0$ from pion decay is expected to become $\sim 1 : 1 : 1$ at Earth. The TeV muon neutrino point flux from a hadronic gamma-ray source located at a distance L and with a

power-law index $\gamma \simeq 2.4$ is thus $F_{\nu_\mu}(> 1 \text{ TeV}) \simeq 2^{1-\gamma} F_\gamma(> 1 \text{ TeV})$, hence

$$F_{\nu_\mu}(> 1 \text{ TeV}) \simeq 3.2 \times 10^{-12} \left(\frac{L}{2 \text{ kpc}} \right)^{-2} \text{ cm}^{-2} \text{ s}^{-1}. \quad (2.71)$$

This should be compared to the results of searches for neutrino point sources in the northern sky, in particular the close-by SNR Cassiopeia A (see Table 2.2), using data taken with AMANDA-II (the predecessor of IceCube) during 2000–2006 [313] and, more recently, with the first 22 strings of IceCube during 2007–08 [314]. The average 90% C.L. upper limit on the integrated ν_μ flux in the energy range 3 TeV to 3 PeV is [314]

$$F_{\nu_\mu} \leq 4.7 \times 10^{-12} \text{ cm}^{-2} \text{ s}^{-1}, \quad (2.72)$$

i.e. still above $\sim 7 \times 10^{-13} \text{ cm}^{-2} \text{ s}^{-1}$ expected from a SNR at 2 kpc, assuming $\gamma = 2.4$.

The full 80 string configuration of IceCube thus has excellent prospects to identify these SNRs. A point source in the northern sky with an E^{-2} muon neutrino flux,

$$F_{\nu_\mu} \simeq 7.2 \times 10^{-12} \text{ cm}^{-2} \text{ s}^{-1}, \quad (2.73)$$

in the TeV-PeV range can be detected with a 5σ significance after three years of observation. This does depend somewhat on the spectral index and energy cut-off, since the signal (after “level 2 cuts”) peaks at an energy of $\sim 10 \text{ TeV}$ [246]. As mentioned previously, our analysis predicts on average ~ 3 nearby gamma-ray sources stronger than Crab with corresponding muon neutrino fluxes larger than $\sim 7 \times 10^{-12} \text{ cm}^{-2} \text{ s}^{-1}$. Note that although the galactic centre is not in the field of view of IceCube, SNRs following the spiral arm structure of the Galaxy are expected to be detected also in the galactic anti-centre direction, as seen in the example distribution shown in the bottom panel of Fig. 2.9.

2.7. Comments on the Time-Dependent Picture

It was recently questioned [315] whether the acceleration of secondaries also holds true in the time-dependent picture of DSA. Intuitively, one would expect that the energy-dependence of the

diffusion coefficient still leads to an increase of the size of the diffusion zone and therefore to a harder spectrum for charged secondaries. The authors of [315] however argue that both numerical simulations and a simple analytical argument show that the secondary fractions do not rise. In the following, we critically examine both these claims.

2.7.1. An analytical argument

The authors of [315] present a simple ‘gedankenexperiment’ which they claim shows that the acceleration of secondary mechanism does not lead to a rise in any secondary-to-primary ratio. The argument compares the flux of secondaries produced and accelerated in the SNR to the flux of primaries in the case where no secondaries get produced (which would be the case, for example for $n_{\text{gas}} = 0$). For the particular case of the anti-proton fraction, assuming that in an inelastic pp collision, the anti-proton produced takes all the energy of the incoming proton, the interactions would in fact only convert part of the proton flux into an anti-proton flux. As both particles are affected in the same way by DSA, the total anti-proton spectrum would be proportional to the proton spectrum in a secondary-less case.

This comparison is however not appropriate. What needs to be compared with the proton spectrum f_p^* in a secondary-less case is not the antiproton flux $f_{\bar{p}}$ but the *sum* of the proton and antiproton flux ($f_p + f_{\bar{p}}$) for the case with secondaries. If the assumptions about the inelasticity being 100% were in fact correct, the sum of antiproton and proton flux ($f_p + f_{\bar{p}}$) should indeed be comparable to the proton flux f_p^* . This, however, does not tell us anything about the individual spectra, f_p and $f_{\bar{p}}$. In fact, the hardness in the antiproton spectrum, $f_{\bar{p}} \propto pf_p^*$ would be balanced by a softer proton spectrum $f_p = (1 - \kappa(p/p_{\text{cr}}))f_p^*$ where p_{cr} is the momentum at which $f_p = f_{\bar{p}}$ and κ is a normalisation constant. Therefore, the antiproton-to-proton ratio, $f_{\bar{p}}/f_p$ would become even harder and in this sense our above argument is conservative in that it ignores the $-pf_p^*$ reduction in the proton flux. However, for the case of antiprotons, the latter correction is negligible as $f_p \gg f_{\bar{p}}$, i.e. $p_{\text{cr}} \gg p_{\text{max}}$.

2.7.2. The numerical model

The authors of [315] further present the results of a Monte Carlo calculation of time-dependent DSA of electrons and protons including the production and subsequent acceleration of secondary

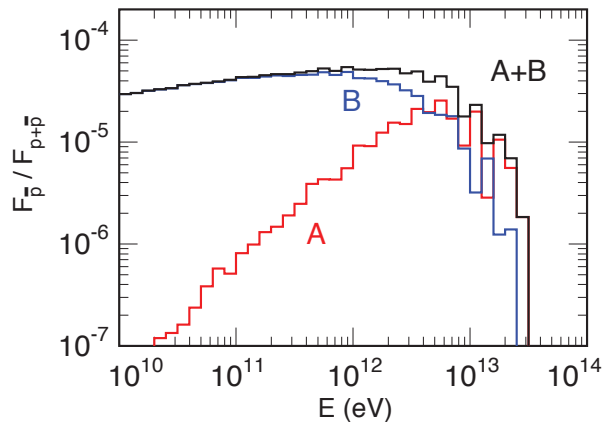


Figure 2.10.: Antiproton-to-proton ratio produced in a time-dependent Monte Carlo calculation of diffusive shock acceleration in the test particle approximation (from [315]). The red (A) and blue (B) lines denote the ratio from the secondaries which have been produced upstream and downstream, respectively, and the black line (A+B) is the sum of both.

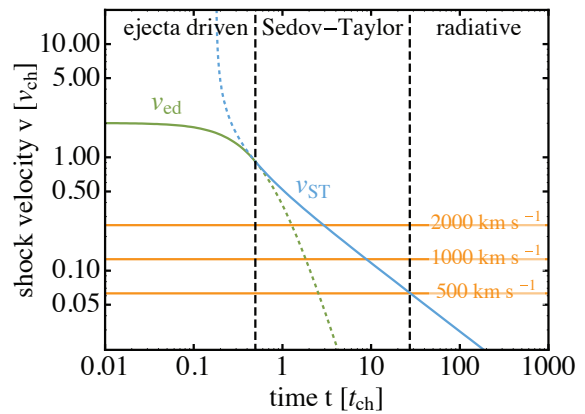


Figure 2.11.: Shock velocity of the SNR as a function of time, both in units of values characteristic for a particular SNR model, see [79]. The blue solid and green solid lines show the analytical model of [79] for the ejecta-driven (ed) and the Sedov-Taylor (ST) phase, respectively. The effective value for the shock velocity adopted in our calculation is 500 km s^{-1} .

antiprotons and positrons. Although the secondary-to-primary ratios of the total spectra $N(p) \propto \int dV p^2 f(p)$ clearly show the presence of a harder component compared to the primary one, the former one seems to be subdominant and not influence the total spectra too much. This is shown in their Fig. 2 which we here reproduce in Fig. 2.10.

However, we believe that this discrepancy is merely due to a different set of parameters adopted. As shown in Eq. 2.8, the normalisation of the harder component depends on the diffusion coefficient D , the velocity of the shock front squared, u_1^2 and the gas density n_{gas} through q_{\pm} . Not only is the value of the diffusion coefficient in [315], D_{Bohm} , smaller than the one adopted in our calculation, $K_B D_{\text{Bohm}}$ with $K_B \sim 20$, but also is the velocity larger: The dynamical SNR model adopted [79] predicts a time-dependent velocity, both for the free expansion and in the Sedov-Taylor phase of a SNR. Our time-independent analysis, however, needs to adopt an *effective* velocity. As we show in Fig. 2.11, the time-dependent velocity is higher than our effective value most of the time. As the velocity enters as the inverse square into the normalisation of the harder component, a small difference in velocity can change the relative importance rather drastically.

We therefore conclude that the discrepancy between our analytical result and the outcome of

the Monte Carlo calculation performed in [315] is most likely due to different parameters for the adopted SNR model. We note that it has not been shown that the time-dependence introduces any additional physical effects to the time-independent picture discussed above.

The true value of the parameters is, however, a separate issue. One possibility, in fact the one pursued in [315], is to adopt an (analytic) model of the SNR dynamics that is believed to reflect the physical behaviour of actual SNRs and feed it into a numerical calculation of the secondary spectra. However, even the parameters of the analytical model are affected by uncertainties. Therefore, one needs to consider different SNR models to cover all possibilities of effects.

Another possibility is to adopt the simplest analytical picture possible, like the simple time-independent test particle approximation above, and to treat the parameters, e.g. diffusion coefficient, velocities, maximum energy, as effective ones. As explained above, these effective values only enter the normalisation in a certain combination. Choosing a value that allows to reproduce measured data, i.e. basically fitting these parameters to the data, allows to make independent, testable predictions for other observables. We have followed this approach already for the charged lepton channels in Sec. 2.4, and we will further use this approach for nuclear secondary-to-primary ratios in Chapter 3.

2.8. Alternative Astrophysical Explanations

We have already addressed the possibility of DM annihilation or decay accounting for the excesses in the positron fraction and total electron-positron flux. Furthermore, we have discussed some of the constraints, for example, from antiprotons, radio waves and gamma-rays, and we have argued that a large fraction of the parameter space necessary to explain the leptonic anomalies are already ruled out.

To round off our discussion of the acceleration of secondaries in old SNRs, we present some alternative astrophysical explanations that have been claimed to explain the excesses.

2.8.1. Pulsars

The idea that pulsars might be responsible for the lepton excess [123, 124] has been around since the first indications of a rise in the positron fraction [316]. Pulsars are highly-magnetised and

quickly spinning neutron stars that transfer (part of) their rotational energy into a magnetised wind. Electrons are accelerated to very high energies by the electric fields present and synchrotron-radiate gamma-rays in the extreme ambient magnetic fields. These gamma-rays are energetic enough to pair-produce high energy electrons and positrons on the ambient magnetic fields or the thermal X-rays from the pulsar itself. The high energy gamma-ray emission is usually interpreted as curvature radiation or ICS from high-energy electrons and positrons. There is disagreement about where exactly the gamma-ray emission is produced: close to the surface of the neutron star (polar cap models) or further away in the light cylinder along the last open field lines (outer/slot gap models).

The total output in electrons and positrons is usually connected to the spin-down power of the pulsar and with an efficiency of a few per cent, most of the pulsars in the ATNF catalogue [317] are predicted to provide outputs of $10^{46...50}$ erg. In fact, probably only mature pulsars, i.e. with ages $\gtrsim 10^5$ yr, can inject electrons and positrons into the ISM as for younger ones all charged particles are trapped inside the pulsar wind nebula (PWN). The spectral index α of the electrons and positrons can be estimated from radio emission interpreted as synchrotron ($\gamma = 1 \dots 1.6$) or from the gamma-rays ($\gamma = 1.4 \dots 2.2$). The range usually considered is $\gamma = 1.4 \dots 2.2$.

As already mentioned, the idea was first developed in Ref. [123], stressing the importance of young and nearby pulsars for the electron-positron flux and the positron fraction at high energies and suggesting Geminga as one of these possible sources. The positron excess can be reproduced for a few mature, nearby pulsars, e.g. Geminga and Monogem, complemented by a distribution of pulsars further away [318]. This is supported by [170] where it is concluded that the scenario with a single pulsar is disfavoured. Other authors focus on the one-source model [319] although this might require too high an efficiency for the conversion of spin-down power into electrons and positrons. It was also shown that the sum of all pulsars covering a broad range of parameters can reproduce the Fermi-LAT and PAMELA data [185].

The way to pinpoint to a (few) pulsar(s) as the origin of the lepton excesses suggested is to look for anisotropies in the arrival directions of electrons and positrons, e.g. with Fermi-LAT. A simple estimate of the anisotropy shows that most favoured scenarios could be detected within a few years time to 2 or 3σ significance [318, 170]. Nearby pulsars as the source of the positrons are of course quite consistent with the absence of antiprotons.

2.8.2. GRBs

Any astrophysical positron source with an injection distinctively harder than the primary electrons from SNRs can in principle explain the PAMELA positron excess. It was recently suggested [320] that a galactic gamma-ray burst (GRB) could be such a source. The GeV electrons and positrons would be pair-produced by scattering of TeV gamma-rays on the afterglow eV background. The energy contained in TeV gamma-rays is about 5% of the total GRB energy, typically $\sim 10^{50}$ erg and the spectral index of the electron-positron pairs is 1.8 ± 0.7 [320].

In fact, an injection of $\mathcal{O}(10^{50})$ erg a few times 10^5 yr ago and with a spectral index between 1.6 and 2.2 nicely fits the data. A harder spectral index can also reproduce a ATIC/PPB-BETS-like feature in the total electron-positron flux while a softer index is in agreement with the Fermi-LAT data. If in fact a GRB or another singular event of similar characteristics (pulsar, hard SNR, microquasar) was responsible for the lepton excesses one would again expect to see a rather large anisotropy in electron and positron fluxes which would be detectable by Fermi-LAT or AMS-02 [321] in a few years' time [320].

2.8.3. Very old supernova remnants

Another idea [322] invokes dense gas clouds around very old SNRs as sites of a production of harder positrons. The authors consider several simultaneous SN explosions $10^{5\cdots 6}$ yr ago inside a dense gas cloud that need to have taken place only hundreds of parsecs from the solar system but could explain the local bubble or other similar structures like Loop I [323, 324]. Once the Sedov-Taylor phase is coming to an end, the compression ratio r (see Sec. 1.2.3) is not given by the Rankine-Hugoniot relation any more but by the ratio of shock velocity and upstream Alfvén velocity, $r \sim \sqrt{2}v_s/v_A$, and is much larger than 4. The spectral index γ of the protons accelerated by DSA is therefore smaller than 2 and the interaction of the protons with the gas in the surrounding cloud produces positrons of a similarly hard spectrum.

For gas clouds of tens of parsecs radius and $\sim 100 \text{ cm}^{-3}$ density, both the positron fraction and, depending on the exact value of the proton spectral index γ considered, even the Fermi-LAT or ATIC/PPB-BETS total electron-positron spectrum can be fitted. However, the maximum proton energy assumed is 100 TeV – a somewhat unrealistic situation, given that such high energy protons

can only be accelerated in the Sedov-Taylor phase when the magnetic field amplification is strong and even the highest energy particles are confined to the shock region.

The model predicts a similar rise in the antiproton-to-proton ratio, due to the contributions from antiprotons produced in a similar manner. Testing this model by the boron-to-carbon ratio might not be conclusive, as the metallicity can vary throughout the Galaxy.

2.8.4. Inhomogeneous source distribution

We have already alluded to the suggestion that the inhomogeneous distribution of SNRs in the galactic disk is responsible for the rise in the positron fraction [271]. The idea is that the SNR density in the spiral arms is amplified by a factor of 4 with respect to the disk, and the propagation cut-off from the nearest spiral arm at ~ 1 kpc leads to a softening of the primary electron spectrum. The secondary production is spatially more homogeneous because it follows the cosmic ray proton density and is therefore not affected by the details of the source distribution. The softening of the electron spectrum therefore leads to a rise in the positron fraction.

While we agree with the call for a realistic source distribution, we argued above in detail that its effect is only to be seen at hundreds of GeV. In particular, we expect the propagation cut-off from sources at distances of ~ 1 kpc to occur at $\mathcal{O}(1)$ TeV, i.e. more than a magnitude *above* the energies at which the positron fraction starts rising. This disagreement can be traced back to propagation parameters used in [271] that are rather unrealistic. In particular, the diffusion coefficient adopted, $D(E) = 6 \times 10^{27} \text{ cm}^2 \text{ s}^{-1}$, is too low and the energy loss rate at 1 GeV, $b_0 = 1.8 \times 10^{-16} \text{ GeV}^{-1} \text{ s}^{-1}$ too high, which strongly affects the diffusion-loss length ℓ^2 , see Eq. 1.48. In addition, the predicted soft electron spectrum seems to be in disagreement with preliminary PAMELA data on the absolute electron flux [164].

2.9. Conclusion

Supernova remnants have long been suspected to be the sources of galactic cosmic rays. We have discussed a recent proposal [243] that proton-proton interactions in the shocks of SNRs followed by the diffusive shock acceleration of the secondary positrons produced can flatten the spectrum of the secondaries relative to that of the primaries. These hard spectra may be the origin of the

recently observed cosmic ray “excesses” — both the e^+ fraction observed by PAMELA [163] and the $e^- + e^+$ flux measured by Fermi-LAT [169] and HESS [186, 192].

We have investigated how gamma-ray emission of SNRs — assumed to be of the same hadronic origin as the positrons — together with cosmic ray data, constrain the acceleration of positrons. We have accounted for the spatial and temporal discreteness of SNRs via a Monte Carlo exercise, drawing samples from a realistic galactic distribution with the observed SN rate. For the diffusion parameters we have adopted standard values derived from cosmic ray nuclear-to-primary ratios, as well as the energy densities of galactic radiation and magnetic fields.

We have compiled a list of all gamma-ray emitting SNRs observed by HESS and determined the mean value of the flux, which fixes the hadronic interaction rate in the SNR. Low energy data from PAMELA on the absolute e^- flux were used to normalize the primary flux of e^- . The contribution from accelerated e^+ was then found by fitting the $e^- + e^+$ flux to Fermi-LAT and HESS data, adjusting the (only) free parameter K_B which determines the diffusion rate near SNR shocks.

The spectra of e^+ and e^- thus derived agree well with the e^+ fraction observed by PAMELA in the range 5 – 100 GeV. The apparent discrepancy at lower energies can be attributed to the uncertainty in solar modulation (charge-sign dependent or independent). Furthermore, convection and diffusive reacceleration of primary electrons that become important at these energies were neglected in our analysis. The flux of e^+ and e^- becomes dominated by the accelerated secondary component at high energies; the corresponding e^+ fraction levels out at ~ 0.4 , reflecting the relative multiplicity of e^+ and e^- produced by p-p interactions.

To be consistent with our overall framework the gamma-rays observed from SNRs have been assumed to be of hadronic origin. The known spatial distribution of SNRs then implies (on average) several nearby sources with a gamma-ray flux comparable to the Crab. We have speculated that some unidentified MILAGRO sources [300] might correspond to such old SNRs. Moreover, the same hadronic processes in SNRs will inevitably produce high energy neutrinos which can be detected in cubic-km telescopes such as IceCube [246]. The neutrino luminosity can be directly related to the gamma-rays and is not connected to the hypothetical acceleration of e^+ and e^- in the sources as in our present model. Nevertheless, similarly to the previous argument, we expect on average a few nearby sources, some of which may also lie within the field of view of IceCube and can thus be detected with high statistical significance after three years of data taking.

While our calculational framework is based on first-order Fermi acceleration by SNR shock waves, we have noted that in detail the observations do not fit the theoretical expectations, e.g. the shock compression ratio inferred from the observed gamma-ray spectrum ($\sim E^{-2.4}$) is 3.1 rather than 4 as is expected for a strong shock [276]. Going beyond the test particle approximation, the generic expectation in such a process is for particle spectra which are much flatter than those observed ($\sim E^{-1.4}$ and slightly *concave*), when the back reaction of the cosmic rays on the shock is taken into account [86]. By contrast, the observed radio spectrum of Cassiopeia A is slightly *convex* and this, as well as the morphology and time evolution of radio emission from such young SNRs, can be well explained in terms of *second-order* Fermi acceleration by plasma turbulence behind the shock wave [325]. Moreover the observed spatial correlation between the gamma-ray emission and the hard X-ray emission from some SNRs argues for a leptonic rather than hadronic origin and further observations are necessary to resolve this issue [326]. It has been argued that cosmic ray protons and nuclei may well have different sources (e.g. “superbubbles” formed by multiple supernovae) than the cosmic ray electrons [327]. The additional predictions made in this work concerning the visibility of hadronic accelerators in gamma-rays and neutrinos, tied to the expectations for the fluxes of the accelerated *secondary* positrons in cosmic rays, will hopefully enable further consistency tests of the SNR origin hypothesis for galactic cosmic rays.

3. Acceleration of Secondary Nuclei

3.1. Introduction

As we discussed in Chapter 2, there is a wealth of suggestions on how to explain the apparent excesses in the positron fraction and in the total electron-positron flux as measured by PAMELA and Fermi-LAT, respectively. In particular, we have devoted our analysis to the investigation of the acceleration of secondaries mechanism which can explain the excesses by considering the production and subsequent acceleration of secondary electrons and positrons in the cosmic ray sources, i.e. supernova remnants (SNRs). This process is guaranteed in the sense that secondary particles will necessarily be generated by the spallation of primary cosmic rays on ambient matter in the sources. As discussed above, the crucial point is the normalisation of this harder component which depends on many parameters that are not directly accessible to observations, for example, the ambient gas density. One parameter in particular, the diffusion coefficient in the cosmic ray source, plays an important role in determining the relative size of the effect of acceleration of secondaries.

One possible way to resolve this problem is to determine the normalisation from other observables. If it is in fact acceleration of secondaries that leads to a rise in the positron fraction then both the ambient density and the diffusion coefficient are large enough such that other secondaries are produced in equally important abundances and also get accelerated. Therefore, we should see similar features of a rise in other secondary-to-primary ratios. We will use observations of such observables as the antiproton-to-proton ratio, titanium-to-iron (Ti/Fe) and boron-to-carbon (B/C) to determine the normalisation of the harder electron-positron component and thereby test the model of the acceleration of secondaries.

In particular, nuclear secondary-to-primary ratios like B/C not only allow us to test this particular model but also to discriminate it against other explanations of the rise in the positron fraction

Table 3.1.: Truth table representing the logical possibilities to explain rises in different secondary-to-primary ratios.

observed rise in			possible explanation		
e^+/e^-	\bar{p}/p	nuclei	DM	pulsars	accn. of secs.
t	t	t	f	f	t
t	t	f	t	f	f
t	f	t	f	f	f
t	f	f	t	t	f

e^+/e^- , e.g. dark matter annihilation or decay (see Sec. 1.3.1) and pulsars (see Sec. 2.8). For instance, if a feature similar to the rise in the positron fraction was also observed in the antiproton-to-proton ratio \bar{p}/p , this would rule out¹ the pulsar explanation of the positron excess as pulsars are not expected to produce any antiprotons. Conversely, and as such a rise is not observed up to the maximum energies of current observations, ~ 130 GeV [149], this sets some constraints on models which in principle predict such a rise in \bar{p}/p . There have, however, been efforts to build dark matter (DM) models that are leptophilic, that is DM predominantly annihilating or decaying into leptons, see Sec. 1.3.1. Similarly, a rise in nuclear secondary-to-primary ratios, like B/C would rule out the DM explanation of the positron excess as DM annihilation/decay should not produce nuclei. Again, the non-observation of such a rise up to energies higher than currently accessible, would in turn rule out the acceleration of secondaries model². These relations are summarised in Table 3.1.

3.2. Antiproton-to-Proton Ratio

The calculation for the antiproton-to-proton ratio [295] is conceptually very similar to that for the positron fraction. Of course, both the production cross section and the inelasticity are different for antiprotons than for positrons. Furthermore, as both protons and antiprotons are stable and their energy losses are negligible above a few GeV, their fluxes can be calculated in the simple leaky box

¹There is a caveat: If in fact neither a dark matter model nor the acceleration of secondaries could explain the full positron excess when fitted to the potential \bar{p}/p feature there might still be room for a contribution from pulsars.

²The acceleration of secondaries model could be saved by arguing that GCR protons and heavier nuclei are produced by different source populations and that the acceleration of secondaries only plays a role in the sources of protons.

model with a grammage parametrised similarly as in Sec. 1.2.7,

$$X_{\text{esc}}(E) = X_0 \left(\frac{E}{10 \text{ GeV}} \right)^{-\delta}, \quad (3.1)$$

with $X_0 = 6 \text{ g cm}^{-2}$ and $\delta = 0.6$. Above 10 GeV, solar modulation is negligible, too.

The antiproton-to-proton ratio now has two contributions: the usual one from the antiprotons produced in spallation of GCR nuclei on the ISM,

$$\frac{J_{\bar{p},ISM}(E)}{J_p(E)} \simeq \frac{2\varepsilon X_{\text{esc}}(E)}{m_p E^{2-a-\delta}} \int_E^\infty dE_0 E_0^{2-a-\delta} \sigma_{p\bar{p}}(E_0, E), \quad (3.2)$$

and one from the antiprotons produced inside the SNRs,

$$\frac{J_{\bar{p},SNRs}(E)}{J_p(E)} \simeq 2 n_1 c [\mathcal{A}(E) + \mathcal{B}(E)], \quad (3.3)$$

where

$$\mathcal{A}(E) = a \left(\frac{1}{\xi} + r^2 \right) \times \int_m^E d\omega \omega^{a-3} \frac{D_1(\omega)}{u_1^2} \int_\omega^{E_{\text{max}}} dE_0 E_0^{2-a} \sigma_{p\bar{p}}(E_0, \omega) \quad (3.4)$$

is from antiprotons produced in the diffusion zone and

$$\mathcal{B}(E) = \frac{\tau_{\text{SNR}} r}{2 E^{2-a}} \int_E^{E_{\text{max}}} dE_0 E_0^{2-a} \sigma_{p\bar{p}}(E_0, E). \quad (3.5)$$

is from the antiprotons produced downstream. Here, $r = 3.8$ is the compression ratio of the shock chosen such that the proton's source spectral index in phase space $a = 3r/(r-1) \simeq 4.1$. The inelasticity of the antiproton production $\xi \simeq 0.17$, the SNR lifetime $\tau_{\text{SNR}} = 10^4 \text{ yr}$, the upstream velocity $u_1 = 0.5 \times 10^8 \text{ cm s}^{-1}$ and the fudge factor $K_B = 20$ in the diffusion coefficient $D = 3.3 \times 10^{22} K_B (E/\text{GeV})^\delta \text{ cm}^2 \text{ s}^{-1}$. The maximum energy is fixed to $E_{\text{max}} = 10 \text{ TeV}$ and for the production cross section $\sigma_{p\bar{p}}$ a parametrisation [112] is used. The factor $\varepsilon \simeq 1.26$ takes into account the contribution from CR nuclei and nuclei in the ISM on the production of antiprotons. We reproduce the antiproton-to-proton ratio calculated in Ref. [295] in Fig. 3.1.

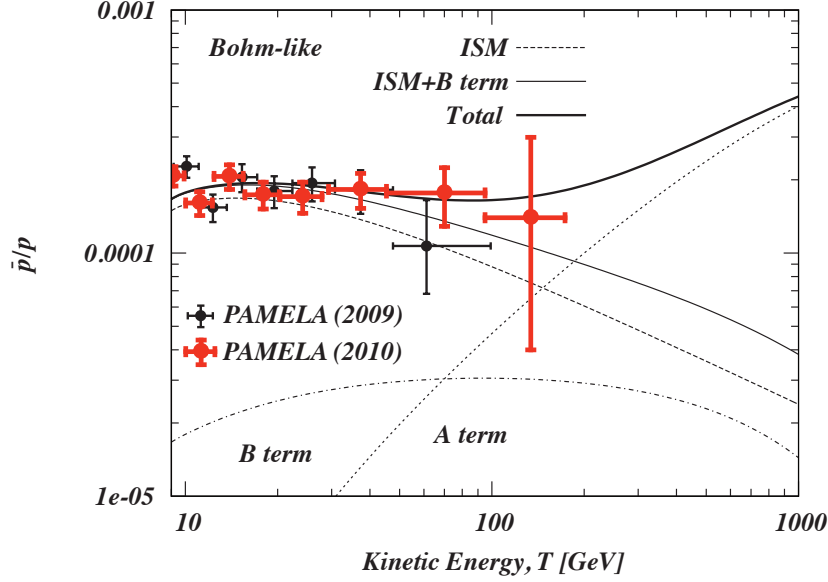


Figure 3.1.: The antiproton-to-proton ratio (adapted from [295]). The \mathcal{A} term (dotted line) and \mathcal{B} term (dot-dashed line) are the secondaries produced in the diffusion zone and in the downstream region, respectively. The data points are from PAMELA measurements [328, 149]. The antiprotons produced by spallation of GCR nuclei on the ISM are shown by the dashed line. The sums of \mathcal{B} term and ISM contribution do not show a qualitatively different behaviour than the ISM contribution alone. The \mathcal{A} term finally leads to the upturn in the total antiproton-to-proton ratio.

3.3. Nuclear Secondary-to-Primary Ratios

3.3.1. Timescales of the problem

The transport equation for any nuclear species i reads

$$u \frac{\partial f_i}{\partial x} = D_i \frac{\partial^2 f_i}{\partial x^2} + \frac{1}{3} \frac{du}{dx} p \frac{\partial f_i}{\partial p} - \Gamma_i f_i + q_i, \quad (3.6)$$

where f_i is the phase space density and the different terms from left to right describe convection, spatial diffusion, adiabatic energy losses as well as losses and injection of particles from spallation or decay. We consider the acceleration of *all* species in the usual setup: in the frame of the shock front the plasma upstream ($x < 0$) and downstream ($x > 0$) is moving with velocity u_- and u_+ respectively. We solve Eq. 3.6 analytically for relativistic energies ε_k greater than a few GeV/nucleon such that $p \approx E$, $\beta \approx 1$ and $N_i dE \approx 4\pi p^2 f_i dp$. At these energies ionization losses can be neglected and the spallation cross sections become energy independent.

There are three relevant timescales in the problem:

1. Acceleration time τ_{acc} (cf. [86]):

$$\tau_{\text{acc}} = \frac{3}{u_- - u_+} \int_0^p \left(\frac{D_i^+}{u_+} + \frac{D_i^-}{u_-} \right) \frac{dp'}{p'} \simeq 8.8 E_{\text{GeV}} Z^{-1} B_{\mu\text{G}} \text{ yr} \quad (3.7)$$

for Bohm diffusion and the parameter values mentioned later.

2. Spallation and decay time τ_i .

$$\tau_i^{\text{spall}} \equiv 1/\Gamma_i^{\text{spall}} \sim 1.2 \times 10^7 \left(\frac{n_{\text{gas}}}{\text{cm}^{-3}} \right)^{-1} \text{ yr.} \quad (3.8)$$

where an average σ_i of $\mathcal{O}(100)$ mb has been assumed. The rest lifetime τ_i^{dec} of the isotopes considered ranges between 4×10^{-2} yr and 10^{17} yr.

3. Age of the SNR under consideration (see Sec. 2.2)

$$\tau_{\text{SNR}} = x_{\text{max}}/u_+ \sim 2 \times 10^4 \text{ yr.} \quad (3.9)$$

There are two essential requirements for a SNR to efficiently accelerate nuclei by the DSA mechanism:

- (a) $\tau_{\text{acc}} \ll \tau_i^{\text{spall}}$, which is equivalent to

$$20 \frac{\Gamma_i^- D_i}{u_-^2} \ll 1 \quad \Rightarrow \quad \epsilon_k \ll 6.4 \times 10^5 \frac{Z_i}{A_i} B_{\mu\text{G}} \text{ GeV.} \quad (3.10)$$

- (b) $\tau_{\text{SNR}} \ll \tau_i$ which implies,

$$\frac{x_{\text{max}}}{u_+} \ll \frac{1}{\Gamma_i} \quad \Rightarrow \quad x \frac{\Gamma_i}{u_+} \ll 1. \quad (3.11)$$

The isotopes for which condition (b) is not satisfied at the lowest energy considered viz. ^{56}Ni , ^{57}Co , ^{55}Fe , ^{54}Mn , ^{51}Cr , ^{49}V , ^{44}Ti and ^7Be do *not* contribute significantly, so their decays in the source region are neglected.

3.3.2. Nuclear spectra at source

We find that the general solution to Eq. 3.6 for $x \neq 0$ is

$$f_i^\pm = \sum_{j \leq i} \left(E_{ji}^\pm e^{\lambda_j^\pm x/2} + F_{ji}^\pm e^{\kappa_j^\pm x/2} \right) + G_i^\pm, \quad (3.12)$$

$$\text{with } \lambda_i^\pm = \frac{u_\pm}{D_i^\pm} \left(1 - \sqrt{1 + 4D_i^\pm \Gamma_i^\pm / u_\pm^2} \right),$$

$$\kappa_i^\pm = \frac{u_\pm}{D_i^\pm} \left(1 + \sqrt{1 + 4D_i^\pm \Gamma_i^\pm / u_\pm^2} \right),$$

where G_i^\pm is the asymptotic value and E_{ji}^+ and F_{ji}^- are determined by the recursive relations:

$$E_{ji}^\pm = \frac{-4 \sum_{m \geq j} E_{mj}^\pm \Gamma_{j \rightarrow i}^\pm}{D_i^\pm \lambda_j^{\pm 2} - 2u \lambda_j^\pm - 4\Gamma_i^\pm}, \quad (3.13)$$

$$F_{ji}^\pm = \frac{-4 \sum_{m \geq j} F_{mj}^\pm \Gamma_{j \rightarrow i}^\pm}{D_i^\pm \kappa_j^{\pm 2} - 2u \kappa_j^\pm - 4\Gamma_i^\pm}. \quad (3.14)$$

We require that the phase space distribution function converges to the adopted primary composition Y_i (at the injection energy p_0) far upstream of the SNR shock:

$$f_i(x, p) \xrightarrow{x \rightarrow -\infty} Y_i \delta(p - p_0), \quad \partial f_i / \partial x(x, p) \xrightarrow{x \rightarrow -\infty} 0. \quad (3.15)$$

We also require the solution to remain finite far downstream. As the phase space density is continuous at the shock front, we connect the solutions in both half planes to $f_i^0 = f_i(x = 0, p)$ and find them to be:

$$f_i^- = f_i^0 e^{\kappa_i^- x/2} + \sum_{j < i} F_{ji}^- \left(e^{\kappa_j^- x/2} - e^{\kappa_i^- x/2} \right) + Y_i \delta(p - p_0) \left(1 - e^{\kappa_i^- x/2} \right), \quad (3.16)$$

$$f_i^+ = f_i^0 e^{\lambda_i^+ x/2} + \sum_{j < i} E_{ji}^+ \left(e^{\lambda_j^+ x/2} - e^{\lambda_i^+ x/2} \right) + G_i^+ \left(1 - e^{\lambda_i^+ x/2} \right). \quad (3.17)$$

Using Eqs. 3.10-3.11, we can linearly expand λ_i^+ and κ_i^- in Eq. 3.13 and the exponentials in Eqs. 3.16-3.17,

$$e^{\lambda_i^+ x/2} \simeq 1 - \frac{\Gamma_i^+}{u_+} x, \quad e^{\kappa_i^- x/2} \simeq \left(1 + \frac{\Gamma_i^-}{u_-} x \right) e^{u_- x / D_i} \quad (3.18)$$

to obtain:

$$f_i^+ = f_i^0 + \frac{q_i^+(x=0) - \Gamma_i^+ f_i^0}{u_+} x. \quad (3.19)$$

where q_i^\pm denotes the downstream/upstream source term: $q_i^\pm = \sum_{j<i} f_j \Gamma_{j \rightarrow i}^\pm$.

Finally we integrate the transport equation over an infinitesimal interval around the shock, assuming that $q_i^+/q_i^- = \Gamma_i^+/\Gamma_i^- = n_{\text{gas}}^+/n_{\text{gas}}^- = r$ and that $D_i^+ \simeq D_i^-$:

$$p \frac{\partial f_i}{\partial p} = -a f_i^0 - a(1+r^2) \frac{\Gamma_i^- D_i^-}{u_-^2} f_i^0 + a \left[(1+r^2) \frac{q_i^-(x=0) D_i^-}{u_-^2} + Y_i \delta(p-p_0) \right], \quad (3.20)$$

where $a = 3r/(r-1)$. This is readily solved by

$$f_i^0(p) = \int_0^p \frac{dp'}{p'} \left(\frac{p'}{p} \right)^a e^{-a(1+r^2)(D_i^-(p) - D_i^-(p')) \Gamma_i^- / u_-^2} \times a \left[(1+r^2) \frac{q_i^-(x=0) D_i^-(p')}{u_-^2} + Y_i \delta(p' - p_0) \right]. \quad (3.21)$$

The Eqs. 3.19-3.21 should be compared to Eqs. 2.5-2.8 in Sec. 2.2 where the loss terms $\Gamma_i f_i$ for ionisation was not taken into account but cooling losses of the electrons and positron were introduced in an *ad hoc* fashion by an exponential cut-off at $E_{\text{cut}} \simeq 20$ TeV. This approach was justified for electrons and positrons as cooling losses have been shown to produce exactly such a functional behaviour with E_{cut} in the right range [329]. The exponential in our Eq. 3.21 leads to a natural cut-off in both the primary and secondary spectra above the energy predicted by Eq. 3.10. However, due to the approximations we have made, the secondary-to-primary ratios cannot be predicted reliably for $4\Gamma_i D_i / u^2 \gtrsim 0.1$, i.e. much beyond ~ 1 TeV.

Starting from the heaviest isotope, Eqs. 3.19 and 3.21 can be solved iteratively to obtain the injection spectrum after integrating over the SNR volume,

$$N_i(E) = 4\pi \int_0^{u+\tau_{\text{SN}}} dx p^2 f_i(p) 4\pi x^2. \quad (3.22)$$

3.3.3. Propagation of nuclei

To account for the subsequent propagation of the nuclei through the ISM we solve the transport equation in the leaky box model, see Sec. 1.2.6, which reproduces the observed decrease of

secondary-to-primary ratios with energy in the range $\sim 1 - 100$ GeV by assuming an energy-dependent residence time. The steady state cosmic ray densities \mathcal{N}_i observed at Earth are then given by recursion, starting from the heaviest isotope $i = 1$,

$$\mathcal{N}_i = \frac{\sum_{j < i} \left(\Gamma_{j \rightarrow i}^{\text{spall}} + 1/\varepsilon_k \tau_{j \rightarrow i} \right) \mathcal{N}_j + \mathcal{R}_{\text{SN}} N_i}{1/\tau_{\text{esc},i} + \Gamma_i}, \quad (3.23)$$

where $\mathcal{R}_{\text{SN}} \sim 0.03 \text{ yr}^{-1}$ is the Galactic supernova rate.

3.4. Parameters

We calculate the source densities N_i and ambient densities \mathcal{N}_i , taking into account all stable and metastable isotopes from ^{64}Ni down to $^{46}\text{Cr}/^{46}\text{Ca}$ for the Ti/Fe ratio, and from ^{18}O down to ^{10}Be for the B/C ratio. Short lived isotopes that β^\pm decay immediately into (meta)stable elements are accounted for in the cross-sections. The primary source abundances are taken from Ref. [142] and we have adopted an injection energy of 1 GeV independent of the species. The partial spallation cross-sections are from semi-analytical tabulations and the total inelastic cross-sections is obtained from an empirical formula [330, 331, 332]. The escape time is modelled according to the usual relation:

$$\tau_{\text{esc},i} = (\rho c)^{-1} X_{\text{esc},i} = (\rho c)^{-1} X_{\text{esc},i}^0 (E/Z_i)^{-\delta} \quad (3.24)$$

where $X_{\text{esc},i}$ is the column density traversed in the ISM and $\rho = 0.02 \text{ atom cm}^{-3}$ is the typical mass density of hydrogen in the ISM. We have neglected spallation on helium at this level of precision as its inclusion will have an effect $< 10\%$. The fit parameters are sensitive to the adopted partial spallation cross-sections, for example $\delta \simeq 0.7$ for the Ti/Fe ratio but ~ 0.6 for the B/C ratio.

The parameters are chosen as in Sec. 2.4.3: $r = 4$, $u_- = 0.5 \times 10^8 \text{ cm s}^{-1}$, $n_{\text{gas}}^- = 2 \text{ cm}^{-3}$ and $B = 1 \mu\text{G}$. The diffusion coefficient in the SNR is

$$D_i(E) = 3.3 \times 10^{22} K_B B_\mu^{-1} E_{\text{GeV}} Z_i^{-1} \text{ cm}^2 \text{ s}^{-1} \quad (3.25)$$

where the fudge factor K_B is the ratio of the diffusion coefficient to the Bohm value and is determined by fitting to the measured Ti/Fe ratio.

3.5. Results

The calculated Ti/Fe ratio together with relevant experimental data is shown in Fig. 3.2. The dashed line corresponds to the leaky box model with production of secondaries during propagation only and is a good fit to the (reanalysed) HEAO-3-C3 data [334]. The solid line includes production and acceleration of secondaries inside the source regions which results in an *increasing* ratio for energies above $\sim 50 \text{ GeV}/n$ and reproduces well the ATIC-2 data [333] taking $K_B \simeq 40$. This is somewhat higher than the value of $K_B = 10 \dots 20$ determined from a fit of the total electron-positron flux to the Fermi-LAT and HESS data (see Sec. 2.5). However, we note that the error bars in the ATIC-2 data are rather large and therefore the uncertainty in K_B is also. In fact, the 1σ and 2σ confidence intervals are $K_B \in [27, 66]$ and $K_B \in [2.7, 90]$, respectively. Therefore, the explanations for the rise in the positron fraction and the excess in the total electron-positron flux is consistent with the explanation for the rise in Ti/Fe. The value of $K_B \simeq 20$ is also consistent with the antiproton-to-proton ratio, see Sec. 3.2.

Fig. 3.3 shows the corresponding expectation for the B/C ratio with the diffusion coefficient scaled proportional to rigidity according to Eq. 3.25. The CREAM data [336] do show a downward trend as has been emphasized recently [339], but the uncertainties are still large so we await more precise measurements by PAMELA which has been directly calibrated in a test beam [340]. Preliminary data show indeed a rise above $\sim 100 \text{ GeV}$ see Fig. 3.3. Agreement with our prediction would confirm the astrophysical origin of the positron excess as proposed in Ref. [243] and Chapter 2 and thus establish the existence of an accelerator of hadronic cosmic rays within a few kpc.

3.6. Conclusion

We have presented a nice and interesting test of the proposed acceleration of secondaries that could in principle explain the GCR lepton excesses, by means of nuclear secondary-to-primary ratios. If we saw a rise in such ratios, this would clearly point at the importance of this effect, allow us to determine the normalisation and perform cross checks with the positron analysis. Furthermore, we would be able to extend our knowledge about the conditions prevailing in old supernova remnants, for example the level of magnetic turbulence, through this additional handle.

Unfortunately, at the moment, the experimental situation is not clear. Although ATIC-2 has

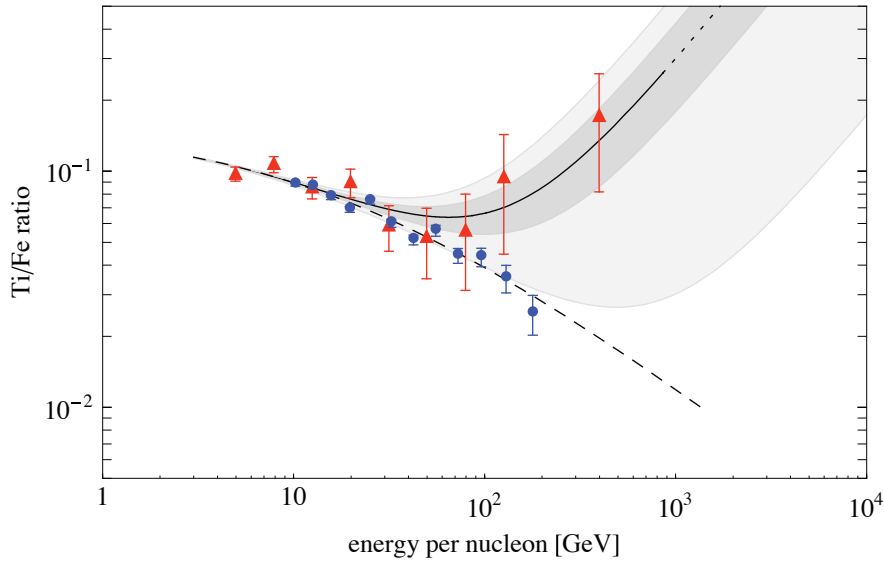


Figure 3.2.: The Ti/Fe ratio in cosmic rays along with model predictions — the ‘leaky box’ model with production of secondaries during propagation only (dashed line), and including production and acceleration of secondaries in a nearby source (solid line - dotted beyond the validity of our calculation) for $K_B = 40$ as determined by fitting to the ATIC-2 data; the 1σ and 2σ uncertainty bands are shown by the shaded dark grey and light grey areas, respectively. The data points are from ATIC-2 (triangles) [333] and HEAO-3-C3 (circles) [334].

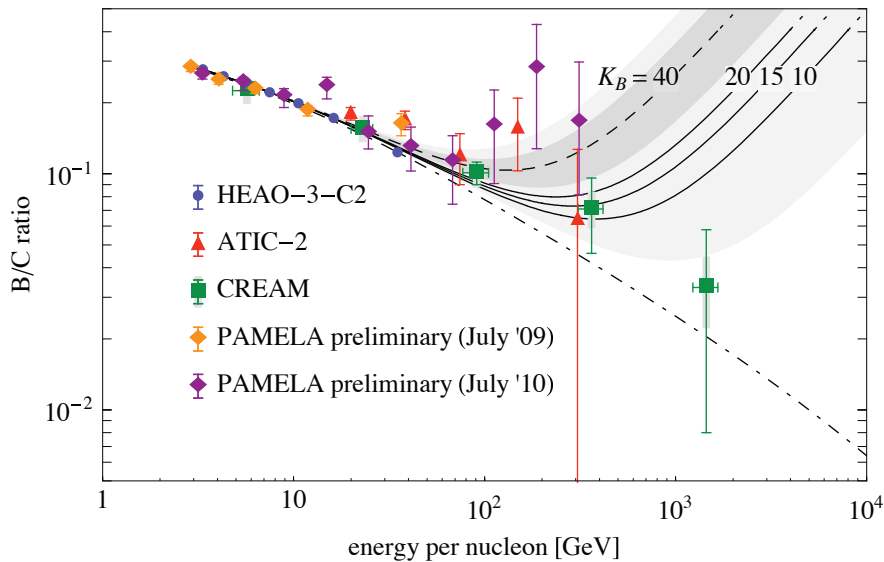


Figure 3.3.: The B/C ratio in cosmic rays along with model predictions — the ‘leaky box’ model with production of secondaries during propagation only (dot-dashed line), and including production and acceleration of secondaries in a nearby source (dashed line), 1σ (dark grey) and 2σ (light grey) uncertainty bands for $K_B = 40$ as determined from Ti/Fe; solid lines for $K_B = 10, 15$ and 20 as suggested by the electron-positron fit (see Sec. 2.5). The data points are from HEAO-3-C2 (circles) [142], ATIC-2 (triangles) [335], CREAM (squares) [336] and PAMELA (diamonds) [337, 338].

clearly observed a rise in Ti/Fe, the older HEAO-3-C3 data are in strong disagreement. Therefore, the ultimate test will be B/C for which the PAMELA experiment is continuously taking data and the official result of their analysis is therefore eagerly anticipated. Finally, the AMS-02 experiment [321] with its superior charge identification, broad energy range and improved statistics (due to the extension of the mission to 10 or even 18 years [341]) will clarify this issue once and for all.

4. Systematic effects in the extraction of the ‘WMAP haze’

4.1. Introduction

Local cosmic ray measurements are not the only possible probe of the galactic lepton population. Electrons and positrons of GeV and TeV energies produce synchrotron radiation and gamma-rays by scattering off the galactic magnetic fields and interstellar radiation fields (ISRFs), respectively. Therefore every contribution in addition to the standard electrons and positrons from supernova remnants (SNRs) must also reflect in galactic diffuse radio and gamma-ray backgrounds.

We have already mentioned the possibility to constrain dark matter (DM) models invented to explain the positron and electron-positron excesses by gamma-ray and radio measurements. The bounds on the annihilation cross section from diffuse measurements are at the moment still at least an order of magnitude above the expectation for a thermally produced weakly interacting massive particle (WIMP). These studies are mostly restricted by modelling of the astrophysical backgrounds, like diffuse emission. It is therefore necessary, to improve our knowledge of these backgrounds to be able to subtract them from the data and uncover possible, exotic contributions.

Some studies try to abbreviate this process by invoking proxies for different physical processes that contribute to the backgrounds. Following the assumed correlation, the data can be fitted for and the background subtracted. One particular type of these studies has found an excess in microwave sky maps – the ‘WMAP haze’ (see Sec. 1.3.4). A crucial ingredient of both studies [232, 234] that identify a haze is the extrapolation of the morphology of the synchrotron radiation template from 408 MHz to the WMAP bands at 23 (K), 33 (Ka), 41 (Q), 61 (V) and 94 (W) GHz, i.e. over two orders of magnitude in frequency. In fact the spatial distribution of the radiating

CR electrons is likely to differ significantly given their energy dependent diffusive transport in the Galaxy. Instead of attempting such a bold extrapolation, other studies, including the analysis by the WMAP collaboration [237], employ the K-Ka difference map as a tracer of synchrotron emission (despite some contamination by free-free emission and an anomalous component which has been interpreted (see, e.g. [342]) as spinning dust [228]). However although both maps are dominated by synchrotron radiation, such a template could also contain any unidentified radiation, such as a possible haze, and therefore cannot exclude it.

CR transport in the Galaxy is dominated by diffusion through interstellar magnetic fields with an *energy-dependent* diffusion coefficient $D(E) = D_0 E^\delta$ where $\delta = 0.3 \dots 0.7$ [275]. Taking the energy loss rate $b(E) = dE/dt = b_0 E^2$ as is appropriate for synchrotron and ICS, the diffusion length λ is

$$\lambda(E) \approx 5 \left(\frac{E}{\text{GeV}} \right)^{(\delta-1)/2} \text{ kpc},$$

for the standard values $D_0 = 10^{28} \text{ cm}^2 \text{ s}^{-1}$ and $b_0 = 10^{-16} \text{ s}^{-1}$ [275]. Therefore, the distance that GeV energy electrons can diffuse is comparable to the kpc scale on which the source distribution varies; moreover it changes by a factor of 2.4 (1.5) for $\delta = 0.3$ (0.7) in the energy range $\sim 4 - 50$ GeV (corresponding to peak synchrotron frequencies between 408 MHz and 50 GHz for a magnetic field of $6 \mu\text{G}$). As a consequence the ~ 50 GeV electrons will trace the source distribution much better than the ~ 4 GeV electrons which diffuse further away from the sources and wash out their distribution. The synchrotron map at 408 MHz *cannot* therefore be a good tracer of synchrotron radiation at much higher, in particular WMAP, frequencies. Relying on such a crude extrapolation of the morphology of synchrotron emission can thus potentially introduce unphysical residuals. We estimate these by simulating synchrotron sky maps at 408 MHz and the WMAP frequencies and feeding these into the template subtraction process [233]. We show that this leads to residuals of the same order as the claimed haze, which can in fact be matched for a particular source distribution in the galactic disk. We conclude therefore that the WMAP haze might be an artefact of inappropriate template subtraction rather than evidence of dark matter annihilation.

4.2. Template Subtraction

The subtraction method is based on a multilinear regression of the CMB subtracted WMAP data using foreground templates for free-free (f), dust correlated (d) and synchrotron emission (s). Technically this can be achieved by assembling the maps represented each by a vector of all pixels, that is \mathbf{f} , \mathbf{d} and \mathbf{s} , into one ‘template matrix’: $P = (\mathbf{f}, \mathbf{d}, \mathbf{s})$. (The template for the haze, \mathbf{h} , is appended later.) The pseudo-inverse P^+ allows the determination of the coefficients $\mathbf{a} = P^+ \mathbf{w}$ that minimise the $\chi^2 = \|\mathbf{w} - P\mathbf{a}\|^2/\sigma^2$ for the different templates at the WMAP frequencies; σ is the mean measurement noise in each frequency band. For details see Ref. [233].

Since we are interested only in the effect of the electron diffusion on the subtraction of the synchrotron foreground we do not use the free-free and dust templates or radio sky maps that are strongly affected by local structures such as Loop I [343]. Instead we simulate both the synchrotron sky map at 408 MHz and the sky maps in the WMAP frequency range with the GALPROP code [126]. We adopt the same mask as in Ref. [233] which excises pixels along the galactic plane, around radio sources and in directions of excessive absorption.

To allow comparison with the results of Ref. [233] we apply the same fitting procedure over the whole sky. In order to determine the magnitude of the ‘haze’ we append a template $\mathbf{h} = (1/\theta - 1/\theta_0)$ to P where $\theta = \sqrt{\ell^2 + b^2}$ is in galactic coordinates and $\theta_0 = 45^\circ$. This corresponds to the ‘FS8’ fit performed in [233] and adding the haze back to the residual maps gives the ‘FS8 + haze’ maps. We determine the latitudinal profile of the residual for $\ell = 0^\circ$ south of the galactic centre direction. As our simulated maps do not contain any localised structures, we do not need to divide the sky into several regions and fit them independently, as was done with the ‘RG8’ fit [233]. We have checked explicitly that doing so does not change the profiles of the residual intensity or the spectral indices.

We have checked that our procedure gives a residual ‘haze’ in agreement with Ref. [233] when we subtract the 408 MHz survey sky map from the WMAP sky maps. Although with the CMB estimator ‘CMB5’ we find a residual intensity of the same magnitude at 23 GHz, its spectral index of about -0.7 is somewhat softer than in Ref. [233].

4.3. Calculation

The transport of CR electrons is governed by a diffusion-convection equation (cf. Eq. 1.39),

$$\frac{\partial n}{\partial t} = \nabla \cdot (D_{xx} \nabla n - \mathbf{v} n) + \frac{\partial}{\partial p} p^2 D_{pp} \frac{\partial}{\partial p} \frac{1}{p^2} n - \frac{\partial}{\partial p} \left(\dot{p} n - \frac{p}{3} (\nabla \cdot \mathbf{v}) n \right) + q,$$

where $n dp$ is the number density of electrons with $p \in [p, p + dp]$, $D_{xx} = D_{0xx}(p/4 \text{ GeV})^\delta$ is the spatial diffusion coefficient, \mathbf{v} is the convection velocity, D_{pp} is the momentum diffusion coefficient and q is the source power density. This equation is numerically solved with the GALPROP code v50.1p in two dimensions, that is assuming azimuthal symmetry around the galactic centre and enforcing the boundary condition $n \equiv 0$ on a cylinder of radius $R = 20 \text{ kpc}$ and half-height z_{max} (see below).

The source power density q factorises into a source energy spectrum $q_0 E^{-\alpha}$ and a spatial variation $\sigma(r) e^{-z/z_{\text{scale}}}$ with $z_{\text{scale}} = 0.2 \text{ kpc}$. For the radial part we consider two possibilities. The distribution of SNRs is expected to be correlated with that of pulsars which is inferred by Lorimer to be [344]

$$\sigma_{\text{Lorimer}}(r) = 64.6 \left(\frac{r}{\text{kpc}} \right)^{2.35} e^{-r/1.528 \text{ kpc}}. \quad (4.1)$$

However, the determination of pulsar distances from their rotation measures relies on knowledge of the thermal electron density throughout the Galaxy and different distributions lead to different functional forms for the inferred radial variation of the pulsar density [345]. Therefore we also consider an exponential source distribution

$$\sigma_{\text{exp}}(r) = \sigma_0 e^{-r/2 \text{ kpc}}, \quad (4.2)$$

following Refs.[346] and [347].

The normalisation D_{0xx} , the scale height z_{max} of the CR halo and the spectral index δ of the diffusion coefficient are usually determined from measurements of CR nuclei and nuclear secondary to primary ratios (see Sec. 1.2.7). The measurement of CR ‘chronometers’ like $^{10}\text{Be}/^9\text{Be}$ is still not precise enough to break the degeneracy between D_{0xx} and z_{max} (see Sec. 1.2.7), so we vary z_{max} between 4 kpc and 8 kpc and vary D_{0xx} only a little, checking that we have rough agreement with

the measured fluxes of nuclei and nuclear secondary-to-primary ratios. On theoretical grounds [103] one expects a spectral break in the diffusion coefficient at ≈ 1 GeV. We fix the break energy to 1 GeV and vary δ_1 and δ_2 below and above the break (keeping $\delta_1 \geq \delta_2$), again trying to satisfy all local CR measurements.

The source electron spectrum is usually assumed to have a break around 4 GeV so we fix the electron source normalisation $q_0\sigma_0$ and the spectral indices α_1 and α_2 below and above the break by fitting the propagated flux to the electron spectrum as measured at Earth [348, 169]. We apply Solar modulation in the spherical approximation [60] with a median potential of $\phi = 550$ MV. Reacceleration and convection play a role at energies below 10 GeV and are therefore important for the 408 MHz map. For the Alfvén velocity v_A which determines the strength of reacceleration via $D_{pp} \propto v_A^2$ we consider the range $0 - 50 \text{ km s}^{-1}$. GALPROP assumes the convection velocity to vary linearly with distance from the galactic plane and we vary the slope dv_{conv}/dz between 0 and $20 \text{ km s}^{-1} \text{ kpc}^{-1}$.

Since the random component of the galactic magnetic field is known to dominate over the regular component [349], we neglect the latter. For the radial dependence we adopt the usual exponential fall-off where the radial scale ρ and the (perpendicular component of the) field strength B_0 at the galactic centre are chosen to reproduce the 408 MHz sky map [350]. Although it was initially believed [198] that an exponential dependence on z could give a satisfactory fit to the 408 MHz latitude profile, the galactic field model was later refined [351] by considering different, non-exponential behaviours which in fact give better fits. We therefore apply the method described in Ref. [352] of determining the emissivity dependence on r for galactic longitude $\ell = \pm 180^\circ$ (towards the galactic anti-centre). With an estimate for the electron density this translates into a z -dependence of the form $a + b \exp[(-|z|/\xi)^\kappa]$ and this is iterated to convergence where we find $a/b = 0.27$, $\xi = 0.51$ and $\kappa = 0.68$.

4.4. Results

4.4.1. Lorimer source distribution

The parameters of the diffusion model, the magnetic field and the electron source spectrum have been adjusted as described above and the values are shown for the Lorimer source distribution,

Table 4.1.: Parameters of source and diffusion models.

	Lorimer	exponential
Source distribution	<i>c.f.</i> Eq. 4.1	<i>c.f.</i> Eq. 4.2
α_1, α_2	1.2, 2.2	1.2, 2.2
D_{0xx}	$5.75 \times 10^{28} \text{ cm}^2 \text{ s}^{-1}$	$5.75 \times 10^{28} \text{ cm}^2 \text{ s}^{-1}$
z_{max}	4 kpc	8 kpc
δ_1, δ_2	0.34, 0.34	0.1, 0.4
v_A	50 km s^{-1}	36 km s^{-1}
dv_{conv}/dz	$10 \text{ km s}^{-1} \text{ kpc}^{-1}$	$15 \text{ km s}^{-1} \text{ kpc}^{-1}$
B_0	$6.3 \mu\text{G}$	$6.8 \mu\text{G}$
ρ	5 kpc	50 kpc

Eq. 4.1, in Table 4.1.

The electron flux measured locally and at the positions $\{(r, z)\} = \{(1, 0), (4, 0), (0, 4)\}$ (in kpc) are shown in Fig. 4.1. We note that close to the galactic centre the electron flux responsible for synchrotron radiation at 408 MHz is not only much softer but also suppressed by over an order of magnitude with respect to its locally measured value. Fig. 4.2 shows the latitudinal profiles of the synchrotron radiation at 408 MHz; in general, the fit is good for $b \lesssim 50^\circ$ but underestimates the emission at larger latitudes. It has been shown [352] that this can potentially be overcome by increasing the scale height of the synchrotron emissivity at larger galactic radii. The remaining discrepancies between the simulated and measured profiles are probably due to the assumption of rotational symmetry. This leads to an underestimation of the synchrotron radiation along tangents of the spiral arms and an overestimation between them. For example, the Carina arm is tangent at 75° and the Sagittarius arm at -40° , so both $\ell = +60^\circ$ and $\ell = -60^\circ$ are between spiral arms and thus slightly overestimated, in particular in the galactic plane. It is also clear that point sources (that have not been subtracted from the 408 MHz data) are not accounted for in our calculation (e.g., Fornax at $\ell \simeq 120^\circ$, $b \simeq -57^\circ$).

The sky map of the residual $r(\ell, b)$ (Fig. 4.3) shows a deficit for $|\ell| \leq 40^\circ$ and $|b| \leq 20^\circ$. Further away from the galactic centre direction there is a slight excess. The residual specific intensity (Fig. 4.4) is of opposite sign but its absolute value is of the same order of magnitude as the ‘haze’ at 23 and 33 GHz.

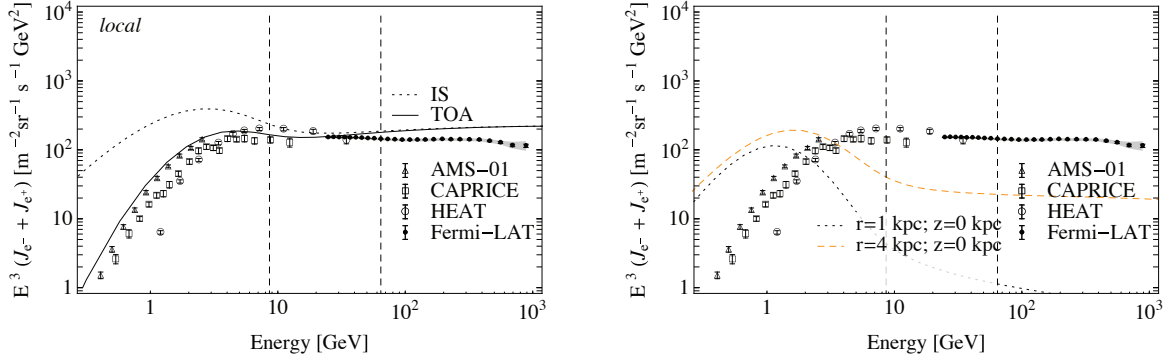


Figure 4.1.: **Left:** The electron (plus positron) flux measured locally by AMS-01, CAPRICE, HEAT [348] and Fermi-LAT [169], compared with the expectation for the Lorimer source distribution, Eq. 4.1; the dotted line is the calculated interstellar flux while the solid line is its Solar modulated value (with $\phi = 550$ MV). The dashed vertical lines show the energy corresponding to peak synchrotron frequencies of 408 MHz and 23 GHz for the local magnetic field. **Right:** The calculated electron (plus positron) flux at the positions $\{(r, z)\} = \{(1, 0), (4, 0)\}$ (in kpc).

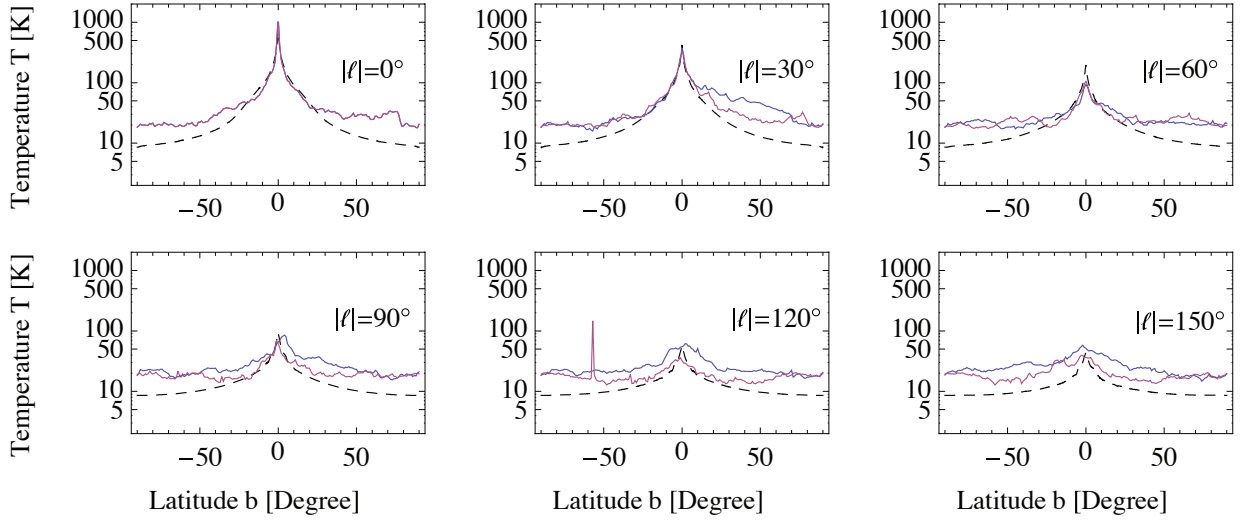


Figure 4.2.: The calculated latitudinal profile of galactic synchrotron radiation at 408 MHz (black dashed line) for galactic longitudes $|\ell| = 0^\circ, 30^\circ, 60^\circ, 90^\circ, 120^\circ$ and 150° . The red (blue) solid line is the observed profile [350] for positive (negative) ℓ .

4.4.2. Exponential source distribution

For the exponential source distribution, Eq. 4.2, the electron fluxes are shown in Fig. 4.5. Close to the galactic centre, it is larger by about an order of magnitude than measured locally and slightly harder. The latitudinal profiles of the synchrotron radiation at 408 MHz are shown in Fig. 4.6.

The residual sky map contains a roughly spherical excess around the centre of the map, although

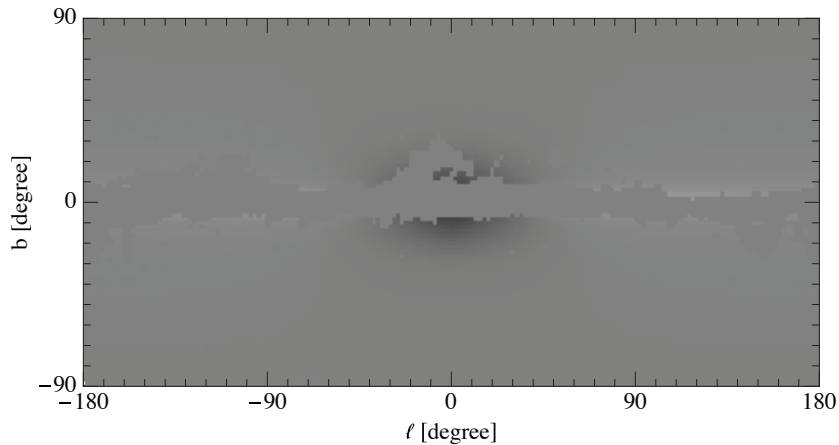


Figure 4.3.: Residual sky map in galactic coordinates for the Lorimer source distribution, Eq. 4.1. The grey scale is linear from -4 to $+4 \text{ kJy sr}^{-1}$ (corresponding to -0.25 to $+0.25 \text{ mK}$ at 22.8 GHz).

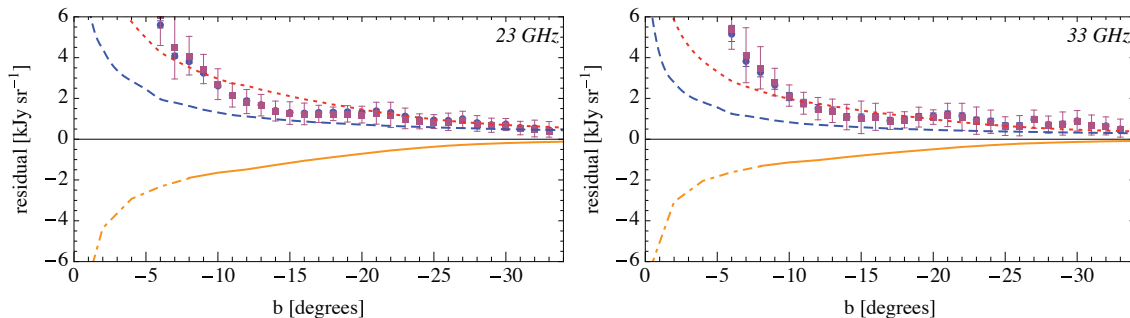


Figure 4.4.: Latitudinal profile of the K band residual outside (solid curve) and under (dot-dashed curve) the mask at 23 GHz (left panel) and 33 GHz (right panel). The square (circle) data points are the ‘haze’ as extracted in Ref. [233] ([239]). The dotted line shows the extrapolated emission at 23 (33) GHz from scaling the simulated 408 MHz emission and the dashed line shows the actual simulated 23 (33) GHz emission.

somewhat more extended in longitude than in latitude (see Fig. 4.7).

We note that the systematic uncertainty of the residual intensity (as determined from real sky maps) induced by chance correlations between the ‘haze’ template and the CMB has been estimated in Ref. [233] and can be read off their Fig. 8 as $\pm 11.8 \text{ h kJy sr}^{-1}$ ($\pm 23.7 \text{ h kJy sr}^{-1}$) in the 23 GHz (33 GHz) band. We therefore allow for an offset of our calculated residual relative to the ‘haze’ template in this range when fitting the residuals from real sky maps. The residual intensity (Fig. 4.8) matches the claimed WMAP haze.

To compare our results to those of Ref. [233], we also determine the average spectral index (for details see Appendix B) in a region south of the galactic centre, $b \in [-45^\circ, 0^\circ]$, $\ell \in [-25^\circ, 25^\circ]$. The

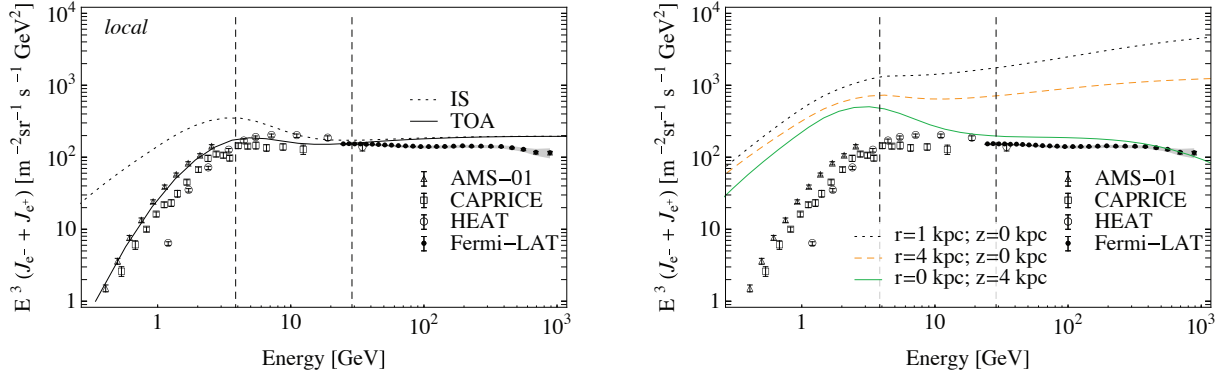


Figure 4.5.: Same as in Fig. 4.1, but for the exponential source distribution, Eq. 4.2.

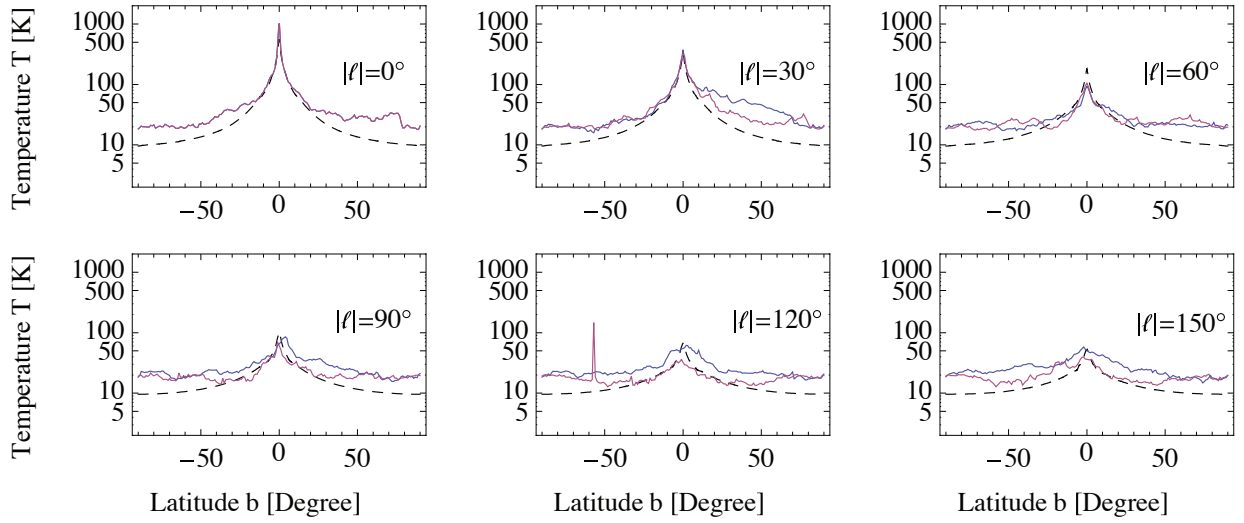


Figure 4.6.: Same as in Fig. 4.2, but for the exponential source distribution, Eq. 4.2.

colour maps of spectral indices scaled by intensity are shown in Fig. 4.9, both for the synchrotron + residual and for the residual alone. Not only is the synchrotron emission much more disk-like than the residual, but the spectral index of the residual is also considerably harder than the synchrotron spectral index. This is to be compared with Fig. 7 of Ref. [233] which exhibits the same qualitative behaviour.

Furthermore, we show the spectral index for the unmasked pixels in the region south of the galactic centre (as defined above) as a function of latitude in Fig. 4.10, again both for the synchrotron + residual and for the residual alone. With average indices of $\langle \beta_{23,33}^H \rangle = -0.44$ for the residual and of $\langle \beta_{23,33}^S \rangle = -1.03$ for the residual + synchrotron in this region, we find that the residual index is harder than the synchrotron index by 0.6, which is in excellent agreement with the findings of

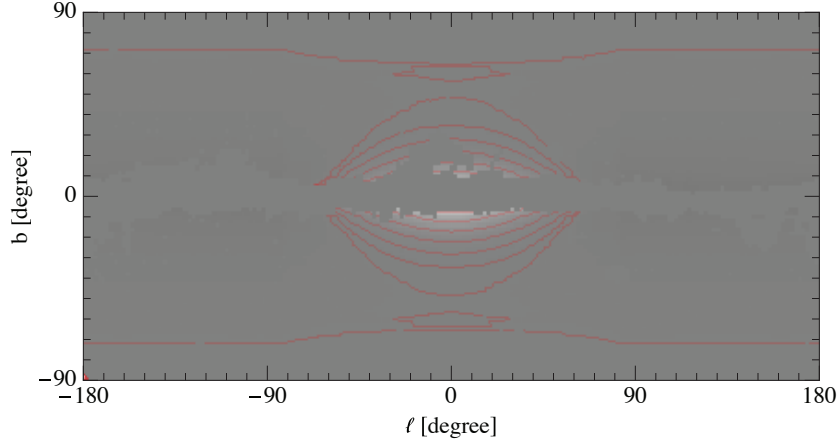


Figure 4.7.: Residual sky map in galactic coordinates for the exponential source distribution, Eq. 4.2. The grey scale is linear from -4 to $+4 \text{ kJy sr}^{-1}$ (corresponding to -0.25 to $+0.25 \text{ mK}$ at 22.8 GHz). The contour lines are logarithmically spaced in intensity between 0.02 and 2 kJy sr^{-1} .

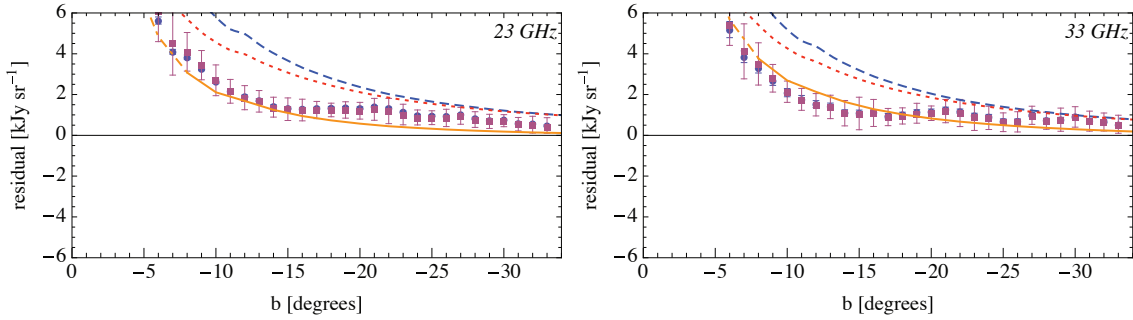


Figure 4.8.: Same as in Fig. 4.4, but for the exponential source distribution, Eq. 4.2. We have added an offset to the calculated residual of $+11.8 \text{ h kJy sr}^{-1}$ ($+23.7 \text{ h kJy sr}^{-1}$) in the 23 GHz (33 GHz) band reflecting the systematic uncertainty from chance correlations between the ‘haze’ template and the CMB.

Ref. [233]. The values of our different model parameters are shown in Table 4.1.

4.5. Discussion

To qualitatively understand these results, consider the longitudinal profile of the synchrotron intensity $I(\ell, b)$; for simplicity let us constrain ourselves to the galactic plane, i.e. $b \equiv 0$. The intensity in any direction ℓ is given by the integral of the synchrotron emissivity over the line of sight and this samples the radial distribution of the relativistic electron density in the range $r \in [d \sin \ell, R]$, where d is the distance of the Sun from the galactic centre. Since the fitting procedure minimises the square of the difference in the maps, the sign and size of the residual is determined not by the

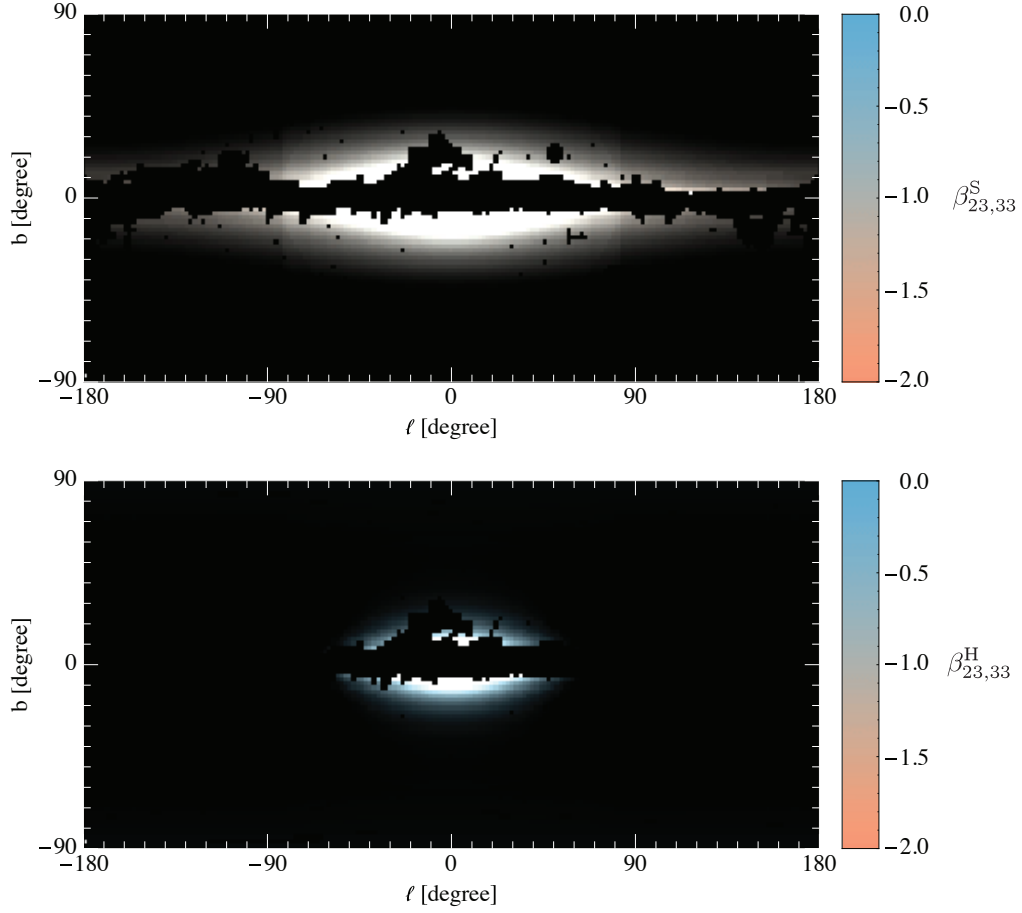


Figure 4.9.: Colour maps of spectral indices between 23 and 33 GHz defined in Eq. B.1 scaled by the 23 GHz intensity for synchrotron + residual (top panel) and residual only (bottom panel).

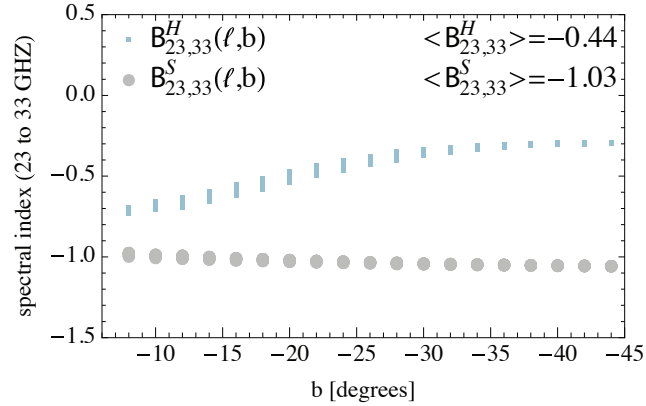


Figure 4.10.: Spectral indices of the unmasked pixels in the region south of the galactic centre ($b \in [-45^\circ, 0^\circ]$, $l \in [-25^\circ, 25^\circ]$) as a function of latitude for residual + synchrotron (large beige circles) and residual alone (small blue squares). The average spectral indices, β_S and β_H , are shown in the upper right corner.

absolute difference but by the difference in the *radial slope* of the emissivity $\varepsilon(r)$ at 408 MHz and the WMAP frequencies. The difference in the slopes reflects the energy dependence of the electron diffusion — higher energy electrons lose their energy more quickly, hence their emissivity traces the source distribution more closely than does the emissivity of low energy electrons.

For the pulsar source distribution, the low energy electrons peak at the galactic centre whereas the high-energy electrons peak further away (see left panel of Fig. 4.11). This leads to a deficit for small radii (translating to small longitudes) and a slight excess further away from the galactic centre (see also Fig. 4.3). For the exponential source distribution the radial distribution of synchrotron emissivity is steeper at higher energies. The template subtraction therefore yields a residual with an excess around the centre direction and a deficit further away along the galactic plane (see right panel of Fig. 4.11).

We note that the size and morphology of the residual is thus sensitive not only to the source distribution but also to the parameters of the diffusion model. For instance, decreasing the Alfvén speed below the value given above reduces the importance of reacceleration, and therefore effectively limits the number of GeV electrons around the galactic centre where otherwise energy losses dominate.

4.6. A Related Study

A related study [353], published at the same time as the present work [3], also tries to determine whether the ‘WMAP haze’ could have a purely astrophysical origin and how to distinguish between this and a DM explanation. As there are some important differences, we will briefly comment on this work.

At first sight, the astrophysical explanation invoked in Ref. [353], a large number of supernova remnants at the galactic centre, might look not too different from our model with the exponential source distribution. However, while we also agree on the importance of diffusion-loss steepened electron spectra for producing the haze there is a major difference between our approaches — while the authors of Ref. [353] consider the haze to be *physical*, we argue that it might in fact be an artefact of the foreground subtraction. Our models are also more constrained insofar as we reproduce the observed radio emission at 408 MHz and match the direct measurements of the

electron spectrum at the Solar position. Furthermore, we allow for spatial dependence of the \mathbf{B} field, and convection and reacceleration of cosmic ray electrons, which are all essential in order to explain all these datasets simultaneously.

4.7. Conclusion

We have investigated systematic effects in WMAP foreground subtraction stemming from the naïve extrapolation of the 408 MHz map. To this end we have considered two illustrative cosmic ray diffusion models assuming different source distributions, the first one based on a pulsar survey, and the second one exponential in galactocentric radius. Both models are able to reproduce the synchrotron radiation at 408 MHz, the locally measured electron flux and are furthermore consistent with nuclear cosmic ray fluxes and secondary-to-primary ratios. When our ‘foreground’ 408 MHz map is subtracted from the 23 GHz map, we find a residual whose size and morphology depends on the source and diffusion model adopted. Thus the energy-dependent diffusion of relativistic electrons makes the 408 MHz sky map a *bad* tracer of synchrotron radiation at microwave frequencies, as had been suspected earlier [354]. Such a template subtraction produces a residual, which for certain values of the source and propagation model can reproduce the ‘WMAP haze’ in intensity and spectrum.

The residual obtained from the exponential source distribution does not perfectly reproduce the morphology found in Ref. [233] (although it is *not* disk-like but rather clustered around the galactic centre). However, a quantitative assessment of the discrepancy is not straightforward, mainly because Ref. [233] does not provide any objective measure, e.g. the ellipticity of equal intensity contours. On the other hand, even the numerical GALPROP model we employed for our analysis is very likely too simple to fully capture the complexity of synchrotron emission in the Galaxy. For instances, not only the source density but also the galactic magnetic field is supposed to be correlated with the galactic spiral arms, which will break the symmetry in r (and hence in ℓ) and can therefore considerably modify the morphology. Furthermore, much of the ‘diffuse’ synchrotron emission from the disk may originate in the shells of old supernova remnants which have grown very large in their radiative phase [355]. Exactly the same argument concerning the energy-dependent diffusion length that we applied to the cosmic ray source distribution can be

applied to such localised structures too. Therefore the 408 MHz survey sky map is not expected to trace the emission from the latter at higher frequencies either. One can easily imagine that such localised structures (of which Loop I may be a nearby example) can at least in part modify the morphology of the residual and bring the simulated map into agreement with the one determined from the subtraction of real templates.

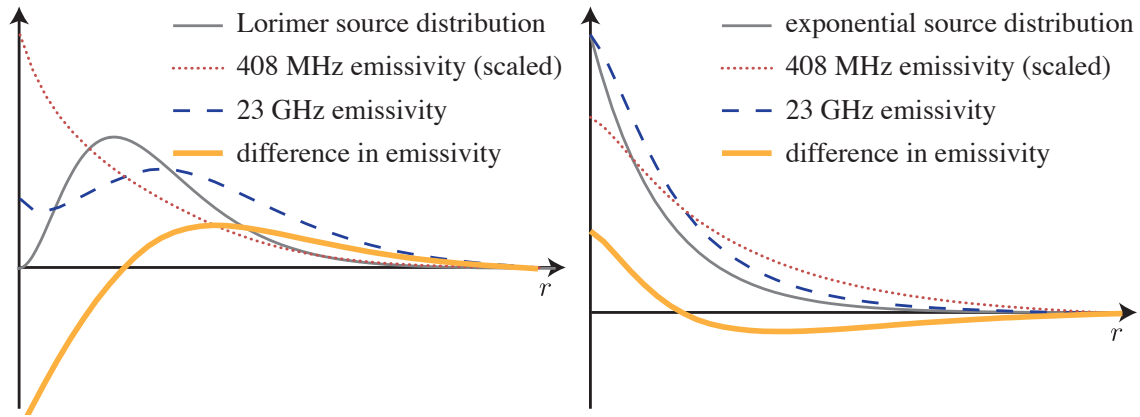


Figure 4.11.: The (scaled) synchrotron emissivity at 408 MHz and 23 GHz, and their difference, for the Lorimer (left panel) and the exponential (right panel) source distribution.

Epilogue

Nearly two years after the excesses in the positron fraction and the total electron-positron flux were reported by the PAMELA and Fermi satellites respectively, the dark matter explanations proposed for these ‘anomalies’ seem to be almost ruled out. On the one hand, the necessarily powerful injection of additional electrons and positrons from annihilating/decaying dark matter in an extended halo is in conflict with radio/microwave and γ -ray observations. On the other hand, a broad range of astrophysical effects have been identified which can account for these excesses and would naturally dominate over plausible dark matter signals. Furthermore, signatures that have been believed to be typical of dark matter have in fact been found to be rather generic: features in the total electron-positron flux at tens and hundreds of GeV can easily be induced by the discreteness of astrophysical sources. Even sharp shoulders in the energy spectrum can be due to a nearby source with a hard spectrum, like a pulsar. Conversely, it appears that an arbitrary spectral signal, even if it has nothing to do with dark matter, can be fitted in a dark matter scenario by harnessing the multitude of free or uncertain model parameters.

Prospects for dark matter indirect detection in charged lepton cosmic ray channels looks therefore rather bleak at the moment. In the long run with the advent of advanced satellite detectors such as AMS-02, we might hope for a better understanding of the astrophysical backgrounds down to perhaps even the per cent level. This would allow us to subtract them and uncover possible dark matter contributions, which in WIMP scenarios would naturally be expected to contribute at this level. Other high energy channels might, however, provide better prospects. Photons, for example, do not only sample a much larger volume than locally measured charged leptons which, as we have seen, originate within a few kiloparsecs of the Solar system. Even more importantly, because of their rectilinear propagation, it is possible to focus on specific targets that have little or no astrophysical backgrounds, e.g. the Galactic halo at high latitude or prominent substructures such

as dwarf spheroidal galaxies. The Fermi satellite as well as the forthcoming Čerenkov Telescope Array will provide important data in this connection.

Of course, the attention given to the lepton excess because of the claimed connection with particle dark matter has played an important sociological role in helping the astroparticle community to appreciate the complexities of galactic cosmic ray physics. The first hints of an anomalous positron fraction were reported over 30 years ago, but only a few prescient works have taken this signal seriously and tried to explain it, e.g. by the contribution from nearby pulsars. We hope very much therefore that the momentum which cosmic ray physics has gained of late will foster improvements in their astrophysical modelling and help us to be open-minded and alert to other possible anomalies that might show up in the data. An example could be the recent observation by the CREAM detector of different spectral indices for protons and helium nuclei. Possible interpretations range from different source populations for protons and heavier nuclei, to secondary production and acceleration of helium in supernova remnants, in much the same way as has been suggested in this thesis for secondary electrons and positrons.

Although dark matter thus seems to be ruled out as an explanation for the lepton excesses this puzzle is far from being solved. Not only is it unclear which sources are responsible for the additional positrons, one might also wonder whether these excesses are local (i.e. particular to the environment of the Solar system) or global (i.e. similarly present in other regions of the Galaxy). In this context, we would like to stress the two-fold role of the nuclear component of galactic cosmic rays: Firstly, if a *rising* secondary-to-primary ratio (e.g. B/C) is observed, this will clearly show that the acceleration of secondaries is the likely cause of the rise in the positron fraction. Secondly, as the local fluxes of stable nuclei obtain contributions from larger distances in the Galaxy than do charged leptons, such a rise would imply that the secondaries are also produced and accelerated in cosmic ray sources elsewhere in the Galaxy.

It has also been suggested that anisotropies in the arrival directions of charged leptons in cosmic rays can help identifying the origin of the additional positrons. We believe however that the uncertainties here are too large and that anisotropies are therefore unlikely to settle the issue. As mentioned above, models that explain the increasing positron fraction and excessive total electron-positron flux by a (few) nearby pulsar(s), usually find anisotropies of at most a few per mil and rely on assumptions concerning the homogeneity of energy losses and diffusion. It is therefore

conceivable that small variations of the diffusion model can drastically alter the predictions. A systematic orientation of the local magnetic fields, for example, can shift the predominant arrival directions in such a way that no correlation with known objects can be made; or it can lead to a spurious anisotropy even for an isotropic source distribution.

The only possible way to investigate the high energy electrons and positrons *elsewhere* in the Galaxy is to look for their secondary radiation, i.e. radio/microwaves synchrotron radiation on Galactic magnetic fields and γ -rays from inverse-Compton scattering on interstellar radiation fields. As we have seen, a prime application of this is again the study of dark matter annihilation or decays into leptons. Of course, this raises the important question of how to improve the modelling of diffuse galactic backgrounds which are of general interest also for other fields of physics, e.g. studies of the polarisation of the cosmic microwave background (CMB). At the moment, large efforts are being made by the Fermi collaboration in explaining the astrophysical contribution to the γ -ray sky. Their approach accounts not only for the ICS contribution using the GALPROP model but also uses a very flexible fitting of ISM densities in galactocentric rings to the π^0 decay generated γ -rays. First results show that the residuals thus obtained are very small but the obvious question is whether this is because of too many model degrees of freedom. Theoretical models might not have fewer parameters but can at least provide some insight into their physical significance. At the moment, however, such models are not able to incorporate, let alone predict, local structure such as the radio ‘loops’ clearly visible in sky maps over a wide range of frequencies. Furthermore, a high degree of degeneracy is to be expected, for example between the GCR source distribution and the structure of the magnetic fields or ISRFs. Attempts at solving the inverse problem, i.e. determining the three-dimensional distribution of emissivity would help in extracting the relativistic electron-positron density throughout the Galaxy as a function of the assumed radiation backgrounds and would bring us closer to identifying individual sources of GCRs.

On a more general level and irrespective of whether the explanations we have suggested for the apparent signals will be confirmed by future data, the moral is that we need both better understanding of the astrophysical sources and of the propagation of galactic cosmic rays.

Many of these efforts will probably be data-driven. For example, Fermi-LAT is presently closing a crucial energy gap in GeV γ -rays that IACTs could not address. This will allow looking for a specific bump in the γ -ray spectra of SNRs that would implicate pion production and hence

hadronic acceleration processes. In general, many arbitrary extrapolations from TeV energies as well as the underlying physics models will be tested. In addition, the improved statistics with respect to, e.g. the EGRET satellite will allow sampling of the spectra of even comparatively faint and distant sources. Furthermore, the superior spatial resolution will allow and/or necessitate going beyond zero- or one-dimensional source models and considering the internal structure of the sources. It might turn out that some common assumptions about the sources are in fact prejudices and cannot be sustained any longer.

With respect to improving the cosmic ray propagation models, what is probably needed is a completely new approach. Many important steps towards realistic models have been taken in the last couple of years. For example, the inclusion of Klein-Nishina corrections to the interactions of electrons and positrons with radiation fields has been recognised to lead to spectral effects at the highest energies. Two other improvements aim at a more realistic modelling of the ISM and its effect on cosmic propagation: Firstly, the structure of the large-scale ordered magnetic field is being given due importance for synchrotron radiation studies. Secondly, the spatial dependence of energy loss rate and diffusion coefficients is beginning to be accounted for in numerical propagation codes. However, what these models lack is a clear physical intuition for *how* these quantities should vary across the Galaxy. Here, the hitherto followed approach of calibrating diffusion models by measurements of local cosmic ray nuclei necessarily reaches its limits: Stable nuclear cosmic rays average over a large volume of the cosmic ray halo (typically several kiloparsecs at GeV energies) and can therefore not resolve structures at smaller scales. At the highest energies, however, local sources become more important and therefore the large bulk of the galactic volume remains inaccessible. Generally speaking, it is difficult to imagine how an enlarged set of parameters that necessarily accompanies every more complex propagation model could be constrained by the same number of observations.

One possible resort could be to devise new sets of observables which are particularly sensitive to some of the parameters. We have already encountered one such example in our analysis of the systematic effects of template subtraction. The degeneracy encountered here was that between the source distribution and the magnetic field configuration. If one can neglect exotic contributions, a new observable like the relative differences of maps at different frequencies could be used to pin down one particular combination of source distribution and magnetic fields.

The more radical approach would be to search for a new propagation model altogether. This would need to provide a self-consistent explanation for many different mechanisms that today's heuristic models invoke in an *ad hoc* fashion. The combination and description of cosmic rays, magnetic fields and the interstellar medium in one framework will require deeper theoretical efforts as well as immense computational power. One can hardly overestimate the difficulties such a program would face, nevertheless it would be a fitting challenge to undertake on the eve of the centenary of the discovery of cosmic radiation by Victor Hess in 1912.

A. Moments of Functions of Random Variables

Suppose we have two random variables, x and y with the probability densities $f_x(x)$ and $f_y(y)$. A function $\phi(x, y)$ of x and y is also a random variable,

$$z = \phi(x, y), \quad \frac{dz}{dx} = \phi'(x, y). \quad (\text{A.1})$$

Let's further assume that ϕ has an inverse function with respect to x ,

$$\phi^{-1}(y, z) = x, \quad \frac{dx}{dz} = \frac{1}{\phi'(\phi(y, z), y)}. \quad (\text{A.2})$$

The m -th moment of z is then

$$\langle z^m \rangle = \int_{-\infty}^{\infty} dz z^m f_z(z) = \int_{-\infty}^{\infty} dz z^m \frac{dF}{dz} = \int_{-\infty}^{\infty} dz z^m \frac{d}{dz} \left[\int \int_{D_z} dy dx f(x, y) \right] \quad (\text{A.3})$$

$$= \int_{-\infty}^{\infty} dz z^m \frac{d}{dz} \left[\int_{-\infty}^{\infty} dy \int_{-\infty}^{\phi^{-1}(y, z)} dx f(x, y) \right] \quad (\text{A.4})$$

$$= \int_{-\infty}^{\infty} dy \int_{-\infty}^{\infty} dz z^m \underbrace{\frac{d}{dz} \left[\int_{-\infty}^{\phi^{-1}(y, z)} dx f(x, y) \right]}_{\text{A.5}} \quad (\text{A.5})$$

$$= \frac{d\phi^{-1}}{dz} \frac{d}{d\phi^{-1}} \int_{-\infty}^{\phi^{-1}(y, z)} dx f(x, y) \\ = \frac{1}{\phi'} f(\phi^{-1}, y)$$

$$= \int_{-\infty}^{\infty} dy \int_{-\infty}^{\infty} dx \frac{dz}{dx} \phi^m(x, y) \frac{1}{\phi'} f(x, y) \quad (\text{A.6})$$

$$= \int_{-\infty}^{\infty} dy \int_{-\infty}^{\infty} dx \phi^m(x, y) f(x, y). \quad (\text{A.7})$$

B. Determination of Spectral Indices From Synchrotron Sky Maps

In general, a spectral index $\beta(\mathbf{x})$ between two different frequencies, ν_1 and ν_2 , can be defined for each given pixel \mathbf{x} by assuming a power law behaviour of the specific intensity, $I(\nu, \mathbf{x})$,

$$\frac{I(\nu_2, \mathbf{x})}{I(\nu_1, \mathbf{x})} = \left(\frac{\nu_2}{\nu_1}\right)^{\beta(\mathbf{x})}. \quad (\text{B.1})$$

However, it turns out that the template method applied to the WMAP data and the 408 MHz sky map leads to a residual with *negative* intensities for some pixels (see e.g., Fig. 6 of Ref. [233]), partly due to over-subtraction and partly because the sky maps are mean-subtracted. We also find negative intensities for some pixels when applying the template subtraction to our mock microwave data and radio template. This does not necessarily imply that the residual is not physical but that a global offset $\Delta I(\nu)$ exists between the residual intensity, I' , as determined from the template subtraction and the intensity of the *actual*, possibly physical residual, I :

$$\Delta I(\nu) \equiv I(\nu, \mathbf{x}) - I'(\nu, \mathbf{x}). \quad (\text{B.2})$$

This makes the determination of the spectral index non-trivial.

At first sight, the analysis presented in Ref. [233] seems to avoid this difficulty by determining the average spectral index in the region south of the galactic centre from the average ratio r' of the intensities at two different frequencies ν_1 and ν_2 , e.g. $\nu_1 = 23$ GHz and $\nu_2 = 33$ GHz. This ratio can be determined from a scatter plot of the pairs of residual intensities $\{I'_{\nu_1}, I'_{\nu_2}\}$ (as determined from the template subtraction), to which a straight line, $I'_{\nu_2}(I'_{\nu_1}) = r'I'_{\nu_1} + \hat{I}'_{\nu_2}$, is fitted, allowing for the ordinate offset \hat{I}'_{ν_2} because of the unknown global offset $\Delta I(\nu)$. The average spectral index

$\langle \beta'_{\nu_1, \nu_2} \rangle$ defined by this procedure is then simply $\log(r')/\log(\nu_2/\nu_1)$. Alternatively, if the spectral index is determined from a scatter plot of the *actual* residual intensities $\{I_{\nu_1}, I_{\nu_2}\}$, then there is no ordinate offset, so the straight line is $I_{\nu_2}(I_{\nu_1}) = rI_{\nu_1}$ and the *actual* average spectral index $\langle \beta_{\nu_1, \nu_2} \rangle = \log(r)/\log(\nu_2/\nu_1)$.

In general, these two descriptions cannot be expected to give a similar spectral index. Even assuming that with an appropriate ‘haze’ template \mathbf{h} the amount of over-subtraction is much smaller than the offset due to the use of mean-subtracted maps, the answer is in general different. In this case, the offset is simply the mean over the n pixels, $\Delta I(\nu) = \langle I(\nu, \mathbf{x}) \rangle$. The coordinate system $\{I'_{\nu_1}, I'_{\nu_2}\}$ is therefore centred at the centre of gravity of the data $\{I(\nu_1, \mathbf{x}), I(\nu_2, \mathbf{x})\}$, and the ordinate offset \hat{I}'_{ν_2} is zero. As usual, the slope of the linear regression $I'_{\nu_2}(I'_{\nu_1}) = r'I'_{\nu_1}$ is

$$r' = \frac{\sum_i I'_{\nu_1}(\mathbf{x}_i)I'_{\nu_2}(\mathbf{x}_i) - n\langle I'_{\nu_1}(\mathbf{x}_i) \rangle \langle I'_{\nu_2}(\mathbf{x}_i) \rangle}{\sum_i I'^2_{\nu_1}(\mathbf{x}_i) - n\langle I'_{\nu_1}(\mathbf{x}_i) \rangle^2}. \quad (\text{B.3})$$

Unless the covariance of I'_{ν_1} and I'_{ν_2} is much larger than the product of their mean values, which is for example the case if the spectral index is constant in the region of interest, this is in general different from the slope r of the straight line $I_{\nu_2}(I_{\nu_1}) = rI_{\nu_1}$,

$$r = \frac{\sum_i I'_{\nu_1}(\mathbf{x}_i)I'_{\nu_2}(\mathbf{x}_i)}{\sum_i I'^2_{\nu_1}(\mathbf{x}_i)}. \quad (\text{B.4})$$

However, since we cannot determine the offset $\Delta I(\nu)$ from data, we need to *define* an offset $\Delta I(\nu)$.

We choose it to be:

$$\Delta I(\nu) = \min_{\mathbf{x}} [I'(\nu, \mathbf{x})], \quad (\text{B.5})$$

such that the intensity is always positive, allowing us to define the spectral index in each pixel. (The exact value chosen for $\Delta I(\nu)$ is actually $(1 + 10^{-3}) \min [I'(\nu, \mathbf{x})]$ to prevent the spectral index from diverging in the pixel where $I(23 \text{ GHz})$ attains its minimum.)

Bibliography

- [1] P. Mertsch and S. Sarkar, “Testing astrophysical models for the PAMELA positron excess with cosmic ray nuclei,” *Phys. Rev. Lett.* **103** (2009) 081104, [arXiv:0905.3152](#) [[astro-ph.HE](#)].
- [2] M. Ahlers, P. Mertsch, and S. Sarkar, “On cosmic ray acceleration in supernova remnants and the FERMI/PAMELA data,” *Phys. Rev.* **D80** (2009) 123017, [arXiv:0909.4060](#) [[astro-ph.HE](#)].
- [3] P. Mertsch and S. Sarkar, “Systematic effects in the extraction of the ‘WMAP haze’,” [arXiv:1004.3056](#) [[astro-ph.HE](#)].
- [4] V. C. Rubin and W. K. Ford, Jr., “Rotation of the Andromeda Nebula from a Spectroscopic Survey of Emission Regions,” *Astrophys. J.* **159** (Feb., 1970) 379–+.
- [5] Y. Sofue and V. Rubin, “Rotation Curves of Spiral Galaxies,” *Ann. Rev. Astron. Astrophys.* **39** (2001) 137–174, [arXiv:astro-ph/0010594](#).
- [6] **SDSS** Collaboration, X. X. Xue *et al.*, “The Milky Way’s Circular Velocity Curve to 60 kpc and an Estimate of the Dark Matter Halo Mass from Kinematics of 2400 SDSS Blue Horizontal Branch Stars,” *Astrophys. J.* **684** (2008) 1143–1158, [arXiv:0801.1232](#) [[astro-ph](#)].
- [7] F. Zwicky, “Die Rotverschiebung von extragalaktischen Nebeln,” *Helvetica Physica Acta* **6** (1933) 110–127.
- [8] F. Zwicky, “On the Masses of Nebulae and of Clusters of Nebulae,” *Astrophys. J.* **86** (Oct., 1937) 217–+.
- [9] M. Bartelmann and P. Schneider, “Weak Gravitational Lensing,” *Phys. Rept.* **340** (2001) 291–472, [arXiv:astro-ph/9912508](#).
- [10] R. A. Alpher, H. Bethe, and G. Gamow, “The origin of chemical elements,” *Phys. Rev.* **73** no. 7, (Apr, 1948) 803–804.
- [11] **Particle Data Group** Collaboration, K. Nakamura *et al.*, “Review of particle physics,” *J. Phys.* **G37** (2010) 075021.
- [12] D. Larson *et al.*, “Seven-Year Wilkinson Microwave Anisotropy Probe (WMAP) Observations: Power Spectra and WMAP-Derived Parameters,” [arXiv:1001.4635](#) [[astro-ph.CO](#)].
- [13] V. Springel *et al.*, “Simulating the joint evolution of quasars, galaxies and their large-scale distribution,” *Nature* **435** (2005) 629–636, [arXiv:astro-ph/0504097](#).

- [14] M. Kuhlen, J. Diemand, P. Madau, and M. Zemp, “The Via Lactea INCITE Simulation: Galactic Dark Matter Substructure at High Resolution,” *J. Phys. Conf. Ser.* **125** (2008) 012008, [arXiv:0810.3614 \[astro-ph\]](#).
- [15] J. Diemand, B. Moore, and J. Stadel, “Earth-mass dark-matter haloes as the first structures in the early universe,” *Nature*. **433** (2005) 389–391, [arXiv:astro-ph/0501589](#).
- [16] M. Milgrom, “A Modification of the Newtonian dynamics as a possible alternative to the hidden mass hypothesis,” *Astrophys. J.* **270** (1983) 365–370.
- [17] R. H. Sanders and S. S. McGaugh, “Modified Newtonian Dynamics as an Alternative to Dark Matter,” *Ann. Rev. Astron. Astrophys.* **40** (2002) 263–317, [arXiv:astro-ph/0204521](#).
- [18] J. D. Bekenstein, “Relativistic gravitation theory for the MOND paradigm,” *Phys. Rev.* **D70** (2004) 083509, [arXiv:astro-ph/0403694](#).
- [19] D. Clowe *et al.*, “A direct empirical proof of the existence of dark matter,” *Astrophys. J.* **648** (2006) L109–L113, [arXiv:astro-ph/0608407](#).
- [20] A. J. Benson, “Galaxy Formation Theory,” [arXiv:1006.5394 \[astro-ph.CO\]](#).
- [21] Ya. B. Zeldovich, *Adv. Astron. Astrophys.* **3** (1965) 241.
- [22] H.-Y. Chiu, “Symmetry between particle and anti-particle populations in the universe,” *Phys. Rev. Lett.* **17** (1966) 712.
- [23] G. Steigman, “Cosmology Confronts Particle Physics,” *Ann. Rev. Nucl. Part. Sci.* **29** (1979) 313–338.
- [24] B. W. Lee and S. Weinberg, “Cosmological lower bound on heavy-neutrino masses,” *Phys. Rev. Lett.* **39** (1977) 165–168.
- [25] D. A. Dicus, E. W. Kolb, and V. L. Teplitz, “Cosmological Upper Bound on Heavy Neutrino Lifetimes,” *Phys. Rev. Lett.* **39** (1977) 168.
- [26] M. I. Vysotsky, A. D. Dolgov, and Ya. B. Zeldovich, “Cosmological limits on the masses of neutral leptons,” *JETP Lett.* **26** (1977) 188–190.
- [27] G. R. Farrar and P. Fayet, “Phenomenology of the Production, Decay, and Detection of New Hadronic States Associated with Supersymmetry,” *Phys. Lett.* **B76** (1978) 575–579.
- [28] B. A. Campbell, S. Davidson, J. R. Ellis, and K. A. Olive, “Cosmological baryon asymmetry constraints on extensions of the standard model,” *Phys. Lett.* **B256** (1991) 484–490.
- [29] H. K. Dreiner and G. G. Ross, “Sphaleron erasure of primordial baryogenesis,” *Nucl. Phys.* **B410** (1993) 188–216, [arXiv:hep-ph/9207221](#).
- [30] H. Goldberg, “Constraint on the photino mass from cosmology,” *Phys. Rev. Lett.* **50** (1983) 1419.
- [31] J. R. Ellis, J. S. Hagelin, D. V. Nanopoulos, K. A. Olive, and M. Srednicki, “Supersymmetric relics from the big bang,” *Nucl. Phys.* **B238** (1984) 453–476.
- [32] T. Appelquist, H.-C. Cheng, and B. A. Dobrescu, “Bounds on universal extra dimensions,” *Phys. Rev.* **D64** (2001) 035002, [arXiv:hep-ph/0012100](#).

- [33] H.-C. Cheng, J. L. Feng, and K. T. Matchev, “Kaluza-Klein dark matter,” *Phys. Rev. Lett.* **89** (2002) 211301, [arXiv:hep-ph/0207125](#).
- [34] G. Servant and T. M. P. Tait, “Is the lightest Kaluza-Klein particle a viable dark matter candidate?,” *Nucl. Phys.* **B650** (2003) 391–419, [arXiv:hep-ph/0206071](#).
- [35] O. Klein, “Quantum theory and five-dimensional theory of relativity,” *Z. Phys.* **37** (1926) 895–906.
- [36] J. L. Feng, A. Rajaraman, and F. Takayama, “Superweakly-interacting massive particles,” *Phys. Rev. Lett.* **91** (2003) 011302, [arXiv:hep-ph/0302215](#).
- [37] J. L. Feng, A. Rajaraman, and F. Takayama, “SuperWIMP Dark Matter Signals from the Early Universe,” *Phys. Rev.* **D68** (2003) 063504, [arXiv:hep-ph/0306024](#).
- [38] L. M. Krauss, “New Constraints on Ino Masses from Cosmology. 1. Supersymmetric Inos,” *Nucl. Phys.* **B227** (1983) 556.
- [39] D. V. Nanopoulos, K. A. Olive, and M. Srednicki, “After Primordial Inflation,” *Phys. Lett.* **B127** (1983) 30.
- [40] J. R. Ellis, J. E. Kim, and D. V. Nanopoulos, “Cosmological Gravitino Regeneration and Decay,” *Phys. Lett.* **B145** (1984) 181.
- [41] J. R. Ellis, D. V. Nanopoulos, and S. Sarkar, “The Cosmology of Decaying Gravitinos,” *Nucl. Phys.* **B259** (1985) 175.
- [42] W. Buchmuller, K. Hamaguchi, M. Ratz, and T. Yanagida, “Supergravity at colliders,” *Phys. Lett.* **B588** (2004) 90–98, [arXiv:hep-ph/0402179](#).
- [43] J. R. Ellis, K. A. Olive, Y. Santoso, and V. C. Spanos, “Gravitino dark matter in the CMSSM,” *Phys. Lett.* **B588** (2004) 7–16, [arXiv:hep-ph/0312262](#).
- [44] F. Wang and J. M. Yang, “SuperWIMP dark matter scenario in light of WMAP,” *Eur. Phys. J.* **C38** (2004) 129–133, [arXiv:hep-ph/0405186](#).
- [45] L. Roszkowski, R. Ruiz de Austri, and K.-Y. Choi, “Gravitino dark matter in the CMSSM and implications for leptogenesis and the LHC,” *JHEP* **08** (2005) 080, [arXiv:hep-ph/0408227](#).
- [46] H. Baer and A. D. Box, “Fine-tuning favors mixed axion/axino cold dark matter over neutralinos in the minimal supergravity model,” [arXiv:0910.0333 \[hep-ph\]](#).
- [47] E. W. Kolb, D. Seckel, and M. S. Turner, “The Shadow World,” *Nature* **314** (1985) 415–419.
- [48] J. L. Feng and J. Kumar, “The WIMPless Miracle: Dark-Matter Particles without Weak-Scale Masses or Weak Interactions,” *Phys. Rev. Lett.* **101** (2008) 231301, [arXiv:0803.4196 \[hep-ph\]](#).
- [49] S. Nussinov, “Technocosmology could a technibaryon excess provide a “natural” missing mass candidate? ,” *Phys. Lett.* **B165** (1985) 55.
- [50] D. B. Kaplan, “A Single explanation for both the baryon and dark matter densities,” *Phys. Rev. Lett.* **68** (1992) 741–743.

- [51] R. D. Peccei and H. R. Quinn, “CP Conservation in the Presence of Instantons,” *Phys. Rev. Lett.* **38** (1977) 1440–1443.
- [52] F. Wilczek, “Problem of Strong p and t Invariance in the Presence of Instantons,” *Phys. Rev. Lett.* **40** (1978) 279–282.
- [53] S. Weinberg, “A New Light Boson?,” *Phys. Rev. Lett.* **40** (1978) 223–226.
- [54] **SINDRUM** Collaboration, R. Eichler *et al.*, “Limits for short-lived neutral particles emitted in μ^+ or π^+ decay,” *Phys. Lett.* **B175** (1986) 101.
- [55] G. G. Raffelt, “Astrophysical methods to constrain axions and other novel particle phenomena,” *Phys. Rept.* **198** (1990) 1–113.
- [56] J. Preskill, M. B. Wise, and F. Wilczek, “Cosmology of the invisible axion,” *Phys. Lett.* **B120** (1983) 127–132.
- [57] L. F. Abbott and P. Sikivie, “A cosmological bound on the invisible axion,” *Phys. Lett.* **B120** (1983) 133–136.
- [58] M. Dine and W. Fischler, “The not-so-harmless axion,” *Phys. Lett.* **B120** (1983) 137–141.
- [59] K. J. Bae, J.-H. Huh, and J. E. Kim, “Update of axion CDM energy,” *JCAP* **0809** (2008) 005, [arXiv:0806.0497](https://arxiv.org/abs/0806.0497) [hep-ph].
- [60] L. J. Gleeson and W. I. Axford, “Solar Modulation of Galactic Cosmic Rays,” *Astrophys. J.* **154** (1968) 1011.
- [61] **Pierre Auger** Collaboration, J. Abraham *et al.*, “Observation of the suppression of the flux of cosmic rays above 4×10^{19} eV,” *Phys. Rev. Lett.* **101** (2008) 061101, [arXiv:0806.4302](https://arxiv.org/abs/0806.4302) [astro-ph].
- [62] K. Greisen, “End to the cosmic ray spectrum?,” *Phys. Rev. Lett.* **16** (1966) 748–750.
- [63] G. T. Zatsepin and V. A. Kuzmin, “Upper limit of the spectrum of cosmic rays,” *JETP Lett.* **4** (1966) 78–80.
- [64] Strong, A. GCR database. <http://www.mpe.mpg.de/~aws/propagate.html>.
- [65] **HiRes** Collaboration, R. U. Abbasi *et al.*, “Indications of Proton-Dominated Cosmic Ray Composition above 1.6 EeV,” *Phys. Rev. Lett.* **104** (2010) 161101, [arXiv:0910.4184](https://arxiv.org/abs/0910.4184) [astro-ph.HE].
- [66] **Pierre Auger** Collaboration, J. Abraham *et al.*, “Measurement of the Depth of Maximum of Extensive Air Showers above 10^{18} eV,” *Phys. Rev. Lett.* **104** (2010) 091101, [arXiv:1002.0699](https://arxiv.org/abs/1002.0699) [astro-ph.HE].
- [67] **Pierre Auger** Collaboration, J. Abraham *et al.*, “Correlation of the highest energy cosmic rays with nearby extragalactic objects,” *Science* **318** (2007) 938–943, [arXiv:0711.2256](https://arxiv.org/abs/0711.2256) [astro-ph].
- [68] **Pierre Auger** Collaboration, J. Abraham *et al.*, “Correlation of the highest-energy cosmic rays with the positions of nearby active galactic nuclei,” *Astropart. Phys.* **29** (2008) 188–204, [arXiv:0712.2843](https://arxiv.org/abs/0712.2843) [astro-ph].

- [69] D. Eichler, “Basic inconsistencies in models of interstellar cosmic-ray acceleration,” *Astrophys. J.* **237** (1980) 809–813.
- [70] R. Cowsik, “Comments on stochastic acceleration of cosmic rays,” *Astrophys. J.* **241** (1980) 1195.
- [71] S. P. Reynolds, “Models of Synchrotron X-Rays from Shell Supernova Remnants,” *Astrophys. J.* **493** (Jan., 1998) 375–+.
- [72] D. Caprioli, P. Blasi, and E. Amato, “On the escape of particles from cosmic ray modified shocks,” *Mon. Not. R. Astron. Soc.* **396** (2009) 2065–2073, [arXiv:0807.4259 \[astro-ph\]](#).
- [73] K. Koyama *et al.*, “Evidence for shock acceleration of high-energy electrons in the supernova remnant SN1006,” *Nature* **378** (1995) 255–258.
- [74] S. G. Lucek and A. R. Bell, “Non-linear amplification of a magnetic field driven by cosmic ray streaming,” *Mon. Not. R. Astron. Soc.* **314** (May, 2000) 65–74.
- [75] A. R. Bell and S. G. Lucek, “Cosmic ray acceleration to very high energy through the non-linear amplification by cosmic rays of the seed magnetic field,” *Mon. Not. R. Astron. Soc.* **321** (Mar., 2001) 433–438.
- [76] I. S. Shklovskii, *Dokl. Akad. Nauk SSSR* **91**(3) (1953) 475.
- [77] L. D. Landau and E. M. Lifshitz, *Fluid mechanics*. Pergamon Press, Oxford, 1959.
- [78] L. I. Sedov, *Similarity and Dimensional Methods in Mechanics*. Academic Press, New York, 1959.
- [79] J. K. Truelove and C. F. McKee, “Evolution of Nonradiative Supernova Remnants,” *Astrophys. J. Suppl.* **120** (Feb., 1999) 299–326.
- [80] J. M. Blondin, E. B. Wright, K. J. Borkowski, and S. P. Reynolds, “Transition to the Radiative Phase in Supernova Remnants,” *Astrophys. J.* **500** (June, 1998) 342–+.
- [81] R. Blandford and D. Eichler, “Particle acceleration at astrophysical shocks: A theory of cosmic ray origin,” *Phys. Rep.* **154** (Oct., 1987) 1–75.
- [82] P. C. Clemmow and J. P. Dougherty, *Electrodynamics of Charged Particles and Plasmas*. Addison Wesley, Chicago, 1969.
- [83] E. M. Lifshitz and L. P. Pitaevskii, *Physical kinetics*. Pergamon Press, Oxford, 1981.
- [84] C. Lacombe, “Acceleration of particles and plasma heating by turbulent Alfvén waves in a radiogalaxy,” *Astron. & Astrophys.* **54** (Jan., 1977) 1–16. [ADS](#).
- [85] E. Fermi, “On the Origin of the Cosmic Radiation,” *Physical Review* **75** (Apr., 1949) 1169–1174.
- [86] M. A. Malkov and L. O’C Drury, “Nonlinear theory of diffusive acceleration of particles by shock waves,” *Rept. Prog. Phys.* **64** (2001) 429–481.
- [87] G. F. Krymskii, “A regular mechanism for the acceleration of charged particles on the front of a shock wave,” *Akademiia Nauk SSSR Doklady* **234** (June, 1977) 1306–1308.

- [88] W. I. Axford, E. Leer, and G. Skadron, “The Acceleration of Cosmic Rays by Shock Waves,” in *International Cosmic Ray Conference*, vol. 11 of *International Cosmic Ray Conference*, pp. 132–+. 1977. [ADS](#).
- [89] R. D. Blandford and J. P. Ostriker, “Particle acceleration by astrophysical shocks,” *Astrophys. J.* **221** (Apr., 1978) L29–L32.
- [90] A. R. Bell, “The acceleration of cosmic rays in shock fronts. I,” *Mon. Not. R. Astron. Soc.* **182** (Jan., 1978) 147–156. [ADS](#).
- [91] L. O. Drury, “An introduction to the theory of diffusive shock acceleration of energetic particles in tenuous plasmas,” *Reports on Progress in Physics* **46** (Aug., 1983) 973–1027.
- [92] J. A. Peacock, “Fermi acceleration by relativistic shock waves,” *Mon. Not. R. Astron. Soc.* **196** (July, 1981) 135–152. [ADS](#).
- [93] F. C. Michel, “The power-law spectrum of shock-accelerated relativistic particles,” *Astrophys. J.* **247** (July, 1981) 664–670.
- [94] D. Breitschwerdt and S. Komossa, “Galactic fountains and galactic winds,” *Astrophys. Space Sci.* **272** (2000) 3–13, [arXiv:astro-ph/9908003](#).
- [95] J. R. Jokipii, “Consequences of a Lifetime Greater Than 10^{*7} Years for Galactic Cosmic Rays,” *Astrophys. J.* **208** (1976) 900–902.
- [96] A. J. Owens and J. R. Jokipii, “Cosmic Rays in a Dynamical Halo. 1. Age and Matter Traversal Distributions and Anisotropy for Nuclei,” *Astrophys. J.* **215** (1977) 677–684.
- [97] A. J. Owens and J. R. Jokipii, “Cosmic Rays in a Dynamical Halo. 2. Electrons,” *Astrophys. J.* **215** (1977) 685–689.
- [98] F. C. Jones, “The History of Cosmic Rays in a Dynamical Halo: A Retrodictive Probability Approach,” *Astrophys. J.* **222** (1978) 1097–1103.
- [99] F. C. Jones, “The dynamical halo and the variation of cosmic-ray path length with energy,” *Astrophys. J.* **229** (Apr., 1979) 747–752.
- [100] J. B. G. M. Bloemen, V. A. Dogiel, V. L. Dorman, and V. S. Ptuskin, “Galactic diffusion and wind models of cosmic-ray transport. I - Insight from CR composition studies and gamma-ray observations,” *Astron. & Astrophys.* **267** (Jan., 1993) 372–387. [ADS](#).
- [101] D. Maurin, R. Taillet, and F. Donato, “New results on source and diffusion spectral features of Galactic cosmic rays: I- B/C ratio,” *Astron. Astrophys.* **394** (2002) 1039–1056, [arXiv:astro-ph/0206286](#).
- [102] F. C. Jones, A. Lukasiak, V. Ptuskin, and W. Webber, “The Modified Weighted Slab Technique: Models and Results,” *Astrophys. J.* **547** (Jan., 2001) 264–271, [arXiv:astro-ph/0007293](#).
- [103] V. S. Ptuskin, I. V. Moskalenko, F. C. Jones, A. W. Strong, and V. N. Zirakashvili, “Dissipation of Magnetohydrodynamic Waves on Energetic Particles: Impact on Interstellar Turbulence and Cosmic Ray Transport,” *Astrophys. J.* **642** (2006) 902–916, [arXiv:astro-ph/0510335](#).

- [104] M. Simon, W. Heinrich, and K. D. Mathis, “Propagation of injected cosmic rays under distributed reacceleration,” *Astrophys. J.* **300** (Jan., 1986) 32–40.
- [105] E. S. Seo and V. S. Ptuskin, “Stochastic reacceleration of cosmic rays in the interstellar medium,” *Astrophys. J.* **431** (Aug., 1994) 705–714.
- [106] A. Crusius and R. Schlickeiser, “Synchrotron radiation in a thermal plasma with large-scale random magnetic fields,” *Astron. & Astrophys.* **196** (May, 1988) 327–337. [ADS](#).
- [107] T. Kobayashi, Y. Komori, K. Yoshida, and J. Nishimura, “The Most Likely Sources of High Energy Cosmic-Ray Electrons in Supernova Remnants,” *Astrophys. J.* **601** (2004) 340–351, [arXiv:astro-ph/0308470](#).
- [108] T. A. Porter, I. V. Moskalenko, A. W. Strong, E. Orlando, and L. Bouchet, “Inverse Compton Origin of the Hard X-Ray and Soft Gamma-Ray Emission from the Galactic Ridge,” *Astrophys. J.* **682** (2008) 400–407, [arXiv:0804.1774 \[astro-ph\]](#).
- [109] R. Schlickeiser and J. Ruppel, “Klein-Nishina steps in the energy spectrum of galactic cosmic ray electrons,” *New J. Phys.* **12** (2010) 033044, [arXiv:0908.2183 \[astro-ph.HE\]](#).
- [110] L. Stawarz, V. Petrosian, and R. D. Blandford, “On the Energy Spectra of GeV/TeV Cosmic Ray Leptons,” *Astrophys. J.* **710** (2010) 236–247, [arXiv:0908.1094 \[astro-ph.GA\]](#).
- [111] T. Delahaye, J. Lavalle, R. Lineros, F. Donato, and N. Fornengo, “Galactic electrons and positrons at the Earth: new estimate of the primary and secondary fluxes,” [arXiv:1002.1910 \[astro-ph.HE\]](#).
- [112] T. Kamae, N. Karlsson, T. Mizuno, T. Abe, and T. Koi, “Parameterization of gamma, e⁺- and neutrino spectra produced by p p interaction in astronomical environment,” *Astrophys. J.* **647** (2006) 692–708, [arXiv:astro-ph/0605581](#).
- [113] S. R. Kelner, F. A. Aharonian, and V. V. Bugayov, “Energy spectra of gamma-rays, electrons and neutrinos produced at proton proton interactions in the very high energy regime,” *Phys. Rev.* **D74** (2006) 034018, [arXiv:astro-ph/0606058](#).
- [114] D. Müller, J. J. Connel, A. Decourchelle, R. Mewaldt, S. Reynolds, A. Strong, H. Völk, and M. Wiedenbeck, “Key Measurements in the Future - Working Group Report,” *Space Sci. Rev.* **99** (Oct., 2001) 353–373. [ADS](#).
- [115] T. Shibata, M. Hareyama, M. Nakazawa, and C. Saito, “A Possible Approach to Three-dimensional Cosmic-Ray Propagation in the Galaxy. II. Stable Nuclei with Energy Change,” *Astrophys. J.* **642** (May, 2006) 882–901.
- [116] C. Evoli, D. Gaggero, D. Grasso, and L. Maccione, “Cosmic-Ray Nuclei, Antiprotons and Gamma-rays in the Galaxy: a New Diffusion Model,” *JCAP* **0810** (2008) 018, [arXiv:0807.4730 \[astro-ph\]](#).
- [117] R. Cowsik, Y. Pal, S. N. Tandon, and R. P. Verma, “Steady State of Cosmic-Ray Nuclei-Their Spectral Shape and Path Length at Low Energies,” *Physical Review* **158** (June, 1967) 1238–1242.

- [118] V. S. Ptuskin, O. N. Strelnikova, and L. G. Sveshnikova, “On leaky-box approximation to GALPROP,” *Astropart. Phys.* **31** (2009) 284–289.
- [119] R. J. Protheroe, J. F. Ormes, and G. M. Comstock, “Interpretation of cosmic ray composition - The path length distribution,” *Astrophys. J.* **247** (July, 1981) 362–373.
- [120] M. Garcia-Munoz, J. A. Simpson, T. G. Guzik, J. P. Wefel, and S. H. Margolis, “Cosmic-ray propagation in the Galaxy and in the heliosphere - The path-length distribution at low energy,” *Astrophys. J. Suppl.* **64** (May, 1987) 269–304.
- [121] V. L. Ginzburg and S. I. Syrovatskii, *The Origin of Cosmic Rays*. Macmillan, New York, 1964.
- [122] R. Cowsik and M. A. Lee, “On the sources of cosmic ray electrons,” *Astrophys. J.* **228** (Feb., 1979) 297–301.
- [123] F. A. Aharonian, A. M. Atoyan, and H. J. Volk, “High energy electrons and positrons in cosmic rays as an indicator of the existence of a nearby cosmic tevatron,” *Astron. Astrophys.* **294** (1995) L41–L44. [ADS](#).
- [124] Atoian, A. M. and Aharonian, F. A. and Völk, H. J., “Electrons and positrons in the galactic cosmic rays,” *Phys. Rev.* **D52** (1995) 3265–3275.
- [125] E. A. Baltz and J. Edsjo, “Positron Propagation and Fluxes from Neutralino Annihilation in the Halo,” *Phys. Rev.* **D59** (1998) 023511, [arXiv:astro-ph/9808243](#).
- [126] I. V. Moskalenko and A. W. Strong, “Production and propagation of cosmic-ray positrons and electrons,” *Astrophys. J.* **493** (1998) 694–707, [arXiv:astro-ph/9710124](#).
- [127] “GALPROP.” GALPROP website. <http://galprop.stanford.edu>.
- [128] D. Maurin, F. Donato, R. Taillet, and P. Salati, “Cosmic Rays below Z=30 in a diffusion model: new constraints on propagation parameters,” *Astrophys. J.* **555** (2001) 585–596, [arXiv:astro-ph/0101231](#).
- [129] F. Donato *et al.*, “Antiprotons from spallation of cosmic rays on interstellar matter,” *Astrophys. J.* **563** (2001) 172–184, [arXiv:astro-ph/0103150](#).
- [130] F. Donato, D. Maurin, and R. Taillet, “ β -Radioactive Cosmic Rays in a diffusion model: test for a local bubble?,” *Astron. Astrophys.* **381** (2002) 539–559, [arXiv:astro-ph/0108079](#).
- [131] A. Putze, L. Derome, and D. Maurin, “A Markov Chain Monte Carlo technique to sample transport and source parameters of Galactic cosmic rays: II. Results for the diffusion model combining B/C and radioactive nuclei,” *Astron. Astrophys.* **516** (2010) A66, [arXiv:1001.0551 \[astro-ph.HE\]](#).
- [132] I. V. Moskalenko, A. W. Strong, J. F. Ormes, and M. S. Potgieter, “Secondary Antiprotons and Propagation of Cosmic Rays in the Galaxy and Heliosphere,” *Astrophys. J.* **565** (Jan., 2002) 280–296, [arXiv:astro-ph/0106567](#).
- [133] J. Alcaraz *et al.*, “Cosmic protons,” *Physics Letters B* **490** (Sept., 2000) 27–35.

- [134] T. Sanuki *et al.*, “Precise Measurement of Cosmic-Ray Proton and Helium Spectra with the BESS Spectrometer,” *Astrophys. J.* **545** (Dec., 2000) 1135–1142, [arXiv:astro-ph/0002481](#).
- [135] M. Boezio *et al.*, “The Cosmic-Ray Proton and Helium Spectra between 0.4 and 200 GV,” *Astrophys. J.* **518** (June, 1999) 457–472.
- [136] W. Menn *et al.*, “The Absolute Flux of Protons and Helium at the Top of the Atmosphere Using IMAX,” *Astrophys. J.* **533** (Apr., 2000) 281–297.
- [137] E. S. Seo *et al.*, “Measurement of cosmic-ray proton and helium spectra during the 1987 solar minimum,” *Astrophys. J.* **378** (Sept., 1991) 763–772.
- [138] I. P. Ivanenko, V. Y. Shestoporov, *et al.*, “Energy Spectra of Cosmic Rays above 2 TeV as Measured by the ‘SOKOL’ Apparatus,” in *International Cosmic Ray Conference*, vol. 2 of *International Cosmic Ray Conference*, pp. 17–+. 1993. [ADS](#).
- [139] K. Asakimori *et al.*, “Cosmic-Ray Proton and Helium Spectra: Results from the JACEE Experiment,” *Astrophys. J.* **502** (July, 1998) 278–+.
- [140] A. J. Davis *et al.*, “On the low energy decrease in galactic cosmic ray secondary/primary ratios,” in *Acceleration and Transport of Energetic Particles Observed in the Heliosphere*, R. A. Mewaldt and others, ed., vol. 528 of *American Institute of Physics Conference Series*, pp. 421–424. Sept., 2000.
- [141] A. J. Davis *et al.*, “The Evolution of Galactic Cosmic Ray Element Spectra from Solar Minimum to Solar Maximum,” in *International Cosmic Ray Conference*, vol. 10 of *International Cosmic Ray Conference*, pp. 3971–+. Aug., 2001. [ADS](#).
- [142] J. J. Engelmann *et al.*, “Charge composition and energy spectra of cosmic-ray nuclei for elements from Be to Ni - Results from HEAO-3-C2,” *Astron. & Astrophys.* **233** (July, 1990) 96–111. [ADS](#).
- [143] S. A. Stephens and R. E. Streitmatter, “Cosmic-Ray Propagation in the Galaxy: Techniques and the Mean Matter Traversal,” *Astrophys. J.* **505** (Sept., 1998) 266–277.
- [144] M. Boezio *et al.*, “The Cosmic-Ray Antiproton Flux between 0.62 and 3.19 GeV Measured Near Solar Minimum Activity,” *Astrophys. J.* **487** (Sept., 1997) 415–+.
- [145] M. Boezio *et al.*, “The Cosmic-Ray Antiproton Flux between 3 and 49 GeV,” *Astrophys. J.* **561** (Nov., 2001) 787–799.
- [146] Y. Asaoka *et al.*, “Measurements of cosmic-ray low-energy antiproton and proton spectra in a transient period of the solar field reversal,” *Phys. Rev. Lett.* **88** (2002) 051101, [arXiv:astro-ph/0109007](#).
- [147] K. Abe *et al.*, “Measurement of cosmic-ray low-energy antiproton spectrum with the first BESS-Polar Antarctic flight,” *Phys. Lett.* **B670** (2008) 103–108, [arXiv:0805.1754 \[astro-ph\]](#).
- [148] M. Aguilar *et al.*, “The Alpha Magnetic Spectrometer (AMS) on the International Space Station: Part I - results from the test flight on the space shuttle,” *Physics Reports* **366** no. 6, (2002) 331 – 405.

- [149] **PAMELA** Collaboration, O. Adriani *et al.*, “PAMELA results on the cosmic-ray antiproton flux from 60 MeV to 180 GeV in kinetic energy,” [arXiv:1007.0821 \[astro-ph.HE\]](#).
- [150] Beach, A. S. *et al.*, “Measurement of the cosmic-ray antiproton-to-proton abundance ratio between 4 and 50 gev,” *Phys. Rev. Lett.* **87** no. 27, (Dec, 2001) 271101.
- [151] M. Simon, A. Molnar, and S. Roesler, “A New Calculation of the Interstellar Secondary Cosmic-Ray Antiprotons,” *Astrophys. J.* **499** (May, 1998) 250–+.
- [152] F. Donato, D. Maurin, P. Brun, T. Delahaye, and P. Salati, “Constraints on WIMP Dark Matter from the High Energy PAMELA \bar{p}/p data,” *Phys. Rev. Lett.* **102** (2009) 071301, [arXiv:0810.5292 \[astro-ph\]](#).
- [153] M. A. Duvernois, J. A. Simpson, and M. R. Thayer, “Interstellar propagation of cosmic rays: analysis of the ULYSSES primary and secondary elemental abundances.,” *Astron. Astrophys.* **316** (Dec., 1996) 555–563. [ADS](#).
- [154] A. Lukasiak, F. B. McDonald, and W. R. Webber, “Voyager Measurements of the Charge and Isotopic Composition of Cosmic Ray Li, Be and B Nuclei and Implications for Their Production in the Galaxy,” in *International Cosmic Ray Conference*, vol. 3 of *International Cosmic Ray Conference*, pp. 41–+. Aug., 1999. [ADS](#).
- [155] J. F. Navarro, C. S. Frenk, and S. D. M. White, “The Structure of Cold Dark Matter Halos,” *Astrophys. J.* **462** (1996) 563–575, [arXiv:astro-ph/9508025](#).
- [156] P. D. Serpico, “On the possible causes of a rise with energy of the cosmic ray positron fraction,” *Phys. Rev.* **D79** (2009) 021302, [arXiv:0810.4846 \[hep-ph\]](#).
- [157] T. Delahaye *et al.*, “Galactic secondary positron flux at the Earth,” *Astron. Astrophys.* **501** (2009) 821–833, [arXiv:0809.5268 \[astro-ph\]](#).
- [158] M. *et al.* Boezio, “The Cosmic-Ray Electron and Positron Spectra Measured at 1 AU during Solar Minimum Activity,” *Astrophys. J.* **532** (Mar., 2000) 653–669.
- [159] **HEAT** Collaboration, S. W. Barwick *et al.*, “Measurements of the Cosmic-Ray Positron Fraction from 1 to 50 GeV,” *Astrophys. J. Lett.* **482** (June, 1997) L191+, [arXiv:astro-ph/9703192](#).
- [160] **AMS-01** Collaboration, M. Aguilar *et al.*, “Cosmic-ray positron fraction measurement from 1-GeV to 30- GeV with AMS-01,” *Phys. Lett.* **B646** (2007) 145–154, [arXiv:astro-ph/0703154](#).
- [161] J. Alcaraz *et al.*, “Leptons in near earth orbit,” *Physics Letters B* **484** (June, 2000) 10–22.
- [162] C. Grimani *et al.*, “Measurements of the absolute energy spectra of cosmic-ray positrons and electrons above 7 GeV,” *Astron. & Astrophys.* **392** (Sept., 2002) 287–294.
- [163] **PAMELA** Collaboration, O. Adriani *et al.*, “An anomalous positron abundance in cosmic rays with energies 1.5.100 GeV,” *Nature* **458** (2009) 607–609, [arXiv:0810.4995 \[astro-ph\]](#).
- [164] M. Boezio, “Recent PAMELA Results.” Talk at UCLA Dark Matter 2010, Marina del Rey, California, 24-26 February , 2010, 2010. <http://www.physics.ucla.edu/hep/dm10/talks/boezio.pdf>.

- [165] J. J. Beatty *et al.*, “New Measurement of the Cosmic-Ray Positron Fraction from 5 to 15GeV,” *Physical Review Letters* **93** no. 24, (Dec., 2004) 241102–+, [arXiv:astro-ph/0412230](#).
- [166] A. Boulares, “The nature of the cosmic-ray electron spectrum, and supernova remnant contributions,” *Astrophys. J.* **342** (July, 1989) 807–813.
- [167] **PPB-BETS** Collaboration, S. Torii *et al.*, “High-energy electron observations by PPB-BETS flight in Antarctica,” [arXiv:0809.0760 \[astro-ph\]](#).
- [168] J. Chang *et al.*, “An excess of cosmic ray electrons at energies of 300-800 GeV,” *Nature* **456** (2008) 362–365.
- [169] **The Fermi LAT** Collaboration, A. A. Abdo *et al.*, “Measurement of the Cosmic Ray e+ plus e- spectrum from 20 GeV to 1 TeV with the Fermi Large Area Telescope,” *Phys. Rev. Lett.* **102** (2009) 181101, [arXiv:0905.0025 \[astro-ph.HE\]](#).
- [170] S. Profumo, “Dissecting Pamela (and ATIC) with Occam’s Razor: existing, well-known Pulsars naturally account for the ‘anomalous’ Cosmic-Ray Electron and Positron Data,” [arXiv:0812.4457 \[astro-ph\]](#).
- [171] J. N. Bahcall and R. M. Soneira, “The universe at faint magnitudes. I - Models for the galaxy and the predicted star counts,” *Astrophys. J. Suppl.* **44** (1980) 73–110.
- [172] M. Cirelli, M. Kadastik, M. Raidal, and A. Strumia, “Model-independent implications of the e+, e-, anti-proton cosmic ray spectra on properties of Dark Matter,” *Nucl. Phys.* **B813** (2009) 1–21, [arXiv:0809.2409 \[hep-ph\]](#).
- [173] P. Brun, T. Delahaye, J. Diemand, S. Profumo, and P. Salati, “The cosmic ray lepton puzzle in the light of cosmological N-body simulations,” *Phys. Rev.* **D80** (2009) 035023, [arXiv:0904.0812 \[astro-ph.HE\]](#).
- [174] M. Ibe, H. Murayama, and T. T. Yanagida, “Breit-Wigner Enhancement of Dark Matter Annihilation,” *Phys. Rev.* **D79** (2009) 095009, [arXiv:0812.0072 \[hep-ph\]](#).
- [175] A. Sommerfeld, “ber die Beugung und Bremsung der Elektronen,” *Ann. Phys.* **403** (1931) 257.
- [176] J. Hisano, S. Matsumoto, and M. M. Nojiri, “Explosive dark matter annihilation,” *Phys. Rev. Lett.* **92** (2004) 031303, [arXiv:hep-ph/0307216](#).
- [177] J. Hisano, S. Matsumoto, M. Nagai, O. Saito, and M. Senami, “Non-perturbative Effect on Thermal Relic Abundance of Dark Matter,” *Phys. Lett.* **B646** (2007) 34–38, [arXiv:hep-ph/0610249](#).
- [178] G. Kane, R. Lu, and S. Watson, “PAMELA Satellite Data as a Signal of Non-Thermal Wino LSP Dark Matter,” *Phys. Lett.* **B681** (2009) 151–160, [arXiv:0906.4765 \[astro-ph.HE\]](#).
- [179] F. Donato, N. Fornengo, D. Maurin, and P. Salati, “Antiprotons in cosmic rays from neutralino annihilation,” *Phys. Rev.* **D69** (2004) 063501, [arXiv:astro-ph/0306207](#).
- [180] N. Arkani-Hamed, D. P. Finkbeiner, T. R. Slatyer, and N. Weiner, “A Theory of Dark Matter,” *Phys. Rev.* **D79** (2009) 015014, [arXiv:0810.0713 \[hep-ph\]](#).

- [181] F. Donato, N. Fornengo, and P. Salati, “Antideuterons as a signature of supersymmetric dark matter,” *Phys. Rev.* **D62** (2000) 043003, [arXiv:hep-ph/9904481](#).
- [182] F. Donato, N. Fornengo, and D. Maurin, “Antideuteron fluxes from dark matter annihilation in diffusion models,” *Phys. Rev.* **D78** (2008) 043506, [arXiv:0803.2640 \[hep-ph\]](#).
- [183] H. Fuke *et al.*, “Search for Cosmic-Ray Antideuterons,” *Phys. Rev. Lett.* **95** (2005) 081101, [arXiv:astro-ph/0504361](#).
- [184] H. Fuke *et al.*, “Current status and future plans for the general antiparticle spectrometer (GAPS),” *Advances in Space Research* **41** (2008) 2056–2060.
- [185] **FERMI-LAT** Collaboration, D. Grasso *et al.*, “On possible interpretations of the high energy electron- positron spectrum measured by the Fermi Large Area Telescope,” *Astropart. Phys.* **32** (2009) 140–151, [arXiv:0905.0636 \[astro-ph.HE\]](#).
- [186] **H.E.S.S.** Collaboration, F. Aharonian *et al.*, “The energy spectrum of cosmic-ray electrons at TeV energies,” *Phys. Rev. Lett.* **101** (2008) 261104, [arXiv:0811.3894 \[astro-ph\]](#).
- [187] K. K. Tang, “The energy spectrum of electrons and cosmic-ray confinement A new measurement and its interpretation,” *Astrophys. J.* **278** (1984) 881–892.
- [188] T. Kobayashi, “High Energy Cosmic-Ray Electrons Beyond 100 GeV,” in *Proceedings of the 30th International Cosmic Ray Conference, Salt Lake City, Utah, USA*, vol. 3 of *International Cosmic Ray Conference*, pp. 61–+. Aug., 1999. [ADS](#).
- [189] M. A. DuVernois *et al.*, “Cosmic-Ray Electrons and Positrons from 1 to 100 GeV: Measurements with HEAT and Their Interpretation,” *Astrophys. J.* **559** (Sept., 2001) 296–303.
- [190] S. Torii *et al.*, “The Energy Spectrum of Cosmic-Ray Electrons from 10 to 100 GeV Observed with a Highly Granulated Imaging Calorimeter,” *Astrophys. J.* **559** (2001) 973–984.
- [191] A. W. Strong, I. V. Moskalenko, and O. Reimer, “Diffuse Galactic continuum gamma rays. A model compatible with EGRET data and cosmic-ray measurements,” *Astrophys. J.* **613** (2004) 962–976, [arXiv:astro-ph/0406254](#).
- [192] **H.E.S.S.** Collaboration, F. Aharonian *et al.*, “Probing the ATIC peak in the cosmic-ray electron spectrum with H.E.S.S.,” *Astron. Astrophys.* **508** (2009) 561, [arXiv:0905.0105 \[astro-ph.HE\]](#).
- [193] P. Meade, M. Papucci, A. Strumia, and T. Volansky, “Dark Matter Interpretations of the Electron/Positron Excesses after FERMI,” *Nucl. Phys.* **B831** (2010) 178–203, [arXiv:0905.0480 \[hep-ph\]](#).
- [194] L. Bergstrom, J. Edsjo, and G. Zaharijas, “Dark matter interpretation of recent electron and positron data,” *Phys. Rev. Lett.* **103** (2009) 031103, [arXiv:0905.0333 \[astro-ph.HE\]](#).
- [195] **LAT** Collaboration, W. B. Atwood *et al.*, “The Large Area Telescope on the Fermi Gamma-ray Space Telescope Mission,” *Astrophys. J.* **697** (2009) 1071–1102, [arXiv:0902.1089 \[astro-ph.IM\]](#).

- [196] J. F. Navarro, C. S. Frenk, and S. D. M. White, “A Universal Density Profile from Hierarchical Clustering,” *Astrophys. J.* **490** (1997) 493–508, [arXiv:astro-ph/9611107](#).
- [197] E. A. Baltz *et al.*, “Pre-launch estimates for GLAST sensitivity to Dark Matter annihilation signals,” *JCAP* **0807** (2008) 013, [arXiv:0806.2911 \[astro-ph\]](#).
- [198] A. W. Strong, I. V. Moskalenko, and O. Reimer, “Diffuse continuum gamma rays from the Galaxy,” *Astrophys. J.* **537** (2000) 763–784, [arXiv:astro-ph/9811296](#).
- [199] H. A. Mayer-Hasselwander *et al.*, “High-energy gamma ray emission from the galactic center,” *Astron. Astrophys.* **335** (1998) 161–172. [ADS](#).
- [200] S. Dodelson, D. Hooper, and P. D. Serpico, “Extracting the Gamma Ray Signal from Dark Matter Annihilation in the Galactic Center Region,” *Phys. Rev.* **D77** (2008) 063512, [arXiv:0711.4621 \[astro-ph\]](#).
- [201] L. Goodenough and D. Hooper, “Possible Evidence For Dark Matter Annihilation In The Inner Milky Way From The Fermi Gamma Ray Space Telescope,” [arXiv:0910.2998 \[hep-ph\]](#).
- [202] V. Vitale and A. Morselli, “Indirect Search for Dark Matter from the center of the Milky Way with the Fermi-Large Area Telescope,” [arXiv:0912.3828 \[astro-ph.HE\]](#).
- [203] **Fermi LAT** Collaboration, A. A. Abdo *et al.*, “Fermi Large Area Telescope Measurements of the Diffuse Gamma-Ray Emission at Intermediate Galactic Latitudes,” *Phys. Rev. Lett.* **103** (2009) 251101, [arXiv:0912.0973 \[astro-ph.HE\]](#).
- [204] S. D. Hunter *et al.*, “EGRET observations of the diffuse gamma-ray emission from the galactic plane,” *Astrophys. J.* **481** (1997) 205–240.
- [205] F. W. Stecker, S. D. Hunter, and D. A. Kniffen, “The Likely Cause of the EGRET GeV Anomaly and its Implications,” *Astropart. Phys.* **29** (2008) 25–29, [arXiv:0705.4311 \[astro-ph\]](#).
- [206] M. Cirelli, P. Panci, and P. D. Serpico, “Diffuse gamma ray constraints on annihilating or decaying Dark Matter after Fermi,” [arXiv:0912.0663 \[astro-ph.CO\]](#).
- [207] G. Dobler, D. P. Finkbeiner, I. Cholis, T. R. Slatyer, and N. Weiner, “The Fermi Haze: A Gamma-Ray Counterpart to the Microwave Haze,” [arXiv:0910.4583 \[astro-ph.HE\]](#).
- [208] T. Linden and S. Profumo, “Systematic Effects in Extracting a ‘Gamma-Ray Haze’ from Spatial Templates,” *Astrophys. J.* **714** (2010) L228–L232, [arXiv:1003.0002 \[astro-ph.GA\]](#).
- [209] M. Su, T. R. Slatyer, and D. P. Finkbeiner, “Giant Gamma-ray Bubbles from Fermi-LAT: AGN Activity or Bipolar Galactic Wind?,” [arXiv:1005.5480 \[astro-ph.HE\]](#).
- [210] J.-M. Casandjian and I. Grenier, for the Fermi Large Area Telescope Collaboration, “High Energy Gamma-Ray Emission from the Loop I region,” [arXiv:0912.3478 \[astro-ph.HE\]](#).
- [211] J. Lavalle, Q. Yuan, D. Maurin, and X. Bi, “Full calculation of clumpiness boost factors for antimatter cosmic rays in the light of Λ CDM N-body simulation results. Abandoning hope in clumpiness enhancement?,” *Astron. & Astrophys.* **479** (Feb., 2008) 427–452, [arXiv:0709.3634](#).

- [212] B. Willman *et al.*, “A New Milky Way Companion: Unusual Globular Cluster or Extreme Dwarf Satellite?,” *Astron. J.* **129** (2005) 2692–2700, [arXiv:astro-ph/0410416](#).
- [213] D. B. Zucker *et al.*, “A Curious New Milky Way Satellite in Ursa Major,” *Astrophys. J.* **650** (2006) L41–L44, [arXiv:astro-ph/0606633](#).
- [214] M. J. Irwin *et al.*, “Discovery of an Unusual Dwarf Galaxy in the Outskirts of the Milky Way,” *Astrophys. J.* **656** (2007) L13–L16, [arXiv:astro-ph/0701154](#).
- [215] S. M. Walsh, H. Jerjen, and B. Willman, “A Pair of Bootes: A New Milky Way Satellite,” *Astrophys. J.* **662** (2007) L83–L86, [arXiv:0705.1378](#) [[astro-ph](#)].
- [216] V. Belokurov *et al.*, “Segue 2: A Prototype of the Population of Satellites of Satellites,” *Mon. Not. R. Astron. Soc.* **397** (2009) 1748–1755, [arXiv:0903.0818](#) [[astro-ph.GA](#)].
- [217] SDSS Collaboration, D. G. York *et al.*, “The Sloan Digital Sky Survey: technical summary,” *Astron. J.* **120** (2000) 1579–1587, [arXiv:astro-ph/0006396](#).
- [218] A. A. Abdo *et al.*, “Observations of Milky Way Dwarf Spheroidal galaxies with the Fermi-LAT detector and constraints on Dark Matter models,” *Astrophys. J.* **712** (2010) 147–158, [arXiv:1001.4531](#) [[astro-ph.CO](#)].
- [219] A. A. Abdo *et al.*, “Fermi LAT Search for Photon Lines from 30 to 200 GeV and Dark Matter Implications,” *Phys. Rev. Lett.* **104** (2010) 091302, [arXiv:1001.4836](#) [[astro-ph.HE](#)].
- [220] A. W. Graham *et al.*, “Empirical models for Dark Matter Halos. I. Nonparametric Construction of Density Profiles and Comparison with Parametric Models,” *Astron. J.* **132** (2006) 2685, [arXiv:astro-ph/0509417](#).
- [221] J. F. Navarro *et al.*, “The Diversity and Similarity of Cold Dark Matter Halos,” [arXiv:0810.1522](#) [[astro-ph](#)].
- [222] Fermi-LAT Collaboration, A. A. Abdo *et al.*, “Constraints on Cosmological Dark Matter Annihilation from the Fermi-LAT Isotropic Diffuse Gamma-Ray Measurement,” *JCAP* **1004** (2010) 014, [arXiv:1002.4415](#) [[astro-ph.CO](#)].
- [223] M. Ackermann *et al.*, “Constraints on Dark Matter Annihilation in Clusters of Galaxies with the Fermi Large Area Telescope,” *JCAP* **1005** (2010) 025, [arXiv:1002.2239](#) [[astro-ph.CO](#)].
- [224] J. Dunkley *et al.*, “CMBPol Mission Concept Study: Prospects for polarized foreground removal,” [arXiv:0811.3915](#) [[astro-ph](#)].
- [225] D. P. Finkbeiner, “A Full-Sky H-alpha Template for Microwave Foreground Prediction,” *Astrophys. J. Suppl.* **146** (2003) 407, [arXiv:astro-ph/0301558](#).
- [226] D. J. Schlegel, D. P. Finkbeiner, and M. Davis, “Maps of Dust IR Emission for Use in Estimation of Reddening and CMBR Foregrounds,” *Astrophys. J.* **500** (1998) 525, [arXiv:astro-ph/9710327](#).
- [227] D. P. Finkbeiner, M. Davis, and D. J. Schlegel, “Extrapolation of Galactic Dust Emission at 100 Microns to CMBR Frequencies Using FIRAS,” *Astrophys. J.* **524** (1999) 867–886, [arXiv:astro-ph/9905128](#).

- [228] B. T. Draine and A. Lazarian, “Electric Dipole Radiation from Spinning Dust Grains,” *Astrophys. J.* **508** (1998) 157–179, [arXiv:astro-ph/9802239](#).
- [229] G. Dobler and D. P. Finkbeiner, “Identification of Spinning Dust in H α -Correlated Microwave Emission,” *Astrophys. J.* **680** (2008) 1235–1242, [arXiv:0712.2238](#) [[astro-ph](#)].
- [230] **WMAP** Collaboration, B. Gold *et al.*, “Five-Year Wilkinson Microwave Anisotropy Probe Observations: Galactic Foreground Emission,” *Astrophys. J. Suppl.* **180** (2009) 265–282, [arXiv:0803.0715](#) [[astro-ph](#)].
- [231] **WMAP** Collaboration, G. Hinshaw *et al.*, “Three-year Wilkinson Microwave Anisotropy Probe (WMAP) observations: Temperature analysis,” *Astrophys. J. Suppl.* **170** (2007) 288, [arXiv:astro-ph/0603451](#).
- [232] D. P. Finkbeiner, “Microwave ISM Emission Observed by WMAP,” *Astrophys. J.* **614** (2004) 186–193, [arXiv:astro-ph/0311547](#).
- [233] G. Dobler and D. P. Finkbeiner, “Extended Anomalous Foreground Emission in the WMAP 3-Year Data,” *Astrophys. J.* **680** (2008) 1222–1234, [arXiv:0712.1038](#) [[astro-ph](#)].
- [234] M. Bottino, A. J. Banday, and D. Maino, “New insights into foreground analysis of the WMAP five-year data using FASTICA,” *Mon.Not.Roy.Astron.Soc.* **402** (2009) 207–225, [arXiv:0910.4405](#) [[astro-ph.CO](#)].
- [235] C. Dickinson *et al.*, “Bayesian component separation and CMB estimation for the 5-year WMAP temperature data,” *Astrophys. J.* **705** (2009) 1607–1623, [arXiv:0903.4311](#) [[astro-ph.CO](#)].
- [236] D. T. Cumberbatch *et al.*, “Can the WMAP Haze really be a signature of annihilating neutralino dark matter?,” [arXiv:0902.0039](#) [[astro-ph.GA](#)].
- [237] B. Gold *et al.*, “Seven-Year Wilkinson Microwave Anisotropy Probe (WMAP) Observations: Galactic Foreground Emission,” [arXiv:1001.4555](#) [[astro-ph.GA](#)].
- [238] D. P. Finkbeiner, “WMAP microwave emission interpreted as dark matter annihilation in the inner Galaxy,” [arXiv:astro-ph/0409027](#).
- [239] D. Hooper, D. P. Finkbeiner, and G. Dobler, “Evidence Of Dark Matter Annihilations In The WMAP Haze,” *Phys. Rev.* **D76** (2007) 083012, [arXiv:0705.3655](#) [[astro-ph](#)].
- [240] T. Linden, S. Profumo, and B. Anderson, “The Morphology of the Galactic Dark Matter Synchrotron Emission with Self-Consistent Cosmic Ray Diffusion Models,” [arXiv:1004.3998](#) [[Unknown](#)].
- [241] M. Kaplinghat, D. J. Phalen, and K. M. Zurek, “Pulsars as the Source of the WMAP Haze,” *JCAP* **0912** (2009) 010, [arXiv:0905.0487](#) [[astro-ph.HE](#)].
- [242] J. P. Harding and K. N. Abazajian, “Morphological Tests of the Pulsar and Dark Matter Interpretations of the WMAP Haze,” *Phys. Rev.* **D81** (2010) 023505, [arXiv:0910.4590](#) [[astro-ph.CO](#)].
- [243] P. Blasi, “The origin of the positron excess in cosmic rays,” *Phys. Rev. Lett.* **103** (2009) 051104, [arXiv:0903.2794](#) [[astro-ph.HE](#)].

- [244] E. Borriello, A. Cuoco, and G. Miele, “Radio constraints on dark matter annihilation in the galactic halo and its substructures,” *Phys. Rev.* **D79** (2009) 023518, [arXiv:0809.2990 \[astro-ph\]](#).
- [245] L. Zhang, G. Sigl, and J. Redondo, “Galactic Signatures of Decaying Dark Matter,” *JCAP* **0909** (2009) 012, [arXiv:0905.4952 \[astro-ph.GA\]](#).
- [246] **IceCube** Collaboration, J. Ahrens *et al.*, “Sensitivity of the IceCube detector to astrophysical sources of high energy muon neutrinos,” *Astropart. Phys.* **20** (2004) 507–532, [arXiv:astro-ph/0305196](#).
- [247] **ICECUBE** Collaboration, R. Abbasi *et al.*, “Limits on a muon flux from neutralino annihilations in the Sun with the IceCube 22-string detector,” *Phys. Rev. Lett.* **102** (2009) 201302, [arXiv:0902.2460 \[astro-ph.CO\]](#).
- [248] J. Hisano *et al.*, “Neutrino Signals from Annihilating/Decaying Dark Matter in the Light of Recent Measurements of Cosmic Ray Electron/Positron Fluxes,” *Phys. Rev.* **D79** (2009) 043516, [arXiv:0812.0219 \[hep-ph\]](#).
- [249] C. Rott, “Search for Dark Matter from the Galactic Halo with IceCube,” [arXiv:0912.5183 \[astro-ph.HE\]](#).
- [250] R. J. Gaitskell, “Direct detection of dark matter,” *Ann. Rev. Nucl. Part. Sci.* **54** (2004) 315–359.
- [251] G. Bertone, ed., *Particle Dark Matter: Observations, Models and Searches*. Cambridge University Press, 2010.
- [252] K. Jedamzik, “Did something decay, evaporate, or annihilate during big bang nucleosynthesis?,” *Phys. Rev.* **D70** (2004) 063524, [arXiv:astro-ph/0402344](#).
- [253] K. Jedamzik, “Neutralinos and Big Bang nucleosynthesis,” *Phys. Rev.* **D70** (2004) 083510, [arXiv:astro-ph/0405583](#).
- [254] J. Hisano, M. Kawasaki, K. Kohri, T. Moroi, and K. Nakayama, “Cosmic Rays from Dark Matter Annihilation and Big-Bang Nucleosynthesis,” *Phys. Rev.* **D79** (2009) 083522, [arXiv:0901.3582 \[hep-ph\]](#).
- [255] K. Jedamzik and M. Pospelov, “Big Bang Nucleosynthesis and Particle Dark Matter,” *New J. Phys.* **11** (2009) 105028, [arXiv:0906.2087 \[hep-ph\]](#).
- [256] F. Iocco, G. Mangano, G. Miele, O. Pisanti, and P. D. Serpico, “Primordial Nucleosynthesis: from precision cosmology to fundamental physics,” *Phys. Rept.* **472** (2009) 1–76, [arXiv:0809.0631 \[astro-ph\]](#).
- [257] S. Galli, F. Iocco, G. Bertone, and A. Melchiorri, “CMB constraints on Dark Matter models with large annihilation cross-section,” *Phys. Rev.* **D80** (2009) 023505, [arXiv:0905.0003 \[astro-ph.CO\]](#).
- [258] T. R. Slatyer, N. Padmanabhan, and D. P. Finkbeiner, “CMB Constraints on WIMP Annihilation: Energy Absorption During the Recombination Epoch,” *Phys. Rev.* **D80** (2009) 043526, [arXiv:0906.1197 \[astro-ph.CO\]](#).

- [259] G. Hütsi, A. Hektor, and M. Raidal, “Constraints on leptonicly annihilating dark matter from reionization and extragalactic gamma background,” *Astron. & Astrophys.* **505** (Oct., 2009) 999–1005, [arXiv:0906.4550 \[astro-ph.CO\]](#).
- [260] T. Kanzaki, M. Kawasaki, and K. Nakayama, “Effects of Dark Matter Annihilation on the Cosmic Microwave Background,” *Prog. Theor. Phys.* **123** (2010) 853–865, [arXiv:0907.3985 \[astro-ph.CO\]](#).
- [261] P. Boehner, G. Gál, and S. F. Brown, eds., *Scriptum in primum librum sententiarum*, vol. 1 of *Opera theologica*. The Franciscan Institute of St. Bonaventure University, St. Bonaventure (N.Y.), 1967. Prologus, Quaestio 1.
- [262] P. Boehner, G. Gál, and S. F. Brown, eds., *Summa logicae*, vol. 1 of *Opera philosophica*. The Franciscan Institute of St. Bonaventure University, St. Bonaventure (N.Y.), 1974. 1, 12.
- [263] B. Katz, K. Blum, and E. Waxman, “What can we really learn from positron flux ‘anomalies’?,” *Mon. Not. R. Astron. Soc.* **405** (July, 2010) 1458–1472, [arXiv:0907.1686 \[astro-ph.HE\]](#).
- [264] M. Pohl and J. A. Esposito, “Electron acceleration in SNR and diffuse gamma-rays above 1-GeV,” *Astrophys. J.* **507** (1998) 327, [arXiv:astro-ph/9806160](#).
- [265] A. W. Strong and I. V. Moskalenko, “A 3D time-dependent model for galactic cosmic rays and gamma-rays,” [arXiv:astro-ph/0106505](#).
- [266] S. P. Swordy, “Stochastic Effects on the Electron Spectrum above TeV Energies,” in *Proceedings of the 28th International Cosmic Ray Conference, Tsukuba, Japan*, vol. 4 of *International Cosmic Ray Conferences*, pp. 1989–+. July, 2003. [ADS](#).
- [267] W. Feller, *An introduction to probability theory and its applications*. Wiley Series in Probability and Mathematical Statistics. Wiley, New York, 3rd ed., 1971.
- [268] B. V. Gendenko and A. N. Kolmogorov, *Limit Distributions for Sums of Independent Random Variables*. Addison-Wesley, Cambridge, MA, USA, 1954. Trans. and annotated by K. L. Chung.
- [269] J. P. Nolan, *Stable Distributions - Models for Heavy Tailed Data*. Birkhäuser, Boston, 2010. In progress, Chapter 1 online at [academic2.american.edu/~jpnolan](#).
- [270] V. V. Uchaikin and V. M. Zolotarev, *Chance and Stability. Stable Distributions and Their Applications*. VSP, Utrecht, 1999.
- [271] N. J. Shaviv, E. Nakar, and T. Piran, “Natural explanation for the anomalous positron to electron ratio with supernova remnants as the sole cosmic ray source,” *Phys. Rev. Lett.* **103** (2009) 111302, [arXiv:0902.0376 \[astro-ph.HE\]](#).
- [272] G. L. Case and D. Bhattacharya, “A New $\Sigma - D$ Relation and Its Application to the Galactic Supernova Remnant Distribution,” *Astrophys. J.* **504** (1998) 761, [arXiv:astro-ph/9807162](#).
- [273] J. P. Vallée, “The Spiral Arms and Interarm Separation of the Milky Way: An Updated Statistical Study,” *Astron. J.* **130** (Aug., 2005) 569–575.

- [274] S. P. Reynolds, “Supernova Remnants at High Energy,” *Annu. Rev. Astron. Astrophys.* **46** (2008) 89.
- [275] A. W. Strong, I. V. Moskalenko, and V. S. Ptuskin, “Cosmic-ray propagation and interactions in the Galaxy,” *Ann. Rev. Nucl. Part. Sci.* **57** (2007) 285–327, [arXiv:astro-ph/0701517](#).
- [276] R. Blandford and D. Eichler, “Particle Acceleration at Astrophysical Shocks: A Theory of Cosmic Ray Origin,” *Phys. Rept.* **154** (1987) 1–75.
- [277] **The H.E.S.S.** Collaboration, F. Aharonian *et al.*, “Detection of TeV gamma-ray Emission from the Shell-Type Supernova Remnant RX J0852.0-4622 with H.E.S.S.,” *Astron. Astrophys.* **437** (2005) L7, [arXiv:astro-ph/0505380](#).
- [278] **H.E.S.S.** Collaboration, F. Aharonian *et al.*, “Discovery of gamma-ray emission from the shell-type supernova remnant RCW 86 with H.E.S.S.,” *AIP Conf. Proc.* **1085** (2009) 332–335, [arXiv:0810.2689](#) [[astro-ph](#)].
- [279] **H.E.S.S.** Collaboration, F. Aharonian *et al.*, “Chandra and H.E.S.S. observations of the Supernova Remnant CTB 37B,” *Astron. Astrophys.* **486** (2008) 829, [arXiv:0803.0682](#) [[astro-ph](#)].
- [280] **H.E.S.S.** Collaboration, F. Aharonian *et al.*, “A detailed spectral and morphological study of the gamma- ray supernova remnant RX J1713.7-3946 with HESS,” *Astron. Astrophys.* **449** (2006) 223–242, [arXiv:astro-ph/0511678](#).
- [281] **H.E.S.S.** Collaboration, F. Aharonian *et al.*, “Primary particle acceleration above 100-TeV in the shell- type supernova remnant RX J1713.7-3946 with deep HESS observations,” *Astron. Astrophys.* **464** (2007) 235–243, [arXiv:astro-ph/0611813](#).
- [282] **H.E.S.S.** Collaboration, F. Aharonian *et al.*, “Discovery of a VHE gamma-ray source coincident with the supernova remnant CTB 37A,” *Astron. Astrophys.* **490** (2008) 685, [arXiv:0803.0702](#) [[astro-ph](#)].
- [283] **H.E.S.S.** Collaboration, F. Aharonian *et al.*, “HESS very-high-energy gamma-ray sources without identified counterparts,” *Astron. Astrophys.* **477** (2008) 353, [arXiv:0712.1173](#) [[astro-ph](#)].
- [284] W. W. Tian *et al.*, “Discovery of the counterpart of TeV Gamma-ray source HESS J1731-347: a new SNR G353.6-0.7 with radio and X-ray images,” [arXiv:0801.3254](#) [[astro-ph](#)].
- [285] **H.E.S.S.** Collaboration, F. Aharonian *et al.*, “Discovery of very high energy gamma-ray emission coincident with molecular clouds in the W28 (G6.4-0.1) field,” [arXiv:0801.3555](#) [[astro-ph](#)].
- [286] **H.E.S.S.** Collaboration, F. Aharonian *et al.*, “The H.E.S.S. survey of the Inner Galaxy in very high- energy gamma-rays,” *Astrophys. J.* **636** (2006) 777–797, [arXiv:astro-ph/0510397](#).
- [287] **MAGIC** Collaboration, J. Albert *et al.*, “Discovery of VHE Gamma Radiation from IC443 with the MAGIC Telescope,” *Astrophys. J.* **664** (2007) L87–L90, [arXiv:0705.3119](#) [[astro-ph](#)].

- [288] **MAGIC** Collaboration, J. Albert *et al.*, “Observation of VHE gamma-rays from Cassiopeia A with the MAGIC telescope,” *Astron. Astrophys.* **474** (2007) 937–940, [arXiv:0706.4065 \[astro-ph\]](#).
- [289] **H.E.S.S.** Collaboration, A. Fiasson *et al.*, “The Monoceros very-high-energy gamma-ray source,” in *Proceedings of the 30th International Cosmic Ray Conference, Merida*, R. Caballero *et al.*, eds., vol. 2, pp. 719–722. Universidad Nacional Autónoma de México, Mexico City, Mexico, 2008. [arXiv:0709.2550 \[astro-ph\]](#). <http://indico.nucleares.unam.mx/contributionDisplay.py?contribId=581&sessionId=103&confId=4>.
- [290] M. Fatuzzo, F. Melia, and R. M. Crocker, “High-energy activity in the unusually soft TeV source HESS J1804-216 toward the galactic center,” [arXiv:astro-ph/0602330](#).
- [291] **HEGRA** Collaboration, F. Aharonian, “Evidence for TeV gamma ray emission from Cassiopeia A,” *Astron. Astrophys.* **370** (2001) 112–120, [arXiv:astro-ph/0102391](#).
- [292] **H.E.S.S.** Collaboration. H.E.S.S. Source Catalogue. <http://www.mpi-hd.mpg.de/hfm/HESS/pages/home/sources/>.
- [293] E. Mocchiutti, “Results from the PAMELA space experiment.” Talk at 2nd Roma Intern. Conf. on Astroparticle Physics, Rome, 13-15 May 2009, 2009. [slides](#).
- [294] Y. Shikaze *et al.*, “Measurements of 0.2-GeV/n to 20-GeV/n cosmic-ray proton and helium spectra from 1997 through 2002 with the BESS spectrometer,” *Astropart. Phys.* **28** (2007) 154–167, [arXiv:astro-ph/0611388](#).
- [295] P. Blasi and P. D. Serpico, “High-energy antiprotons from old supernova remnants,” *Phys. Rev. Lett.* **103** (2009) 081103, [arXiv:0904.0871 \[astro-ph.HE\]](#).
- [296] B. Beischer, P. von Doetinchem, H. Gast, T. Kirn, and S. Schael, “Perspectives for indirect dark matter search with AMS-2 using cosmic-ray electrons and positrons,” *New J. Phys.* **11** (2009) 105021.
- [297] **H.E.S.S.** Collaboration, F. Aharonian *et al.*, “Very high energy gamma rays from the direction of Sagittarius A*,” *Astron. Astrophys.* **425** (2004) L13–L17, [arXiv:astro-ph/0408145](#).
- [298] **H.E.S.S.** Collaboration, R. C. G. Chaves, E. de Ona Wilhemi, and S. Hoppe, “The H.E.S.S. galactic plane survey,” *AIP Conf. Proc.* **1085** (2009) 219–222.
- [299] **H.E.S.S.** Collaboration, R. C. G. Chaves, “Extending the H.E.S.S. Galactic Plane Survey,” [arXiv:0907.0768 \[astro-ph.HE\]](#).
- [300] A. A. Abdo *et al.*, “TeV gamma-ray sources from a survey of the galactic plane with Milagro,” *Astrophys. J.* **664** (2007) L91–L94, [arXiv:0705.0707 \[astro-ph\]](#).
- [301] **H.E.S.S.** Collaboration, E. de Ona Wilhemi, A. Djannati, and M. Renaud, “The unidentified source HESS J1908+063/MGRO J1908+06,” *AIP Conf. Proc.* **1085** (2009) 273–276.
- [302] A. A. Abdo *et al.*, “Milagro Observations of TeV Emission from Galactic Sources in the Fermi Bright Source List,” *Astrophys. J.* **700** (2009) L127–L131, [arXiv:0904.1018 \[astro-ph.HE\]](#).

- [303] **Fermi LAT** Collaboration, A. A. Abdo *et al.*, “Fermi Large Area Telescope Bright Gamma-ray Source List,” *Astrophys. J. Suppl.* **183** (2009) 46–66, [arXiv:0902.1340 \[astro-ph.HE\]](#).
- [304] M. L. Costantini and F. Vissani, “Expected neutrino signal from supernova remnant RX J1713.7-3946 and flavor oscillations,” *Astropart. Phys.* **23** (2005) 477–485, [arXiv:astro-ph/0411761](#).
- [305] F. Vissani, “Neutrinos from galactic sources of cosmic rays with known gamma-ray spectra,” *Astropart. Phys.* **26** (2006) 310–313, [arXiv:astro-ph/0607249](#).
- [306] F. L. Villante and F. Vissani, “How precisely neutrino emission from supernova remnants can be constrained by gamma ray observations?,” *Phys. Rev.* **D78** (2008) 103007, [arXiv:0807.4151 \[astro-ph\]](#).
- [307] L. Anchordoqui, F. Halzen, T. Montaruli, and A. O’Murchadha, “Neutrino Flux from Cosmic Ray Accelerators in the Cygnus Spiral Arm of the Galaxy,” *Phys. Rev.* **D76** (2007) 067301, [arXiv:astro-ph/0612699](#).
- [308] M. D. Kistler and J. F. Beacom, “Guaranteed and prospective galactic TeV neutrino sources,” *Phys. Rev.* **D74** (2006) 063007, [arXiv:astro-ph/0607082](#).
- [309] J. F. Beacom and M. D. Kistler, “Dissecting the Cygnus Region with TeV Gamma Rays and Neutrinos,” *Phys. Rev.* **D75** (2007) 083001, [arXiv:astro-ph/0701751](#).
- [310] F. Halzen and A. O Murchadha, “Neutrinos from cosmic ray accelerators in the Cygnus region of the galaxy,” *Phys. Rev.* **D76** (2007) 123003, [arXiv:0705.1723 \[astro-ph\]](#).
- [311] F. Halzen, A. Kappes, and A. O’Murchadha, “Prospects for identifying the sources of the Galactic cosmic rays with IceCube,” *Phys. Rev.* **D78** (2008) 063004, [arXiv:0803.0314 \[astro-ph\]](#).
- [312] M. C. Gonzalez-Garcia, F. Halzen, and S. Mohapatra, “Identifying Galactic PeVatrons with Neutrinos,” *Astropart. Phys.* **31** (2009) 437–444, [arXiv:0902.1176 \[astro-ph.HE\]](#).
- [313] **IceCube** Collaboration, R. Abbasi *et al.*, “Search for Point Sources of High Energy Neutrinos with Final Data from AMANDA-II,” *Phys. Rev.* **D79** (2009) 062001, [arXiv:0809.1646 \[astro-ph\]](#).
- [314] **IceCube** Collaboration, R. Abbasi *et al.*, “First Neutrino Point-Source Results From the 22-String IceCube Detector,” *Astrophys. J.* **701** (2009) L47–L51, [arXiv:0905.2253 \[astro-ph.HE\]](#).
- [315] M. Kachelriess, S. Ostapchenko, and R. Tomas, “Antimatter spectra from a time-dependent modeling of supernova remnants,” [arXiv:1004.1118 \[astro-ph.HE\]](#).
- [316] D. Müller and K. K. Tang, “The Cosmic Ray Positron Enigma,” in *International Cosmic Ray Conference*, vol. 3 of *International Cosmic Ray Conference*, pp. 249–+. 1990. [ADS](#).
- [317] R. N. Manchester, G. B. Hobbs, A. Teoh, and M. Hobbs, “The ATNF Pulsar Catalogue,” *Astron. J.* **129** (2005) 1993, [arXiv:astro-ph/0412641](#).
- [318] D. Hooper, P. Blasi, and P. D. Serpico, “Pulsars as the Sources of High Energy Cosmic Ray Positrons,” *JCAP* **0901** (2009) 025, [arXiv:0810.1527 \[astro-ph\]](#).

- [319] H. Yuksel, M. D. Kistler, and T. Stanev, “TeV Gamma Rays from Geminga and the Origin of the GeV Positron Excess,” *Phys. Rev. Lett.* **103** (2009) 051101, [arXiv:0810.2784 \[astro-ph\]](#).
- [320] K. Ioka, “A Gamma-Ray Burst/Pulsar for Cosmic-Ray Positrons with a Dark Matter-like Spectrum,” *Prog. Theor. Phys.* **123** (2010) 743–755, [arXiv:0812.4851 \[astro-ph\]](#).
- [321] AMS Collaboration. AMS Webpage. <http://ams.cern.ch/>.
- [322] Y. Fujita *et al.*, “Is the PAMELA anomaly caused by the supernova explosions near the Earth?,” *Phys. Rev.* **D80** (2009) 063003, [arXiv:0903.5298 \[astro-ph.HE\]](#).
- [323] T. W. Berghoefer and D. Breitschwerdt, “The origin of the young stellar population in the solar neighborhood - a link to the formation of the Local Bubble?,” *Astron. & Astrophys.* **390** (July, 2002) 299–306, [arXiv:arXiv:astro-ph/0205128](#).
- [324] D. Breitschwerdt and M. A. de Avillez, “The History and Future of the Local and Loop I Bubbles,” *Astron. & Astrophys.* **452** (June, 2006) L1–L5, [arXiv:astro-ph/0604162](#).
- [325] R. Cowsik and S. Sarkar, “The evolution of supernova remnants as radio sources,” *Mon. Not. R. Astron. Soc.* **207** (1984) 745. [ADS](#).
- [326] M. Pohl *et al.*, “Section on Supernova remnants and cosmic rays of the White Paper on the Status and Future of Ground-based Gamma-ray Astronomy,” [arXiv:0810.0673 \[astro-ph\]](#).
- [327] Y. Butt, “Beyond the myth of the supernova-remnant origin of cosmic rays,” *Nature* **460** (2009) 701.
- [328] O. Adriani *et al.*, “A new measurement of the antiproton-to-proton flux ratio up to 100 GeV in the cosmic radiation,” *Phys. Rev. Lett.* **102** (2009) 051101, [arXiv:0810.4994 \[astro-ph\]](#).
- [329] G. M. Webb, L. O. Drury, and P. Biermann, “Diffusive shock acceleration of energetic electrons subject to synchrotron losses,” *Astron. & Astrophys.* **137** (Aug., 1984) 185–201. [ADS](#).
- [330] R. Silberberg and C. H. Tsao, “Partial Cross-Sections in High-Energy Nuclear Reactions, and Astrophysical Applications. I. Targets With $z \leq 28$,” *Astrophys. J. Suppl.* **25** (Apr., 1973) 315–333.
- [331] R. Silberberg and C. H. Tsao, “Comparison of methods for calculating cross sections at high energies in astrophysics,” *Astrophys. J. Suppl.* **35** (Oct., 1977) 137–144.
- [332] R. Silberberg and C. H. Tsao, “Spallation processes and nuclear interaction products of cosmic rays,” *Phys. Rep.* **191** (Aug., 1990) 351–408. [ADS](#).
- [333] V. I. Zatsepin *et al.*, “Energy dependence of Ti/Fe ratio in the Galactic cosmic rays measured by the ATIC-2 experiment,” *Astronomy Letters* **35** (May, 2009) 338–342, [arXiv:0905.0049 \[astro-ph.HE\]](#).

- [334] **Copenhagen - Saclay** Collaboration, V. Vylet *et al.*, “Energy Spectra Between 10 and Several Hundred GeV/Nucleon for Elements From $_{18}\text{Ar}$ to $_{23}\text{V}$: Results from HEAO-3,” in *Proceedings of the 21st International Cosmic Ray Conference, Adelaide, Australia*, vol. 3 of *International Cosmic Ray Conference*, pp. 19–+. 1990. [ADS](#).
- [335] A. D. Panov *et al.*, “Relative abundances of cosmic ray nuclei B-C-N-O in the energy region from 10 GeV/n to 300 GeV/n. Results from ATIC-2 (the science flight of ATIC),” [arXiv:0707.4415 \[astro-ph\]](#). Proc. 30th International Cosmic Ray Conference, Merida, ed. T. Caballero and others (Mexico City: Universidad Nacional Autonoma de Mexico, 2007).
- [336] H. S. Ahn *et al.*, “Measurements of cosmic-ray secondary nuclei at high energies with the first flight of the CREAM balloon-borne experiment,” *Astropart. Phys.* **30** (2008) 133–141, [arXiv:0808.1718 \[astro-ph\]](#).
- [337] **PAMELA** Collaboration, P. Picozza, “Detection of antimatter in our galaxy.” Talk at “TAUP 2009”, International Conference on Topics in Physics and Astrophysics, Laboratori Nazionali del Gran Sasso, 1-5 July 2009. [slides](#).
- [338] **PAMELA** Collaboration, R. Spavoli, “Understanding cosmic rays and searching for dark matter with pameela.” Talk at “AXION-WIMP 2010”, The 6th Patras Workshop on Axions, WIMPs and WISPs, Zürich University, 5-9 July 2010. [slides](#).
- [339] M. Simet and D. Hooper, “Astrophysical Uncertainties in the Cosmic Ray Electron and Positron Spectrum From Annihilating Dark Matter,” *JCAP* **0908** (2009) 003, [arXiv:0904.2398 \[astro-ph.HE\]](#).
- [340] D. Campana *et al.*, “Capability of the PAMELA Time-Of-Flight to identify light nuclei: results from a beam test calibration,” *Nucl. Instrum. Meth.* **A598** (2009) 696–701, [arXiv:0810.3830 \[astro-ph\]](#).
- [341] A. Kounine, “Status of the AMS Experiment.” Talk at TeV Particle Astrophysics, Paris, 19-23 July 2010, 2010. [slides](#).
- [342] A. de Oliveira-Costa *et al.*, “The Quest for Microwave Foreground X,” *Astrophys. J.* **606** (2004) L89–L92, [arXiv:astro-ph/0312039](#).
- [343] E. M. Berkhuijsen, “A Survey of the Continuum Radiation at 820 MHz between Declinations -7° and 85° . A Study of the Galactic Radiation and the Degree of Polarization with Special Reference to the Loops and Spurs,” *Astron. & Astrophys.* **14** (Oct., 1971) 359–+. [ADS](#).
- [344] D. R. Lorimer, “The Galactic population and birth rate of radio pulsars,” [arXiv:astro-ph/0308501](#).
- [345] D. R. Lorimer *et al.*, “The Parkes multibeam pulsar survey: VI. Discovery and timing of 142 pulsars and a Galactic population analysis,” *Mon. Not. R. Astron. Soc.* **372** (2006) 777–800, [arXiv:astro-ph/0607640](#).
- [346] B. Paczynski, “A test of the galactic origin of gamma-ray bursts,” *Astrophys. J.* **348** (Jan., 1990) 485–494.

- [347] S. J. Sturmer and C. D. Dermer, “Statistical Analysis of Gamma-Ray Properties of Rotation-powered Pulsars,” *Astrophys. J.* **461** (Apr., 1996) 872–+. [ADS](#).
- [348] A. W. Strong and I. V. Moskalenko, “A Galactic Cosmic-Ray Database,” [arXiv:0907.0565 \[astro-ph.HE\]](#).
- [349] R. Beck, “Measuring interstellar magnetic fields by radio synchrotron emission,” [arXiv:0812.4925 \[astro-ph\]](#).
- [350] C. G. T. Haslam *et al.*, “A 408 MHz all-sky continuum survey. II - The atlas of contour maps,” *Astron. & Astrophys. Suppl. Series* **47** (Jan., 1982) 1–+. [ADS](#).
- [351] E. Orlando *et al.*, “Cosmic-ray electrons, synchrotron and magnetic fields in the Galaxy,” [arXiv:0907.0553 \[astro-ph.GA\]](#).
- [352] S. Phillipps *et al.*, “Distribution of galactic synchrotron emission. II,” *Astron. & Astrophys.* **103** (Nov., 1981) 405–414. [ADS](#).
- [353] M. McQuinn and M. Zaldarriaga, “Testing the Dark Matter Annihilation Model for the WMAP Haze,” [arXiv:1004.1189 \[astro-ph.HE\]](#).
- [354] **WMAP** Collaboration, C. Bennett *et al.*, “First Year Wilkinson Microwave Anisotropy Probe (WMAP) Observations: Foreground Emission,” *Astrophys. J. Suppl.* **148** (2003) 97, [arXiv:astro-ph/0302208](#).
- [355] S. Sarkar, “Does the galactic synchrotron radio background originate in old supernova remnants,” *Mon. Not. R. Astron. Soc.* **199** (Apr., 1982) 97–108. [ADS](#).